

Diss. ETH No. 27701

Investigation of Surface Dynamics in Lithium ion Batteries

A thesis submitted to attain the degree of
DOCTOR OF SCIENCES of ETH Zürich

(Dr. Sc. ETH Zürich)

presented by

PETER BENEDEK

M. Sc. ETH in Interdisciplinary Sciences

born December 26, 1990

citizen of Aarwangen, BE, Switzerland

accepted on the recommendation of

Prof. Dr. Vanessa Wood, examiner

Prof. Dr. Nicola Spaldin, co-examiner

Dr. Fanni Jurányi, co-examiner

benedekp@ethz.ch

2021

Institute for Electronics
ETH Zürich
Gloriastrasse 35
8092 Zürich
Switzerland



MaDE
Materials and Device
Engineering Group

Acknowledgments

This PhD thesis would have never been possible without the aid of numerous people and institutions. I am very grateful for the financial support from European Research Council. I thank the ISIS and the SINQ neutron and muon sources that have awarded numerous days of beam time with very dedicated beam line scientists. In addition, I would like to thank the ScopeM center of microscopy at ETH Zürich and the Piz Daint Supercomputer for allowing me to use their resources to study interface effects. The group of Prof. Dr. Sotiris Pratisnis is thanked for giving me access to his BET system. Dr. Marisa Medarde is acknowledged for her magnetic characterization measurements. Also I appreciate the support of Prof. Dr. Jun Sugiyama who provided an old sample of LiFePO_4 that he analyzed via $\mu^+\text{SR}$ in an earlier publication [181].

Special thanks go to my supervisor Prof. Dr. Vanessa Wood for an environment where I had the freedom to evolve as a scientist and got all the support needed to pursue this project. I am also extremely thankful for every single member of the Institute for Electronics for their scientific, emotional, and moral support. I will always cherish the time that I spent with all my coworkers.

I also acknowledge all my seven students during my doctoral studies. It was a giant privilege to work with Xueyan Zhao, Ryo Asakura, Simone Fasciati, Samuel Zumtaugwald, Pascal Jud, Melis Yetkin, and Jean-Marc Sujata who all pivoted from different research disciplines to Li ion batteries and brought wonderful new insights into my projects, eventually teaching me at least as much as I taught them.

Special thanks go to all my collaborators who supported me to work in many scientific disciplines out of my core expertise. I will never forget the many hours I spent at beam times together with Dr. Fanni Juranyi, Prof. Dr Yasmine Sassa and the SMaRT team around Prof. Dr. Martin Månson, Ola Forslund, Elisabetty Nocerino, and Dr. Nami Matsubara. The many scientific discussions that we had during these times have paved the way to a vast number of additional experiments and calcula-

tions.

I would also like to thank Prof. Dr. Saiful Islam, Dr. Hungru Chen and Dr. Nuri Yazdani who assisted me in learning the necessary skills in density functional theory simulations. Big thanks go also to Emanuel Billeter and Dr. Andreas Borgschulte who introduced me to the intricacies of x-ray photoemission spectroscopy over very insightful dinners.

I am also grateful about the numerous smaller collaborations that are not related to this thesis directly but shaped me as a scientist. I would especially like to thank Joel Winiger, and Prof Dr. Jürg Leuthold for the great team work for the co-development of a method to scalably synthesize BaTiO₃ thin films for plasmonic modulation.

I thank Prof. Dr. Nicola Spaldin and Dr. Fanni Jurányi for agreeing to be part of the doctoral comitee. Even though they are not experts in Li ion batteries, their expertise in material modelling, neutron scattering, and muon spin spectroscopy have allowed me to learn always something new the meetings I had with them.

Finally, I would like to thank my family, my girlfriend Céline Prange, and all my friends. Without their continuous moral support, dedication, and example, I would have never managed to embark in a career in science.

Zürich, August 2021

Peter Benedek

Abstract

To be able to solve the 21st century's renewable energy challenge, energy storage is key. While numerous strategies have been proposed and implemented for stationary energy storage, so far only lithium ion batteries have had large success for mobile applications such as cars and smartphones. However, to be able to further penetrate the market, improvements in charging speeds are critical. Therefore, strategies to characterize and reduce ionic and electronic resistances at the material interfaces are required. This doctoral thesis introduces a new strategy to quantify ion diffusion at interfaces of commercially relevant materials by applying a combination of i) morphology controlled synthesis, ii) experiments at large scale facilities, iii) *ab initio* molecular modelling, and iv) electrochemical measurements. We provide a full picture of the underlying processes that induce changes in charge dynamics hence paving the way to new strategies to engineer interfaces.

Part 1 introduces the challenges in LIB technology and what large scale facilities can contribute towards their solution. Thanks to the large public attention that LIBs have attracted, numerous new experiments at synchrotrons and other particle accelerators have been adapted to the special needs of lithium ion batteries in the last decade, creating new opportunities for an understanding and optimization of the complex interactions within the LIB.

Part 2 focuses on the morphology controlled hydrothermal synthesis of LiFePO_4 platelet particles. We introduce a novel low-temperature synthesis of micrometer sized platelet particles that maintain a high crystallinity. We end up with a size series of particles with different surface to volume ratios, offering the possibility to track surface effects. By in-

roducing coatings, we can then actively change the surface environment.

Part 3 studies the effect of the surface reconstruction on lattice vibrations. Performing inelastic neutron scattering experiments on the size series synthesized earlier, we can separate bulk and surface effects. We find changes in the Fe–O and Li–O phonon modes at the LiFePO₄-carbon interface hence suggesting changes in the charge dynamics. Following up on these results, we quantify the activation barrier of interface diffusion in **Part 4** via a combination of muon spin spectroscopy, electrochemical characterizations, and nudged elastic band simulations. With an activation barrier of ~ 180 meV, the Li diffusion barrier through the LiFePO₄ (010) surface is strongly reduced.

In **Part 5** we add more complexity to our system by characterizing the impact of surface terminations to charge dynamics. Extending our approach to electronics, we get important insights in the full mechanism of interface dynamics. We find that the strongly enhanced interface ion dynamics in carbon coatings are in fact a result of enhanced electronic transport that allows for decoupled ion and electron motion. Based on this finding, we rationally engineer particle coatings that can homogeneously (de)lithiate cathode active materials hence creating coatings that allow for longer active material lifetime without affecting charging rate capability.

Zusammenfassung

Damit die Stromversorgung des 21. Jahrhunderts durch erneuerbare Energien zu ermöglichen, ist Energiespeicherung eine grosse Herausforderung. Insbesondere die Speicherung von Energie für lokale und mobile Anwendungen (z.B. im Transportsektor) setzt hohe Ansprüche an die Energiedichte und Lebensdauer welche bis dato nur durch Lithium-Ionen-Akkumulatoren (LIBs) erreicht werden kann. Um jedoch weitere Akzeptanz in der Bevölkerung zu erreichen, sind Verbesserungen der Ladegeschwindigkeiten von entscheidender Bedeutung. Dies kann aber nur erreicht werden wenn Widerstände zwischen den Grenzflächen der Batteriekomponenten charakterisiert und optimiert werden können. Diese Doktorarbeit stellt eine neue Strategie zur Quantifizierung der Ladungsträgerdiffusion an Grenzflächen kommerziell relevanter Materialien vor, die auf einer Kombination aus i) morphologiekontrollierter Synthese, ii) Experimenten in Teilchenbeschleunigern, iii) *ab initio* molekularer Modellierung und iv) elektrochemischen Messungen basiert. Es entsteht ein vollständiges Bild der zugrunde liegenden Transportmechanismen, die so durch gezielte Fortschritte im Bereich der Materialbeschichtungen den Weg zu neuen Technologien ebnen.

Teil 1 der Doktorarbeit setzt den Fokus ganz auf neue Experimente die durch Teilchenbeschleunigern ermöglicht werden. Dank der großen öffentlichen Aufmerksamkeit die LIBs auf sich gezogen haben, sind im letzten Jahrzehnt zahlreiche dieser Experimente an die besonderen Bedürfnisse von Lithium-Ionen-Akkumulatoren angepasst und komplexe Wechselwirkungen abgebildet worden. Nach einem kurzen Einblick in die Komplexität der stattfindenden Reaktionen in Akkumulatoren, werden in diesem Teil Experimente an Synchrotrons, Neutronenquellen, Elektronenmikroskopen und Myonen-Quellen vorgestellt. Am Ende des Kapitels folgt ein Ausblick in die zukünftige Entwicklung der Teilchenbeschleuni-

ger und wie sie weiter die Zukunft der LIBs prägen werden.

Teil 2 konzentriert sich auf die kontrollierte hydrothermale Synthese von LiFePO_4 - Plättchenpartikeln. Eine neuartige Niedertemperatur-synthese von mikrometergroßen LiFePO_4 Plättchen wird vorgestellt, die neben der Partikelgrösse eine hohe Kristallinität aufweist. Basierend auf dieser Synthese werden dann Partikel mit verschiedenen Grössen und damit unterschiedlichen Oberflächen-Volumen Verhältnissen hergestellt. Durch das Beschichten dieser Partikel können die Oberflächenumgebung aktiv verändert und Oberflächeneffekte gesteuert werden.

Teil 3 untersucht die Auswirkung der Oberflächenrekonstruktion auf Gitterschwingungen. Durch inelastische Neutronenstreuungsexperimente an den zuvor synthetisierten Partikeln verschiedener Grösse können wir Volumen und Oberflächeneffekte trennen. Änderungen in den Fe-O- und Li-O-Phonon-Schwingungsmoden an der LiFePO_4 - Kohlenstoff-Grenzfläche die auf Änderungen im Ladungstransport hindeuten, werden gemessen und analysiert. Um den Einfluss dieser Oberflächenveränderungen auf die Lithiumdiffusion zu verstehen, wird die Aktivierungsbarriere der Grenzflächendiffusion in **Teil 4** über eine Kombination aus Myonen-spinspektroskopie, elektrochemischen Charakterisierungen und Nudged Elastic Band Simulationen charakterisiert. Eine stark reduzierte Lithium Diffusionsaktivierungsbarriere von ~ 200 meV wird entdeckt.

In **Teil 5** wird der Einfluss verschiedener Oberflächenbeschichtungen im Ladungstransport betrachtet. Durch die Ausweitung der Studien auf sowohl die ionische als auch die elektronische Leitfähigkeit werden wichtige Einblicke in den vollständigen Mechanismus des Grenzflächentransports erhalten. Es stellt sich heraus, dass der verbesserte Li-Ionentransport an der LiFePO_4 - Kohlenstoff Grenzfläche ein Ergebnis eines verbesserten elektronischen Transports ist, der eine entkoppelte Ionen- und Elektronenbewegung ermöglicht. Basierend auf diesen Erkenntnissen konstruieren wir eine Partikelbeschichtung, die Elektrodenmaterialien homogen (ent)laden können, und dadurch ohne Beeinträchtigung der Ladezeit eine längere Lebensdauer der LIBs ermöglichen.

Contents

Abstract	v
Zusammenfassung	vii
Nomenclature	xiii
1 Part I: The role of Large Scale Facilities in Li ion Battery Research	1
1.1 Motivation	1
1.2 Photon Large Scale Facilities	4
1.3 Neutron Large Scale Facilities	12
1.4 Electron Microscopy Centers	17
1.5 Spin-Polarized Beams at Large Scale Facilities	21
1.6 Summary and Outlook	25
2 Part II: Morphology Control in the Synthesis of LiFePO₄ Nanoparticles	31
2.1 Remarks on Part II	31
2.2 Low-Temperature Hydrothermal Synthesis of LiFePO ₄	32
2.3 LiFePO ₄ Platelet Size Control	41
2.4 Coating LiFePO ₄ Nanoparticles	44
2.5 Part II: Summary	47
3 Part III: Studying Surface Phonons of Li ion Battery active materials	49
3.1 Remarks on Part III	49
3.2 Motivation	49
3.3 Results and Discussion	52
3.4 Summary	58

4	Part IV: Quantifying Diffusion through Battery Interfaces	59
4.1	Remark on Part IV	59
4.2	Motivation	60
4.3	<i>Ab initio</i> Calculations	63
4.4	Muon Spin Spectroscopy Measurements	65
4.5	Electrochemical Characterization	69
4.6	Discussion and Conclusion	71
5	Part V: Controlling Li ion battery (de)intercalation dynamics through interface design	73
5.1	Remarks on Part V	73
5.2	Motivation	75
5.3	Rationale for the investigated system	79
5.4	Investigation of ion dynamics in LiFePO_4	82
5.5	Consequences for the Li (de)intercalation	88
5.6	Decoupling Electronic and Ionic Transport	91
5.7	Conclusion and Outlook	93
6	Concluding Remarks	95
6.1	Summary	95
6.2	Outlook	96
A	Supporting Information to Part I	101
A.1	Experimental Methods	101
A.2	Low Temperature Synthesis of LFP: Electrochemical Characterization	103
A.3	Energy Consumption Analysis	104
A.4	X-ray diffraction and Rietveld refinement	108
A.5	Sampling Tool	110
A.6	Electrochemistry of the LFP sample after 48 h of synthesis	112
A.7	Time dependence of energy consumption	113
A.8	Carbon Coating Step	114
A.9	Size and Morphology Analysis	115
	Appendix	101

B	Supporting Information to Part III	121
B.1	Experimental Methods	121
B.2	Preparation of FePO_4 particles via electrochemical delithiation	123
B.3	Electrochemical performance	126
B.4	$^7\text{LiFePO}_4$ platelet particles: Transmission electron microscopy (TEM) images	128
B.5	Inelastic neutron scattering measurements	129
B.6	Impurity and defect analysis	132
B.7	Rietveld refinement	134
B.8	Density functional theory calculations: Slabs	135
B.9	Density functional theory calculations: Bond length distribution	136
C	Supporting Information to Part IV	139
C.1	Experimental Methods	139
C.2	<i>Ab initio</i> Calculations	143
C.3	Morphology of the LiFePO_4 platelet samples	144
C.4	LiFePO_4 structure and impurity analysis	146
C.5	μ^+ SR spectral analysis	148
C.6	Electrochemical Characterization	159
D	Supporting Information to Part V	163
D.1	Experimental Methods	163
D.2	Muon spin spectroscopy analysis: Fitting Approach	174
D.3	Muon spin spectroscopy: Validation of fitting parameters	177
	Bibliography	219
	Curriculum Vitae	249

Nomenclature

Acronyms

LIB	Lithium ion battery
FEL	Free electron laser
Linac	Linear accelerator
SAXS	Small angle x-ray scattering
WAXS	Wide angle x-ray scattering
XRD	X-ray Diffraction
PDF	Pair distribution function
XAS	X-ray absorption spectroscopy
XANES	X-ray absorption near edge structure
EXAFS	Extended x-ray absorption fine structure
RIXS	Resonant inelastic x-ray scattering
(X)CT	(X-ray) Computed tomography
PXCT	Ptychographic x-ray computed tomography (also coherent bragg diffraction imaging, CDBI)
TXM	Transmission x-ray microscopy
NPD	Neutron powder diffraction
SANS	Small angle neutron scattering
NDP	Neutron depth profiling
QENS	Quasi-elastic neutron scattering
INS	Inelastic neutron scattering
SEM	Scanning electron microscopy
(S)TEM	(Scanning) Transmission electron microscopy
EDS	Energy-dispersive x-ray scattering (also EDX, EDXS)
EDS-STEM	Energy-dispersive x-ray scattering scanning transmission electron microscopy
ED	Electron diffraction

Nomenclature

EELS	Electron energy loss spectroscopy
cryo-EM	Cryogenic electron microscopy
FIB SEM	Focused ion beam scanning electron microscopy
μ^+ SR	Muon spin spectroscopy (or Muon spin resonance)
NMR	Nuclear magnetic resonance
DNP-NMR	Dynamic nuclear polarization nuclear magnetic resonance
EPR	Electron paramagnetic resonance
CV	Cyclic Voltammetry
GITT	Galvanostatic intermittent titration
EIS	Electrochemical impedance spectroscopy
FTIR	Fourier transform infrared spectroscopy
ATR	Attenuated total reflection
AFM	Atomic force microscopy
XPS	X-ray photoemission spectroscopy

CBD	Carbon black - binder domain
SEI	Solid electrolyte interphase
LFP	Lithium iron(II) phosphate, LiFePO_4
EG	Ethylene glycol
C_{tot}	Precursor concentration
$L_{[010]}$	[010] Channel length
$d_{(010)}$	(010) Platelet particle diameter
1 C	1 full battery charge in 1 hour

DFT	Density functional theory
PDOS	Phonon density of states
NEB	Nudged elastic band (in the context of simulations)
AIMD	<i>Ab initio</i> molecular dynamics

1 Part I: The role of Large Scale Facilities in Li ion Battery Research

1.1 Motivation

As suitable energy storage devices for renewable energy, lithium ion batteries (LIBs) are a crucial part to achieve a net carbon neutral society. Yet, to fulfill the vast challenges regarding energy storage in the future, further development in LIB technologies are essential. Thereby, the key objective is to increase three performance parameters (without increasing the cost per kWh): *energy density*, *rate capability*, and *cycle life* (**Figure 1.1a**). This target, however, is not simple at all [115, 218]. The materials used in LIBs cover basically all the known material classes from organic liquid electrolytes and binder polymers over to transition metal oxide ceramics and metallic current collectors [145, 161]. They form an interwoven structural network with a multitude of interfaces. As a result, not just the materials but also the interfaces between the materials in their 3D structure have to be understood and stabilized [36, 115]. This makes optimizations in LIBs a multiscale problem with characteristic length scales spanning ten orders of magnitude from Ångstroms to Meters [118].

While such an analysis is already challenging in a static case, a continuous flow of electrons and ions takes place during, LIB operation. Thus, the materials and the structure will change upon battery cycling and create both chemical and mechanical stresses that destabilize the material interfaces [17, 118]. In addition, the relevant dynamics in LIBs occur

with characteristic time scales ranging from local ion transport ($t \sim 1$ ps) to battery aging ($t \sim 1$ a) spanning eighteen orders of magnitude [67]. As a result, a very detailed understanding of the reactions that occur in LIBs is required for rational optimization.

Due to all these intricacies, an understanding of the key processes in LIBs cannot be met with electrochemical characterizations alone and even supporting measurements using laboratory scale equipment quickly reach their experimental limits. As a result, most experimental research involved in understanding the complex interactions that occur in LIBs rely on an additional key ingredient: *experiments at shared large-scale facilities*.

On a completely pragmatic view, there is little difference between large-scale facilities and lab scale equipment except for their size (Figure 1b). Similar to lab equipment, beam lines at large-scale facilities can only provide beams of x-ray photons, neutrons, electrons, and spin-polarized particles. These beams will then interact with the sample via the same five general mechanism as in any other lab equipment: reflection, absorption, transmission, (in)elastic diffraction, and (induced) decay. Both the particles and their interactions are independent of the setup's size.

The only difference of large-scale facilities is their design. Compared to lab scale equipment typically bought from companies, large-scale facilities can be seen as complex experimental sites where beamline scientist constantly try to improve the provided experimental environment. As a result, not just the particle beam brilliance but also the beamline optics, energy, the sample environment, and particle detection can create ever improving new possibilities such as novel *operando* LIB measurements [15].

In the following, we will discuss how large scale facilities have been able to contribute to the understanding of LIBs. We will also mention some of the limitations of the setups and efforts to overcome those in near future.

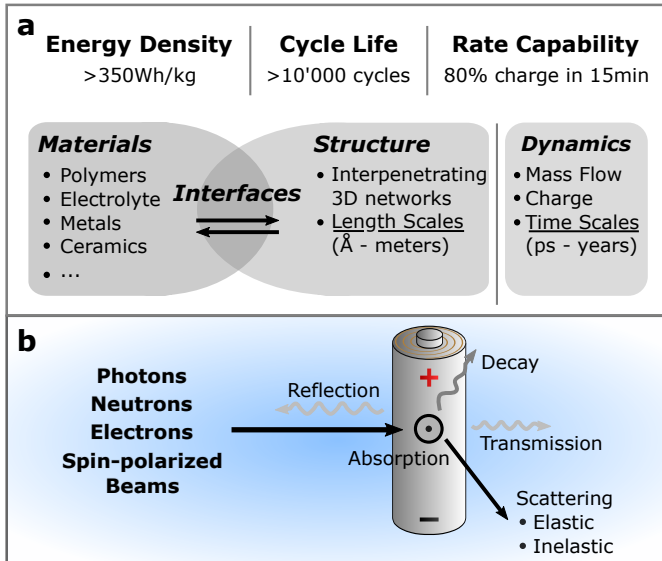


Figure 1.1: a) Future LIB technologies targets for energy density, cycle lifetime and rate capabilities. To meet these targets the challenges between materials, (micro)structure, and interfaces have to be solved in the highly dynamic Li ion battery. b) Summary of all the techniques that can be provided at large-scale facilities with their matter of interaction within the studied samples.

1.2 Photon Large Scale Facilities

Characterization of matter with the aid of photons can be considered as the parent of all characterization techniques. Starting with wave optics and luminescence experiments, the interaction of photons with materials is well understood and has created a vast number of spectroscopical methods. Especially photons with wavelength close to interatomic distances, i.e., *x-rays*, have received large attention due to their high energy, their scattering interaction with the electronic structure of the system, and deep penetration depth.

There are different ways to generate x-rays. On a lab scale, they are often generated in x-ray tubes where an accelerated electron hits a metal target thereby causing characteristic photon radiation. In large scale facilities such as synchrotrons and free electron lasers, x-rays are generated by undulating high energy electrons. Using the second method, one can achieve extremely high x-ray beam brilliance and coherence, resulting in unmatched x-ray flux.

The most commonly used method to study LIB materials is x-ray scattering. X-ray scattering is well established on a laboratory scale and can provide structural information of electrode materials. One can distinguish two types of x-ray scattering: small angle x-ray scattering (SAXS) and wide angle x-ray scattering (WAXS or XRD). Both methods can be measured very well on a laboratory scale with high resolution x-ray scattering spectra available in minutes [25, 175].

When moving to *in operando* scattering, however, the time resolution may not be sufficient anymore. In this case, the high intensity of the synchrotron beam can offer full spectra in periods as short as four seconds hence allowing to study lattice dynamics in LIBs at (dis)charging rates of 10 C and a very high resolution (1 C describes a full charge in one hour) [114]. As a result, structural transitions and kinetic effects can be obtained at commercially relevant time scales.

Another disadvantage of lab-scale setups is the relatively large field of view (typically in the range of cm). The x-ray optics combined with the high intensity of synchrotrons allow to resolve local inhomogeneities in LIBs, such as the formation of lithiation phases in a graphite electrode as a function of distance from the separator (see **Figure 1.2a**) [228]. Using this experiment, ionic gradients within a graphite electrode can be resolved (**Figure 1.2b**), providing visual proof how the effective transport of the electrolyte through the anode becomes rate-limiting [53].

While XRD can resolve very small repetition units such as lattice constants, SAXS can provide information about the nanostructure of system e.g. pore sizes and particle shapes. Again, synchrotron measurements can offer faster *in operando* measurements that facilitate studying the electrochemical double layer in confined nanoporous systems [157]. Also, thanks to the large detectors at synchrotrons, a simultaneous measurement of XRD and SAXS is possible and allows for a calculation of the pair distribution function (PDF). As a result, intercalation reactions [76, 176] and the growth of interphases [170, 190] can be studied at very high detail.

With their relatively large energy, x-rays can be absorbed by atoms and excite core electrons to a free electronic state. Thereby, x-ray absorption spectroscopy (XAS), or more specifically, x-ray absorption near-edge structure (XANES) and extended x-ray absorption fine structure (EXAFS) are methods to analyze the chemical environment and the oxidation state of the respective atoms. This makes EXAFS/XANES experiments especially suitable to study the mechanisms of electrode material reduction and oxidation. Especially, transition metal oxide cathodes that contain multiple transition metals have benefited by XAS as it could determine the electroactive species at a certain potential *in operando* [146, 187]. Furthermore, XAS can assist in understanding the electrochemical reactions at very high voltages, e.g. when LiCoMnO_4 is charged to a voltage of 5.3 V [38].

Similar to XAS, resonant inelastic x-ray scattering (RIXS) absorbs x-rays to excite a core electron to a free electronic state. This creates a core

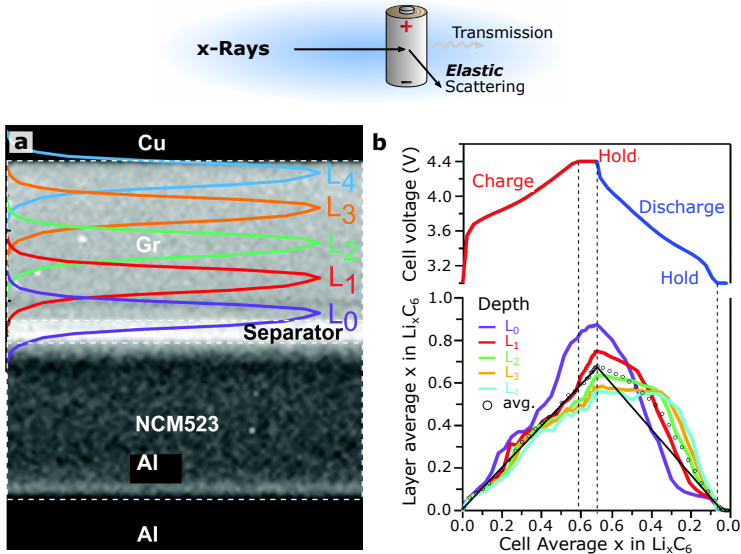


Figure 1.2: a) Projection of a cross section of a $\text{LiNi}_{0.5}\text{Co}_{0.2}\text{Mn}_{0.3}\text{O}_2$ versus graphite electrode. The L_0 - L_4 regions depict the layers of x-ray diffraction (XRD) measurements. b) Operando XRD measurements of the regions L_0 - L_4 show that the average Li content in the graphite layer is not uniform but rather highest close to the separator while charging. Conversely, the Li concentrations requires the longest time to reduce in the L_4 region. The images are adapted from [228].

hole state that subsequently is filled by an electron in the valence band while releasing x-rays to reach to lower energy state. As a result, RIXS can give insights about the valence band energies and binding states, making it an effective tool to study the partial density of states of a given element [222]. In LIBs, it can be used to analyze structural transitions and the resulting changes in the density of states. Using RIXS together with *ab initio* simulations has shown that the oxygen redox feature in the RIXS spectra of $\text{Li}_2\text{Ir}_{1.5}\text{Sn}_{0.5}\text{O}_3$ (Figure 1.3a) is closely coupled to the formation of Li-Sn/Ir antisite defects (Figure 1.3b) which shift the oxygen partial density above the fermi level (Figure 1.3c) and cause the oxygen oxidation reaction [93].

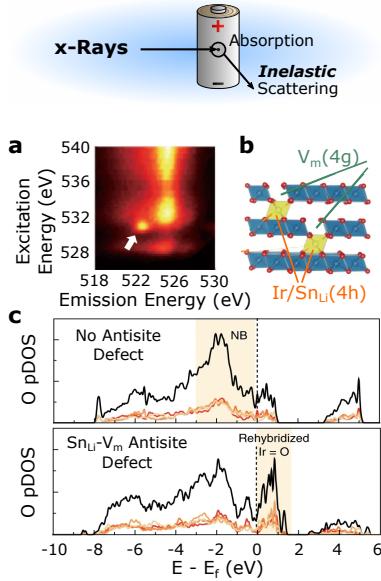


Figure 1.3: a) Resonant inelastic x-ray scattering (RIXS) pattern of the O K-edge in $\text{Li}_2\text{Ir}_{1.5}\text{Sn}_{0.5}\text{O}_3$. The white arrow marks a characteristic feature found in oxidized oxygen. b)-c) Proposed mechanism of the oxygen oxidation. The formation of antisite defects moves the Ir-O double bonds above the Fermi level and making them prone to oxidation. Images adapted from [222].

As with visible light, x-rays can be used for imaging. The high penetration depth allows to take images in transmission mode with contrasts arising from attenuation, phase shifts, or diffraction [71]. X-ray imaging can be performed on a lab scale with computed tomography (CT) where CT measurements can provide images of commercial cells in a resolution of a few micrometers within a few hours [160]. Using synchrotrons with much higher brilliance, these images can be taken much faster up to a time resolution of microseconds, enabling to study ultrafast reactions such as the thermal runaway of a commercial 18650 cell [60].

To be able to resolve the electrode structure, x-ray optics in the synchrotron can be installed which magnify the image but typically also

tend to reduce the field of view and increase the required imaging time [156]. Furthermore, tuning the incident x-ray energy can lead to different image contrasts. For instance, setting the x-ray energy to the XAS region of an element, oxidation state contrast imaging can be achieved. This can allow to map the dynamic phase separation behavior of electrode materials, e.g. LiFePO_4 , in the electrode [105].

Three-dimensional (3D) imaging of structures can be performed using tomography. These measurements require multiple images taken of the same area. As a result, the synchrotron beam could damage the samples. To avoid this, higher energy x-rays with lower absorption can be used. With these harder x-rays, 3D micro x-ray computed tomography (XCT) can be performed *in operando*. First *operando* XCT measurements were based on attenuation contrast imaging of the expansion of SnO_x anodes [54]. For graphite anodes, however, pure attenuation contrast is not sufficient anymore and has to be combined with phase contrast imaging [155].

Using appropriate optics (e.g., creating divergent x-ray beams that geometrically magnify the image area [156]), 3D tomography can be performed to analyze the structure of particles with resolutions down to 50 nm. Such analysis is sufficient to understand ageing and electrochemomechanical properties in secondary particles [196]. Furthermore, measurements on full electrodes can provide insights on the distribution of the carbon black binder domain (CBD) in a Silicon/Graphite anode (**Figure 1.4**). Such an approach has enabled to measure the degree of electrical disconnection of Si particles due to the growth and retraction of the solid electrolyte interphase (SEI) [140]. Note, that to enhance the contrast of the CBD, carbon black has to be replaced with carbon coated metal nanoparticles [137].

A final way to perform high-resolution 3D imaging of LIBs is by diffractive imaging. Theoretically, the resolution in diffractive imaging is only limited by the wave length of the incident x-rays [71, 136]. As a result, diffractive imaging is extremely promising for nanostructure and interface analyses. Among the diffraction imaging methods, ptycographic x-

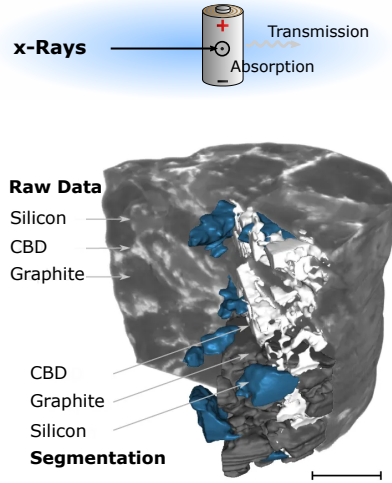


Figure 1.4: Raw and Segmented X-ray computed tomography (XCT) image of a silicon-graphite electrode with resolved carbon black binder domain (CBD). Figure taken from [140].

ray computed tomography (PXCT) has received large attention. PXCT bases on a combination of scanning transmission x-ray microscopy and CT where the tomographic projections are calculated from 2D diffraction patterns that are collected on localized points of the sample. It has been used for cathode materials such as LiFePO_4 nanoparticles [232] and, more recently, single secondary particles of $\text{LiNi}_{1-2x}\text{Mn}_x\text{Co}_4\text{O}_2$ ([162]). In all these measurements, the resolution of the particles depends on the incident energy, measurement time, and sample size. In the above examples, the true resolution of the small LiFePO_4 network resulted at *sim*11 nm (**Figure 1.5**) while larger secondary particles reach a resolution of 40 nm [194]. Very recently, also the 3D structure of electrodes has been imaged. By first milling a pristine electrode using a pulsed laser milling technique, Müller et al. [139] could image a silicon - carbon composite electrode with a resolution of 40 nm that allowed for a detailed characterization of the interactions between the CBD and the active materials.

The remaining limitations of PXCT are based on measurement time and sample size. To date, only 2D images can be measured *in operando*. While this allows to measure particle strain maps with a resolution of ~ 100 nm [57], 3D imaging still requires approximately one day for a high resolution 3D reconstruction. Concerning sample size, the cell may not be larger than $50 \mu\text{m}$ for a suitable 3D reconstruction, making a reproducible cell design with commercial cycling behavior challenging.

Overall, 3D x-ray imaging has improved extremely in recent years. Yet, large challenges remain when it comes to studying nanometer sized interfaces at microstructurally representative length scales of tens of micrometers. At these interfaces, also the effect of beam damage will play a crucial role and will require special low-dose spectroscopic approaches on tailor-made electrochemical cells that are developed to counteract beam damage [28, 143].

While synchrotrons are by far the most important large-scale source of x-rays to date, x-ray photons from FEL sources should not be forgotten. Though no FEL studies have been published on LIB materials yet, the unique combination of high flux and femtosecond pulses will allow to study the effect lattice and electron dynamics thereby creating a unique chance to characterize correlation between electronics and ion diffusion that has only been studied theretically, so far [62]. Therefore, we expect that FELs will play a critical role to understand the fundamental transport mechanisms at battery material interfaces in the near future [174].

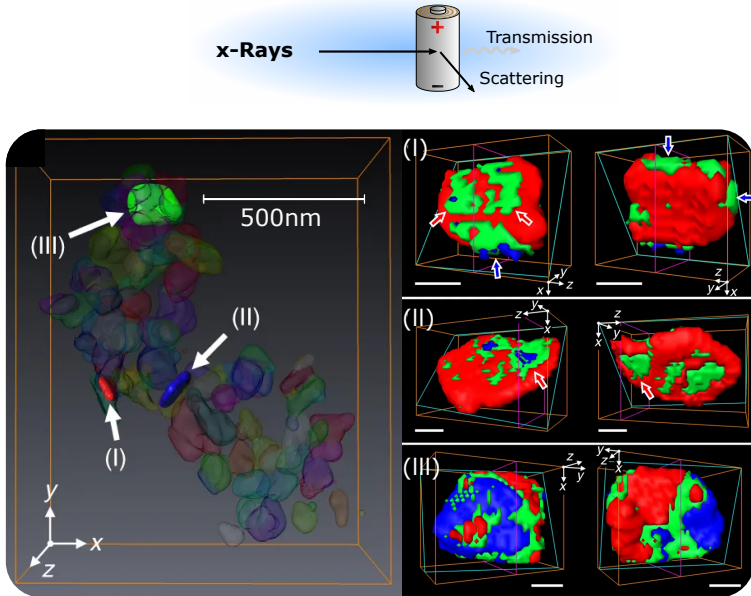


Figure 1.5: Ptychographic x-ray computed tomography (PXCT) image of partially delithiated $\text{Li}_{0.5}\text{FePO}_4$ particles. Three arbitrary particles show the resolution capabilities with the ability to separate between LiFePO_4 rich (red), FePO_4 rich (blue) and the solid solution Fe_xPO_4 rich voxels (green). The scale bar for the single particles is 50 nm. Images adapted from [232].

1.3 Neutron Large Scale Facilities

Compared to synchrotron x-ray scattering techniques, neutron scattering has a few key advantages. While x-rays scatter with the electron density in the solid, neutrons scatter with nuclei and nuclear spins. As a result, the scattering cross section does not depend on the core electron number but on the isotope. This makes neutrons beneficial when studying small elements such as hydrogen or lithium in Li ion battery materials [241]. The capability of resolving lighter elements, however, comes at a cost. Neutron beams are difficult to generate and handling requires large-scale spallation or reactor sources. Furthermore, neutrons have relatively small scattering cross sections and penetrate deep into the samples hence requiring large sample amounts in the range of grams [168].

With the capability of resolving the positions of lithium ions accurately, neutron powder diffraction (NPD) experiments on *ex situ* samples play an important role in structure characterization [166] which can even give insights about the bulk lithium ion dynamics in a material [144] or the pair distribution function [173]. In addition, due to the large penetration depth of lithium ions, NPD allows for studying structural changes occurring in a full cylindrical 18650 cell *in operando* [29]. Recent advances in neutron beamline optics and sample environment even allow for high quality NPD scans in times as short as 10 s making NPD scan times compatible to synchrotron x-rays [108].

The capability of measuring full cells has drawn a lot of interest towards operando small angle neutron scattering (SANS) as well. Similar to SAXS, SANS measurements can provide information about the pore size distribution in a size regime of 1 nm to 300 nm and are ideally suited to study changes in the nanostructure of LIBs [169]. A good application is studying the growth of the SEI in mesoporous carbons as a function of the electrolyte [82, 83]. Using operando SANS, the SEI volume growth, the lithium content of the SEI layer, and the pore-pore distance change can be determined simultaneously (**Figure 1.6**). Thus, *operando* SANS can provide a link between SEI growth and its effect on the electrode

microstructure.

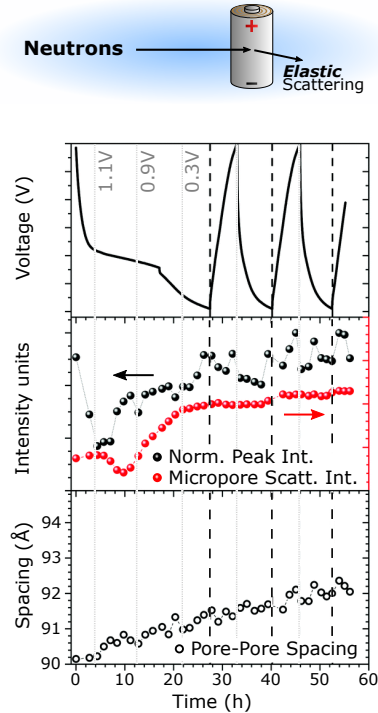
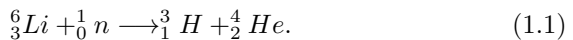


Figure 1.6: *Operando* small angle neutron scattering (SANS) measurements of mesoporous carbon vs. Li cells with 4 M LiTFSI as electrolyte salt. The increase of the micropore scattering intensity arises from LiTFSI molecules aggregating and forming the SEI within the pores. In parallel, the pore-pore spacing increases due to co-intercalation into the carbon network. Image adapted from [83].

Another technique to measure local lithium concentrations is neutron depth profiling (NDP). The technique is based on the induced decay of ${}^6\text{Li}$ nuclei when activated with a neutron (**Figure 1.7a**),



The thus created tritium and helium nuclei travel then through the sample and get detected (see **Figure 1.7b**). Thereby, their resulting energy can give an insight about the depth where the ${}^6\text{Li}^+$ ion lay and a very accurate depth profile of the lithium ion concentration can be made *in operando* [203].

With the aid of NDP, a preliminary test could show that lithium did not intercalate into the Al current collector when Sn was used as a negative electrode [112]. This opens the possibility of replacing the Cu current collector with lower cost and thinner Al. Another, more recent, study [206] showed the irreversible lithium ion loss in garnet-type all-solid state lithium ion batteries as a function of Li plating and stripping cycles (**Figure 1.7c**). A constant portion of irreducible lithium plating was forming close to the Cu current collector which became ionically disconnected from the solid electrolyte when the cell was charged.

Due to the low energy of neutrons in the range of 10-1000 meV, inelastic scattering measurements can be performed with a very high energy resolution. Quasi-elastic neutron scattering (QENS) can be considered a standard experiment to study the solid molecular and ionic diffusion in solids [90, 165, 197]. In addition, inelastic neutron scattering (INS) can provide insights into the lattice dynamics, ionic transport, and thermal conductivity of the active materials [141, 225]. Even phonons modes at the interface between an active material particle and its coating can be analyzed via a combination of inelastic neutron scattering measurements, a particle size series (**Figure 1.8a**) and *ab initio* simulations (**Figure 1.8b**). Using this combination, a higher phonon energy of Li-O surface lattice vibrations was found at the (010) surface of LiFePO_4 (see **Chapter 3**) hence suggesting stronger Li-O bonds and enhanced surface transport.

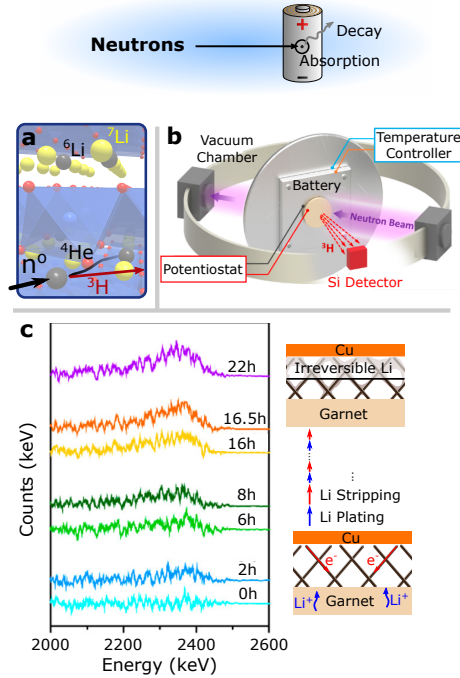


Figure 1.7: a) Working principle of neutron depth profiling (NDP) where a neutron hits the ${}^6\text{Li}$ and induces a decay into ${}^3\text{H}$ and ${}^4\text{He}$. b) NDP experimental design. c) *Operando* NDP measurements on Li deposition in a Carbon nanotube network. With increasing stripping and plating cycles the irreversible Li content close to the copper current collector increases resulting in a peak at the NDP spectra at a ${}^3\text{H}$ energy of 2400 keV. Images b-c adapted from [206].

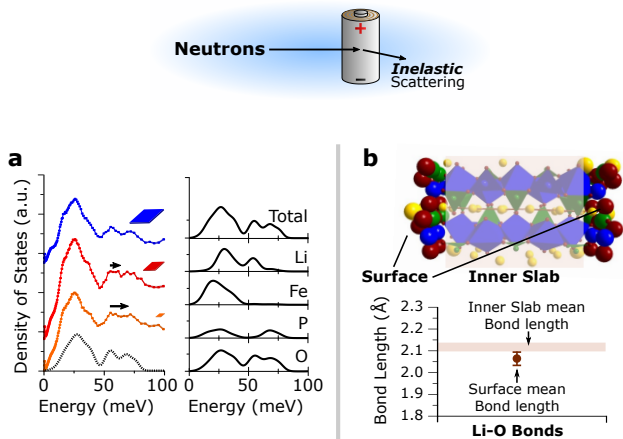


Figure 1.8: a) Inelastic neutron scattering (INS) spectra of LiFePO_4 particles as a function of particle size suggesting an energy increase of the Li-O phonon energy at the surface. b) A comparison of *ab initio* DFT simulations to determine the average within the slab and at its surface supports the findings. Images adapted from [23].

1.4 Electron Microscopy Centers

Compared to x-rays and neutrons, the key difference of electrons is their negative charge. While this reduces the interaction volume significantly, it makes deflecting and accelerating the electrons simpler. As a result, electron beams of high flux can be created in relatively small systems such as the column of an electron microscope. Furthermore, the introduction of aberration corrected electron lenses has enabled sub-Ångstrom resolution measurements [89].

Most electron microscopes are typically lab scale tools. Their versatility, required maintenance, numerous detector systems, corrected lenses, and cost, however, has led to the creation of microscopy centers that often times work proposal-based much alike large scale facilities. In this section, we will mostly focus on the results that such high-end microscopes in microscopy centers have provided in the past years.

To date, scanning electron microscopy (SEM) and (scanning) transmission electron microscopy ((S)TEM) can be seen as a standard for material characterization. While these methods can be used to image objects with resolutions down to atomic scale[224], they can also be used for elemental analyses. When the electron beam hits the sample, element specific x-rays are reflected that can be detected via energy dispersive x-ray spectroscopy (EDS) [233]. The electron beam can also scatter elastically with the sample and create local electron diffraction (ED) patterns. Finally, the electrons can scatter via an inelastic scattering pathway where they can lose energy due to, e.g., the excitation of electrons. As a result, electron energy loss spectroscopy (EELS) can provide local information about the electronic and lattice structure similar to XAS (**Figure 1.9a**). In LIBs, this can be very useful to study interphase effects between electrode and solid electrolyte which otherwise would not be possible to resolve [213] (**Figure 1.9b**).

In situ characterizations using sealed liquid cells [221] or direct reactions with Li metal [102] can give insights about material expansion [27], the growth of interphases [102], or provide insights about lithiation kinetics. The latter can be studied using a combination of ED and

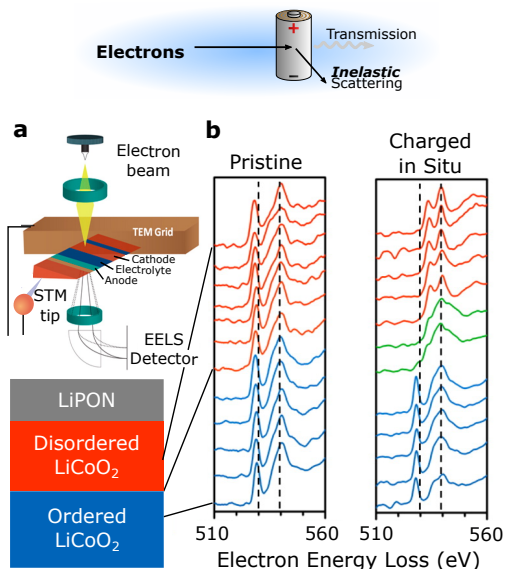


Figure 1.9: a) Experimental design to study the solid-solid interface between LiCoO₂ and the LiPON solid electrolytes. b) Electron energy loss spectroscopy (EELS) patterns collected at different points at the ordered-disordered LiCoO₂ interface. When the cell is charged *in situ*, a phase between ordered and disordered LiCoO₂ arises. This interphase contains Li₂O₂ and Li₂O. Images adapted from [213].

high accuracy STEM (**Figure 1.10a**) and has provided high resolution lithiation maps in LiFePO₄ nanoparticles and could even reveal local Li concentration reversal reactions due to the phase separation reaction (**Figure 1.9b-f**) [238].

However, due to the strong interaction of charged electrons with the sample, the electron beam can strongly damage organic matter such as the electrolyte, the binder, and the SEI. To overcome this issue, the sample can be rapidly frozen with liquid ethane or argon and kept in a cryogenic environment in the electron microscope [209]. Cryogenic electron microscopy (cryo-EM) has enabled studying the SEI in its pristine state on numerous electrode materials (see [209] for a summary). Based on these findings, fluorine-containing additives could be introduced which

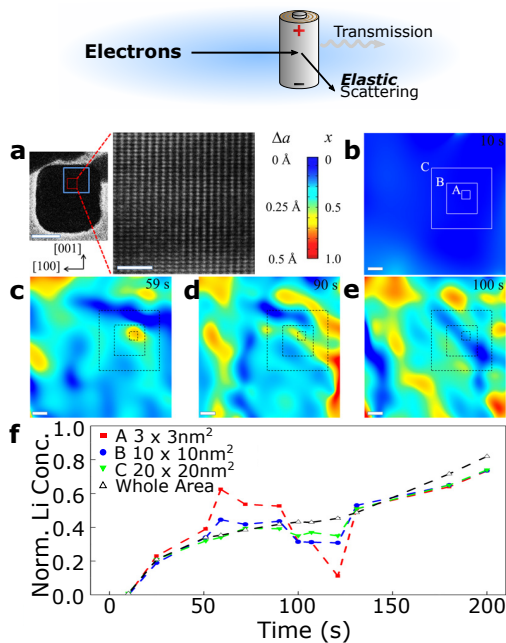


Figure 1.10: a) Bright field image of a LiFePO₄ nanoparticle with an enlarged area of the particle. The scale bar is 50 nm or 5 nm, respectively. b)-e) Heat map of lithium content x in Li _{x} FePO₄ at different time steps (blue to red for increasing x). The scale bars are 5 nm. f) Normalized Li concentration through different nanoparticle regions (see b) as a function of time. Locally, the Li concentration peaks and then reduces itself. On a larger scale, the Li concentration equilibrates to the typical LiFePO₄ polarization curve. Image adapted from [238].

enable a dense growth of the SEI that does not create large stresses in the cell [8, 35, 78] (**Figure 1.11**).

While (S)TEM measurements can provide important interphase and material information, very thin samples in the range of 100 nm are required. Therefore, (meso)structural predictions are practically impossible. SEM, however, is based on measuring reflected electrons making it prone to studying surfaces on practically arbitrarily thick samples. To be still able to get depth information, the imaged surface can be milled

with a focused ion beam (FIB), revealing a new surface to be analyzed in the SEM. Repeating this step numerous times eventually creates a tomographic 3D structure of the system. FIB-SEM tomography can resolve the structure of separators [96, 97] and full electrodes [73]. However, as both milling and infilling can damage the microstructure of the sample, a combination of microscopy with other techniques (e.g. electrochemical impedance spectroscopy [99]) is needed for data validation. Furthermore, FIB milling is a slow process, making FIB-SEM tomography of larger samples very challenging. To overcome this technical challenge, Xe Plasma milling has been recently introduced and will greatly enhance milling speeds hence generating a larger representative volume at a faster rate [30, 216].

FIB-SEM imaging can also be extended to study the mechanical properties of electrodeposited lithium. By selecting single electrodeposited Li dendrites with the FIB, Citrin et al. could measure elastic moduli on single dendrites while imaging them in the SEM [42].

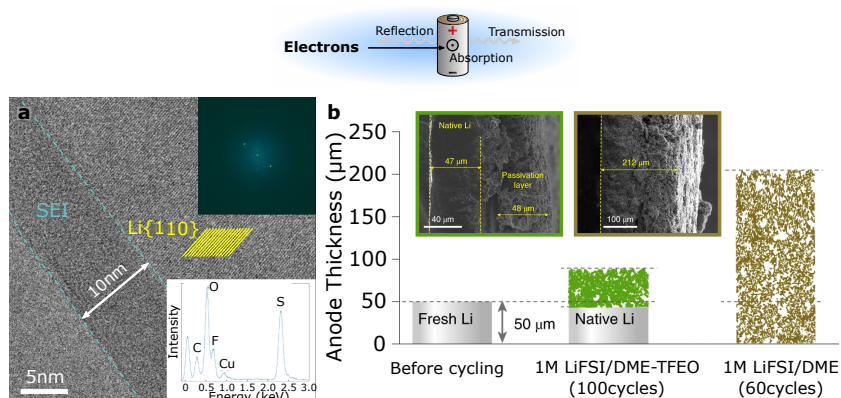


Figure 1.11: a) Cryogenic electron microscopy (cryo-EM) image of the solid electrolyte interphase (SEI) grown on a Li metal anode. The inset below shows the energy-dispersive x-ray scattering (EDS) spectrum which suggests an inorganic-rich SEI. b) Cross sections of Li metal anodes before and after 60 and 100 cycles, respectively. The LiFSI electrolyte solution with DME-TFEO additive creates a dense SEI thereby passivating the Li layer and reducing the dendrite growth. Images adapted from [35].

1.5 Spin-Polarized Beams at Large Scale Facilities

While the techniques mentioned before can help understand the structure and dynamics in time scales down to milliseconds, lithium ion diffusion through materials and interfaces can be many orders of magnitude faster. To resolve such fast processes, pump-probe experiments, e.g. nuclear magnetic resonance (NMR) are required. In ^7Li NMR (**Figure 1.12a**), Li ion diffusion can be measured by analyzing the ^7Li spin relaxation rate [185]. Using such an approach, ionic diffusion can be determined for different materials, e.g. lithium containing ceramics [214] and lithium air batteries [52].

^7Li NMR measurements are very sensitive to magnetic moments of iron and cobalt hence making ^7Li NMR measurements unsuitable for transition metal based cathode materials [127, 179]. To overcome this issue, a spin-polarized beam of antimuons is implanted into the sample. Similar to NMR, the muons then probe local spin fluctuations due to the mobile Li ions (**Figure 1.12b**). Such muon spin resonance ($\mu^+\text{SR}$) measurements allow to determine Li ion diffusion coefficients and activation barriers in a number of transition metal oxides [178] and lithiated graphites Li_xC_6 [198].

Recent advancements in particle accelerators enabled so-called β -NMR measurements where resonance experiments are performed by implanting a ^8Li ion [122, 178] (**Figure 1.12c**). When the free ^8Li ion is implanted, the ^8Li nuclear spin will interact with the local structure and, based on its relaxation, can give insights about the ^8Li dynamics moving in the lattice. As a result, Li diffusion can be measured in materials that contain very little Li ions such as polymers with different salt concentrations [133, 134] (**Figure 1.12d**).

Due to the raising attention of $\mu^+\text{SR}$ by the battery community, numerous advancements have been achieved in recent years in terms of sample design. This includes the developments of *in situ* cell prototypes

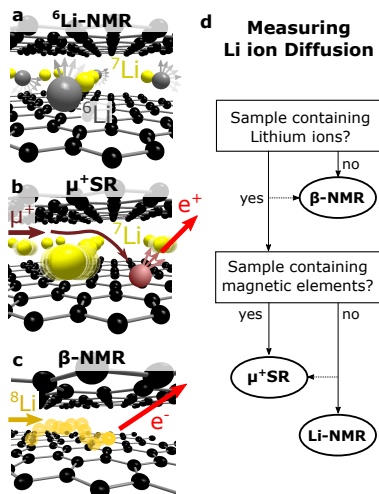


Figure 1.12: a)-c) Working principle of a) Li-NMR exemplified on ${}^7\text{Li-NMR}$, b) $\mu^+\text{SR}$ and c) $\beta\text{-NMR}$. d) Flow chart of using polarized beams for lithium ion diffusion measurements.

[132] and a detailed characterization of ionic transport at interfaces between active materials and their coatings [21]. Furthermore, both muons and ${}^8\text{Li}$ ions are charged particles and their penetration depth can be modulated with electric fields (**Figure 1.13a**). This allows to measure lithium ion hopping in both thin films and powders (**Figure 1.13b**) [134] and, with improvements on the muon beam lines with respect to beam intensity, could allow for new depth and interface dependent studies of ion dynamics.

Other than diffusion, spin polarization experiments can give insights about the chemical structure in disordered materials. Dynamic nuclear polarization (DNP) NMR is a very accurate tool to measure chemical shifts with a high sensitivity to surfaces [84, 101]. This makes DNP NMR an ideal tool to study the organic components in the SEI (**Figure 1.14**). In addition, the isotopic ratios of materials can be studied and give insights about the isotope exchange rates of ${}^6\text{LiFePO}_4$ in a ${}^7\text{Li}$ -electrolyte environment. Specifically, it can reveal the effect of antisite defects in

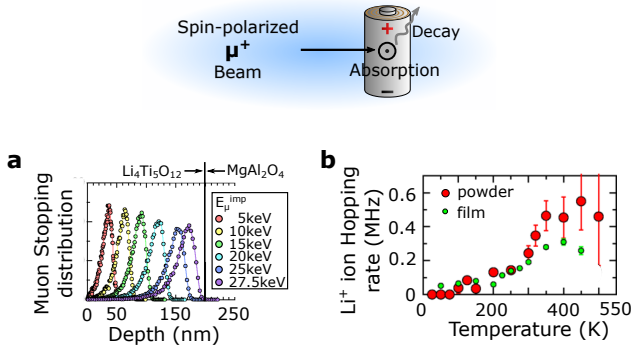


Figure 1.13: a) Muon stopping depth in a $\text{Li}_4\text{Ti}_5\text{O}_{12}$ anode. b) Lithium ion hopping rate of $\text{Li}_4\text{Ti}_5\text{O}_{12}$ powder and thin films (film thickness: 190 nm) as a function of temperature. The hopping rate shows a good overlap between the two samples. Images taken from [134].

LiFePO_4 [113]. Apart from NMR, *operando* electron paramagnetic resonance (EPR) is a great tool to study electronic property changes in oxidation states of transition metals e.g. in lithium rich layered transition metal oxides [189].

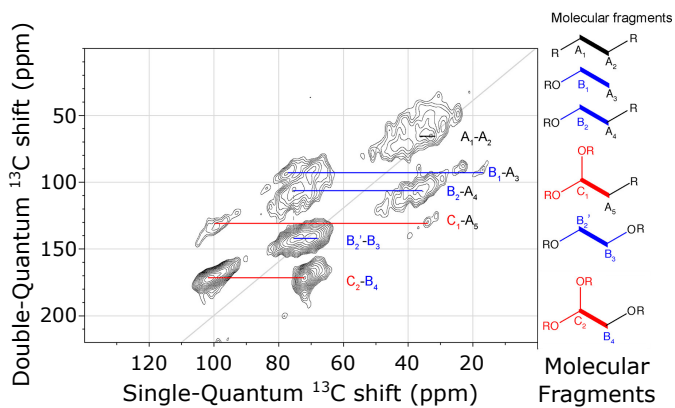


Figure 1.14: Two-dimensional DNP-NMR spectrum of the outer SEI on reduced graphene oxide. The molecular fragments found in the SEI are shown right of the two-dimensional spectrum. Image adapted from [101].

1.6 Summary and Outlook

The possibility of better time, energy, and size resolution in large-scale facilities has had a large impact on understanding LIBs. Each beam of particles can help understand important aspects of materials, structure, and interfaces. While neutrons and x-rays can provide complementary structural and material information on large size scales, recent findings in cryo-EM have allowed to determine interphase stability and structure. Furthermore, the introduction of diffraction contrast based imaging have allowed to bridge the gap between these size scales.

In parallel, *operando* characterization techniques continue to improve at all large-scale facilities and realize acquisition times in the range of seconds. The future of Li ion battery characterizations at these facilities looks very bright. Many large-scale neutron and muon facilities are in the process of upgrades to increase both the flux of particles to the samples and the detection systems leading to an overall increase of the signal to noise ratio by at least an order of magnitude (see **Table 1.1** and **Table 1.2**). Similarly, also synchrotron sources and electron microscopes are constantly improved.

While improvements on the sources are very important, they are by not sufficient. An increase of beam flux hitting the sample requires an active investment in optimized detector stations that are able to read out the additional detectors generated and data analysis tools that can cope with increased stream of data. But if these additional requirements are synchronized well, upgrades open a vast room for opportunities in the design of new beam lines. Exemplary for this is the plan of upgrading the linear accelerator (Linac) at the Oak Ridge National Laboratories. The increase of power due to the Linac will need numerous upgrades of the first target station and requires a very close collaboration with the Oak Ridge Supercomputing Center that is aiming to provide on-site data analysis and computational services [6]. In addition, the Linac upgrade will enable to build a second neutron target station with high intensity cold neutrons and a new μ^+ SR center. Similarly, the European Spallation Source will not only have an extraordinarily strong proton source

but also beam paths in the range of ~ 100 m hence allowing for extremely high accuracy in scattering angles that are especially interesting for total scattering and PDF analysis. Finally, the Japanese muon source at J-PARC which has finished their upgrade in 2018, is pioneering with a special high flux low energy μ^+ SR beam line that, once it is ready, is expected to be able to measure depth-resolved μ^+ SR with resolutions in the range of 10 nm while maintaining high enough flux for fast ion dynamics measurements.

In synchrotrons, the flux is less of an issue compared to the sample environment and the optics. The main challenges will lie in optimizing the setups further towards the needs of the LIB community. Exemplary for this are activities to reduce beam damage or to improve PXCT algorithms and data collection times [31]. Considering electron microscopy, aberration corrected low dose microscopes are continuously improving. Possibly, this could allow studying the formation of interphases *in situ* under more relevant ambient conditions.

With this set of tools available to study LIBs, the remaining challenge will be the analysis of the highly complex interactions between each battery part in a correlative manner. This includes a top-down process from commercially relevant batteries where regions of interest are studied in more detail via correlative imaging techniques [31]. As suggested in the Battery 2030+ initiative roadmap [2], this will crucially require a closer collaboration between computational data analysis groups, experimentalists, and beamline scientists. Having said that, beamline experiments alone will never capture the complexities of LIBs. Virtually all the studies mentioned in this review rely heavily on computational simulations, be it either for data analysis or to back up the results. This makes developments in computational methods (deep learning, ab initio modelling, reconstruction algorithms, etc.) as crucial as advancements on beam lines. In addition, translatability of the findings to commercial LIBs can only be assured if electrochemical characterization techniques are applied rigorously as well. This does also mean that publications should include some benchmark cell parameters [69] that could help both scientific and industrial partners in the interpretation of the results. Overall, battery

research remains a highly interdisciplinary field that requires a lot of collaborative efforts to achieve significant fundamental understanding of the limiting reactions and device improvements.

Table 1.1: Summary of the upcoming upgrades of the strongest neutron sources worldwide.

<i>Neutron Source</i>	<i>Planned Upgrades</i>	<i>Ready for Users</i>
<i>ILL</i> [4] (France)	Replacement of wave guides and detector banks: Count rate and solid angle improvements. 1-3 orders of magnitude improvement depending on setup.	2023
<i>SNS</i> [6] (USA)	Linac power upgrade up to 2.8 MW power (now 1.4 MW). Introduction of second target station (STS)	2025
<i>ESS</i> [3] (Sweden)	Long pulse length system with multiple wave lengths measurements in a single pulse. High intensity + high resolution beam lines.	2023
<i>J-PARC</i> [5] (Japan)	Replacement of target in 2019. New target with 0.5MW power with long term goal of 1 MW power	Ready
<i>ACNS</i> (Australia)	Only minor beam line and sample environment upgrades are scheduled in the near future	since 2008
<i>ISIS</i> [1] (United Kingdom)	Equipment upgrades of the 35 year old target station in 2021/2022, 2 MW power. Longer term: Endeavour program with next-generation instruments	2022, later for new instruments
<i>CSNS</i> (China)	Initial power of 0.12MW with possibility to go up to 0.5 MW	2022

Table 1.2: Summary of the upcoming upgrades of the strongest μ^+ SR sources worldwide.

<i>Muon Source</i>	<i>Planned Upgrades</i>	<i>Ready for Users</i>
<i>J-PARC</i> [5] (Japan)	New Muon Beam Line commissioned (U1). Beam line with ultraslow muons for surface characterizations and depth profiling	U1: 2022 (others: Ready)
<i>ISIS</i> [1] (United Kingdom)	Refurbishment of the Riken-RAL μ SR beam line, Planning of the Super MuSR beam line	2022
<i>SEEMS</i> (USA, at SNS)	Project is in planning phase. Facility projected to have two orders of magnitude more muon flux than J-PARC and ISIS	~2028-2030

2 Part II: Morphology Control in the Synthesis of LiFePO_4 Nanoparticles

2.1 Remarks on Part II

To allow for a comprehensive experimental characterization of the dynamics at the interfaces of Li ion battery materials, a high control of the particle crystallinity, size, and shape are crucial. Choosing LiFePO_4 (LFP) and its (010) termination as an exemplary material interface, we perform a detailed characterization of the hydrothermal synthesis to achieve an in-depth control of particle morphology and bulk/surface crystallinity. **Chapter 2.2** focuses on the effects of particle crystallinity as a function of temperature and time. By controlling precursor concentration and introducing ethylene glycol (EG) as additive, we can achieve a very high crystallinity of LFP platelet particles without the need of high reaction temperatures. As a result, we can create LFP particles with a very low energy consumption [22]. **Chapter 2.3** describes the control of particle size of LFP nanoparticles. While maintaining the platelet shape, we propose a strategy to change the particle size by more than one order of magnitude without affecting the crystallinity of the LFP samples [21, 23]. **Chapter 2.4** is devoted to the coatings of LFP nanoparticles with special focus on the preparation of pristine surfaces and a zinc(II) oxide termination.

This work was performed in close supervision of Prof. Dr. Maksym Yarema. The hydrothermal reactors needed by him were designed by Nils Wenzler.

2.2 Low-Temperature Hydrothermal Synthesis of LiFePO_4

2.2.1 Motivation

Lithium iron(II) phosphate (LFP) is a commercially-used lithium ion battery (LIB) cathode material that offers some advantages over other cathode materials due to the fact that it does not contain cobalt, and that it has a flat voltage profile and a high rate capability [91]. It is commercially produced in a solid-state synthesis route; however, this well-established preparation offers less morphology and composition control than wet chemistry approaches [231]. A large number of solvothermal syntheses have emerged for LFP [130], especially using water as solvent (i.e., hydrothermal syntheses) [33, 37, 50, 55, 107, 119, 130, 158, 223, 227]. Typically, these hydrothermal syntheses are performed with a precursor concentration in the range of 0.1-0.3M, at temperatures between 150 °C and 200 °C, and for a time on the order of ten hours [33, 103, 158, 227]. Rather high process temperatures (150-200 °C) pose two issues towards commercialization: (i) the energy consumption for hydrothermal production of LFP is significantly higher than for the solid-state LFP synthesis and (ii) the vapor pressure of water can reach more than 10 bar, requiring a special reactor design [51]. A commercially viable LFP hydrothermal synthesis will therefore require reduction of the reaction temperature.

To find the parameters at which the specific energy consumption of a hydrothermal synthesis process could compete with the solid state one, we develop a model to estimate the energy required for the hydrothermal-based synthesis of LFP from mine to ready-to-use cathode material. Extending upon existing literature [51, 86, 111, 123, 164, 177], we consider the impact of the key parameters such as synthesis temperature, precursor concentration, and reaction time on the specific energy consumption. Details of the model are given in **Appendix A.3**, and the dependence specific energy on reaction temperature and precursor concentration is shown in **Figure 2.1**. The energy consumption of the hydrothermal synthesis is largely related to the large heat capacity of water, which

makes the heating of the reactor (not the time held at a specific temperature) energy intensive. Our model shows that the reaction temperature as well as the precursor concentration, C_{tot} play a role in energy usage. The larger C_{tot} , the smaller the specific energy consumption because, at lower concentrations, a smaller mass of LFP is created for the same heated volume of water. For temperatures of 150 °C, a hydrothermal synthesis can only compete with the 3 MJ/kg energy consumption of a solid-state synthesis if the precursor concentration were at the solubility limit of LiOH in water. With decreasing the reactor temperature, the dependence of energy consumption on concentration weakens, allowing a larger range of possible precursor concentrations.

Based on this analysis, we aim to develop a synthesis at 115 °C that still yield battery grade material. At this temperature, the specific energy consumption can be lowered to 3 MJ/kg using a feasible precursor concentration (i.e., one below the solubility limit) and the vapor pressure in the reactor will be about 1.5 bar, presenting convenient operating conditions, similar to a pressure cooker.

The hydrothermal synthesis of high-quality LFP at low temperatures is a challenging chemistry task [37, 158, 223]. Low temperature syntheses result in slow growth kinetics and produce LFP with poor crystallinity and a large number of antisite defects (i.e. Fe atoms populating the Li positions). These antisite defects block the [010] Li transport channels in the LFP structure and ultimately decrease specific charge capacities [40, 61, 144, 208]. Moreover, the slow growth kinetics lead to a low number of nuclei, leading to thicker LFP particles and thus longer [010] Li channel lengths such that there is a higher probability of antisite defects blocking them [125].

Here, we present a study of low-temperature hydrothermal synthesis of LFP platelets. In particular, we optimize the precursor concentration and reaction time in order to achieve battery-grade LFP material. We then perform the carbon coating of LFP platelets and show electrochemical performance on par with that synthesized at higher temperatures with specific discharge capacities of up to 150 mAh/g at C/5 and 120 mAh/g at 1 C rate.

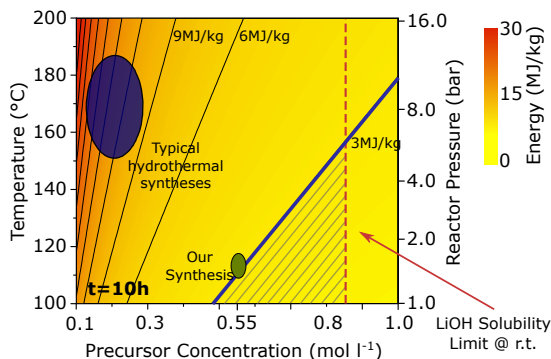


Figure 2.1: Specific energy consumption of the LFP synthesis step as a function of hydrothermal reaction temperature and total precursor concentration. The blue shaded region indicates the energy consumption of typical hydrothermal syntheses, the synthesis reported here is indicated green. The iso-energy line corresponding to 3 MJ/kg is shown in bold, corresponding to the specific energy consumption of a solid-state synthesis. The shaded triangular region below this line represents a temperature and precursor concentration window where a hydrothermal synthesis consumes less energy than a solid-state synthesis.

2.2.2 Results & Discussion

Figure 2.2 shows our low temperature synthesis approach. As detailed in the Experimental methods, we use typical precursors for hydrothermal synthesis of LFP: LiOH , H_3PO_4 , and $\text{FeSO}_4 \cdot 7\text{H}_2\text{O}$ [33, 37, 55, 103, 119, 158, 223, 227]. We also use ethylene glycol (EG) as an additive [158, 227], which is known to decrease the solubility of the precursors, increase the number of nucleation sites, and thereby achieve smaller particle dimensions[227]. Here, to ensure that the role of the EG is primarily in coordination of the LFP surfaces and to be close to a possible commercial application, we work with small additive concentrations and select a fixed molar ratio of $[\text{Li}^+] : [\text{Fe}^{2+}] : [\text{PO}_4^{3-}] : [\text{EG}] = 3 : 1 : 1 : 0.1$ for all syntheses.

To assess our ability to control material quality as well as particle shape and size with our low temperature hydrothermal synthesis, we systematically look at the effect of (1) precursor concentration and (2)

2.2 Low-Temperature Hydrothermal Synthesis of LiFePO_4

reaction time. Since density function theory (DFT) calculations suggest that the symmetric stretching band of the PO_4 group is redshifted when the antisite defect concentration is increased [158], we use Fourier transform infrared (FTIR) spectroscopy to assess material quality. Scanning electron microscopy (SEM) enables us to obtain approximate the particle morphology [167].

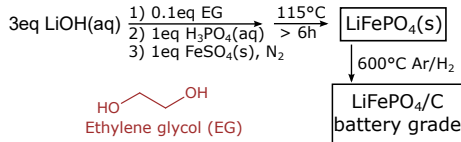


Figure 2.2: Preparation procedure of battery grade LiFePO_4 .

Even though it is generally accepted that the total precursor concentration influences the supersaturation [95] and therefore the reaction kinetics, crystallinity, and particle size, it has not been extensively studied in hydrothermal syntheses of LFP [55]. We investigate measurements performed on LFP samples after 16 h of reaction. The FTIR spectra of the PO_4 stretching modes of each sample at different concentrations are shown in **Figure 2.3a**. Increasing the precursor concentration, C_{tot} , results in LFP particles that show sharper spectral features and a shift of the PO_4 stretching band towards lower wavenumbers, both indicating smaller defect concentration (**Figure 2.3b**). These FTIR results are consistent with Rietveld refinements on X-Ray diffractograms (**Figure A.2**) [120], from which we find a decrease of antisite defects with increased C_{tot} (Fig. 3S†). The decrease in antisite defect with increasing precursor concentration can be explained by faster reaction kinetics at higher concentrations, whereby the LFP crystals form faster and have more time within the set reaction time of 16 hours to recrystallize. This is supported by SEM images (**Figure 2.3c**) showing that, at low C_{tot} , the particles are not all evolved, while uniform platelets are formed for increasing C_{tot} .

Increasing the precursor concentration also affects the particle morphology. With increasing C_{tot} , the average particle thickness decreases from 220 nm to 150 nm (**Figure 2.3d**) while the platelet diameter re-

mains approximately constant around $1.6 \mu\text{m}$ (**Figure 2.3e**). These results can be explained by DFT calculations [61] and previous experimental results [158, 227], which suggest that both water and EG cap the (010) facet, inhibiting growth in the [010] direction.

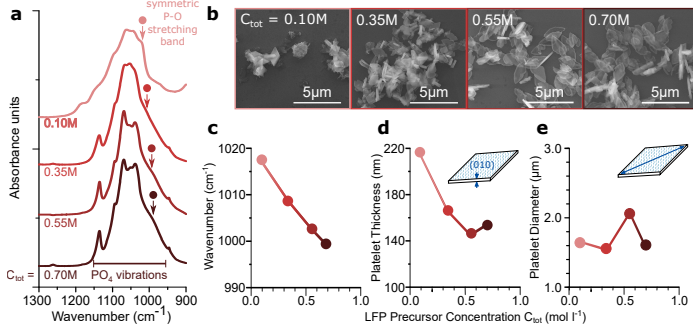


Figure 2.3: Dependence of defect concentration and particle morphology as a function of molar concentration of precursors, C_{tot} , in water. Precursors are fixed in a ratio of $[\text{Li}] : [\text{Fe}] : [\text{PO}_4] : [\text{EG}] = 3 : 1 : 1 : 0.1$. (a) FTIR spectra and (b) position of the symmetric P–O stretching band peak for samples synthesized at different precursor concentrations. (c) SEM images, (d) mean particle thickness, and (e) mean particle diameter are also shown for different precursor concentrations.

To investigate the optimal reaction time for a low temperature hydrothermal synthesis, we construct a sampling reactor that enables us to remove material at different times during the reaction (see **Appendix A.5**). We consider a reaction with a precursor concentration $C_{\text{tot}} = 0.55 \text{ M}$. As shown in **Figure 2.4a**, with increasing reaction time, the average particle thickness tends to increase slightly and the distribution of thicknesses broadens (i.e. $130 \text{ nm} \pm 50 \text{ nm}$ at 3 h to $150 \text{ nm} \pm 70 \text{ nm}$ at 72 h), reflecting the Ostwald ripening process [148]. At the same time, defect concentration (as quantified by the peak position of the symmetric PO_4 stretching band) decreases with longer reaction times (**Figure 2.4b**) due to recrystallization of LFP. This poses a trade-off, because for the highest charge capacity both thin platelet morphology LFP particles (i.e. short [010] Li channels) and low antisite defect concentrations are required. We thus expect a reaction time in the middle of those tested (e.g. 48 h)

to exhibit the best electrochemical performance.

To test the electrochemical performance of our newly obtained material, we prepare the LFP particles for electrochemical cycling by carbon coating them. The LFP particles are mixed with D-glucose, pressed into pellets, and annealed at 600 °C resulting in LFP particles with a coating of 3 wt% of carbon. XRD, FTIR, SEM, and transmission electron microscope (TEM) measurements suggest that the carbon coating step removes the solvent incorporated in the crystal and provides a conductive coating but does not affect the particle crystal structure or the antisite defect concentration. As described in the methods (see **Appendix A.2**), electrodes are made from different particle batches and cycled vs. lithium in a half-cell configuration.

Figure 2.4c shows the electrochemical voltage vs. capacity curves for C/10 (dis)charge for three LFP batches prepared with the same precursor concentration of $C_{\text{tot}} = 0.55 \text{ M}$ and reaction times of 16, 48, and 72 hours. All three samples exhibit a flat voltage plateau and low polarization at a C/10 rate. Our parameter sweep indicated that the best electrochemical performance should result from particles synthesized for ~ 48 hours, and indeed this sample performs best with a specific discharge capacity $>150 \text{ mA h g}^{-1}$. Importantly, such high discharge capacity of LFP material is already comparable to values obtained by high temperature hydrothermal syntheses and improves upon previous reports for low temperature hydrothermal LFP synthesis [158, 223]. Furthermore, our LFP samples show only very small capacity fading after 50 charge/discharge cycles (**Figure A.5**). Using galvanostatic cycling, the specific discharge capacity at different C rates ($1\text{C} = 0.17 \text{ A g}^{-1}$) is determined from the LFP particles synthesized for 48 hours. **Figure 2.4d** shows the average discharge capacity and standard deviation of sample electrodes prepared in different batches. The specific charge capacity drops to 130 mA h g^{-1} , when the cycling rate is increased to 1C, which is comparable to high temperature hydrothermal LFP syntheses [33, 37, 55, 103, 119, 158, 223, 227].

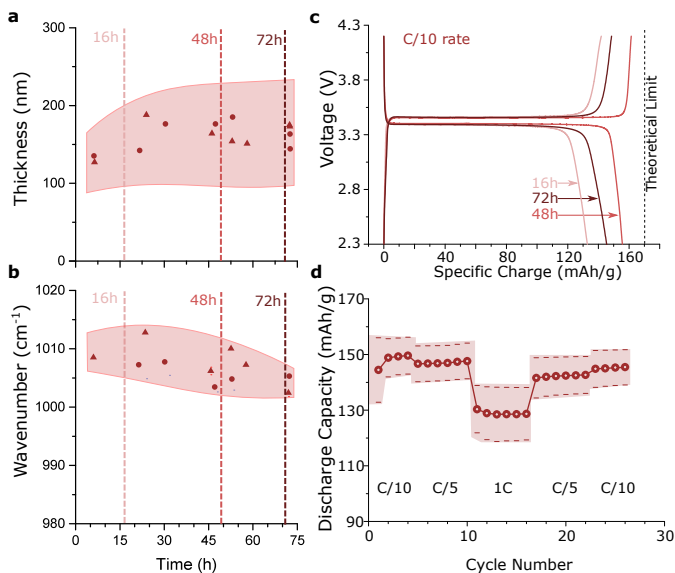


Figure 2.4: Two different batches (circles, triangles) of LFP platelets synthesized under the same conditions are sampled as a function of reaction time and their thickness (a) and the peak position of the symmetric P-O stretching mode (b) is plotted. Shading indicates the standard deviation of the measurements. (c) Polarization curves at C/10 rate of LFP samples prepared with different reaction times. (d) Specific discharge capacity at different C rates ($1\text{ C} = 0.17\text{ A g}^{-1}$) of LFP synthesized at 115°C at a precursor concentration of $C_{\text{tot}} = 0.55\text{ M}$ and a reaction time of 48 h. Shading indicates the error bars on the measurements, which are determined by measuring five cells containing different electrodes prepared from two different batches of material.

2.2.3 Summary

Table 2.1 summarizes the specific energy consumption of our proposed hydrothermal synthesis, a high temperature hydrothermal approach proposed by Chen et al. [37] and a solid state synthesis. This comparison includes the carbon-coating step in our hydrothermal synthesis for which we assume an extra energy consumption of 2 MJ kg^{-1} . By increasing the concentration and decreasing reaction time, our synthesis saves more than 30% compared to high temperature hydrothermal syntheses, but still consumes more energy than solid state syntheses. However, an ex-

cess of lithium is used in the hydrothermal process, which leads to the formation of Li_2SO_4 . If this co-product was recycled, the precursor energy consumption would decrease by up to 50 % eventually making the synthesis beneficial from an energy perspective. Of course, energy consumption during synthesis is only a small part of the costs of the overall material production. For instance, the aforementioned temperature dependent pressure in the reactor has a high impact on investment cost due to increased safety requirements. However, while increased reaction time has only a small effect on energy consumption (heating up to and not holding the temperature is the energy intensive step as highlighted in **Figure A.6**), it does impact throughput. Therefore, a multi-parameter optimization of temperature, reaction time, and the process (e.g. using flow reactor set-up) would be necessary for commercial introduction of a hydrothermal process.

In conclusion, we synthesized LFP platelet particles in a hydrothermal synthesis with a low reaction temperature of 115 °C. Increased precursor concentration together with small amounts of EG as an additive lead to highly crystalline particles with a platelet-shaped morphology having small dimensions along [010]. Using a sampling setup, we found the counteracting effects of recrystallization and Ostwald ripening lead to an optimal reaction time in the range of 48 hours. Our analysis shows that reduction of reaction temperature and increase of precursor concentration can bring the energy consumption of a hydrothermal synthesis in line with that of a solid state approach, while enabling particle size and shape control not available with solid state approaches. This work highlights the open potential for optimization of hydrothermal processes at lower temperatures and higher concentrations.

Table 2.1: Overview of the specific energy consumption of LFP prepared by different synthetic approaches.

	Solid State Synthesis	High Temperature hydrothermal	Our Approach
Synthesis Energy	3 MJ kg^{-1}	19 MJ kg^{-1}	5 MJ kg^{-1}
Precursor Energy	22 MJ kg^{-1}	26 MJ kg^{-1}	26 MJ kg^{-1}
Reactor Pressure	1 bar	10 bar	1.6 bar
<i>Total Energy</i>	25 MJ kg^{-1}	45 MJ kg^{-1}	31 MJ kg^{-1}

2.3 LiFePO₄ Platelet Size Control

To experimentally observe differences between the (010) surface and interior electron/ion dynamics, we produce platelet-shaped LFP particles of four different sizes, *Large*, *Meso*, *Medium*, and *Nano* (**Figure 2.5**). Platelet size can be systematically decreased by increasing the reaction temperature and the percentage of ethylene glycol (EG) as a co-solvent, which increases supersaturation and decreases nucleation rate [50, 55, 61, 158, 212, 223]. We make *Large* platelets in 0.4 v% EG at a reaction temperature of 115 °C *Meso* platelets in 0.4 v% EG at 180 °C, *Medium* platelets in 50 v% EG at 180 °C, and *Nano* platelets in 100 v% EG at 180 °C. See Appendix B.1 for the Experimental details.

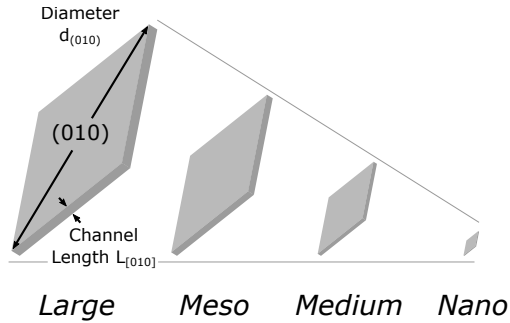


Figure 2.5: Schematic drawing of the LiFePO₄ platelet particle size series.

Figure 2.6 shows SEM images of the platelet samples, and **Table 2.2** and **Table 2.3** summarize the particle size and shape parameters, respectively. We measure [167] platelet thickness, which is equivalent to the [010] channel length $L_{[010]}$ and the diameter $d_{(010)}$ of the platelet (010) surface (see **Figure 2.5**). Assuming a circular platelet shape, we then estimate (**Appendix A.9**) characteristic parameters such as a length to thickness aspect ratio and the percentage of atoms located at the (010) surface. Due to the platelet-morphology, for all samples, the majority of the surface is a (010) facet. In the case of the *Nano* sample, almost 11% of the atoms thus populate the (010) surface, while in the *Large* sample only 0.4% of atoms occupy this surface. This means that the dynamic contribution of the *Nano* LFP sample will exhibit a

significant contribution from the (010) surface, while the contribution from the (010) surface will be negligible for the *Large* LFP.

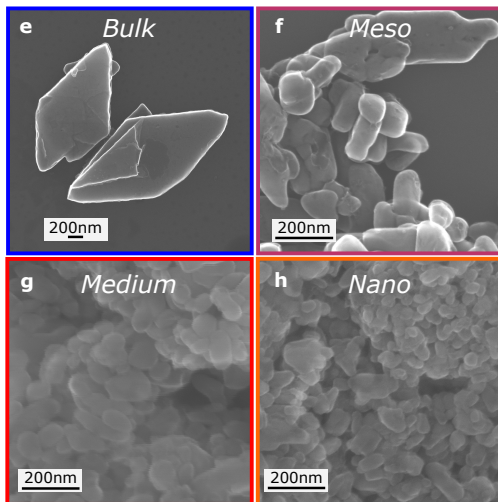


Figure 2.6: Scanning electron microscopy (SEM) images of the a) Large, b) Meso, c) Medium, and d) Nano LFP samples. Their size characterization is summarized in **Table 2.2**.

Table 2.2: Measured dimensions of the LiFePO_4 (010) platelet particles.

	Length $L_{(010)}$	Diameter $d_{(010)}$
<i>Nano</i>	11 (2) nm	55 (13) nm
<i>Medium</i>	48 (13) nm	117(29) nm
<i>Meso</i>	66 (23) nm	270 (120) nm
<i>Large</i>	300 (90) nm	1600 (500) nm

Table 2.3: Morphology characteristics obtained from the platelet dimensions of the LiFePO_4 (010) platelet particles.

	Aspect ratio	Atoms on (010) surface	(010) to entire surface ratio	Atoms on other surfaces
<i>Nano</i>	5.0 (24)	10.9 (20)%	71 (8)%	5.7 (13)
<i>Medium</i>	2.4 (13)	2.5 (7)%	55 (12)%	2.7 (7)%
<i>Meso</i>	4.1 (32)	1.8 (6)%	67 (17)%	1.2 (5)%
<i>Large</i>	5.3 (33)	0.40 (12)%	73 (12)%	0.20 (6)%

2.4 Coating LiFePO_4 Nanoparticles

To study the effect of different surface terminations on Li ion interface diffusion, we look at four different surface terminations. First, in **Part 3** and **Part 4**, we study electronically conductive carbon coated LiFePO_4 particles that allow us to solely on ionic conductivity at the interface. In **Part 5**, we extend our analysis to a pristine and an electronically insulating ZnO coating. Finally, we create a combined ZnO/C coating.

C coating

To achieve a commercially relevant battery performance, LiFePO_4 particles have to be coated with a conductive coating, typically carbon [207]. All LFP samples shown in **Part 2**, **3**, and **4** with carbon.

To coat LFP particles with 3 wt% carbon, we add D-glucose (Sigma) to the uncoated LFP particles (**Figure 2.7a**). We then grind the mixture thoroughly, press a pellet, and anneal it under Ar/3 wt% H_2 for 6 h at 600°C. A uniform carbon coating with a typical thickness of 2-7 nm (depending on the particle size) forms (**Figure 2.7b**). Raman spectroscopy measurements on the C coated LFP particles suggests that the carbon layer is amorphous and contains both sp^3 and sp^2 hybridized C-C bonds (**Figure 2.7c**).

Pristine surface termination

For the pristine LiFePO_4 particles, the LFP particles obtained from the hydrothermal synthesis are first etched with 0.1 M H_3PO_4 (Sigma) to reduce organic residues. After drying and pressing into a pellet, the LFP particles are annealed in Ar/3 wt% H_2 for 16 h at 400°C. Based on energy dispersive x-ray scattering scanning transmission electron microscopy (EDS-STEM) maps, the resulting LFP particles has a pristine termination with an undetectable surface layer (**Figure 2.8b**).

ZnO Coating

We coat the LFP powders with 3wt% ZnO in three steps. As with the pristine particles, we first etch the raw LFP particles with 0.1 M H_3PO_4 . Secondly, we grind the particles together with zinc acetate (Sigma) and press them into pellets. These pellets are then annealed under Ar/3 wt%

H_2 flow for 16 h at 400°C . Using this method, we obtain a uniform ~ 3 nm thick amorphous, ZnO coating (see **Figure 2.8c**).

ZnO/C Coating

The combined ZnO/C coating is made along the ZnO coating step. After etching the hydrothermally obtained raw LFP particles, a 2.5 wt% ZnO / 2.5 wt% C coating is prepared by pressing a ground mixture of LFP, zinc acetate, and D-glucose into pellets. These pellets are then annealed under Ar/3 wt% H_2 flow for 8 h at 500°C . We observe a C coating with local ZnO clusters (see **Figure 2.8d**).

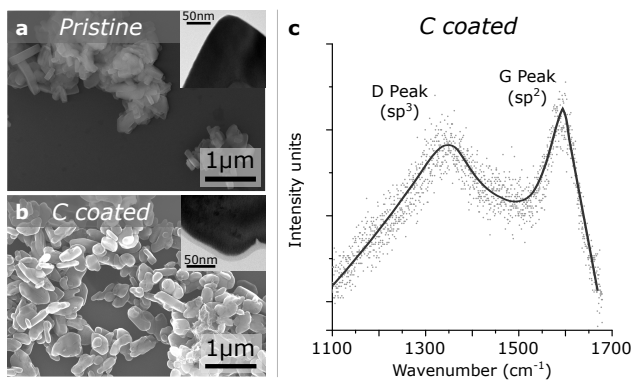


Figure 2.7: a,b) Scanning and transmission electron microscopy (SEM and TEM) images of a) the pristine and b) the C coated *Large* LFP particles. c) Raman spectrum of the C coated LFP particles.

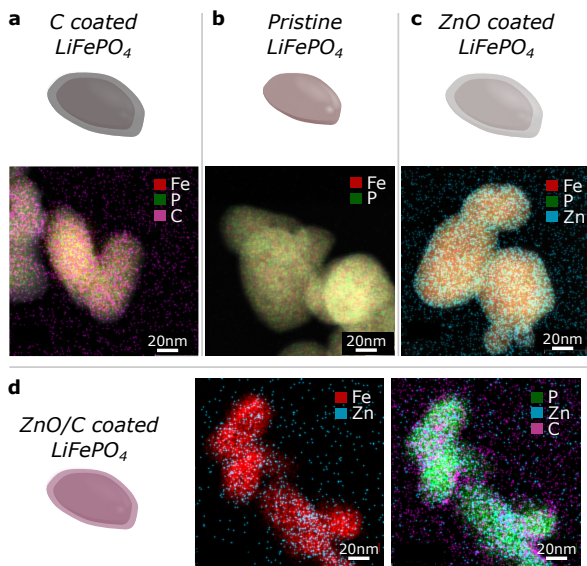


Figure 2.8: Energy dispersive x-ray scattering scanning transmission electron microscopy (EDS-STEM) images of a) C coated, b) Pristine, c) ZnO coated, and d) ZnO/C coated LiFePO_4 Nano particles.

2.5 Part II: Summary

The investigations of the hydrothermal LiFePO_4 synthesis have allowed us to have an effective control of particle size, shape, and crystallinity. Modifying the EG concentration, reaction temperature and reaction time enables LFP platelet particles with the (010) surface as main surface and a size control between 10 nm and 300 nm. Together with the following ZnO and carbon coating steps, we lay the ground for the follow-up studies in the next chapters that will focus on studying the charge dynamics at the surfaces of these particles.

In parallel, we found a new low-temperature solvent-based LFP synthesis route that can pave the way for novel technologies, moving away from batch-type reactions to flow reactors.

3 Part III: Studying Surface Phonons of Li ion Battery active materials

3.1 Remarks on Part III

After a successful synthesis of LFP particles with different morphologies (see **Part 2**), we have the necessary tools to study interface dynamic properties of the battery materials. In this chapter, we will focus on the studying the changes of collective lattice vibrations (or *Phonons*) at the surface.

This work is based on a collaboration with the research groups of Prof. Dr. Martin Mansson (MM), Dr. Fanni Juranyi (FJ), and Prof. Dr. M. Saiful Islam (MSI). While MM and FJ assisted with the neutron scattering measurements at the SINQ neutron spallation source of the Paul Scherrer Institute, the group of MSI performed the computational work on the bulk phonon density of states (PDOS) of LiFePO_4 and FePO_4 .

3.2 Motivation

Interface reactions of lithium ion battery active materials in their electrode environment are key to further improvements in performance, safety, and lifetime. Such active material interface reactions include ion exchange to or from the electrolyte, electron charge transfer [116, 121, 128] to or from the conducting additives (e.g., carbon-black and binder composite), or electrolyte reactions which can create solid elec-

trolyte interphases [58, 204] and enable catalytic phase changes [58, 59]. Local distortions of the crystal lattice of the active material and their vibrational energy can influence the rates at which these physical and chemical processes occur [121, 159, 199]. In this chapter we experimentally and computationally investigate how surface vibrational modes at the surface of active materials can differ from those in the interior of an active material particle and how surface coatings can be used to control the vibrational structure of the surface.

We select LiFePO_4 (LFP) as a model material (**Figure 3.1**). Due to its olivine structure, LFP features one-dimensional bulk transport of lithium ions in the $[010]$ direction [144] and therefore exhibits one surface (the (010) surface) that is particularly important to consider when studying interface effects. Furthermore, because the lithium channels along the $[010]$ direction can be easily blocked by antisite defects [41, 81, 87, 130], commercial LFP is found as nanoparticles with short channel lengths (i.e. short $L_{[010]}$) and large surface to volume ratios. Both these aspects make LFP a useful system to systematically study how vibrational modes at the surface of a battery active material differ from those in the interior of the particle.

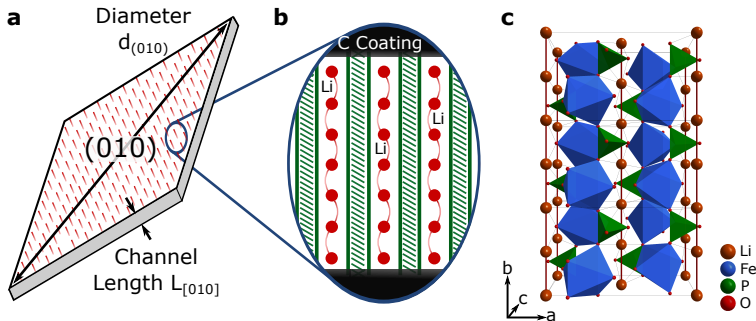


Figure 3.1: a) Schematic drawing of the LiFePO_4 (LFP) platelet particles. b) Schematic view of the Li ion transport channels along the $[010]$ direction and the carbon coating at the particle surface. c) Crystal structure of LFP.

To experimentally observe differences between surface and interior vibrational modes, we produce platelet-shaped, carbon coated LFP particles (see **Figure 3.2** of four different sizes, *Large*, *Meso*, *Medium*, and *Nano*, and measure their phonon density of states (PDOS) using inelastic neutron scattering (INS). To reduce ^6Li neutron absorption [168], we prepare enriched ^7LFP samples. With the morphology controlled synthesis of LFP (see **Chapter 2.3**), the ratio of atoms at the (010) surface to atoms in the particle interior ranges over from 0.4% for the *Large* sample to 11% for the *Nano* LFP. This means that the vibrational density of states of the *Nano* LFP sample will exhibit a significant contribution from the (010) surface, while the contribution from the (010) surface will be negligible for the *Large* LFP.

In order to identify the contribution of lithium atoms in the vibrational states observed, we electrochemically delithiated these LFP particles to FePO_4 (see **Appendix B.2**). Due to the limited charge capacity of the *Large* FePO_4 sample, we delithiated the *Nano* and *Meso* LFP particles (see electrochemical data of samples in **Figure B.4** and **B.5**). We therefore study three LFP particle sizes (*Nano*, *Medium*, and *Large*) and two delithiated LFP sizes (*Nano* and *Meso*).

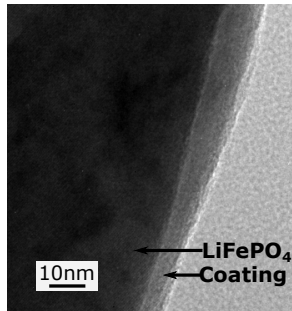


Figure 3.2: Transmission electron microscopy (TEM) image of the *Large* LFP sample with the carbon coating. TEM images of the *Medium* and *Nano* sample are shown in **Figure B.6**.

3.3 Results and Discussion

Using the samples above, we perform INS measurements to measure the phonon density of states. The data from the low- (below 15 meV) and high- energy (above 100 meV) range of the INS spectra partly lack accuracy due to paramagnetic scattering of Fe^{3+} and neutron time-of-flight acquisition frame overlap, respectively. To minimize the influence of the paramagnetic scattering, we discard the scattering vectors with values less than 3 \AA^{-1} [13, 64]. More details are found in the Experimental methods in **Appendix B.5**.

The measured PDOS of the *Nano*, *Medium*, and *Large* LFP platelets are shown in **Figure 3.3a** and that of *Nano* and *Meso* delithiated LFP (i.e. FePO_4) are shown in **Figure 3.3b**. The PDOS of the *Large* LFP are consistent with previous INS measurements [64]. PDOS calculations based on density functional theory (DFT) methods [18, 26, 92, 154, 192] show good agreement with the experimental *Large* LFP and *Meso* FePO_4 measurements.

In the energy range between 50 and 80 meV (**Figure 3.3a** box), we observe a difference in the phonon density of states as a function of particle size. With decreasing particle size, the two distinct peaks seen in the *Large* LFP sample merge into a plateau feature in the *Nano* sample. The phonon density of states spectra of the delithiated FePO_4 (**Figure 3.3b**), however, show no difference between the *Meso* and *Nano* sample, indicating that the change in the phonon density of states in LFP as a function of particle size is potentially related to different vibrations involving Li ions. Indeed, the element specific partial phonon density of states (**Figure 3.3c**) indicate that in the vibration modes around 50-80 meV primarily P-O and Li-O bonds are involved. We perform Fourier transform infrared spectroscopy (FTIR) and XRD in order to confirm that the changes in the phonon density of states as a function of size stem from the percentage of (010) surface atoms relative to atoms in bulk LFP and not from impurities or structural defects. The most common structural defects in LiFePO_4 are Li/Fe antisite defects [41, 81],

which have been shown to influence the stretching P-O vibration mode at ~ 120 meV (980 cm^{-1}) [158]. However, FTIR analyses of the *Large*, *Medium*, and *Nano* particles show no substantial changes of that mode (**Figure B.11**). From XRD, we find traceable amounts (<10 wt%) of Li_3PO_4 in the XRD spectra of the *Nano*-sized sample (**Figure B.12**). However, the P-O phonon mode in the range of 50 to 80 meV in Li_3PO_4 is broad [182], which suggests that the influence of Li_3PO_4 is unlikely to be the sole cause of the merging of the peaks into a plateau (**Figure B.13**).

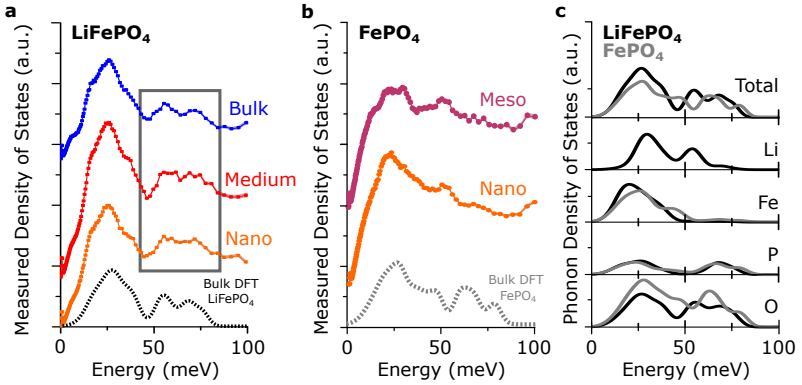


Figure 3.3: The experimentally measured phonon density of states for a) LiFePO_4 (LFP) and (b) delithiated LFP (i.e., FePO_4) samples of different sizes. The shading around the points indicates the error of the measurement. The dashed lines show the calculated phonon density of states. c) Calculated total and elemental partial phonon density of states of LFP (black) and FePO_4 (gray) from bulk density functional theory simulations. Full spectra are shown in **Figure B.10**.

Having confirmed that the changes in the phonon density of states as a function of particle size most likely come from the differences between vibrational modes at the (010) surface and those in the bulk of LFP, we look into the possible atomistic origins of these surface modes. **Figure 3.3** shows that as the sample size decreases (i.e., the percentage of (010) surface atoms increases), a feature appears between the P-O and Li-O modes suggesting a redshift (reduction of phonon energy) of the P-O or a blue-shift (increase of phonon energy) of the Li-O vibrations with

additional broadening.

Shifts in vibrational energies can occur under tensile or compressive stress [147] or due to surface reconstruction [65]. Since Rietveld refinements on our samples do not show any tendency of a change in the lattice parameter when moving from bulk to nano-sized particles (**Figure B.14**) [120], we therefore conclude that the shift in the vibrational energies comes from how the LFP (010) surface interacts with the carbon coating or from Li deficiencies and surface defects at the particle surface [12].

The exact nature of the coated carbon is not known [207] and different surface reconstructions are possible: loosely bound carbon coating atoms could leave the LFP surface unaffected as if it were surrounded by vacuum. Alternatively, the affinity of carbon and oxygen could lead to a weak C-O bond between coated carbon atoms and the phosphate groups in LFP. Residual oxygen atoms in the coating are not likely due to the reductive Ar/H₂ environment used during the coating process. Finally, Li vacancies could result in a lithium-deficient LFP surface with local Fe³⁺ centers.

To determine whether any of these scenarios explain the observed change in the phonon density of states, we perform DFT calculations on slabs with dimensions of 1 unit cell length in [100], 3.5 unit cell lengths in [010], and 2 unit cell lengths in [001] (**Figure 3.4**) [70, 110, 182, 200, 201, 208]. The (010) surface has one of three different terminations: vacuum, a carbon atom in the vicinity of a surface oxygen, or missing Li ion (**Figure 3.5a-c**). Each structure is relaxed, and we extract the distributions of Li-O, P-O, and Fe-O bond lengths for the surface and the interior of the slab (**Figure B.16** and **B.17**). The mean Li-O, P-O, and Fe-O bond lengths from the interior of the slab and the slab surface are plotted in **Figure 3.5d-f** and compared to the experimental bond lengths. Despite the average Fe-O bond lengths being underestimated by about 0.08 Å, the average bond lengths in the slab interior match well with the values found experimentally, indicating that our simulations are representative of observed trends.

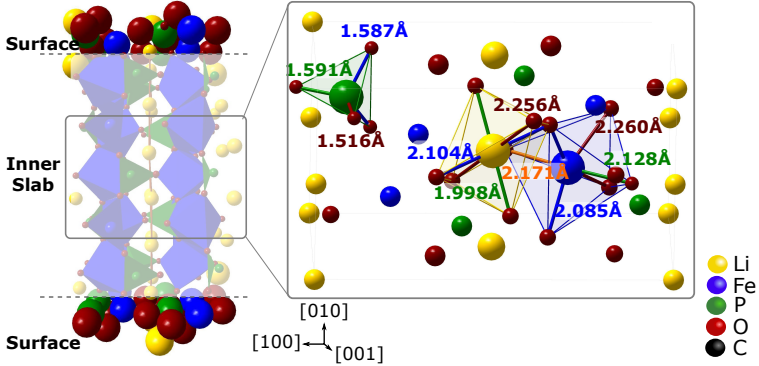


Figure 3.4: Rendering of the particle slab on which the DFT calculations are performed, showing the atoms included as an inner slab and the surface contributions. Inset: depiction of metal–oxygen bond lengths in bulk LiFePO₄ obtained from Rietveld refinement.

While the calculated Li–O, P–O, and Fe–O bond lengths in the interior of the slab are independent of surface termination, the Li–O and Fe–O bond lengths change as a function of the slab surface; these results indicate that surface reconstruction and the vibrations at the (010) surface of LFP will be different than in the interior of the particle. Only the P–O bond (**Figure 3.5e**) is unaffected by the three different surface terminations. The mean Fe–O bond length decreases at the particle surface for all three surface terminations (**Figure 3.5f**), particularly in the case of a Li deficient surface. This can be explained by the fact that the absence of one lithium atom (Li vacancy) changes the oxidation state of an Fe from Fe²⁺ to Fe³⁺, thereby increasing the strength of the ionic bond. The weakest effect on the Fe–O bond length is found in the case of a carbon environment, where a C–O bond in the vicinity of the Fe atom may counteract the bond length reduction of an undercoordinated Fe atom at the surface. The mean Li–O bond length is also shorter at the vacuum terminated surface and the carbon terminated surface, compared to the particle interior (**Figure 3.5d**). Both a vacuum termination and a carbon termination result in an undercoordinated Li ion. This ion will try to compensate its electronic charge by moving towards the oxygen atoms thus reducing the Li–O bond length. This is reduced in the Li

deficient case due to the smaller number of surface Li atoms.

The reduction of the Li-O bond length with a vacuum or a carbon termination at the (010) surface of LFP helps to rationalize the dependence of the PDOS on the particle size. A shorter Li-O bond suggests a larger bond strength and higher energy vibrations, in agreement with the observed blue-shift in the phonon density of states in the region of Li-O vibrations (**Figure 3.3**). This effect is strongest when the surface is terminated by vacuum or carbon atoms. Li deficiency at the surface, however, only weakly reduces the Li-O bond lengths, but changes the Fe-O bonds in a strong manner that should manifest itself in the Fe-O vibrations. A small blue shift in the Fe-O vibrational energy predicted from the DFT calculations should also be present when comparing vacuum and carbon terminated (010) surfaces. However, these small shifts may not be observed because these vibrations are in an energy range dominated by paramagnetic scattering (**Figure 3.3c**).

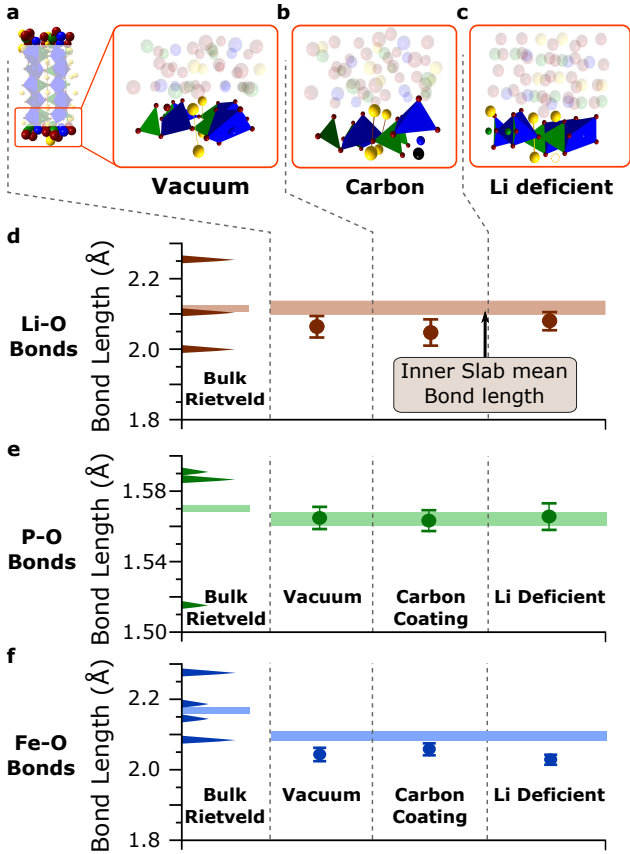


Figure 3.5: Three different LFP surfaces are simulated: b) a vacuum terminated surface, b) a carbon terminated surface, and c) a Li-deficient surface. The mean calculated bond lengths in the inner part of the slab (line) and for the different surfaces (points) and the experimental bond lengths obtained from Rietveld refinement (left) are shown for d) Li-O, e) P-O, and f) Fe-O. The width of the line and the error bars for the calculated values indicate deviations in the mean value for the given dataset.

3.4 Summary

In conclusion, using an effective combination of INS and ab initio simulation techniques we found that the Li-O bonding character at the (010) surface and the interior of the LFP particle are different. This surface reconstruction is related to the carbon surface termination of the LFP. These findings have implications for lithium ion transport in battery active materials. Lattice vibrations assist the quasi one-dimensional lithium ion transport and the (de)intercalation of the lithium into and out of the material [121, 159]. Indeed, the important role of phonons in enabling lithium ion conduction [159, 193] is seen by the fact that lithium ion vacancy hopping is reported at a temperature of 250 K (corresponding to a thermal energy of ~ 20 meV) [11, 181]; while Li ion diffusion along the [010] channels occurs with an estimated migration barrier energy of 300–600 meV [45, 80, 138, 149]. Changing the vibrational densities and energies at the surface will influence, for example, the relative activation energies of lithium ion transport on the surface and in the bulk of the particle and therefore the rate-dependent lithiation behavior [105]. Furthermore, the predicted shift in the Fe-O bonding in the case of a lithium deficient region (i.e., during delithiation) suggests that the activation energy associated with lithium transport may vary as a function of state-of-charge.

This work highlights the fundamental importance of active particle coatings of battery electrodes. We showed that changing the coordination and bonding of surface atoms can be used to selectively tune the vibrational energies at the surface. These insights are of significant importance for further improvements in the electrochemical performance of lithium ion battery materials and devices, particularly in relation to reducing surface reactivity and degradation.

4 Part IV: Quantifying Diffusion through Battery Interfaces

4.1 Remark on Part IV

The findings in **Part 3** suggest a change of Li ion dynamics at the LiFePO_4 interface that is caused by a change in the surface reconstruction. However, phonon density of states calculations cannot provide a clear answer as to how ionic transport, that is typically a multi-phonon process, will be influenced by the particle surface termination. In this part, we combine electrochemical, computational, and spectroscopic techniques to quantify Li ion diffusion at the LiFePO_4 -carbon interface [21].

The work shown in the section is part of a collaboration between Dr. Fanni Jurányi (Paul Scherrer Institute (PSI)) and the research group of Prof. Dr. Martin Månsson (KTH Stockholm) who both assisted in the Muon spin spectroscopy measurements performed at the ISIS Neutron and Muon source in the UK. In addition, DFT simulations were performed with the help of Dr. Nuri Yazdani. Finally, the magnetic properties of the samples were measured by Dr. Marisa Medarde at PSI.

4.2 Motivation

Lithium-ion battery performance and cycle life [58, 115] are linked to the internal resistances in the cell. High ionic and electronic resistances can result in large voltage drops and ionic concentration gradients, particularly at high currents. This in turn can lead to lost capacity, lithium plating, and hitting both thermal and voltage limits. Understanding the origins of resistances and how to reduce them is thus key to obtaining better batteries that allow short (dis)charge times [10, 115].

Internal resistances stem from processes with characteristic length scales spanning from a single particle to the full cell level (**Figure 4.1a**). Electronic resistances on the cell level are tuned by the thicknesses of the current collectors, the carbon black and binder phases, and their adhesion to the current collector and the active particles [63]. On the electrode scale, the effective ionic resistivity of the electrolyte arises from resistance of the liquid electrolyte itself [236] and the microstructure of the electrodes and the separator [53, 96]. Strategies to mitigate these resistance losses include improvements of the electrolyte conductivity through additives and microstructural design [53, 97, 220, 236].

At the single-particle scale (**Figure 4.1b**), resistances occur in the bulk of the material and at the particle-electrolyte interface. Ionic transport in the bulk of the battery active materials can be experimentally measured with a number of complementary techniques and is relatively well understood. Diffusion coefficients can be measured by both resonance-based [16, 34, 56, 90, 179, 181] and electrochemical techniques [9, 59, 124]. Diffusion paths can be derived from diffraction experiments [144] and *ab initio* simulations [226], with the latter typically providing estimates of activation energies for the diffusion process [45, 81, 138, 199].

Understanding the charge at the active particle-electrolyte interface is key because both ions and electrons have to be transferred across this interface and spatially separated to the electrolyte and the carbon black phase (**Figure 4.1c**). Ions and electrons can diffuse on surfaces via a hopping mechanism [45, 186], which can be facilitated by partial

solvation of the ions [63]. Indeed, the particle–electrolyte interface is particularly complex and hard to study. In addition to the difficulty of decoupling effects of the center of the particle (i.e., the bulk) from the particle surface and from the different effects occurring at the interface, the interface of the active particles changes during cycling. Furthermore, the passivating solid electrolyte interphase forms on the active particles during the first cycles and adds complexity because of the multiple products from electrolyte decomposition [204, 217, 233].

In this part, we focus on interface diffusion, that is, the diffusion through the first atomic layer(s) of the active particle, where the bulk diffusion will be altered because of surface reconstruction effects, and show with theory and experiment that the activation energy for diffusion of lithium through this interface differs from the activation energy in the particle bulk. Choosing LiFePO_4 (LFP) as a model material because of the preferential path for lithium diffusion in LFP in the [010] direction, we concentrate on interface diffusion through the (010) surface [138, 144]. We begin with *ab initio* simulations to gain insights into differences that can be expected between the diffusion through the interface and through the bulk. In experiments, we isolate the activation energies from interface and bulk diffusion by performing experiments on particles of different sizes, prepared with ratios of atoms at the (010) surface to atoms in the bulk ranging from 1:100 to 10:100. With muon spin spectroscopy (μ^+ SR), we measure local ion diffusion [127, 179] and find activation energies in agreement with the simulations. Cyclic voltammetry (CV) measurements on LFP half cells show that the differences in interface and bulk diffusion are apparent in electrochemical experiments. Because the work presented in **Part 3** indicates that the type of surface reconstruction occurring on LFP (010) can be influenced by the type of coating on the LFP, our findings point to the possibility of engineering particles with surface reconstructions that reduce the resistance associated with charge and ionic transport at interfaces.

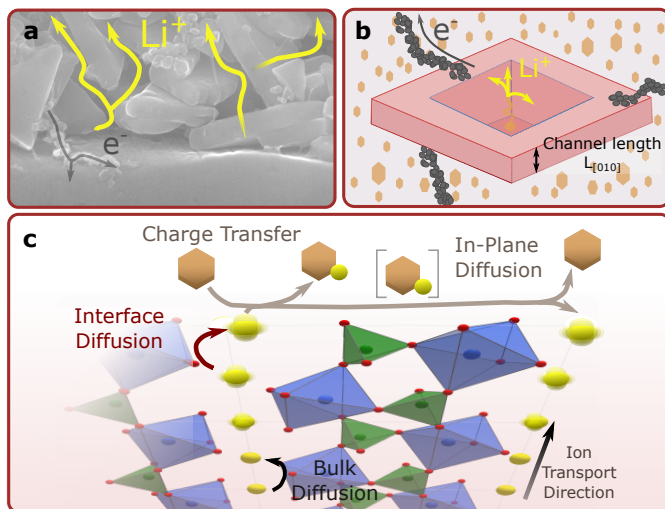


Figure 4.1: a) Lithium and electron diffusion in a lithium-ion battery electrode while charging. b) Lithium-ion and electron diffusion at a single-particle level. Electrons move through the carbon black network, while lithium ions are transferred by the electrolyte (marked in brown hexagons). c) Mechanisms of ion diffusion in a system of one-dimensional ion transport channels. Four processes can be distinguished: bulk diffusion (*i.e.*, away from the particle interface), charge transfer, in-plane diffusion, and interface diffusion.

4.3 *Ab initio* Calculations

Lithium-ion diffusion D_{Li} is a thermally activated hopping process and is typically described in the form

$$D_{Li} = D_0 \exp\left(-\frac{E_a}{kT}\right), \quad (4.1)$$

where D_0 is the exponential prefactor and E_A is the activation energy.

To gain insight about the changes in the lithium-ion trajectory and the associated energy barrier between the interface and the bulk, we perform nudged elastic band (NEB) simulations [32, 70, 72, 110, 153, 200, 201]. We choose the LFP slab from **Part 3**, which contains (2.0/3.5/1.0) unit cells along the ([100]/[010]/[001]) directions and has periodic boundary conditions along the [100]/[001] directions (which creates an infinite (010) platelet). The size of this slab is optimized such that the middle of the slab has on average bulk crystalline properties, while the number of atoms (196) is small enough to enable reasonable computing times. We remove two lithium atoms from the slab (one at the surface and one in the center of the slab) and geometrically relax it. We then calculate the trajectory of a Li atom to these vacancies at the slab surface and in the bulk (see **Figure 4.2a**). To save computational resources, these calculations are performed with fixed atom positions except for the traveling lithium ion. We find that the lithium ions follow a curved path to the vacancy parallel to the (001) plane, passing over an energy barrier of 450–750 meV (**Figure 4.2b**). The reported range is due to the fact that in the finite slab with a lithium vacancy studied here, the starting and ending energies are not symmetric as small local distortions of the lattice have a relatively large impact on the energy. In a perfect crystal, there will be a symmetric ion diffusion trajectory because of the mirror plane parallel to the crystallographic [010] direction of LFP (space group Pnma). Nonetheless, an energy barrier of 450–750 meV is in good agreement with previous studies of bulk diffusion [45, 56, 138, 152, 183, 237] (indicated in **Figure 4.2b** with shading). At the (010) surface of the slab, the path is shifted toward the local potential minima (**Figure C.1a**) of the less constrained surface. The energy barrier for diffusion across the interface

layer is 230 meV, which corresponds approximately to half of the bulk energy barrier. This is consistent with our understanding of reorganization energy upon lithium hopping: at the surface, the lithium ion is not fully coordinated and therefore fewer atoms must move in response to its presence. These results also align with previous computational work on the $\text{LiFePO}_4(010)/\text{Li}_3\text{PO}_4(100)$ interface [182], which also found enhanced lithium-ion mobility at the interface. Therefore, in experiments, we expect to see an interface diffusion activation energy that is lower than the bulk diffusion activation.

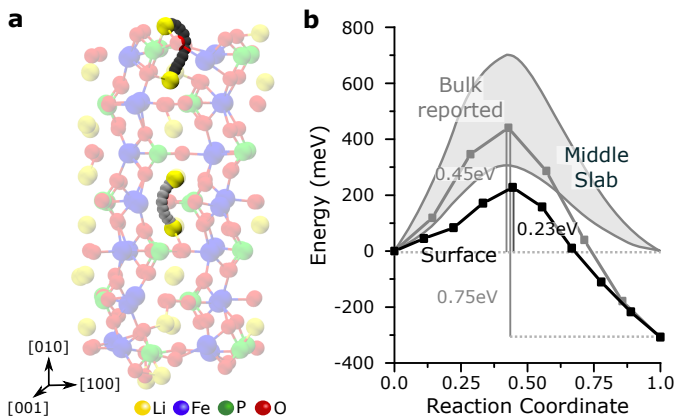


Figure 4.2: a) Lithium-ion trajectories found in the slab by performing NEB calculations. b) Resulting energy of the paths shown in a). The gray area in the background shows the range of reported values from earlier simulations.

4.4 Muon Spin Spectroscopy Measurements

To experimentally confirm the decreased activation energy for interface diffusion in LFP, we perform μ^+ SR measurements. μ^+ SR is a well-established method to track local magnetic fields in solids and has been used to measure lithium-ion motion in active materials [127, 178, 179].

We perform measurements on *Large* ($[010]$ channel length $L_{[010]} = 121(26)$ nm), *Medium* ($L_{[010]} = 51(12)$ nm), and *Nano* ($L_{[010]} = 9.6(26)$ nm) platelets prepared via a solvothermal approach followed by a combined annealing and carbon-coating step. The differently sized particles lead to a (010) surface with bulk atom ratios: 1.0% for the *Large* platelets, 2.5% for *Medium* platelets, and 12.5% for *Nano* platelets. Details about the particle synthesis (that follows the same route as described in **section 2.3**, the morphology, and defect characterization can be found in **Appendix C.1**. Note, that the values for the size of the *Large*, *Medium*, and *Nano* samples differ slightly from the ones found in **Part 3** due to a change of the lithium hydroxide precursor to a cleaner but non-enriched $\text{LiOH}\cdot\text{H}_2\text{O}$.

μ^+ SR is based on the implantation of spin-polarized anti-muons in a solid, where they get trapped in potential minima (**Figure 4.3a**) and couple to local spins until they decay ($\tau = 2.2 \mu\text{s}$) into positrons, which can be detected [229]. In the case of LFP, there are two possible potential minima for anti-muons (μ^+) in the proximity of oxygen atoms near either the Fe or Li sites [181]. This leads to spin coupling with either the lithium or iron nuclei or the unpaired iron electrons. If lithium ions are mobile, the nuclear field experienced by the implanted anti-muon changes as a function of time and the field fluctuation rate can be taken as a measure for lithium-ion hopping [178]. The field fluctuation rate is extracted by fitting the time-dependent difference in the number of positrons observed at the detectors in front of and behind the sample (i.e., the asymmetry, A_{FB}).

For each sample, example asymmetry curves for a few different temperatures and zero magnetic field ($B = 0$ G) conditions are shown in **Fig-**

ure 4.3b-d. The temperature dependence of the field fluctuation rate (ν_{KT1}), extracted from simultaneous fitting of all asymmetry curves at all magnetic field strengths and all temperatures, is shown for each sample in **Figure 4.3e-g**. A detailed explanation of the asymmetry curve fitting procedure [184] is found in **Appendix C.5**.

The *Large* sample shows nearly temperature-independent relaxation of the asymmetry over the measured temperature range (100-400 K) (**Figure 4.3b**), suggesting quasi-static nuclear spin contributions (i.e., no moving ions). Indeed, the extracted field fluctuation rate (ν_{KT1}) is constant with temperature (**Figure 4.3e**). In contrast, the muon spin asymmetry relaxation becomes slower for the *Medium* and *Nano* particles at high temperatures (**Figure 4.3c,d**), indicating ion dynamics. For these samples, we find a temperature-dependent field fluctuation rate that exhibits an Arrhenius-type behavior with an activation energy of 160 meV (**Figure 4.3f,g**).

We identify this field fluctuation as coming from lithium ions moving in the interface layer, for which a 230 meV energy barrier was determined from NEB calculations. Because the NEB calculations indicate a larger energy barrier ~ 400 meV for lithium ions in the center of a particle (i.e., bulk diffusion), a field fluctuation due to lithium hopping in the particle center will be negligible below 550 K (see the inset in **Figure 4.3e**) and therefore not visible in these μ^+ SR data. Considering the surface-to-volume ratio of the particles, the interface contribution to the diffusion for the “Large” sample will be approximately $3 \times$ smaller than that in the *Medium* sample and $12 \times$ smaller than that in the *Nano* sample. Therefore, moving from *Nano* to *Large* samples, the signal-to-noise ratio for local field fluctuations will become progressively smaller, making it increasingly difficult to identify the motion of lithium ions through the interface in *Medium* and *Large* particles. It is therefore reasonable that (1) the error bars for the *Medium* sample (**Figure 4.3f**) are larger compared to the *Nano* sample (**Figure 4.3g**) and (2) we only observe background field fluctuations for the *Large* sample (**Figure 4.3e**).

In earlier μ^+ SR studies on LFP, activation energies between 60 and 100 meV were found [11, 16, 85, 180, 181], which was identified as bulk LFP diffusion, although this was not consistent with other measurements and calculations. We note that all of the studied particles had [010] channel lengths in the range of the *Medium* platelets or smaller (see **Figure S10** for images from Sugiyama et al. [181]), suggesting that this signal may have in fact come from what we identify as the interface diffusion.

Finally, although the μ^+ SR results agree with the results for interface diffusion expected from calculations, it is important to remember that we do not know for certain how the anti-muons and the lithium ions interact. For example, implantation of a positively charged anti-muon [98] may activate the diffusion process by repelling the lithium ion, moving it within the lattice. Detailed simulations of anti-muons in different materials could provide important insights into this and increase the opportunities to tailor μ^+ SR to explore specific phenomena.

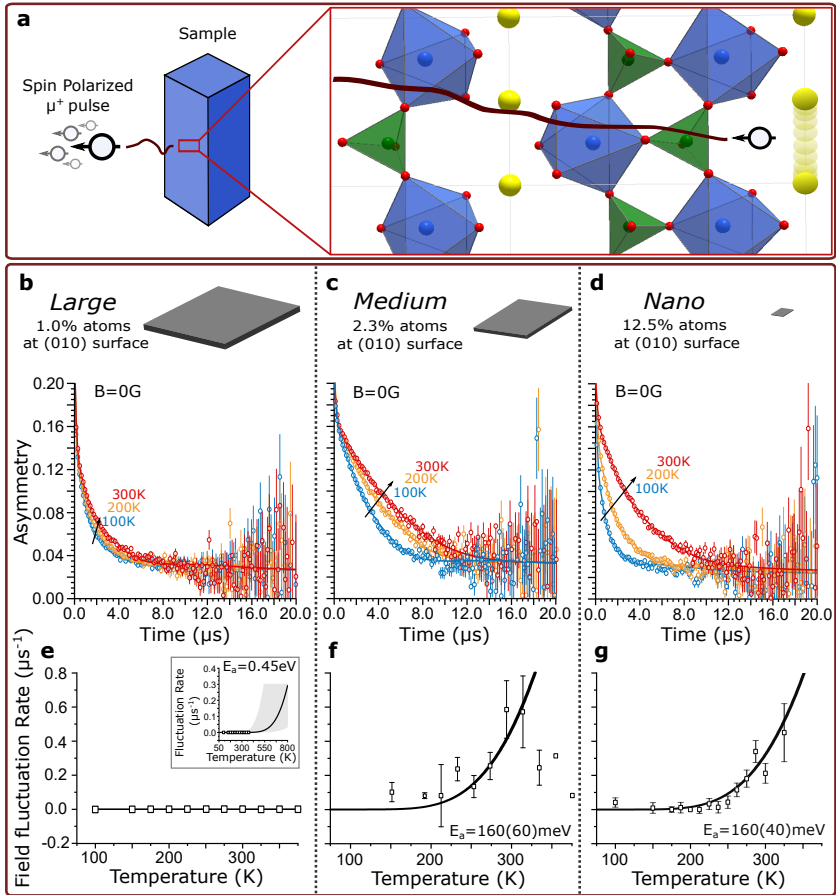


Figure 4.3: a) Working principle of μ^+ SR measurements. A pulse of spin-polarized anti-muons impinges on the sample, and the anti-muons stop at a local energy minima. b-d) Example μ^+ SR spectra (asymmetry curves) of the *Large*, *Medium*, and *Nano* samples at different temperatures and magnetic field $B=0$ Gauss. e-g) Temperature dependence of the field fluctuation rate, ν_{KT1} , for the samples *Large*, *Medium*, and *Nano* extracted from fitting of the asymmetry curves (see **Appendix C.5**). The inset in e) shows an Arrhenius-type fit with an activation energy of 450 ± 150 meV.

4.5 Electrochemical Characterization

The findings from μ^+ SR and NEB simulations build a consistent picture that interface diffusion through the (010) surface layer has a lower activation energy than that in the bulk. To determine whether this is observable and relevant during electrochemical cycling, we perform CV measurements on *Large*, *Medium*, and *Nano* as a function of different temperatures to extract the activation energy.

We choose CV over galvanostatic intermittent titration (GITT) [188] and electrochemical impedance spectroscopy (EIS) [9, 188] because the electrochemically active area in LFP electrodes is a function of charging rate and particle size and only saturates at high currents [106]. To rule out other contributions to the activation energy, measurements are repeated for 6-10 cells per sample, with each LFP electrode having a different thickness. In the case of the *Nano* sample, the carbon black content is also varied.

We determine the activation energy in three steps. First, for each sample, the CV spectra are recorded at different sweep rates (**Figure 4.4a**). Second, we correct the maximal current for contributions from the electrochemical double layer and use the Randle–Sevcik equation [208] to calculate the diffusion coefficient. This is repeated at four different temperatures (**Figure 4.4b**) and the temperature dependence of the diffusion coefficient is plotted in an Arrhenius-type fit, resulting in the activation energy of the diffusion process (**Figure 4.4c**). See **Appendix C.6** for details of the electrochemical experiments analysis.

We obtain activation energies of 176(31), 271(23), and 341(34) meV for the *Nano*, *Medium*, and *Large* samples, respectively. The findings from CV are consistent with those from μ^+ SR and NEB simulations, where the activation energy for interface diffusion is expected to be smaller than that for bulk diffusion. We note that the fast sweep rates in the CV eliminate the features coming from lithium ions that are impeded by antisite defects, which have an activation energy of above 600 meV [45]. This results in smaller activation energies than the ones obtained from

EIS or GITT [9].

One might assume that the observed differences in activation energy between the *Nano* and *Large* samples occur either because of the formation of a solid solution in the nanoparticles which is not present in larger particles [14] or from charge transfer dynamics. However, the solid solution or charge transfer argument would not be able to explain the lower activation energy observed in the μ^+ SR measurements, which probe the local dynamics on fully lithiated LFP particles without any electrolyte (i.e., lack of the electrolyte prevents the formation of a solid solution).

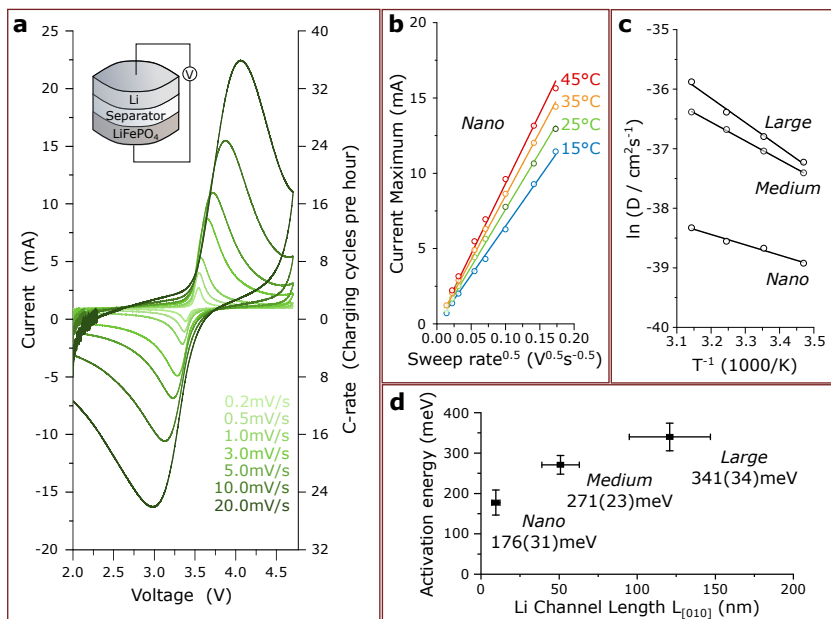


Figure 4.4: a) CV measurement at different sweep rates performed on LFP electrodes in a half-cell geometry. b) Linear fit of the maximal current vs the sweep rate at different temperatures for the *Nano* sample (after correcting for the contribution of the electrochemical double layer). The slope of this curve gives values for the diffusion coefficient, D . c) Linear regression of the natural logarithm of the diffusion coefficient ($\ln D$) vs the inverse temperature (T^{-1}) for each sample. The slope is the activation energy for the diffusion process. d) Resulting activation energies for the samples. Error bars come from the measurements performed on a number of samples.

4.6 Discussion and Conclusion

In conclusion, μ^+ SR, when combined with theory and electrochemical validation, can be used to study ion diffusion in lithium-ion battery active materials. The implementation of a synthesis approach that enables control over particle size and shape, and thereby systematic variation of the particle surface area-to-volume ratio, allows us to separate effects at the surface of a battery active particle from diffusion deeper in the particles. **Table 4.1** summarizes the activation barrier obtained from simulations and experiments. Both CV and μ^+ SR measurements suggest an activation energy, E_a , for delithiation below ~ 160 - 170 meV for the interface diffusion and 350 meV or higher for bulk diffusion, which is consistent with NEB calculations indicating an energy barrier of ~ 230 meV at the interface and ~ 450 meV in the bulk. The differences between calculated and experimental activation barriers probably arise from the carbon coating of LFP particles and from the fact that neighboring atoms were fixed during the NEB calculations. Thus, nanosizing LFP not only improves the accessible capacity of the particles by decreasing the number of antisite defects within a channel [125] but also offers a larger surface with reduced activation energy associated with solid-state diffusion and thereby the associated overpotential.

These findings also shed fundamental understanding into the mechanism of delithiation in LFP. Fast diffusion of lithium at the interface will favor solid solution formation over phase separation during LFP delithiation [142]. Although this can be induced at very high rates in larger LFP particles [114], LFP nanoparticles show solid solution formation also at lower rates. Our findings suggest that this formation of a solid solution in small LFP particles is not only a result of the strain within the two phase regime but also of the fast interface diffusion in LFP [104, 105, 142].

These results highlight the importance of understanding the impact of the surface reconstruction on charge and ion transport. Controlling the interface diffusion may become a valuable method to induce a solid solution to reduce stresses within the electrode. In addition to the delithiation process studied here, future studies should consider lithi-

ation, which could be performed by studying FePO_4 particles, where a few recent studies suggest interesting ion-gradient fluctuation phenomena [238]. It is also key to understand the role of the electron at the interface. Within an LFP particle, it is assumed that the electron moves with the lithium ion via a small polaron hopping mechanism, such that studying the lithium ion is sufficient. At the particle interface, however, a conductive carbon coating could result in a change in electron density and motion of the electron relative to the ion. These approaches to study dynamical changes at the interface of particles will aid in the engineering of particle surfaces.

Table 4.1: Summary of obtained activation barriers for the bulk and interface diffusion.

Method	E_a Bulk diffusion	E_a Interface diffusion
NEB	450-750 meV	230 meV
μ^+ SR	350 meV	160(40) meV
CV	341(34) meV	176(31) meV

5 Part V: Controlling Li ion battery (de)intercalation dynamics through interface design

5.1 Remarks on Part V

Finding a strongly reduced lithium diffusion barrier at the $\text{LiFePO}_4\text{-C}$ interface opens the question whether and how other surface terminations might affect the interface dynamics. In **Part 5**, we characterize the effect of other terminations on both electronic and ionic diffusion. This is done in the context of spinodal decompositions where recent findings [105] suggest that interface dynamics play a key role in the phase separation kinetics of battery active materials. Basing our analysis on in-depth simulations, muon spin spectroscopy and electrochemical analyses, we develop a theory of how interface diffusion is affected by electronically conductive and insulating coatings and predict future coatings that can suppress the unwanted phase separation of active Li ion battery materials.

The work shown in the section is part of a collaboration between seven research groups. Together with Dr. Fanni Jurányi (Paul Scherrer Institute (PSI)) the research groups of Prof. Dr. Martin Månsson (KTH Stockholm) and Prof. Dr. Yasmine Sassa (Chalmers University of Technology), and Dr. Stephen Cottrell (ISIS), muon spin spectroscopy measurements have been performed at the ISIS Neutron and Muon source in the United Kingdom. The group of Dr. Andreas Borgschulte (Eid-

genössische Materialprüfungsanstalt, EMPA) assisted in the XPS measurements. Finally, the magnetic properties of the samples were measured by Dr. Marisa Medarde at PSI. Xueyan Zhao and Dr. Ramesh Shunmugasundaram assisted in the optimization of the electrochemical properties of the coated LiFePO_4 electrodes. Finally, Annina Moser collected transmission electron microscopy images.

5.2 Motivation

To be able to store energy in lithium ion batteries (LIB) reversibly over thousands of cycles, homogeneous transport of electrons and lithium throughout the entire cell is crucial. To achieve such an evenly distributed current density in a complete cell, LIBs consist of complex, hierarchical structures containing electrochemically active materials, ion conducting electrolytes, and electron conducting carbon black-binder [36]. While optimization of the slurry mixing and electrode fabrication is used to achieve uniformity on the microscale, maintaining uniformity on the nanoscale requires engineering of the active particles and their interfaces to the electric and ionic networks [106, 109, 139, 171, 238]. One challenge is the change of the Li concentration within the active materials that influences the chemical potential and intercalation dynamics [20]. While many insertion materials (e.g., layered transition metal oxides) typically maintain a single solid solution phase (**Figure 5.1a**), the active particle can suffer from a spinodal decomposition into Li rich and Li poor phases seen as a characteristic plateau in voltage vs. capacity plots during (dis)charge (**Figure 5.1b**). This phase separation implies a non-uniform current distribution in and around the active particles. As a result, local current hotspots and new phase boundaries give rise to overpotentials, leading to loss of (dis)charging rate capability, specific capacity, and ageing [126, 142].

Significant work has been conducted during the last decades to understand and solve phase separation on a single particle level. Leveraging LiFePO_4 (LFP) as a model material that exhibits a single, two-phase decomposition into LiFePO_4 and FePO_4 domains, researchers have identified three key phenomena. First, when the primary particle size decreases below the characteristic phase boundary size (~ 50 nm [14, 124, 205]), the formation of multiple phases within one single particle is destabilized by the coherent strain between the two phases leading to a formation of a solid solution (**Figure 5.2a**) [19]. Second, phase separation is affected by the (dis)charging rate. For rates above 5C, a solid solution can be maintained over a larger state-of-charge window [74, 114, 240], particularly during lithiation [20, 109, 142]. Third, particles with a solid

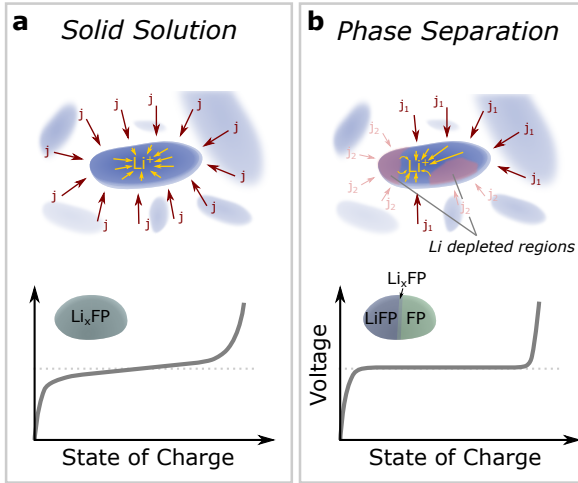


Figure 5.1: Comparison of the local current density in the vicinity of the active particles in the case of a) solid solution behavior and b) phase separation and the resulting voltage polarization.

solution Li_xFePO_4 left at open circuit potentials in electrolyte revert to phase separated LiFePO_4 and FePO_4 due to an electrolyte-induced surface diffusion route [105, 240].

The theoretical framework developed by Nadkarni *et al.* [142] and confirmed by Li *et al.* [105, 109] explains these findings through the exchange current densities and charge transfer overpotentials that change as a function of lithiation and which lead to auto-catalysis or -inhibition of spinodal decomposition [20, 126]. In a simplified picture [104], two scenarios emerge (**Figure 5.2b**): I) When the charge transfer reaction rate is small, Li ions move at the particle surface to form Li rich and Li poor regions such that the exchange current density remains constant and phase separation occurs. II) At charge transfer reaction rates faster than the surface diffusion, lithium intercalates directly into Li_xFePO_4 and solid solution formation is favored. Therefore, the critical current, which delineates the regimes where lithiation occurs via spinodal decomposition or via solid solution, is determined by the lithium and electron

surface diffusivity and the charge transfer reaction rate. However, due to the lack of understanding of how charge transport occurs at the surface of Li ion battery materials, particularly those coated with ceramics [100, 239] or, in the case of LiFePO_4 , carbon [49], reduction of the critical current has been achieved by experimental trial and error.

Here, we computationally and experimentally study interfacial charge dynamics in order to rationally design and demonstrate a coating that reduces the critical current, therefore enabling lithiation via a solid solution mechanism over a broad range of discharge rates. We synthesize LiFePO_4 particles with different surface coatings in order to experimentally study the lithium ion dynamics at the surface of LiFePO_4 and its impact on the lithiation mechanism. We gain further insight into our experimental findings via density functional theory and ab initio molecular dynamics calculations of surface electronics and ionics. Based on these findings, we propose and demonstrate a coating that enables solid solution Li_xFePO_4 at cycling rates as low as C/10 while also maintaining the rate capability and (dis)charge capacity. This work highlights how coatings can be used to control charge dynamics at interfaces and provides a rational approach to designing novel coatings to suppress phase separation in lithium-ion battery active materials.

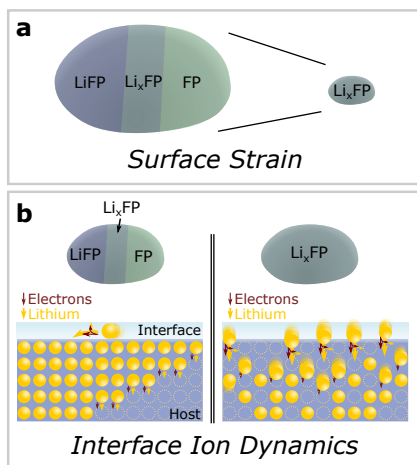


Figure 5.2: Strategies to mitigate phase separation. a) By reducing the particle size, surface strain can destabilize the spinodal decomposition. b) Charge dynamics at the particle interface can lead to two scenarios. When the surface charge diffusion is faster than the charge transfer, lithium ions can phase separate into Li rich and Li poor regions. Conversely, a reduction of the surface charge diffusion allows for solid solution behavior

5.3 Rationale for the investigated system

Whether lithiation occurs via phase separation or solid solution will be determined by the rate at which lithium ions and electrons arrive at or leave a particle and the relative rates of bulk diffusion, interface diffusion, surface diffusion for that particle (**Figure 5.3a**). For a coated particle, one must further consider the impact of charge motion in the coating. Ideally, we would be able to measure each diffusion rate; however, in practice, it is extremely challenging to experimentally differentiate bulk, interface, and surface diffusion.

Our selection of LFP as a model system simplifies some of the considerations for bulk diffusion significantly since it is well-established that lithium diffusion occurs in one dimension along the [010] direction. For the particle bulk, previous work has shown that the lithium ion and electron (obtained from oxidation of Fe from Fe^{2+} to Fe^{3+}) move collectively through the lattice via a small polaron hopping mechanism (**Figure 5.3b**) [56, 138]. The lithium hopping to a neighboring site (separated by 3 \AA) via an interstitial site at $\sim 1.8 \text{ \AA}$ is activated by a multi-phonon process with an activation barrier of approximately 350 meV [45, 66, 138].

More challenging is differentiating between surface and interface diffusion. We know that surface reconstruction affects the local LFP structure and vibrational motion at the surface (see **Part 3**) and, undercoordination of the LFP surface leads to a lower activation barrier of $\sim 200 \text{ meV}$ for Li interface diffusion (see **Part 4**). In the case of surface diffusion, electrolyte molecules (or water) can shuttle Li ions from one site to another and carbon-coated particles accelerate this surface diffusion process [105].

We therefore use LFP with different coatings in order to systematically distinguish between processes involving the particle bulk, interface layers, surface, and coatings. Specifically, we compare uncoated LFP, LFP with an electronically insulating ZnO coating, and LFP with a conductive C coating. Because Li concentrations in coatings are low [39, 207], differences in the experimental or computational findings on Li dynamics in the steady-state can be attributed to either surface or interface diffusion. The contrasts in the electronic properties of the conductive carbon

and insulating ZnO allow us to distinguish between surface electronic effects.

We synthesize coated LiFePO_4 nanoparticles based on the synthesis shown in **Part 2.4**. (**Figure 5.4a**) [22, 23]. We work with particles ~ 60 nm in diameter (**Figure 5.4b**), which means that size should not influence whether phase separation occurs (size below which solid solutions occur is 50 nm [19, 124, 205]). An amorphous zinc oxide or carbon coating is obtained by annealing zinc(II) acetate or D-glucose, respectively, with the LiFePO_4 nanoparticles at 400-600°C (see **Part 2**). Energy dispersed x-ray scattering scanning tunneling microscopy (**Figure 5.4c**) indicate an approximately 3-5 nm thick amorphous coating (**Figure D.1**). X-ray diffraction (**Figure D.2**) and Fourier transform infrared spectroscopy (**Figure D.3**) suggest that the bulk properties of the LiFePO_4 samples are unaffected by the coating. X-ray photoemission spectroscopy (XPS) show no change in the Fe2p energy states and that all surfaces are

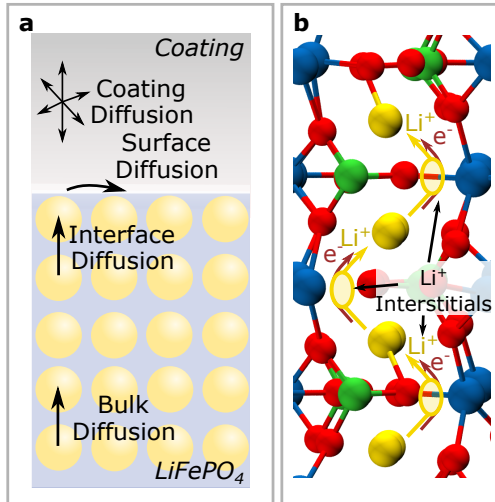


Figure 5.3: a) Schematic image of the four different diffusion pathways have to be considered in coated LiFePO_4 particles. b) General bulk diffusion mechanism in LiFePO_4 . Li ions and electrons move collectively along the lattice via one interstitial Li ion site.

Fe^{2+} terminated [46], confirming that the LiFePO_4 surface is unaffected by the coating (**Figure 5.4c** and **Figure D.4**).

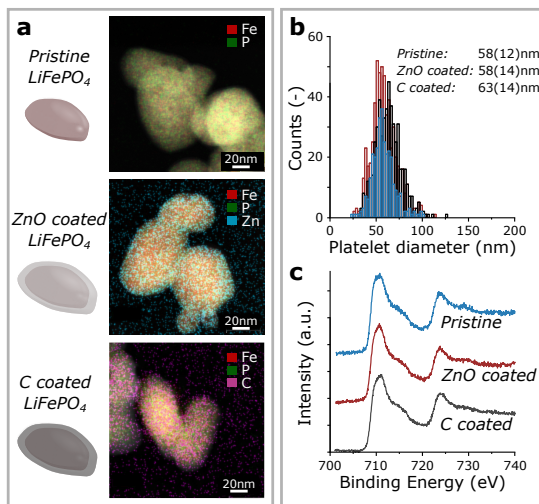


Figure 5.4: a) Energy dispersive x-ray scattering scanning transmission electron microscopy image of the pristine, ZnO, and C coated LiFePO_4 nanoparticles. b) Particle size dispersion of the three samples. c) X-ray photoemission spectra of the three samples, displayed at the Fe L edge.

5.4 Investigation of ion dynamics in LiFePO₄

To measure lithium-ion dynamics, we employ muon spin spectroscopy (μ^+ SR), where one measures the spin relaxation behavior of a pulse of spin-polarized antimuons implanted into the sample [178, 214]. We select μ^+ SR for three reasons. Firstly, as a resonance-based technique, μ^+ SR can probe local motion of the Li ions. As a result, the absence of the Li ions in the coating layers allows us to neglect coating diffusion contributions. Secondly, the high gyromagnetic ratio of muons allows to distinguish between paramagnetic Fe and dynamic Li contributions in LiFePO₄ [181], making it more suitable than more conventional lithium nuclear magnetic resonance spectroscopy. Thirdly, we could show in **Chapter 4** that, by using carbon coated LFP nanoparticles with a high surface to volume ratio and thus a large percentage of surface atoms contributing to a signal, μ^+ SR is sensitive to lithium diffusion at the interface.

Here, we fit the μ^+ SR data over the investigated temperature range of 100-400 K (**Appendix D.2**) and find that carbon-coated LFP particles show an Arrhenius-type behavior with an activation energy of 160(30) meV, which we associate with lithium ion hopping (**Figure 5.5**). In contrast, the ZnO coated and pristine terminated samples exhibit no signal, which means that, similar to lithium hopping in bulk LFP, any lithium hopping within or at the surface of the ZnO-coated LFP occurs with an activation energy above 350 meV (which would only be visible above 400 K).

If undercoordination were the only reason for the reduced interface diffusion activation barrier, the pristine sample should also show a low activation energy for surface ion hopping (see **Part 4**). Therefore, we hypothesize that possible differences of electronic structure (with which Li ion motion is coupled) might impact the Li ion hopping in the C coating as well.

We computationally study the electronic properties of the LFP particles with ZnO and C coatings locally impact lithium dynamics. We

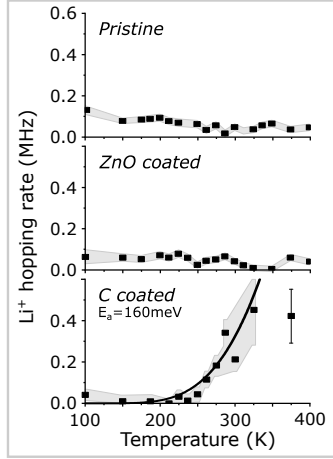


Figure 5.5: Li ion hopping rate of the coated LiFePO_4 (LFP) nanoparticle powders obtained from muon spin spectroscopy. On the carbon coated LFP, Li ion dynamics show an activation energy of 160 meV.

perform density functional theory (DFT) using the CP2k package that, as a hybrid plane wave and orbital based method, offers a high sensitivity to local surface effects [79, 153, 201]. We construct and geometrically relax LFP slabs with a thickness of 3.5 unit cells along the [010] direction with periodic boundary conditions perpendicular to the [010] direction to obtain quasi-infinite platelet particles (**Figure 5.6a**) with (i) a pristine LiFePO_4 (010) surface (**Figure 5.6b**), (ii) an amorphous ZnO-coated LiFePO_4 (010) surface (**Figure 5.6c**), and (iii) a covalently-bonded, carbon-coated LiFePO_4 (010) surface (**Figure 5.6d**). We validate these calculations by comparing the calculated electronic structure to that determined by XPS and UV-visible absorption spectroscopy (**Figure D.4-D.5**).

We determine the elemental and positional origin of each electronic state (**Figure D.9-D.11**), allowing us to plot the partial electron density of states (PEDOS) within the slab (**Figure 5.6a**) and at the surfaces (**Figure 5.6b-d**). In agreement with literature calculations and measurements [131, 151, 182, 208], the pristine LFP slab has a band gap of

3.6 eV within the slab with hybridized Fe-O valence band states and Fe conduction band states (**Figure 5.6a**). At the pristine surface (**Figure 5.6b**), the valence and conduction band states remain unchanged, suggesting only minor differences in electronic structure between surface and bulk. This is further supported when looking at the highest occupied and lowest unoccupied electronic states (inset of **Figure 5.6b**), where significant contributions to the electronic wave functions arise from deeper within the slab. When the (010) surface is terminated with ZnO (**Figure 5.6c**), electronic states stemming from ZnO are present within the LFP band gap. The carbon termination (**Figure 5.6d**) also results in mid-gap states. However, in contrast to the ZnO case where the mid-gap wave function states are strongly localized in the ZnO layer (inset **Figure 3d**), the carbon coating leads to a Fe-O-C hybridization with electronic density between the coating and the particle bulk (inset **Figure 5.6d**). These results suggest that, while the ZnO termination will not significantly affect electronic or ionic transport at the LFP surface, the carbon coating will cause a delocalized electronic bond between carbon and Fe. As a result, electron transport at the LFP-carbon interface is likely no longer a slow small polaron hopping process. This will positively impact on Li ion dynamics at the LFP surface, which is consistent with our findings from the μ^+ SR measurements.

We confirm the enhanced Li ion dynamics computationally by performing *ab initio* molecular dynamics simulations (AIMD) on the LiFePO_4 slabs described above at a cryostat temperature of 1000 K, where the thermal energy is high enough to observe lithium ion hopping without impacting the structural integrity of the slab [45, 144, 182] (**Figure D.12**). First, we calculate the lithium mean squared displacement (MSD) using the pinball model [88], where all atoms are fixed to their 0 K equilibrium position except for the Li atoms (**Figure D.13**), in order to study the motion of the Li atoms independent of the motion of other atoms in the lattice. In all samples, the Li ions exhibit small quasi-harmonic fluctuations at a frequency of approximately 5-15 THz, which corresponds to typical Li-O vibrations in LFP [23, 182] (**Figure D.1**); however, the amplitude of these vibrations varies significantly among the samples (**Figure 5.7**). Within the slabs and at the surface of the

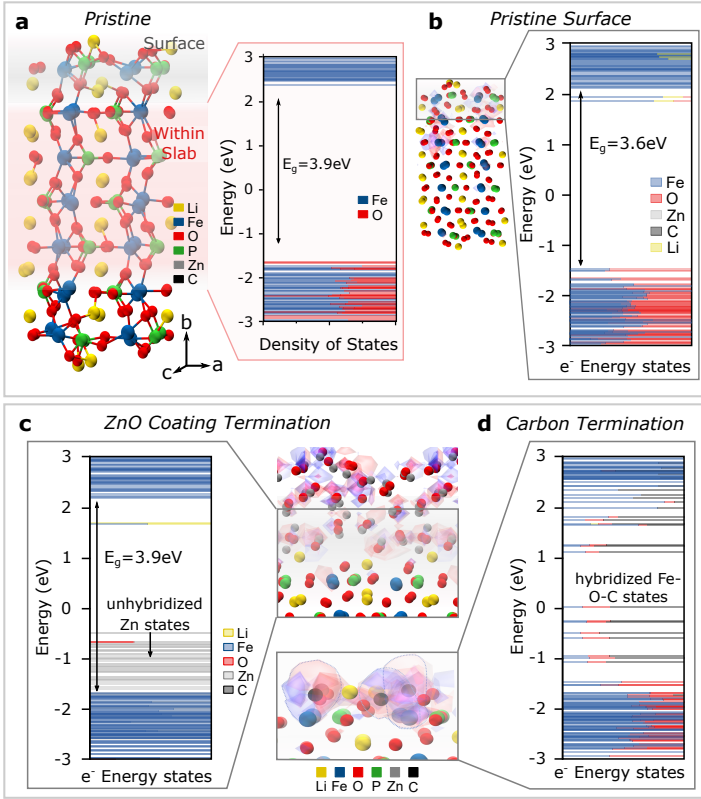


Figure 5.6: a) Structure of the LFP slabs with a classification between atoms at the surface and within the slab. Furthermore, the partial electron density of states (PEDOS) is shown for the pristine LFP sample within the slab. b-d) Energy level diagram of the b) pristine, c) ZnO terminated, and d) C terminated LFP surface. For all samples, an image of the three highest occupied and three lowest unoccupied wave functions is shown.)

ZnO and pristine terminated samples, Li atoms fluctuate with a MSD of $\sim 0.5 \text{ \AA}^2$, implying an amplitude of motion of 0.7 \AA . In contrast, in the carbon coated samples, the MSD increases to 1.1 \AA^2 , leading to a doubling of the amplitude of lithium motion to $\sim 1.0 \text{ \AA}$. Since the distance between two interstitial Li hopping sites is $\sim 1.8 \text{ \AA}$ [144], the quasi-harmonic Li ion motion in the carbon termination can make up for almost 60% of

the hopping distance, compared to 40% for the pristine and ZnO terminated LFP surface. As a result, the energy needed from the host lattice to enable Li ion hopping in the carbon-coated LFP will be relatively small. Increased Li-ion hopping between free lattice sites is indeed what we find from the AIMD simulations where all atoms are allowed to move (**Figure D.14**). Within the slab, at the pristine surface, and with a ZnO termination, vibrations of the host lattice increase the MSD to 2.0 \AA^2 , 4.0 \AA^2 , and 3.0 \AA^2 , respectively. Meanwhile, in the carbon terminated LFP, the vibrations of the host lattice increase the MSD one order of magnitude higher to 25 \AA^2 .

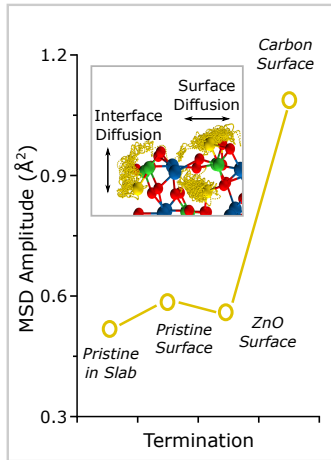


Figure 5.7: Amplitude of the Li atom mean squared displacement (MSD) when the host lattice is fixed. The Li atoms are significantly more flexible close to the carbon termination with the other interfaces being relatively similar to Li ion dynamics. Inset: Li ion trajectory of the pristine LFP sample when all atoms are allowed to move.

Based on AIMD, we also distinguish between surface and interface diffusion. From the Li atom trajectories (inset **Figure 3f** and **Figure D.11**), we can infer that Li ions are mobile at the LFP interface along both the surface and interface diffusion directions. However, the effective distance travelled by the ions is different in the two cases. From the MSD (**Figure D.15-D.16**), we find that, while interface and surface

diffusion are very local in the ZnO and pristine terminated LFP, the surface diffusion dominates for the carbon-coated LFP.

Our combined experimental and computational approach on differently coated LFP particles suggests that the carbon termination shows strongly enhanced interface and surface diffusion. We observe that the electronic structure difference at the LFP-coating interface does play an additional key role. We hypothesize that the hybridization of Fe orbitals with carbon causes a new electron transport pathway, decoupling the existing combined electron-Li ion transport route and allowing the Li ion to move freely at the LFP-coating interface. This results in the observed reduction of the interface diffusion energy barrier and the fast surface diffusion.

5.5 Consequences for the Li (de)intercalation

We expect that these differences in Li ion surface diffusion for the different coatings will influence the lithiation reaction we find for the LFP samples. Specifically, we anticipate that ZnO and pristine coated LFP with their slow surface diffusion will have a reduced critical current and favor lithiation via a solid solution while fast surface diffusion in carbon coated LiFePO₄ will have an enhanced critical current that drives phase separation.

To check this, we perform *in-operando* x-ray diffraction (XRD) measurements on LiFePO₄ half cells (**Figure 5.8a-c**). For reasons of the XRD data quality, all operando XRD spectra are measured at a rate of 0.1C; however, measurements at a fast rate of 1C show the same charge–discharge behavior as at 0.1C (**Figure D.17**). Focusing on the LiFePO₄/FePO₄ (020)/(211) peaks that are sensitive to the lithium ion distribution [109, 114], we see that the surface terminations indeed lead to different behavior during discharge (i.e. lithiation). In agreement with our expectations, only the carbon coated sample (**Figure 5.8a**) exhibits a miscibility gap indicative of phase separation. Meanwhile, the pristine (**Figure 5.8b**) and ZnO-coated (**Figure 5.8c**) LiFePO₄ particles demonstrate solid solution behavior (monotonous change in the XRD peak) and a curved voltage plateau (dQ/dV plot in **Figure D.19**).

During charge (i.e., delithiation), we would expect a miscibility gap in all samples due to the auto-catalytic nature of the spinodal decomposition [20, 105, 142]. We find this is indeed the case for the pristine LFP sample where a miscibility gap is observed that contains the same Li rich FePO₄ and Li deficient LiFePO₄ phases as the C coated LFP sample where a miscibility gap between Li_{0.2}FePO₄ and Li_{0.8}FePO₄ is observed. In the ZnO coated LFP sample, however, the miscibility gap is strongly diminished and only appears between Li_{0.55}FePO₄ and Li_{0.7}FePO₄. Looking closer at the XRD pattern of the ZnO coating at a normalized state of charge of 50% (**Figure 5.9a**; other samples shown in **Figure D.18**), we observe an asymmetry between lithiation and delithiation. During discharge (lithiation), the (020) and (211) peaks broaden

into each other as reported for solid solution lithiation [142]. During delithiation, the peaks only shift and lift the degeneracy without significant broadening, indicative of compressive strain [44]. We hypothesize that the rigid ZnO coating causes this added coherency strain during delithiation, thereby causing the miscibility gap to reduce [43, 135]. The benefits of the ZnO coating thus appear to be two-fold: it blocks Li surface diffusion forcing solid solution lithiation during discharge and also changes the mechanical properties at the surface broadening the range of a $\text{LiFePO}_4 / \text{FePO}_4$ solid solution during delithiation (charge).

While these findings on ZnO coatings appear promising, they highlight an underlying conflict in interface engineering. As expected for a conductive coating that facilitates charge transfer to/from the carbon black network [77], the rate capability of the C coating is strongly enhanced compared to the pristine or ZnO coating (**Figure 5.9b**). While enhanced electronic conductivity through carbon coatings is crucial to extract the desired capacities above 150 mAh/g, decoupling electron and Li ion diffusivity enables fast surface diffusion which leads to phase separation instead of the solid solution lithiation. In contrast, a coating that forces lithium diffusion into the particle instead of along the LFP sur-

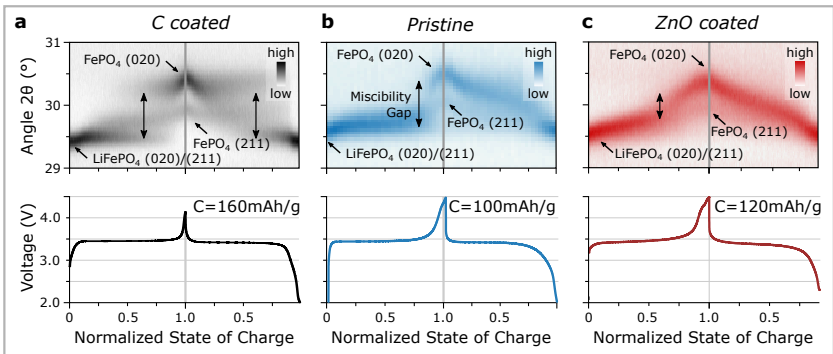


Figure 5.8: *Operando* x-ray diffraction spectra of the $\text{LiFePO}_4/\text{FePO}_4$ (020) peak as a function of state of charge for a) C coated, b) Pristine, and c) ZnO coated LiFePO_4 nanoparticles. All spectra were measured at a current of 17 mA/g, corresponding to a rate of $C/10$.

face such as a ZnO coating results in the desirable solid solution based lithiation, but lower achievable capacities.

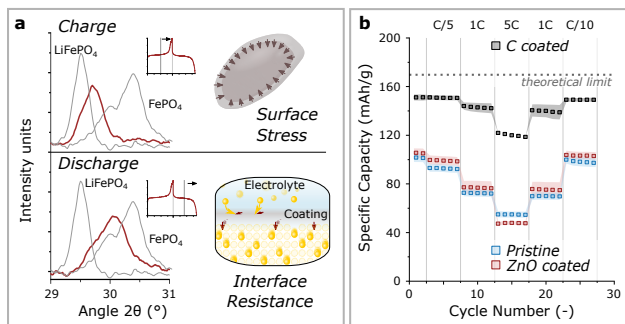


Figure 5.9: a) Comparison of the x-ray diffraction spectra of the ZnO coated LiFePO_4 sample at 50% (dis)charge. During particle charge, surface stress prevents phase separation. During discharge, the resistance due to the ZnO coating leads to a situation where charge transfer is faster than Li diffusion. b) Discharge Capacity of the coated LiFePO_4 samples at different (dis)charge rates.

5.6 Decoupling Electronic and Ionic Transport

To facilitate solid solution (and thus reduce inhomogeneous currents) while decoupling electronic and ion transport (and thereby enabling improved rate capabilities), we propose a coating that promotes electron delocalization while impeding the long-range surface diffusion of lithium. To test this hypothesis, we propose a carbon coating that contains ZnO regions, and prepare LiFePO_4 particles with such a 2.5 wt% ZnO and 2.5 wt% carbon coating by mixing zinc acetate and D-glucose during the coating step (**Figure D.20**). As sketched in **Figure 5.10**, we expect that delocalized electronic transport will occur in the carbon phase while the lithium ion surface diffusion will be impeded by the ZnO clusters, which will instead promote lithium ion transport through the coating into the particle. Indeed, operando XRD of the ZnO/C coated LFP (**5.11a**) reveals the same solid solution behavior for the ZnO-coated LiFePO_4 (**Figure 5.8c**). However, the electrochemical impedance of the ZnO/C coated LFP remains the same as for the carbon coated LFP (**Figure D.19**), and the rate capability of the ZnO/C-coated LiFePO_4 is on par with carbon coated LFP (**Figure 5.11b**). Optimization of the ZnO and C ratios and their distribution within the coating would likely offer additional possibilities to improve the material performance.

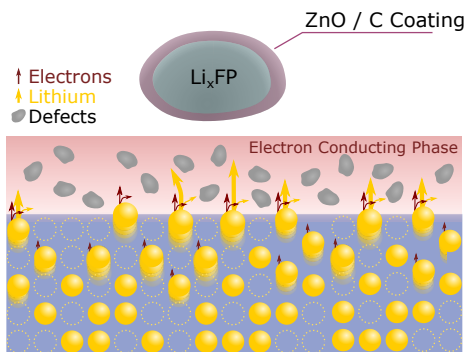


Figure 5.10: Schematic explanation of the ZnO+C Coating. Due to the ZnO defect regions, the surface diffusion of Li is impeded and the coating mechanically stabilized while the carbon matrix still allows for high rate capability and capacity retention.

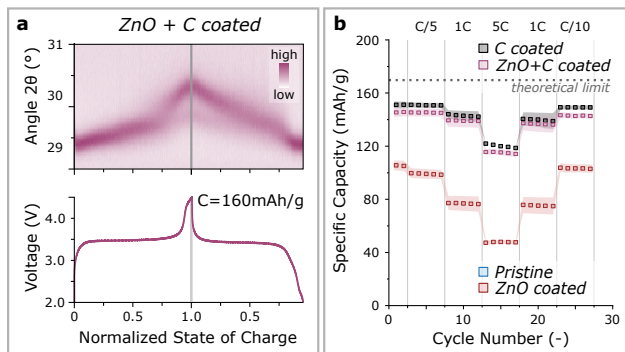


Figure 5.11: a) *Operando* x-ray diffraction spectra of the $\text{LiFePO}_4/\text{FePO}_4$ (020) peak as a function of state of charge for ZnO+C coated LiFePO_4 nanoparticles, measured at a current of 17mA/g , corresponding to a rate of C/10. b) Discharge Capacity of the coated LiFePO_4 samples at different (dis)charge rates.

5.7 Conclusion and Outlook

This work highlights how surfaces can be used to control the (de)lithiation in battery active materials. Our findings provide an explanation for the discrepancies in the reported LFP ion diffusivities. For example, Kang *et al.* [91] showed that a complex amorphous coating could lead to very high rate capabilities in LFP. Based on our findings, we hypothesize that the high diffusivity arises due to a hybridization of the Fe surface states that allows for enhanced charge dynamics. Also the inconsistency of measured LFP diffusivities using μ^+ SR can be linked to surfaces, where solid state syntheses that are more prone to create amorphous interfaces [207], typically lead to higher diffusivities [16, 181] than solvothermal syntheses that typically form insulating hydroxide-terminated surfaces [11, 85].

The finding that phase separation can be effectively eliminated by creating coatings that impede Li hopping but allow for fast charge transfer into the material can be transferred to other phase separating battery chemistries (e.g. Li air batteries [75], transition metal oxides [150], etc.) and materials where small polaron transport is the only available electron transfer path. Furthermore, our approach to study interface dynamics is transferable to other systems where interface dynamics has yet to be understood, e.g. solid electrolyte interphases [117, 170] and solid state electrolyte interfaces [17]. Continuous developments of μ^+ SR based on in situ setups [132], muon focusing to interfaces [219], and beam line upgrades will allow for increasing capabilities to measure surface dynamics in the near future. Combining this with novel modelling descriptions that include electronic contributions in the lithium ion diffusion process [62] might pave the way to understand charge transfer through complex systems, allowing new battery chemistries with higher rate capabilities, capacities, and longer battery life.

6 Concluding Remarks

6.1 Summary

In this thesis, we describe a new method to study charge dynamics at interfaces between different battery components. Starting with the development of a hydrothermal synthesis of LiFePO_4 platelet particles with an excellent size and coating control (see **Part 2**), we obtain particles with large surface to volume ratios and different surface terminations.

Applying a size series of these particles, we perform first studies of ion dynamics on carbon coated LiFePO_4 particles. By measuring the variations of lattice vibrations between large and nanoparticles via inelastic neutron scattering (**Part 3**), we find that Li–O surface vibration modes are shifted to higher energies, suggesting a change in the dynamic structure of LiFePO_4 . Combining, muon spin spectroscopy studies on the same size series of carbon coated LiFePO_4 particles with nudged elastic band simulations and detailed cyclic voltammetry measurements (**Part 4**), we obtain a quantitative estimate of the Li ion interface diffusion activation energy of ~ 200 meV, approximately half as what we would find within the bulk of LiFePO_4 .

In **Part 5** we further study surface diffusion in coated LiFePO_4 nanoparticles. Extending our combined theoretical and experimental approach to both ionic and electronic mobility, we find that the carbon coating creates an additional electron conduction pathway that is faster than the initial coupled Li ion - small polaron hopping mechanism. As a result, Li ion hopping and electronics are decoupled, hence resulting in enhanced Li ion surface diffusion.

Based on our results, we rationally design a combined ZnO/C coating with ZnO regions that hinder Li ion surface diffusion and hence reduce the phase separation reaction during battery operation. By introducing this coating, we obtain a complete suppression of phase separation on particles that maintain a high specific capacity of 150 mAh at a fast rate of 1C.

In summary, we have shown a method to both understand and engineer ionic and electronic transport at the active material surface hence creating a completely new set of tools for future coating applications.

6.2 Outlook

The findings in this thesis have the potential to contribute to the solution of some of the remaining questions in LIBs. Regarding LiFePO_4 charge dynamics, a separated quantification of surface and interface diffusion would improve our understanding very much. To achieve this, additional measurements on particles with different grain orientations or on grown thin films will be needed. Furthermore, our work here could not present a definitive proof that the changes of electronic transport at the LFP-carbon surface are indeed due to the separation of small polaron hopping and Li ion diffusion. Well designed measurements of Mössbauer spectroscopy could aid here to disentangle small polaron effects and provide a conclusive answer.

The method shown here to study interface diffusion can be readily transferred to many of the other interfaces that occur in Li ion batteries. Understanding the complex charge dynamics through the solid electrolyte interphase that consists of multiple components could provide improved battery lifetime, cost, and rate capability in future battery technologies. With cryogenic electron microscopy providing increasingly more insights in the structure of the solid electrolyte interphase, first attempts to study the dynamics via inelastic neutron scattering and muon spin resonance have become feasible.

Our combined measurement approach can also be applied to characterize ion dynamics through solid-solid interfaces in next-generation solid state batteries. These new type of batteries promise to be safer at much higher stored energy but, to date, suffer from interfacial resistances that hamper cycling rates. Using the combined computational and experimental approach on a series of modified interfaces could help to understand how to tune ion dynamics, e.g. via the introduction of additional buffer layers between the battery components. For this, however, many of the structural details of the bulk of these components have yet to be understood before a clear separation of bulk and surface effects can be made.

The results shown here are not only significant for Li ion battery research. The theories of spinodal decomposition and exchange current density were developed for the adsorption of atoms on a surface [20]. With that in mind, many of the discussions can be directly translated for applications in basically all processes in which molecules tend to adsorb inhomogeneously to surfaces (*e.g.* catalysts, flow reactors, filtering systems, electrolysers, etc.). As a result, studying interface dynamics in these systems might set new routes to high performance applications.

Apart from measuring material interfaces, the underlying techniques that we have used to study interface transport can be further developed. On the experimental side, developing *in operando* capabilities for both μ^+ SR and INS would be extremely interesting as they would help track the ion dynamics changes as a function of lithium concentration. Similarly, finding strategies to create depth profiles with low-energy muons that are provided at PSI, J-PARC and, from ~ 2030 on, LNS could pave the way to study interface dynamics in a much more direct and faster manner. On the computational side, including the interactions of the positively charged muons with the lattice in the DFT simulations would allow for very interesting studies. While some groups have started to implement muons to study the spin coupling between elements [47, 215], a slightly simplified DFT+ μ that would allow for long production time AIMD runs would extremely benefit the entire solid state ionics community and make μ^+ SR an even more powerful tool. Furthermore, it would

6 Concluding Remarks

be amazing to implement some of our analysis strategies in a neural network based predictive system such as the BIG-MAP, eventually allowing us to predict better coatings faster.

Appendix

Appendix A

Supporting Information to Part I

A.1 Experimental Methods

A.1.1 Low temperature hydrothermal synthesis

In a typical synthesis of LFP, a 20 mL solution of LiOH (Sigma) and the ethylene glycol (EG) (Sigma) is transferred into a 50 mL stainless steel reactor. While stirring, 20 mL of H₃PO₄ solution is added dropwise. A white precipitate of Li₃PO₄ forms. Ground FeSO₄ · 7H₂O (Sigma) powder is quickly added to the dispersion and the reactor is purged with N₂ for 10 min. The final molar ratio [Li] : [Fe] : [PO₄] : [EG] in the solution is kept 1 : 1 : 3 : 0.1. After purging, the reactor is heated with a heating mantle. When the synthesis is finished, the resulting off-white powder is washed in H₂O and ethanol and dried at 80 °C.

A.1.2 Platelet size controlled synthesis

All LiFePO₄ samples were synthesized in a solvothermal reaction with EG (Acros) and distilled water as solvents. As a first step, enriched ⁷Li₃PO₄ was synthesized. For this, we prepare a 3 M solution of ⁷LiOH · H₂O (>99.95% ⁷Li, Nukem Chemicals) and a 1 M solution of H₃PO₄ (Sigma) in H₂O. 400 ml of both solutions are then mixed together and stirred for a few hours to equilibrate. LPO results as a white precipitate, which is filtered and washed with water. This ⁷Li₃PO₄ precursor powder was then used for all reactions. The *Large* sample is made by dispersing the ⁷Li₃PO₄ in 40 ml distilled water in a hydrothermal reactor of 50 ml volume. We then add preground FeSO₄ · 7H₂O powder and EG to the

solution to reach a precursor concentration of 0.8M and EG concentration of 0.08M. The reactor is then closed, heated to 115°C with a heating mantle and kept at the temperature for six hours while constantly stirring. We wash the resulting off-white powder three times in water, once in ~ 0.1 M H_3PO_4 and once in ethanol.

Table A.1 summarizes the reaction conditions for the *Meso*, *Medium*, *Nano* platelet particles which were prepared similarly to the *Large* particles, but with different temperatures and EG concentrations. Note that the reaction conditions of the *Large* sample have been changed during the course of this thesis. While the reaction time for the *Large* sample was 6 h in the studies mentioned in **Part III**, the reaction time has been increased in **Part IV** to achieve a higher electrochemical performance.

Table A.1: Summary of the hydrothermal conditions.

	<i>Nano</i>	<i>Medium</i>	<i>Meso</i>	<i>Large</i>
Temperature	180 °C	180 °C	180 °C	115 °C
Time	6 h	6 h	6 h	48 h (Part IV), 6 h (Part III)
EG content	100 v%	50 v%	0.08 mol l ⁻¹	0.08 mol l ⁻¹
C _{tot}	0.8 mol l ⁻¹	0.8 mol l ⁻¹	0.8 mol l ⁻¹	0.8 mol l ⁻¹

A.1.3 Coating LiFePO₄ nanoparticles

We coat the LFP particles with 3 wt% ZnO and carbon by grinding LFP particles together with zinc acetate (Sigma) or D-glucose (Sigma), respectively. The mixture is then pressed into pellets and annealed under Ar/3%H₂ flow. For the annealing conditions, carbon coated LiFePO₄ was coated with at 600 °C for 6 h and ZnO coated LiFePO₄ was prepared at 400 °C for 16 h, To prevent agglomeration of the particles and to reduce defects, the pristine sample was also annealed at 400 °C for 16 h. All samples were heated to the target temperature in 30 min.

For the mixed ZnO/C coated LFP samples, zinc acetate and D-glucose is ground together with LiFePO₄ to achieve a ratio 2.5 wt% ZnO, 2.5 wt% carbon and 95 wt% LFP. To maintain a high crystallinity of C while en-

sureing that the ZnO coating does not decompose in the reducing H₂/Ar atmosphere, the annealing temperature is set to 500 °C for 8 h.

A.1.4 Particle Characterization

To determine the particle dimensions, scanning electron microscopy (SEM) images in secondary electron mode are taken using a Hitachi SU-8200 or, in the case of the nanoparticle thickness, with the Nanoscope Dimension 3100 atomic force microscope (AFM). The dimensions of 100-200 particles are measured using ImageJ [167], see **Figure A.8** for details. Fourier transform infrared spectroscopy (FTIR) spectra are obtained on an attenuated total reflection (ATR) setup with Ge single crystal on a Bruker Vertex 70 spectrometer. The observed symmetric PO₄ stretching band is fit with a Gaussian function. X-ray powder diffraction spectra are measured in a 2 Θ range between 15° and 85° using a Rigaku Smartlab diffractometer. Rietveld refinements are performed with the Maud software[120].

Transmission electron microscopy images of the coated samples are taken with the FEI F30 and, in the case of energy-dispersive x-ray scattering, the FEI Talos transmission electron microscopes. Raman spectra were measured with the NTEGRA Spectra micro Raman spectrometer.

A.2 Low Temperature Synthesis of LFP: Electrochemical Characterization

To test LFP electrodes, 70 wt% of active material, 20 wt% of Super C64 carbon black (Timcal), and 10 wt% of Kynar HSV900 polyvinylidene fluoride binder are dispersed in N-methyl-2-pyrrolidone (Sigma). Resulting slurries are blade coated on an aluminum sheet and dried at 120 °C under vacuum for 8 h. Half cells were prepared under argon atmosphere, using glass fiber separator soaked with 500 μ l of the electrolyte, a 1 M solution of LiPF₆ in 1:1 ethylene carbonate and dimethyl carbonate (BASF), between the LFP cathode and lithium metal reference. The cycling measurements are performed at room temperature on a Biologic VMP3

potentiostat. The reported values (data points) and errors (shaded regions) in **Figure 2.4** come from the average and standard deviation of measurements on different electrodes prepared with materials from different synthesis batches, but with the same reaction conditions.

A.3 Energy Consumption Analysis

We estimate the energy required for precursor production and synthesis of lithium iron phosphate (LFP) via a hydrothermal approach. The energy consumption required for precursor production (per kg LFP) is calculated from different life cycle assessments [51, 86, 123] and is summarized in **Table A.2**. As iron (II) sulfate is a byproduct of the iron industry, the energy consumption for its production is neglected.

To estimate the energy consumption of the hydrothermal synthesis as a function of process parameters, we assume a hydrothermal reactor with a volume $V = 10 \text{ m}^3$, a surface $A = 25 \text{ m}^2$ and an insulating wall with the thickness $x = 0.1 \text{ m}$. Following the analysis of Majeau-Bettez [123] and Dunn [51], the total energy consumption per kg LFP is split into three terms,

$$\frac{E_{tot}}{m_{LFP}} = \frac{(E_{heat} + E_{loss})}{\eta_{tot}m_{LFP}} + E_{prec} - \frac{E_{rec}}{m_{LFP}}, \quad (\text{A.1})$$

where E_{heat} is the energy required to heat the reactor, E_{loss} is the energy loss at the reactor walls, E_{prec} is the energy required to prepare the precursors per kg LFP, and E_{rec} is the energy recovered after the reaction, which we assumed to be half of the heating energy E_{heat} . The term η_{tot} is a product of reaction yield and the heater efficiency. To compare results, the total energy consumption is normalized to the LFP mass, produced per batch, m_{LFP} .

The energy loss through the wall is estimated with the conduction heat transfer equation (A.2), where λ is the heat exchange coefficient, t is the

reaction time, and T_r , T_0 are the reactor and the ambient temperatures, respectively. Typical values are found in **Table A.2**.

$$E_{loss} = \frac{\lambda A (T_r - T_0) t}{x} \quad (\text{A.2})$$

In contrast to previous work, here we model the energy consumption during reactor heating assuming that (i) the reactor is not completely filled and (ii) water evaporates into the gas phase. These assumptions give a better estimate of the energy consumption than models where the entire liquid volume is assumed to evaporate. This assumption is particularly important for low temperature syntheses, where only a small fraction of liquid converts to the vapor phase.

We define a filling factor, f , (see **Figure A.1**) and split the required heating energy in a vapor phase term E_{vap} and a liquid phase term E_{liq} . We assume that the liquid phase is incompressible and the volume change due to evaporation is negligible. Also, we assume ideal gas conditions of the gas phase and take the specific heat to be constant (e.g., neglect salt contributions in the liquid phase). We thus obtain,

$$E_{heat} = E_{vap} + E_{liq} \quad (\text{A.3})$$

$$E_{vap} = m_{vap} \Delta_v H + \int_{T_0}^{T_f} m_{vap}(T) C_{vap}^{sp} dT \quad (\text{A.4})$$

$$E_{liq} = \int_{T_0}^{T_f} (m_{tot} - m_{vap}(T)) C_{liq}^{sp} dT \quad (\text{A.5})$$

$$m_{vap}(T) = \frac{M_{H_2O} p(T) (1 - f) V}{RT} \quad (\text{A.6})$$

where $\Delta_v H$ is the enthalpy of evaporation, m_{vap} is the mass of water in the vapor phase, C_i^{sp} is specific heat of the phase i , R is the universal gas constant, M_{H_2O} is the molar mass of water, and $p(T)$ is the temperature dependent vapor pressure [111, 177].

Further improvement to our model could be achieved by taking into account the change in volume of the liquid phase with temperature (*i.e.*,

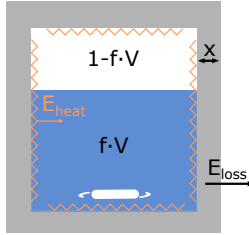


Figure A.1: Schematic of the reactor.

allowing for a pressure and temperature dependent heat capacity). However, since the heat capacity of water tends to increase with salt strength and temperature [163], our current model can be considered as an upper limit for the required heating energy.

In **Table A.2**, we compare the energy consumption for precursor production and LFP production via a low temperature hydrothermal synthesis and solid state approach.

Table A.2: Mass of precursors needed for LFP synthesis, energy needed for precursor synthesis, and energy needed for LFP synthesis in a hydrothermal and solid state approach.

	Mass (kg) of precursor needed for 1 kg LFP	Energy (MJ kg ⁻¹) required for precursor	Energy (MJ kg ⁻¹) required for LFP
Hydrothermal			26.3
FeSO ₄	1.23	–	–
H ₃ PO ₄	0.62	12[3]	7.4
LiOH	0.46	41[1]	18.9
Solid State			21.6
Li ₂ CO ₃	0.23	41[1]	9.4
Fe ₃ O ₄	0.49	0.72[1]	0.4
(NH ₄) ₂ HPO ₄	0.84	14[3]	11.8

Table A.3: Values and expressions used in the energy consumption analysis.

Thermodynamic Constants		
Evaporation enthalpy [164]	$\Delta_v H$	2.26 kJ kg ⁻¹
Heat capacity liquid phase [164]	C_{liq}^{sp}	4.2 kJ kg ⁻¹
Heat capacity gas phase [164]	C_{vap}^{sp}	1.9 kJ kg ⁻¹
Specific density	ρ_{H_2O}	1000 kg m ³
Ambient temperature	T_0	298 K
Reaction yield	y	0.95
Vapour pressure [111, 177]	$p(T)$	$10^{4.65 - \frac{1440}{T-64.8}}$, $T \in [273, 373 K]$ 1, $T \in [373, 379 K]$ $10^{3.56 - \frac{644}{T-198}}$, $T \in [379, 479 K]$
Reactor temperature	T_r	Free variable
Precursor concentration	C_{tot}	Free variable
Reaction time	t	Free variable
Reactor parameters		
Reactor volume	V	10 m ³
Reactor surface	A	25 m ²
Wall thickness	x	0.1 m
Heat transfer coefficient	λ	0.04 W m ⁻¹ K ⁻¹
Heat retention		50 %
Heater efficiency	η	0.8

A.4 X-ray diffraction and Rietveld refinement

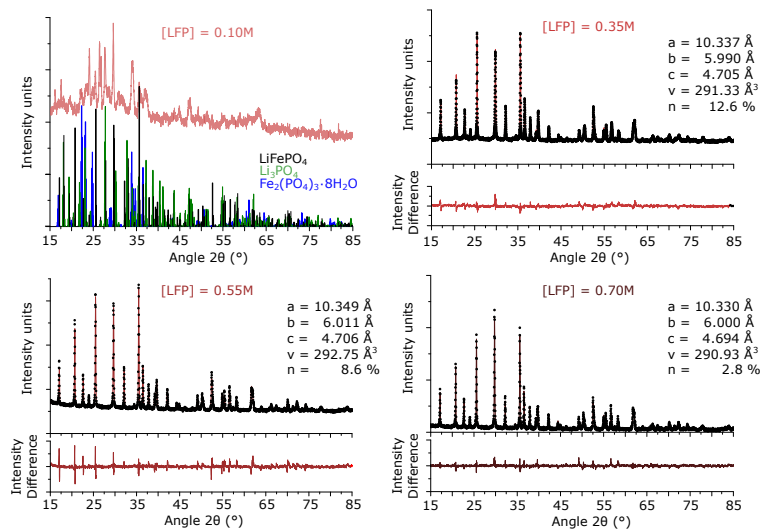


Figure A.2: Rietveld refinement of the XRD spectra of LFP particles synthesized at different precursor concentrations, C_{tot} . For $C_{\text{tot}} = 0.1 \text{ M}$, no refinement was possible due to further Li_3PO_4 and $\text{Fe}_2(\text{PO}_4)_3 \cdot 8\text{H}_2\text{O}$ impurities. For the other LFP samples, the resulting crystal parameters, the unit cell volume and the antisite defect concentration (n) are given. The difference between refinement and the data is plotted below for each diffractogram.

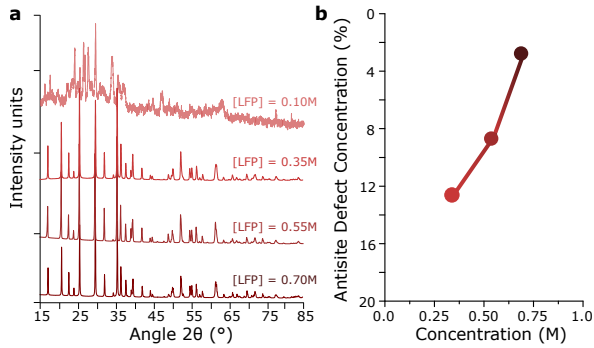


Figure A.3: a) Comparison of XRD patterns of LFP samples synthesized at different precursor concentrations, C_{tot} . b) Plot of the resulting antisite defect concentration of the LFP sample as a function of precursor concentration. The antisite defect concentration was obtained from the Rietveld refinements of the LFP data in Figure A.2

A.5 Sampling Tool

To take material out of the pressurized reactor, a sampling tool was designed (**Figure A.4**). The sampling unit was designed to fit on our stainless steel reactors. For sampling, a 100 mL reactor size was chosen to ensure that sufficient material remains in the reactor after multiple sampling steps. The LFP product synthesized in the 100 mL reactor with sampling is similar to the material produced in a standard 50 mL reactor.

The sampling unit is separated from the reactor with a needle valve. The needle valve remains closed during the reaction except for times when a sample is being taken.

During sampling, material from the reactor automatically enters the sampling unit once the needle valve is opened due to the pressure difference between the reactor and the sampling unit. The valve is closed after a period of time (1 s to 1 min depending on the pressure difference), trapping material in the sampling unit so that it can then be collected through the tap.

After taking a sample, the sampling unit is cleaned to prevent contamination during subsequent sampling steps. First, the tap is closed and the sampling unit is pressurized via N₂. This causes any remaining material to be pushed back into the reactor when the needle valve is opened. Second, the needle valve is closed, after which, the sampling unit is washed with water and dried with the N₂ stream.

Throughout the reaction, the reactor temperature is monitored with a thermocouple. Material sampling typically results in a temperature change on the order of 1-3 °C for at most several minutes. The disturbance of the reaction due to obtaining a sample causes a reduced crystallinity of the platelets visible in the FTIR spectra and a larger error during the particle size measurements. The changes are within the measurement error.

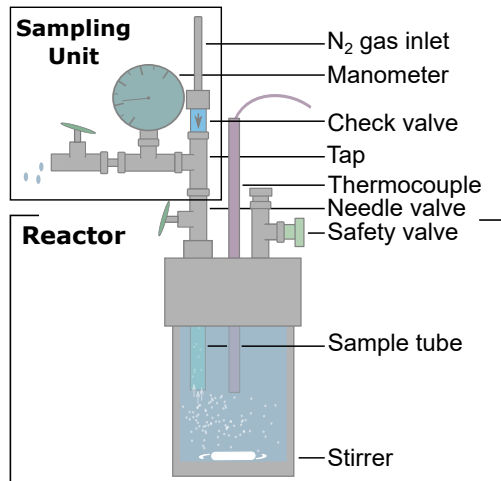


Figure A.4: Schematic of the sampling reactor.

A.6 Electrochemistry of the LFP sample after 48 h of synthesis

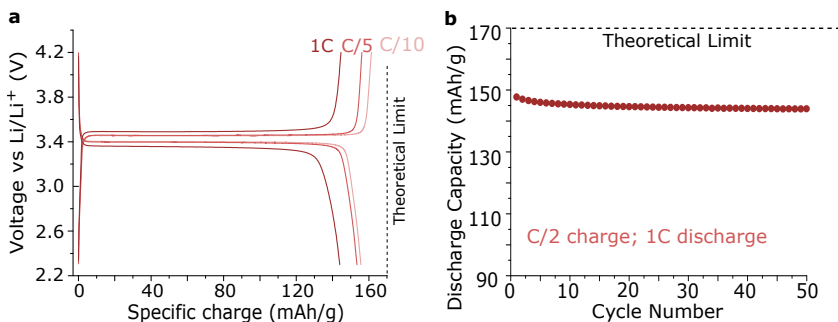


Figure A.5: a) Galvanostatic curves showing (dis)charge of LFP samples (reaction time: 48 h) at different C-rates. b) Discharge capacity as a function of cycles measured at 1C discharge and C/2 charge.

A.7 Time dependence of energy consumption

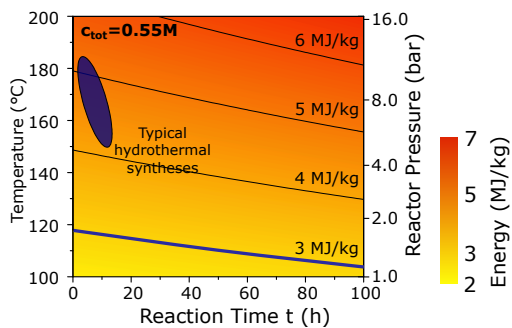


Figure A.6: Specific energy consumption of the LFP synthesis step as a function of hydrothermal reaction temperature (reactor pressure) and reaction time. The energy consumption of typical hydrothermal syntheses of LFP particles is indicated with the blue shading. The 3 MJ kg^{-1} energy consumption for a solid state approach is highlighted (blue region and blue line, respectively).

A.8 Carbon Coating Step

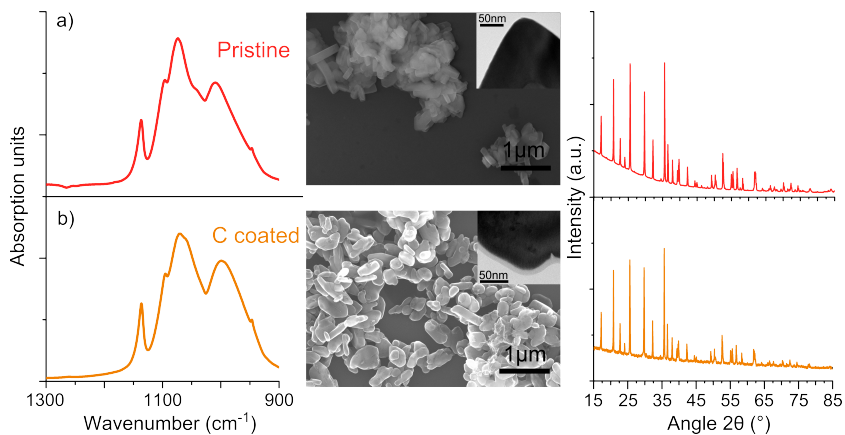


Figure A.7: Comparison of FTIR spectra, SEM and TEM images, and XRD patterns for LFP particles a) before and b) after annealing. The small change in the asymmetric PO₄ stretching mode likely comes from loss of water and some high temperature recrystallization during the annealing step. The XRD patterns show similar degrees of crystallization before and after annealing, indicating that no additional phases arise during the annealing.

A.9 Size and Morphology Analysis

A.9.1 Size Distribution Measurement

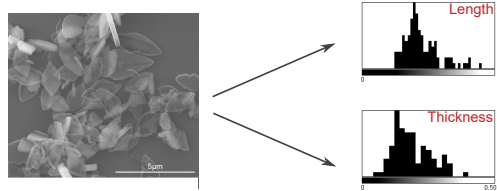


Figure A.8: Example size distributions for the LFP particles. The mean distance and the standard deviation of the particle length and thickness for each sample is obtained from the size distributions obtained by measuring 100-200 particles in multiple SEM images.

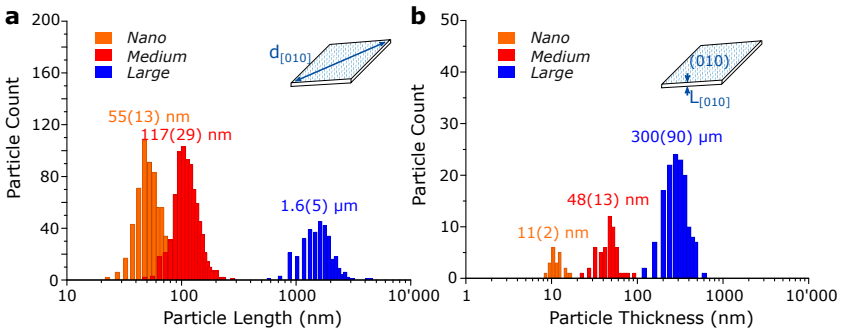


Figure A.9: Size distribution of the *Nano*, *Medium*, and *Large* LFP platelet samples. The particle diameter $d_{(010)}$ and channel length $L_{[010]}$ distributions are shown in a) and b), respectively.

A.9.2 Morphology Calculations

From the channel length $L_{[010]}$ (equal to the particle thickness) and the platelet diameter $d_{(010)}$, we calculate size parameters P such as the aspect ratio and the percentage of atoms on the (010) surface. The error of all those parameters is then obtained via a first order Taylor expansion

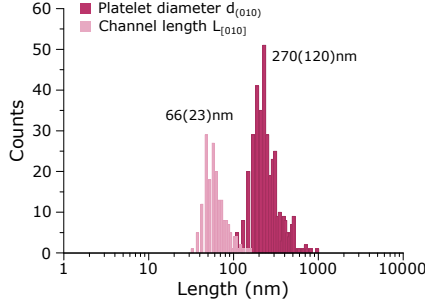


Figure A.10: Platelet diameter and channel length distribution of the *Meso* LFP samples.

of the standard deviations of $L_{[010]}$ and $d_{(010)}$ (A.7).

$$dP(L_{[010]}, d_{(010)}) = \sqrt{\left(\frac{\partial P}{\partial L_{[010]}}\right)_{d_{(010)}}^2} dL_{[010]} + \sqrt{\left(\frac{\partial P}{\partial d_{(010)}}\right)_{L_{[010]}}^2} d(d_{(010)}) \quad (\text{A.7})$$

Aspect Ratio We define the aspect ratio of the platelet particle, AR , as the ratio between $d_{(010)}$ and the channel length $L_{[010]}$. With (A.7), the error of the aspect ratio, dAR , is then given by (A.9).

$$AR = \frac{d_{(010)}}{L_{[010]}} \quad (\text{A.8})$$

$$dAR = \frac{d(d_{(010)})}{L_{[010]}} + \frac{d_{(010)}}{L_{[010]}^2} dL_{[010]} \quad (\text{A.9})$$

Atoms on (010) surface To calculate the relative ratio of atoms on the (010) surface, $n_{(010)}$, we consider all atoms in the topmost unit cell of the (010) surface. Therefore, we calculate how many unit cells appear along the b direction. This reduces the calculation to a one-dimensional problem and we can simply divide the two surface unit cells by all the unit cells along the b direction (A.10) with the error $dn_{(010)}$ (A.11).

$$n_{(010)} := \frac{N_{(010)}}{N_{tot}} = \frac{2b}{L_{[010]}} \quad (\text{A.10})$$

$$dn_{(010)} = \frac{2b}{L_{[010]}^2} dL_{[010]} \quad (\text{A.11})$$

(010) to entire surface ratio The geometric (010) surface ratio, $a_{(010)}$ is calculated assuming that the particles are disks with a circular (010) facet and a diameter of $L_{(010)}$. This assumption is motivated by the fact that the edges in the *Nano*, *Medium*, and *Meso* particles are rounded after annealing. For the diamond shaped *Large* sample this assumption is less accurate. The ratio of the top surface and the entire surface is:

$$a_{(010)} := \frac{A_{(010)}}{A_{tot}} = \frac{2\pi \left(\frac{d_{(010)}}{2}\right)^2}{\left(2\pi \left(\frac{d_{(010)}}{2}\right)^2 + \pi d_{(010)} L_{[010]}\right)} \quad (\text{A.12})$$

$$= \frac{d_{(010)}}{d_{(010)} + 2L_{[010]}} \quad (\text{A.13})$$

$$da_{(010)} = \frac{2L_{[010]}}{(d_{(010)} + 2L_{[010]})^2} d(d_{(010)}) + \frac{2d_{(010)}}{(d_{(010)} + 2L_{[010]})^2} dL_{[010]} \quad (\text{A.14})$$

Atoms on other surfaces The calculation of the percentage of atoms on other surfaces than the (010) surface is more complex. Again, we assume circular disk shaped platelets with diameter $L_{(010)}$. The assumption enables us to study a two-dimensional cut along the (010) surface and measure the number of unit cells along the circle edge. As for the (010) surface, the number of atoms on the edge scales with the number of edge unit cells. The calculation of the edge unit cell number, however, is more difficult than before due to the orthorhombic unit cell of LFP (which in our 2D picture becomes rectangular). Since the lattice vectors c and a do not match, a different amount of unit cells will be found along every direction of the circular disk. This is equivalent to the case of having an

ellipse with a square unit cell, which makes calculations easier (**Figure A.11**). Therefore, we apply the coordinate transformation

$$r \equiv \frac{L_{[010]}}{2}, a, c \mapsto r_a, r_c, \quad (\text{A.15})$$

with

$$r_i = \frac{r}{i} = \frac{L_{[010]}}{2i}, \quad i \in \{a, c, \}, \quad (\text{A.16})$$

that transforms the circular disk in an ellipse with the two semi-minor axes r_a and r_c . These axes represent the number of unit cells along these directions. Therefore, the number of surface atoms not on (010) is given by the ratio of the transformed ellipse circumference, C_{ell} , and the ellipse area A_{ell} .

$$\frac{N_{surf} - N_{(010)}}{N_{tot}} = \frac{C_{ell}}{A_{ell}} = \frac{r_a \int_0^{2\pi} \sqrt{1 - \left(1 - \frac{r_c^2}{r_a^2}\right) \cos^2 \phi} d\phi}{\pi r_a r_c} \quad (\text{A.17})$$

Rearranging and replacing r_a and r_c using (A.16) leads to (A.18) with the error (A.19). The circumference integral is then numerically evaluated.

$$\frac{C_{ell}}{A_{ell}} = \frac{2c \int_0^{2\pi} d\varphi \sqrt{1 - \left(1 - \frac{a^2}{c^2}\right) \cos^2 \varphi}}{\pi L_{[010]}} \quad (\text{A.18})$$

$$d\left(\frac{C_{ell}}{A_{ell}}\right) = \frac{2c \int_0^{2\pi} d\varphi \sqrt{1 - \left(1 - \frac{a^2}{c^2}\right) \cos^2 \varphi}}{\pi L_{[010]}^2} dL_{[010]} \quad (\text{A.19})$$

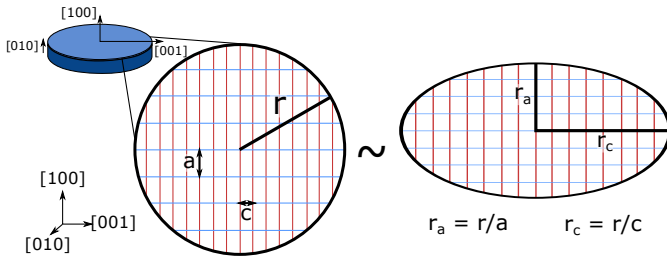


Figure A.11: Schematic image of the LFP disk used for the calculations and its transformation to an ellipse with a square lattice.

Appendix B

Supporting Information to Part III

B.1 Experimental Methods

Electrochemical Measurements LFP electrodes are prepared by coating an N-methyl-2-pyrrolidone (NMP, Sigma) based slurry on an aluminum current collector. The slurry contains 70 wt% active material, 20 wt% carbon black (Timcal Super C65), and 10 wt% polyvinylidene fluoride (Kynar HSV900). This leads to typical uncalendered dry active coating thicknesses of 40-60 μm with variation due to the different tap densities of the samples and thus different viscosities in the slurries. A glass fiber separator, electrolyte consisting of 1 M LiPF_6 in a 1:1 solution of ethylene carbonate and dimethyl carbonate (BASF), and a metallic lithium counter electrode complete the cell. Galvanostatic electrochemical analysis was performed on coin cells using the Astrol Bat-Flex potentiostat.

Inelastic neutron scattering measurements and analysis Inelastic neutron scattering (INS) measurements are performed at the FOCUS time-of-flight spectrometer at the neutron spallation source SINQ, Paul Scherrer Institute, Switzerland. For the measurement, 2-3 g of sample material is added in a cylindrical aluminium holder. A neutron wavelength of 2.4 Å (i.e., neutron energy of 14.2 meV) was used. Data collection time is 8-10 hours per sample. The resulting data are reduced using the Dave

software [13]. In the software, the background of the empty holder is subtracted and the detector efficiency is taken in account by normalisation to a vanadium standard having similar geometry as the samples. Finally, the phonon density of states was obtained using the MSlice environment in Dave, where the appropriate range of the scattering vectors Q was selected.

Simulations LiFePO₄ phonon spectra are simulated based on the density functional perturbation theory [18] as implemented in VASP [92], in conjunction with the Phonopy code [192]. The electron exchange and correlation energy are described using the PBEsol functional [154]. Valence electrons are described using a plane wave basis set with a cutoff energy of 500 eV. The interactions between valence and core electrons are treated using the projector augmented-wave (PAW) method [26]. The k-space is sampled with a k-point mesh with spacings smaller than 0.05 Å⁻¹.

Geometry calculations on LFP slabs are performed within the CP2K program suite utilizing the quickstep module [201]. Calculations were carried out using a dual basis of localized Gaussians and plane-waves [110]10 with a 300 Ry plane-wave cutoff. Double-Zeta-ValencePolarization (DZVP) [200], Goedecker–Teter–Hutter pseudopotentials [70] for core electrons, and the Perdew–Burke–Ernzerhof (PBE) exchange correlation functional were used. Convergence to 10⁻⁸ in Self-Consistent Field calculations is enforced. Electronic correlation within the d orbital of Fe was included through the $+U$ strategy with $U = 4.3$ eV [182, 208].

Unit cell dimensions of $[a, b, c] = [9.91, 6.095, 4.636]$ Å were determined through a cell optimization using a conjugate gradient optimization. LFP slabs are constructed with unit cell dimensions $[100] \times [010] \times [001] = 1 \times 3.5 \times 2$ in a simulation cell with dimensions $[a, 35 \text{ Å}, 2c]$. Periodic boundary conditions are used in all directions. All atoms in all systems are relaxed through geometry optimization, performed with the Quickstep module utilizing a Broyden–Fletcher–Goldfarb–Shanno (BFGS) optimizer with a 24 meV Å⁻¹ maximum force for convergence criteria.

B.2 Preparation of FePO_4 particles via electrochemical delithiation

For our FePO_4 particles, we need samples that are directly comparable to the LFP particles. To achieve these requirements, we electrochemically delithiate our LFP samples by making composite electrodes and cycling them in pouch cells. The samples are then washed in an Ar glovebox.

The LFP electrodes are prepared with 80 wt% active material LFP, 10 wt% Carbon black (Super C65), and 10 wt% PVDF (Kynar HSV900) binder. To enable us to obtain enough delithiated LFP, we prepare four-layer pouch cells with copper foil as a counter electrode and a glass fiber sheet separating the LFP electrodes from the copper foil (**Figure B.1a**). Electrical contacts are welded to the four cathodes and to the four anode electrodes (**Figure B.1b**). The stack is then dried under vacuum in the antechamber of the glovebox at 120 °C for 5-10 hours. The stack is put into a polyethylene plastic bag to keep the electrolyte conserved in the pouch cell and prevent electrical shorts. The electrolyte, a 1 M solution of LiPF_6 in a 1:1 mixture ethylene carbonate and dimethyl carbonate (BASF), is then added into the plastic bag and the whole structure and sealed into an aluminium pouch. Finally, a uniform pressure is applied on the pouch cells.

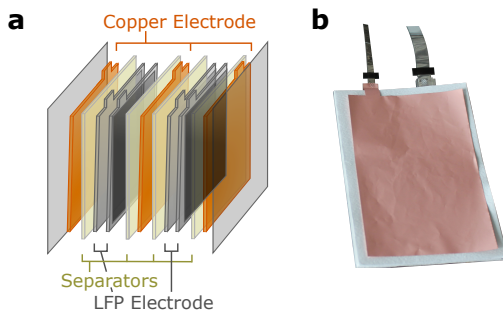


Figure B.1: a) Schematic image of the stacking of the four-layer pouch cell before welding the tabs to a contact. b) Image of the stacked electrode with the welded contacts on the cathode and anode tabs.

The pouch cells are charged at C/50 to 4.2 V followed by a potentiostatic step during which the lithium is plated on the copper foil. After charging, the pouch cells are transferred into the glovebox (**Figure B.2a**), where they are cut open and the electrode layers carefully separated. We infer lithium dendrites on the copper electrode and the separator that formed during the charging process (**Figure B.2b**). The delithiated electrode are scratched from the aluminum current collector of the cathode and collected in a centrifuge tube (**Figure B.2c,d**). NMP is added to the centrifuge tube to dissolve the PVDF during sonication. The resulting black dispersion is centrifuged to separate the lighter carbon black particles from LFP. After repeating the washing step three times, clean delithiated particles are obtained at the bottom of the centrifuge tube (**Figure B.2e**). The resulting powder is dried and analyzed by XRD and SEM (**Figure B.3**). The (020) peak indicate pure FePO_4 for *Nano* and a small residual LFP phase for the *Meso* particles (**Figure B.3b**).

B.2 Preparation of FePO_4 particles via electrochemical delithiation

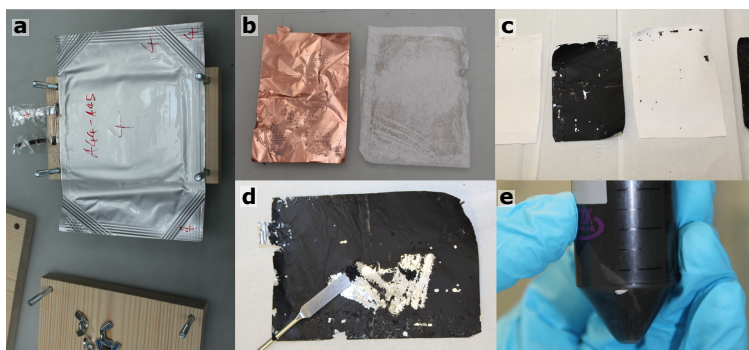


Figure B.2: Preparation steps of the FePO_4 samples after cycling. a) Image of a cycled pouch cell. The wood plates are used to apply pressure on the pouch cell and the scotch tape around the contacts to avoid accidental short circuits during transfer to the glovebox. b) Image of the lithiated copper current collector and the glass fiber separator showing evidence of lithium dendrites. c) Image of the other side of the glass fiber separator and the LFP electrode. We observe no dendrites growing through the separator. d) Once the stacked pouch cell is disassembled, the electrode material is scratched from the electrode with a spatula and transferred in a centrifuge tube. e) After extensive washing and centrifuging, the dark brown LFP powder is separated from the PVDF and carbon black mixture and isolated.

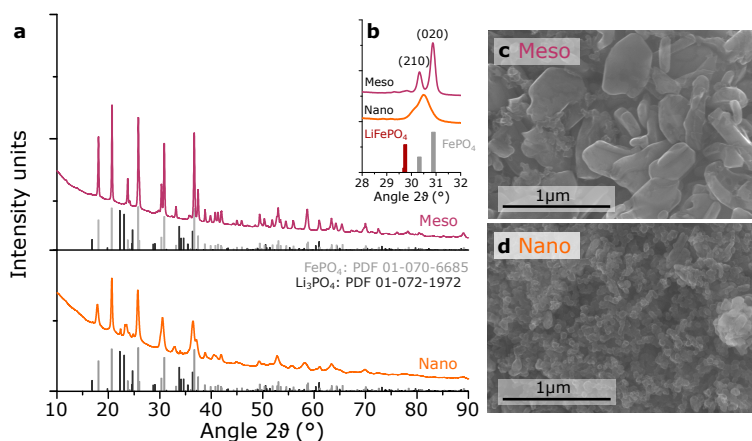


Figure B.3: a) Schematic image of the stacking of the four-layer pouch cell before welding the tabs to a contact. b) Image of the stacked electrode with the welded contacts on the cathode and anode tabs.

B.3 Electrochemical performance

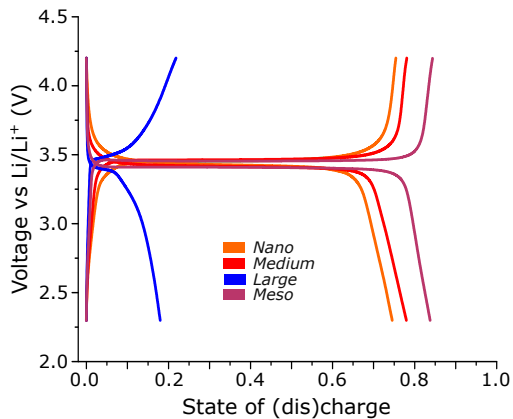


Figure B.4: Galvanostatic (dis)charge curves of the LFP samples used in this study for a rate of $C/10$ corresponding to a specific current of 17 mA g^{-1} . The galvanostatic curves here are from the second $C/10$ cycle.

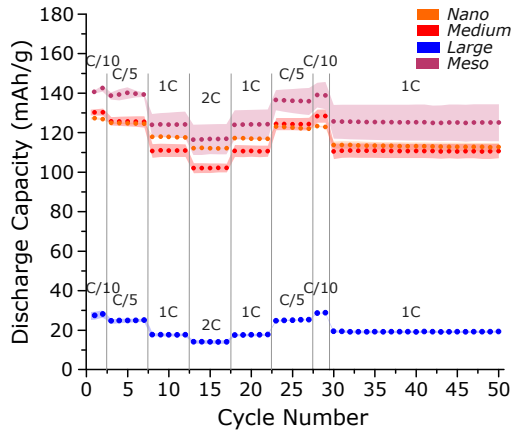


Figure B.5: Rate-dependent discharge capacity of the samples used in this study. The dots show the average capacity from at least three cells from different slurries with the standard deviation depicted by the shading. The given rate was used for both charge and discharge.

B.4 ${}^7\text{LiFePO}_4$ platelet particles: Transmission electron microscopy (TEM) images

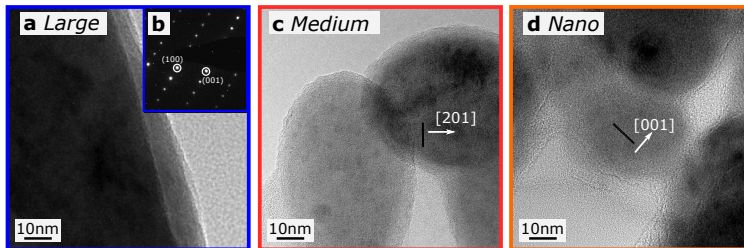


Figure B.6: TEM image of the *Large* sample with b) the selected area diffraction pattern. c),d) TEM images of the *Medium* and *Nano* particles, respectively with the crystallographic [201] or [001] direction depicted, respectively.

B.5 Inelastic neutron scattering measurements

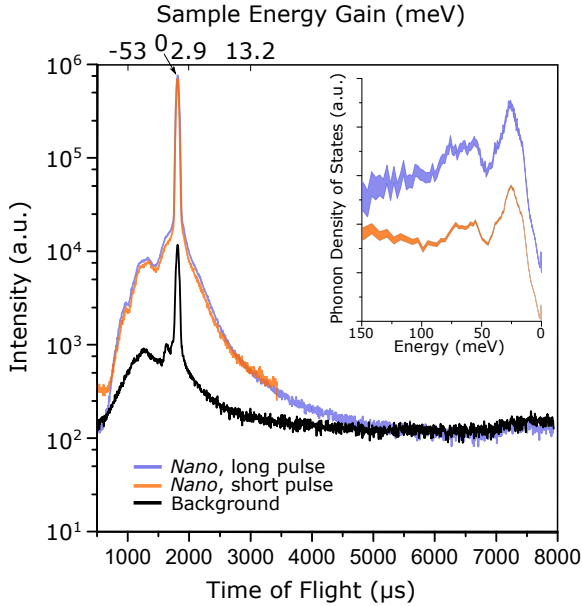


Figure B.7: Time-of-flight spectrum of the *Nano* sample. Due to beam time restrictions, a short time of flight pulse of 4 ms was chosen. On such a short pulse, neutrons from the previous pulse reach the sample at the start of the next pulse. This effect is called frame overlap and leads to an artifact in the PDOS (see inset) where the PDOS seemingly increases at high energy transfers. Comparing the PDOS measured on *Nano* LFP with (orange) and without (blue) the frame overlap, one can infer that frame overlap does not affect the shape of the PDOS in the important energy range in this study (50-100 meV).

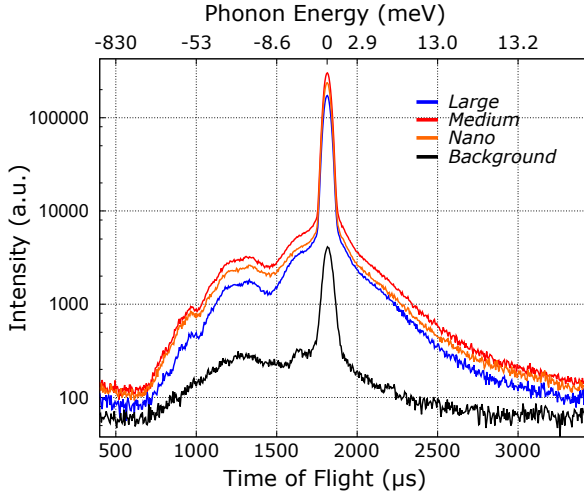


Figure B.8: Time-of-flight spectra of the LiFePO_4 samples measured in this study. As mentioned above, all samples have a short pulse, leading to significant frame overlap.

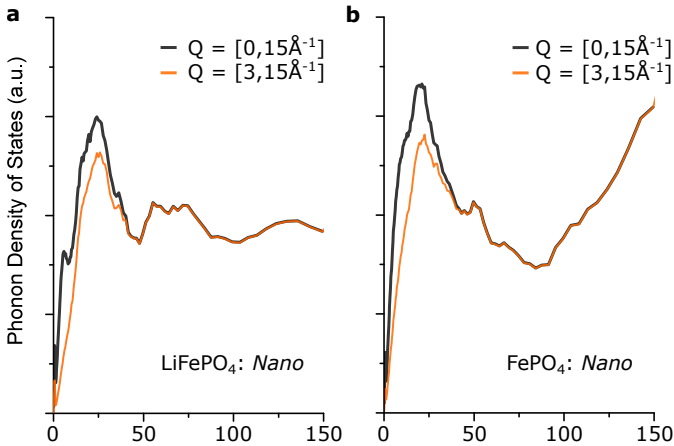


Figure B.9: Phonon density of states spectra of a) *Nano* LiFePO_4 and b) *Nano* FePO_4 as a function of selected scattering vectors Q . The influence of paramagnetic scattering can be significantly reduced by analyzing a restricted Q range above 3 \AA^{-1} (orange).

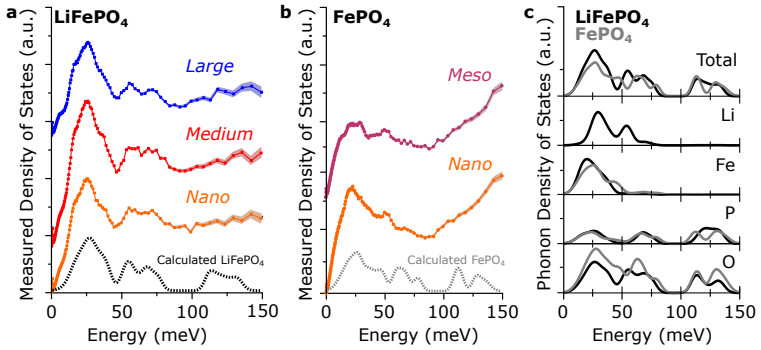


Figure B.10: The experimentally-measured phonon density of states for a) LiFePO_4 (LFP) and b) delithiated LFP (i.e., FePO_4) samples of different sizes. The shading around the points indicates the error of the measurement. The dashed lines show the calculated phonon density of states. c) Calculated total and elemental partial phonon density of states of LFP (black) and FePO_4 (gray) from bulk density functional theory simulations.

B.6 Impurity and defect analysis

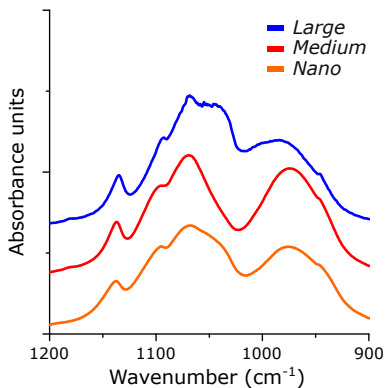


Figure B.11: FTIR spectra in the P-O vibrational range of the *Nano*, *Medium*, and *Large* samples show that the right-most peak is positioned at around 980 cm^{-1} , suggesting the same antisite defect concentration in the three samples. Note, that the Li_3PO_4 impurity in the *Nano* sample leads to a shoulder at 1050 cm^{-1} .

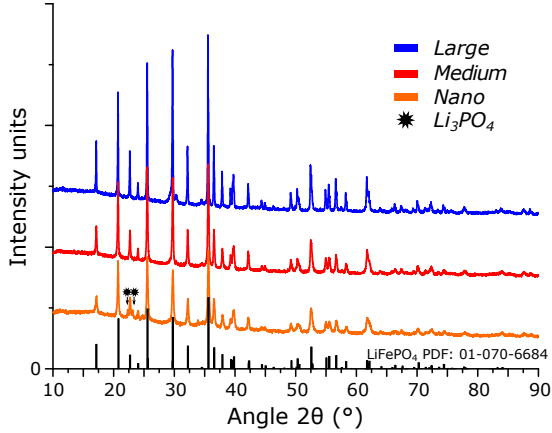


Figure B.12: X-ray diffraction spectra of *Large*, *Medium*, and *Nano* LFP. We find that the samples are single phase LiFePO_4 except for the Li_3PO_4 impurity in the *Nano* samples (marked with an asterisk).

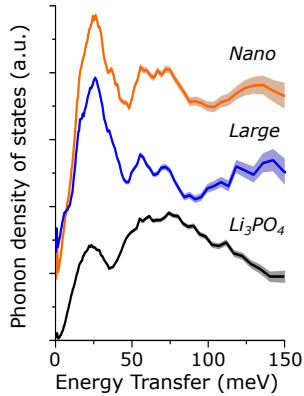


Figure B.13: Comparison of phonon density of states of the *Nano* and *Large* samples with the measured phonon density of states of $^7\text{Li}_3\text{PO}_4$. Note the very broad, almost constant, Li_3PO_4 phonon mode in the range of interest of 50-100 meV.

B.7 Rietveld refinement

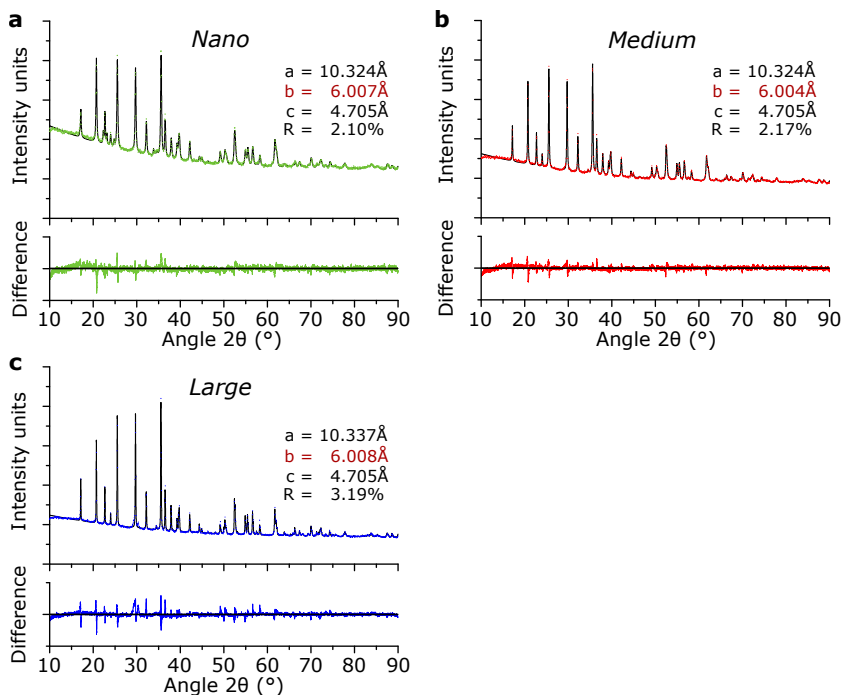


Figure B.14: Rietveld Refinements of the *Large*, *Medium*, and *Nano* LiFePO_4 samples used in this study. For all the three samples the unit cell volume does not change significantly, indicating a similar defect concentration and small strain effects.

B.8 Density functional theory calculations: Slabs

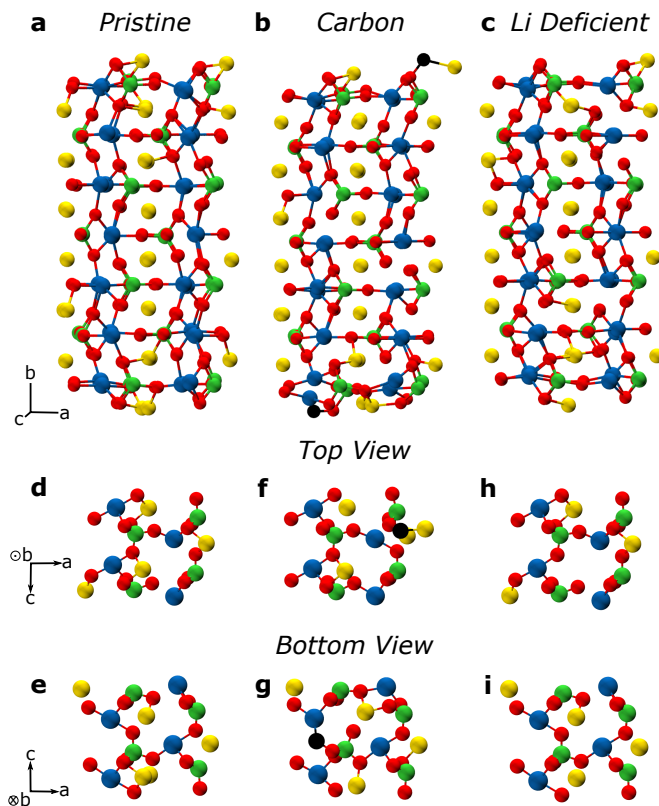


Figure B.15: Schemes of the slabs used for the CP2k calculations after their geometrical optimization. a)-c) Full slabs of the pristine LFP slab, the slab with one carbon atom on each side, and the Li deficient slab, respectively. d)-f) Top view of the slab for each of the three cases. g)-i) Bottom view of the slab for each of the three cases.

B.9 Density functional theory calculations: Bond length distribution

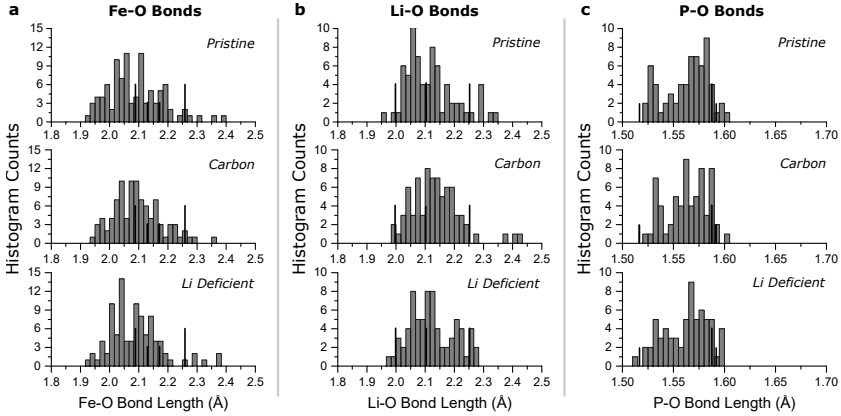


Figure B.16: Histograms of the a) Fe-O, b) Li-O, and c) P-O bond lengths in the interior of the LFP slabs. Black bars mark the bond lengths obtained from the Rietveld refinement of the *Large* LFP sample.

Table B.1: Overview of the LFP unit cell parameters and average bond lengths.

	a (Å)	b (Å)	c (Å)	Li-O (Å)	P-O (Å)	Fe-O (Å)
Inner Slab	9.910	6.095	4.636	2.116	1.563	2.088
Bulk DFT	10.26	5.989	4.689	2.133	1.554	2.142
<i>Large</i>	10.34	6.008	4.705	2.119	1.570	2.165

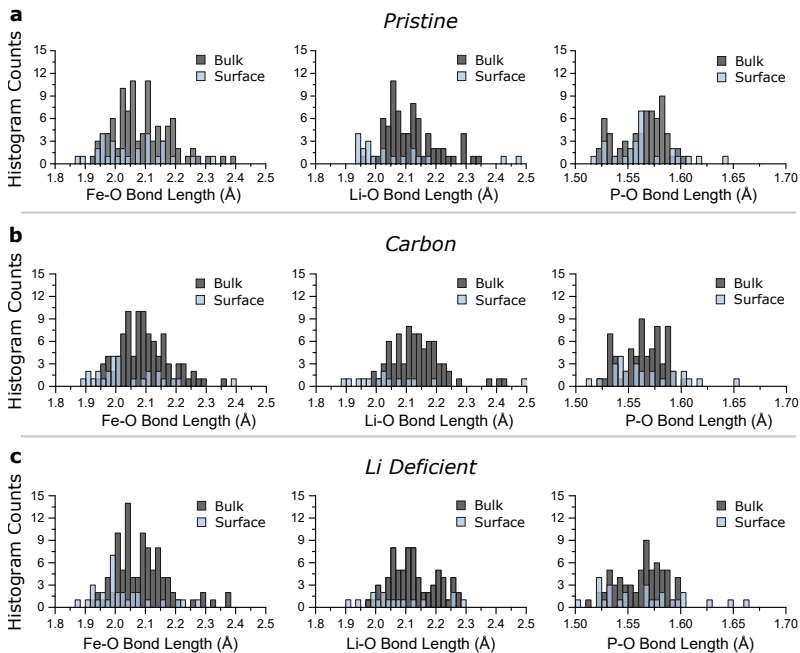


Figure B.17: Comparison of the interior (dark grey) and the surface bond lengths (light blue) of the slabs for the a) vacuum, b) carbon, and c) lithium deficient surface termination. The distribution of bond lengths broaden and, in the case of Li-O and Fe-O bonds, shift towards smaller energies.

Appendix C

Supporting Information to Part IV

C.1 Experimental Methods

Particle Synthesis We prepare LiFePO_4 samples in a hydrothermal synthesis approach following the synthesis approach in **Section 2.3**. Comparing the size series mentioned in Part II, two minor differences were performed. Firstly, the enriched $^7\text{LiOH}\cdot\text{H}_2\text{O}$ precursor was replaced with $\text{LiOH}\cdot\text{H}_2\text{O}$ that contains the natural Li isotope ratio. Secondly, the reaction time of the *Large* particles was changed to 48 h. See **Appendix A.1** for more experimental details.

Particle Characterization The LiFePO_4 particle morphology is determined with a combination of microscopic methods and a Micromimetrics Tristar II Plus Brunauer Emmett Teller (BET) setup. Scanning Electron Microscopy (SEM) images are collected with a Hitachi SU-8200, transmission electron microscopy (TEM) images with a FEI F30, and atomic force microscopy with a Nanoscope Dimension 3100 AFM. The lengths and thicknesses of up to 1000 particles was then measured using the ImageJ suite [167]. For the *Nano* sample many of the platelets lie flatly on the substrate and hence we use the z-deflection of the AFM cantilever to determine the particle thickness.

X-ray diffraction (XRD) measurements are performed on a Rigaku Smartlab diffractometer using $\text{CuK}\alpha 1$ radiation in Bragg-Brentano symmetry and a 2θ range between 10° and 90° . Rietveld refinements are carried out with the Maud software [120]. Fourier transform infrared (FTIR) spectra are collected with a Bruker Vertex 70 attenuated total reflection setup on a Ge single crystal substrate. Mössbauer spectra are measured using a ^{57}Co source and a scintillator detector. For the measurement, LFP electrodes made for the electrochemical analysis serve as the sample.

Magnetic characterizations of the samples were performed with the magnetic property measurement system (MPMS). The measurements were carried out on the MPMS devices of the Laboratory for Multiscale Materials Experiments, Paul Scherrer Institute, Villigen, Switzerland. The effective magnetic moment, μ_{eff} , is related to the slope of the inverse of the magnetic susceptibility, χ_m , via the Curie-Weiss law [181, 229],

$$\frac{1}{\chi_m} = \frac{T - \Theta_W}{C}, \quad \mu_{eff} = \sqrt{\frac{3CM_{LFP}k_B}{N_A\mu_0}} \quad (\text{C.1})$$

where Θ_W is the Weiss temperature, C the Curie constant, M_{LFP} the molar mass of LiFePO_4 , k_B the Boltzmann constant, and N_A the Avogadro constant.

μ^+ SR Measurements μ^+ SR measurements [229] are performed on the EMU setup at the ISIS muon and neutron facility at the Rutherford Appleton Laboratories in Harwell, UK. For the experiments, about 1.5 g of each LFP sample is pressed into a pellet and then transferred into a titanium sample holder with a $50\ \mu\text{m}$ titanium window. The holder is then fixed on the thermostat of a closed cycle refrigerator (CCR) and cooled down to 50 K from where it is subsequently heated in 12.5-50 K steps. At each temperature step, four to five μ^+ SR spectra are collected: (i) a weak transverse field measurement $H_{w\text{TF}}=20\ \text{G}$, (ii) a zero field measurement $H_{\text{ext}}=0$, and (iii-v) measurements at longitudinal fields selected such that a proper data fitting is possible. The subsequent

data analysis is performed with the muSR Fit software [184]. For details about the μ^+ SR analysis, see **Appendix C.5**.

Simulations We perform density functional theory (DFT) calculations with the quickstep module in the CP2k program suite [201]. All calculations are carried out with a dual basis of localized Gaussians and plane waves [110] with a 280 Ry plane wave cut-off. We use Double-Zeta-Valence Polarization (DZVP) [200], Goedecker-Teter-Hutter (GTH) [70] pseudopotentials for the core electron energy calculation and the Perdew-Burke-Enzerhof (PBE) exchange correlation functional [153]. To include the electronic correlation of the d orbitals in Fe, a GGA+U approach is chosen with an effective on-site Hubbard term U_{eff} of 4.3 eV [182, 208].

All simulations are performed on a rectangular LFP slab of a size of 1, 3.5, and 2 unit cells along the [100], [010], and [001] lattice directions. Based on previous results [182], the unit cell dimensions are set to $[a, b, c] = [10.4361\text{\AA}, 6.0950\text{\AA}, 4.7447\text{\AA}]$ leading to an effective simulation cell of $[a, 35\text{\AA}, 2c]$ with some free space at the b direction to allow for (010) surface relaxation. Finally, we enforce periodic boundary conditions along the a and c direction.

Before running more detailed calculations (see below), we relax the LFP slab via a geometric optimization implemented in the Quickstep module. We utilize a Broyden-Fletcher-GoldfarbShanno (BFGS) optimizer with a 10^{-4} h/a₀ (15.4 meV/Å) maximum force for convergence criterion. Unless mentioned differently, a convergence to 10^{-8} in self-consistent field is enforced.

Nudged elastic band (NEB) simulations are performed using the improved tangent method [72]. Initially, we geometrically relax four LFP slabs with one single Li vacancy, two slabs with the vacancy at neighbouring sites at the surface along the [010] channel and two with neighbouring sites deeper in the bulk. These four slabs serve as the input for the NEB calculations that provide the energy of the trajectory for a Li ion moving from the initial site to the vacancy. See **Table C.1** for the initial and final coordinates of the moving Li ion. The effective energy

Appendix C Supporting Information to Part IV

Table C.1: Coordinates for the initial and final position of the moving Li ion during the NEB calculations.

	Initial Li Position (x,y,z) Å	Final Li Position (x,y,z) Å
<i>Surface</i>	(5.054, 25.198, 6.720)	(4.809, 27.887, 6.973)
<i>Bulk</i>	(5.171, 16.236, 7.024)	(5.168, 18.844, 7.105)

on the trajectory is calculated on 10 intermediate points. To reduce the computation time to acceptable amounts, we calculated the energies while fixing every atom in the lattice except for the moving Li ion and reduced the convergence to 10^{-6} in self-consistent field.

C.2 *Ab initio* Calculations

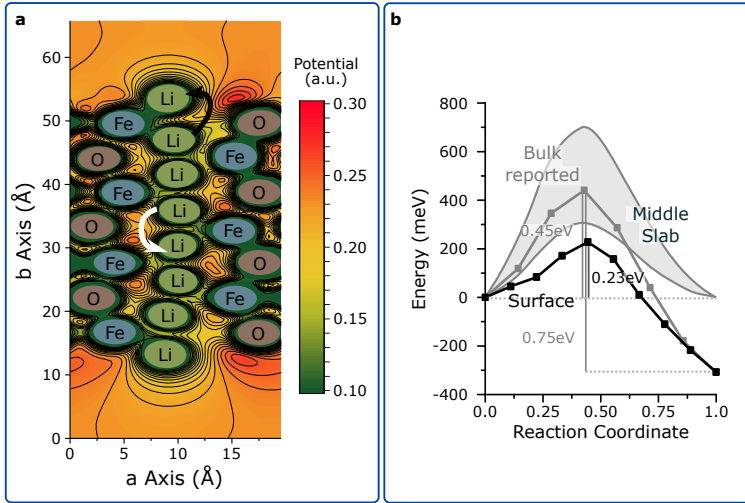


Figure C.1: a) Contour map of the electrostatic potential in the LiFePO_4 slab parallel to the (001) plane at $c = 7 \text{ \AA}$, which corresponds to the plane where the nudged elastic band (NEB) simulations are carried out (depicted with the arrows here). The atomic core potentials are set constant such that the potential landscape next to the atoms becomes visible. Red areas describe points of lower energy for positively charged particles (such as the anti-muon or the lithium ion). We find a low energy area close at the surface towards which the NEB trajectory is shifted. In addition, we see that within the bulk, the local potentials are not completely symmetric throughout the ion trajectory for the NEB characterization. This could cause the discrepancy between initial and final energy position found in the NEB calculations (b).

C.3 Morphology of the LiFePO_4 platelet samples

Table C.2: Particle Specific Size parameters. The channel length and platelet diameter are measured scanning electron microscopy (SEM) or atomic force microscopy (AFM). The surface atom ratios are calculated based on the procedure reported in section **A.9**. The specific surface area is measured with a Brunauer-Emmett-Teller (BET) setup.

	Channel length (nm)	Platelet Diameter (nm)	Atoms on (010)	Atoms on other Surface	Sp. Surface (m^2/g)
<i>Nano</i>	9.6(26)	66(17)	12.5(3)%	4.7(12)%	35.16(19)
<i>Medium</i>	51(12)	220(6)	2.4(6)%	1.4(4)%	11.44(5)
<i>Bulk</i>	121(26)	990(26)	0.99(21)%	0.32(8)%	9.01(4)

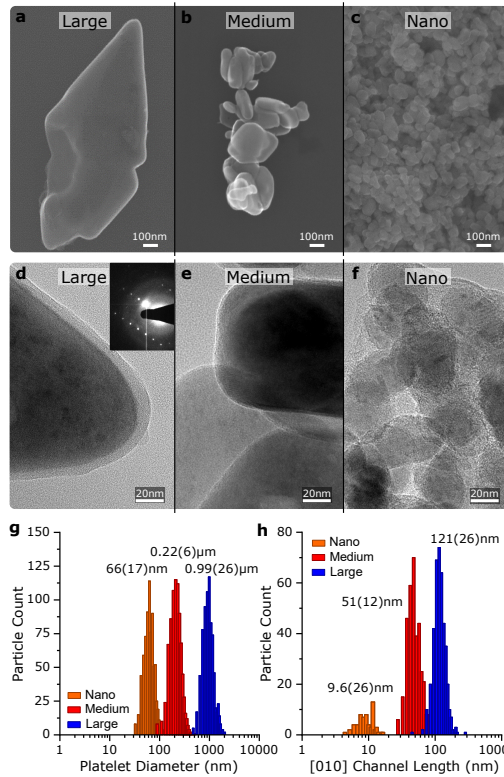


Figure C.2: a-c) Scanning electron microscopy images of representative particles for the *Large*, *Medium*, and *Nano* sample. d-f) Transmission electron microscopy images of *Large*, *Medium*, and *Nano* sample particles and their coatings. Inset d): Selected area electron diffraction pattern of the *Large* platelet confirming the (010) orientation of the particle. g,h) Platelet diameter and channel length distribution of the *Large*, *Medium* and *Nano* sample. Note that the channel length for the *Nano* sample could only be determined via atomic force microscopy and hence resulted in smaller statistics.

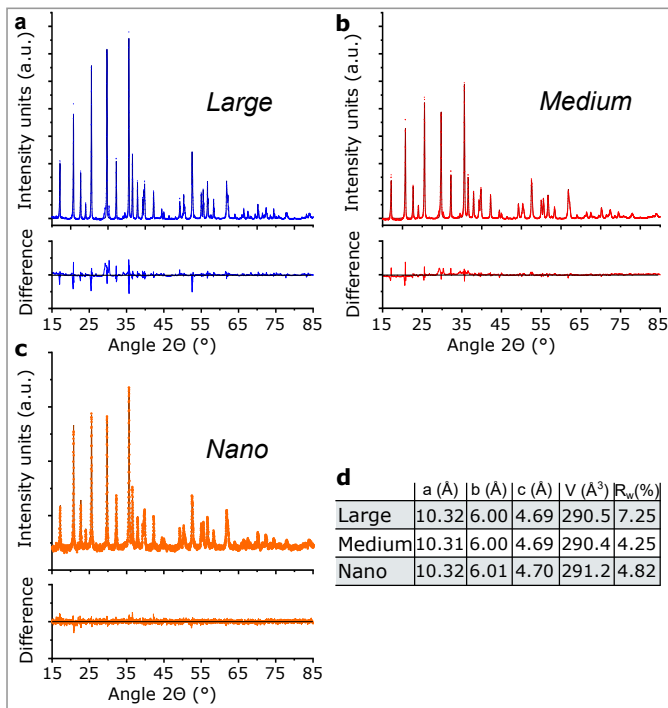
C.4 LiFePO₄ structure and impurity analysis

Figure C.3: a-c) Rietveld refinement of the x-ray spectra of each LiFePO₄ sample. We find an unassignable impurity in the *Large* and *Medium* sample that does not appear in the *Nano* sample. Yet, the main phase is crystalline LiFePO₄. d) Lattice parameters obtained from the Rietveld refinement. The lattice volume of the *Large* and *Medium* are considerably smaller than for the *Nano* sample. This could arise from tensile stress due to the carbon coating or from lithium deficiencies in the *Large* and *Medium* sample. The error of the lattice parameter obtained from Rietveld refinement is less than 0.01 Å.

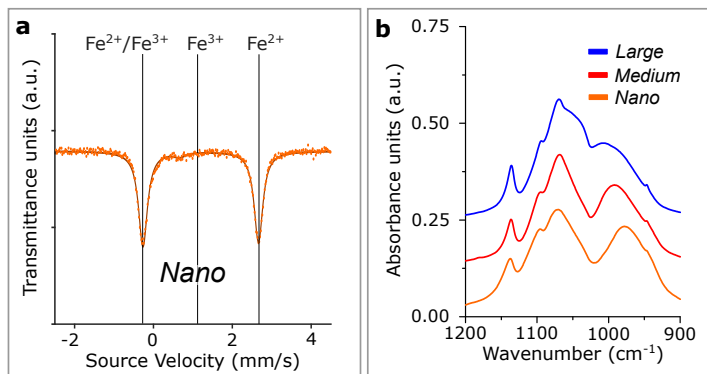


Figure C.4: a) Mössbauer spectrum of the *Nano* sample. The Fe^{2+} doublet is well visible while the Fe^{3+} doublet does not appear. This suggests a negligible amount of Fe^{3+} impurities. b) FTIR spectra of the P-O vibrations of each LiFePO_4 sample. The spectra overlap well with the theoretical spectra (see [7]). We find a characteristic shift of the antisymmetric P-O bonding mode from the *Large* to the *Nano* sample characteristic for the increase of ethylene glycol as co-solvent.

C.5 μ^+ SR spectral analysis

C.5.1 Weak transfer field fit

Measuring the forward-backward polarization P in a weak transverse field serves to analyse different magnetic contributions in a solid. The weak transverse field induces a precession of the muon spin causing an oscillation of the asymmetry between positive and negative values. The interactions with the surrounding atoms depolarize (damp) these oscillations with atom specific depolarization. For the measurement of LFP, we assume contributions from a slow relaxing magnetic background P_S , from fast relaxing iron centers P_F , and from oscillating paramagnetic contributions P_{TF} .

$$P = P_S + P_F + P_{TF} \quad (\text{C.2})$$

This leads to the time dependant fit function,

$$P = A_0 P(t) = A_S e^{-\lambda_S t} + A_F e^{-\lambda_F t} + A_{TF} \cos(\omega t + \Phi) e^{-\lambda_{TF} t} \quad (\text{C.3})$$

where A_i is the maximal asymmetry, λ_i the field depolarization rate, ω the Larmor frequency, and Φ the phase of the oscillation. Fits are shown in **Figure C.5**, with deviations in the slow relaxing regime.

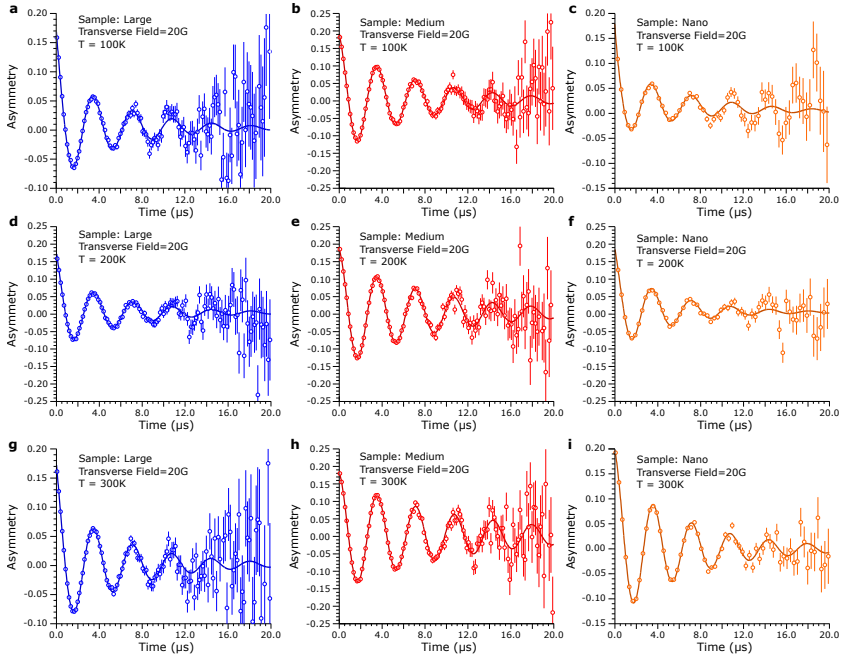


Figure C.5: Weak transverse field measurements at a-c) 100 K, d-f) 200 K and g-i) 300 K of the samples *Large*, *Medium*, and *Nano*, respectively.

C.5.2 Longitudinal field fits

To fit the forward-backward asymmetry with an applied longitudinal field, we include contributions from the titanium sample holder, a fast electronic component coming from effects such as the paramagnetic spins of the iron atom, and two dynamic nuclear spin contributions,

$$A_0P(t) = A_{BG} + A_F e^{-\lambda_F t} + A_{KT1} G(H, \Delta_{KT1}, \nu_{KT1}, t) e^{-\lambda_{KT1} t} + A_{KT2} G(H, \Delta_{KT2}, \nu_{KT2}, t) e^{-\lambda_{KT2} t} \quad (\text{C.4})$$

$$G(H, \Delta, \nu, t) = G^{(0)} + \nu \int_0^t d\tau G^{(0)}(t - \tau) G(H, \Delta, \nu, \tau), \quad (\text{C.5})$$

$$G^{(0)} = e^{-\nu t} \left[1 - \frac{2\Delta^2}{(\gamma_\mu H)^2} \left(1 - e^{-\frac{\Delta^2 t^2}{2}} \cos(\gamma_\mu H t) \right) \right] + e^{-\nu t} \left[\frac{2\Delta^4}{(\gamma_\mu H)^3} \int_0^t d\tau e^{-\frac{\Delta^2 \tau^2}{2}} \sin(\gamma_\mu H \tau) \right] \quad (\text{C.6})$$

where A_i are maximal asymmetries, λ_i is the field depolarization rate of each process, G are Gaussian dynamic Kubo-Toyabe (KT) functions, H is the applied field, Δ the nuclear dipolar field distribution width, and ν the field fluctuation rate. In the case of LiFePO_4 , earlier experiments assume that the latter is proportional to the diffusion coefficient [181].

$$D_{Li}(T) \propto \nu(T) \quad (\text{C.7})$$

For each sample at each temperature all longitudinal field spectra are then fitted simultaneously. Example data and fits are shown in **Figure C.6**.

This analysis approach is similar to that used in previous studies with the only difference that we have two Gaussian dynamic Kubo-Toyabe function. The fit with a single Kubo-Toyabe function is shown in **Figure C.7**.

Since the KT2 field fluctuation rates do not change appreciably with temperature, they are set to be temperature-independent. **Figure C.8.** shows a comparison of the field fluctuation rates, normalized asymmetries, and field distribution widths for the *Large* sample with and without KT2 set constant.

Theoretically, the zero and longitudinal field μ^+ SR data can also be fit by a single Lorentzian (instead of Gaussian) Kubo-Toyabe function. This would imply however, the presence of inhomogeneously distributed magnetic impurities (either isolated or islands/clusters) within a disordered lattice. The Mössbauer data (**Figure C.4a**) and x-ray diffraction data (**Figure C.3**) do not support such interpretation of the μ^+ SR data.

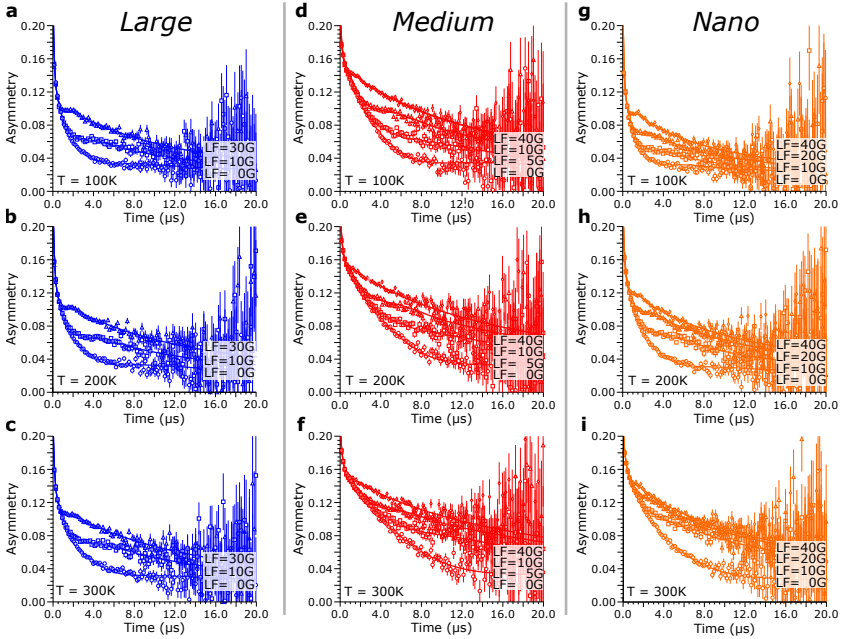


Figure C.6: Longitudinal Field fit of the μ^+ SR spectra at different 100 K, 200 K, and 300 K for the samples a-c) *Large*, d-f) *Medium*, and g-i) *Nano*.

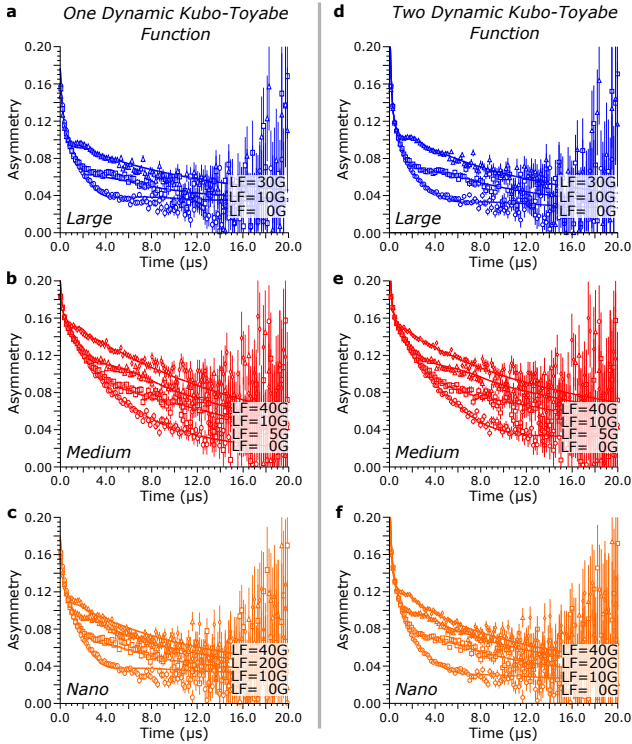


Figure C.7: Comparison of the longitudinal field measurements at 200 K using a-c) one single and d-f) two Gaussian dynamic Kubo-Toyabe function(s) (KT). While the single Gaussian KT fits relatively well for the *Medium* sample (except for high longitudinal fields), the double Gaussian KT provides a better fit for the *Nano* and *Large* samples.

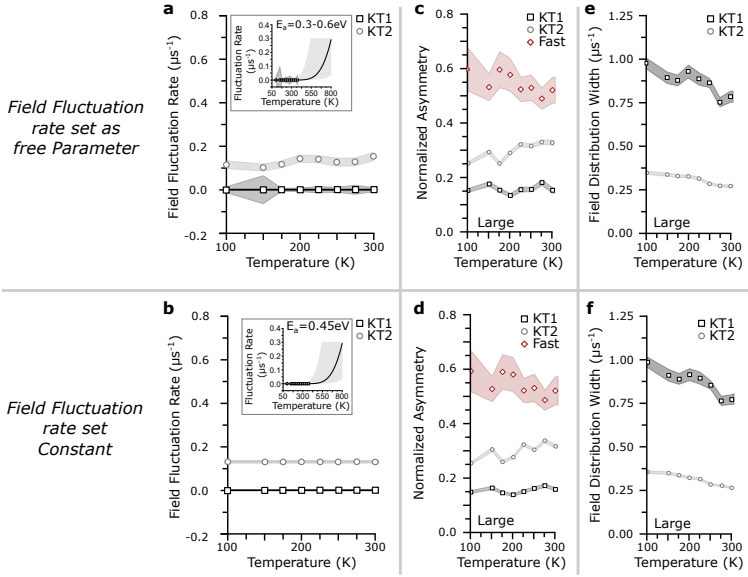


Figure C.8: Comparison of the fitted results of the *Large* sample when the field fluctuation rate of the 2nd Kubo-Toyabe function, ν_{KT2} , is a free parameter (a,c,e) or a constant (b,d,f) in the fit. No significant differences between field fluctuation rate (a,b), normalized asymmetries (c,d), and field distribution width (e,f) are visible. For the interpretation of the parameter changes, see **Appendix C.5.3**.

C.5.3 Interpretation of the fitting parameters

From the fitting procedure, we obtain temperature-dependent maximal asymmetry parameters and depolarization rates (**Figure C.9**). In this section, we discuss the trends in the “fast” relaxation, “KT1”, and “KT2” processes. We explain why our attribution of the field fluctuation rate “KT1” to interface lithium diffusion makes sense and why we hypothesize that the “fast” process is associated with magnetic Fe impurities on the surface of the particles and that the field fluctuation rate “KT2” process is associated with background ion fluctuations.

The normalized maximal asymmetries give qualitative estimates of the fraction of muons sensing a certain process (**Figure C.9a-c**). At low temperatures, close to 60% of the signal for the *Large* and *Nano* samples come from the fast relaxation of an electronic spin coupling [181] (A_F). With increasing temperature, A_F decreases slightly in the *Large* sample and strongly in the *Nano* sample. Meanwhile, in the *Medium* sample, A_F is smaller than A_{KT2} and no significant temperature dependence is observed. The asymmetry ratios for the **Medium** sample are similar to the uncoated LFP sample analysed by Sugiyama [181].

To explain the trend in the *Large* and *Nano* samples and their seemingly anomalous behaviour compared to the *Medium* sample, we note that: (1) a fast electronic component that is large at low temperature and that decreases with increasing temperature is often related to a magnetic impurity and (2) the strong changes for the *Nano* sample indicate the surface likely plays an important role.

We therefore perform magnetic susceptibility measurements on the three samples and an LFP sample without carbon coating (**Figure C.10**). Above the antiferromagnetic phase transition at 50 K, we find a high temperature paramagnetic behaviour for all samples. The expected effective moment, μ_{eff} , for LFP is reported in the range of 4.8 and 5.6. μ_{eff} for the uncoated *Nano* is comparable to this value (5.38), while the coated *Nano* and the *Large* show large μ_{eff} (11.67 and 14.03, respectively). Meanwhile, the *Medium* sample has a μ_{eff} of 6.79, slightly

higher than that of the uncoated sample.

Zaghib *et al.* [234] also found an increase of magnetic moment when they coated particles with carbon. One possible explanation is that the strain of the coating together with the change in surface reconstruction could affect the iron-oxygen-iron exchange coupling and affect the magnetically frustrated spin system in LFP [191, 230]; however, this would not explain the background in the magnetic susceptibility measurements. Alternatively, a magnetic impurity in the form of iron(III) oxide could form on the surface; however, Mössbauer spectra show no evidence of iron(III) oxide in our particles (**Figure C.4a**).

We hypothesize that in the reducing atmosphere in which the carbon coating is performed, some Fe(II) reduces to Fe(0), resulting in magnetic iron impurities at the surface of the LFP. With the larger surface area of the *Nano* compared to the *Large*, we expect more Fe impurities in the “Nano” particles. We further hypothesize that the platelet particles of the *Medium* sample tend to agglomerate as indicated in the SEM images in **Figure C.11**. As a result, the carbon coating may only cover the surface of the agglomerate, leaving the primary particles of the *Medium* sample largely uncoated and having few iron impurities at the particle surfaces. This is consistent with relatively small change of specific surface area between *Large* and *Medium* (see **Table C.2**).

This hypothesis is also consistent with the fact that, at 300 K, where the exchange coupling of the iron impurities is reduced due to thermal fluctuations, the fractions of the asymmetries of the *Nano* and *Medium* samples are similar. Furthermore, the depolarization rate, λ_F (**Figure C.9d**) related to the relaxation of the fast process decreases with increasing temperature for *Nano* and *Large* samples. This consistent with the fact that the fast process observed in the *Nano* and *Large* samples comes from magnetic impurities.

The nuclear dipolar field distribution width Δ decreases for every Kubo-Toyabe function following a typical motional narrowing mechanism [127, 180] (**Figure C.9d**). The decrease in Δ is consistent with

the fact that at higher temperatures, there is more atomic motion so that the linewidth (distribution in frequencies) narrows. Δ should also saturate at low temperatures. We hypothesize that we do not see this saturation at low temperatures due to magnetic impurities.

The large decrease in Δ_{KT1} for the *Nano* sample compared to the *Large* could be due to the fact that the reduced Li-O distance at the surface (see Part4) leads to a smaller Li- μ^+ spacing hence increasing the Li- μ^+ coupling and the effective value of Δ_{KT1} .

The process KT2 increases slightly in importance with higher temperatures (**Figure C.9a-c**) and causes motional narrowing (**Figure C.9e-g**). It might arise from local atomic motion that occurs with slower frequency than interface lithium diffusion ($\Delta_{\text{KT1}} > \Delta_{\text{KT2}}$ and $\nu_{\text{KT1}} > \nu_{\text{KT2}}$) throughout the bulk of the particle ($A_{\text{KT1}} < A_{\text{KT2}}$). Furthermore, the constant field fluctuation rate suggests a much lower activation energy than lithium interface diffusion (**Figure C.9h-j**).

Thus, we have a surface-related magnetic effect (“fast” component) and a background (KT2) that may come from slow fluctuations of ions that appear in the μ^+ SR measurement, but these can be satisfactorily separated from the lithium diffusion component (KT1).

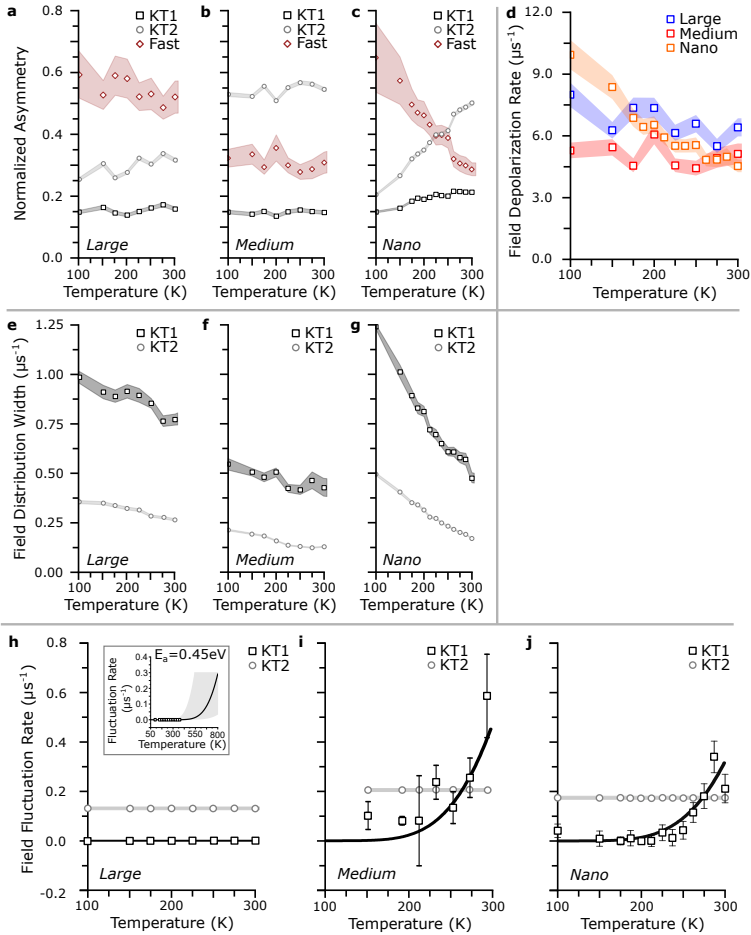


Figure C.9: Temperature dependence of the longitudinal field μ^+ SR fitting parameters and their standard deviations (marked as coloured area behind the points). a-c) Normalized asymmetries of the platelet samples. d) Field depolarization rate of the fast relaxation process. e-g) Field distribution width of the two Gaussian dynamic Kubo-Toyabe functions KT1 and KT2. h-j) Temperature-dependant field fluctuation rates KT1 and KT2.

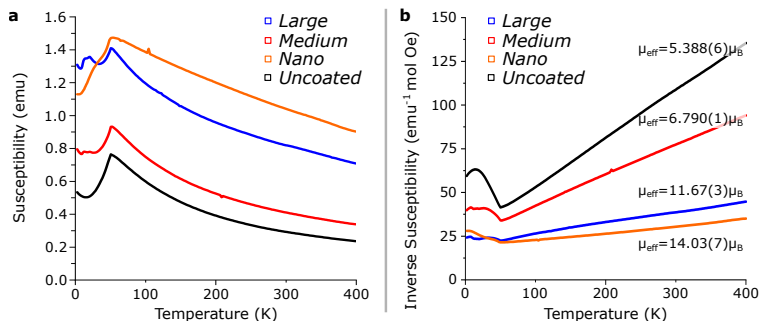


Figure C.10: a) Mass normalized susceptibility of different samples as a function of temperature. All samples exhibit a very similar behavior at high temperature, except for a shift of the background. This suggests a contribution of a magnetic impurity (such as Fe) which is largest for the *Large* and the *Nano* sample. b) Inverse molar magnetic susceptibility as a function of temperature. We obtain effective magnetic moments of each sample via equation (C.1).

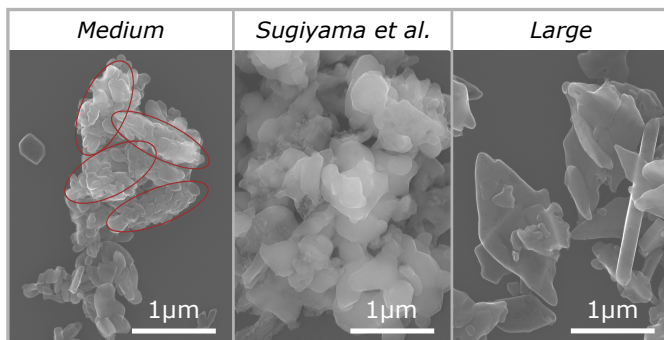


Figure C.11: Scanning electron microscopy images of the *Medium* and *Large* sample with the sample studied by Sugiyama *et al.* [181]. As with the other two samples, the particles consist of platelets. The diameter of these particles is relatively polydisperse ranging from well below 100 nm to 1 μm. In average, however, they are larger than the *Medium* particles and substantially smaller than the *Large* platelets. Circled areas in the *Medium* sample that show fragments of diamond shaped secondary particles.

C.6 Electrochemical Characterization

C.6.1 Cell Preparation

For all the electrochemical characterization, we assemble coin cells in a half-cell configuration with lithium metal as reference electrode. Between the two electrodes, a glass fibre separator is placed and soaked with electrolyte, a 1 M solution of LiPF_6 in a 1:1 mixture of ethylene carbonate and dimethyl carbonate (BASF).

Unless mentioned differently, we make the LFP electrodes by preparing N-methyl-2-pyrrolidone based slurries with 70 wt% LFP together, 20 wt% Carbon black (Super C64, Timcal), and 10 wt% Polyvinylidene fluoride (Kynar HSV900). The slurries are doctor blade coated on an aluminium foil and dried under dynamic vacuum at 100 °C. The resulting electrode sheet is then calendared and 18 mm electrodes punched out.

The electrochemical measurements are performed on three different potentiostat systems. Galvanostatic rate capability measurements are done on the Astrol BATT-FLEX potentiostat at a controlled temperature of 25 °C. Cyclic voltammetry (CV) measurements are run on the Biologic VMP3 potentiostat. To equilibrate the temperature and control the state of health in the LFP half-cell, a C/5 charge/discharge cycle is added at each temperature before the CV runs with different sweep rates. Electrochemical impedance spectroscopy (EIS) measurements are performed on a Biologic BCS815 potentiostat in a two-electrode setup where the lithium counter electrode serves as the reference. For temperature sweeps, the cells are placed into a Binder MK53 temperature chamber.

C.6.2 Cyclic voltammetry (CV) analysis

To analyze the CV data at different sweep rates v , we use the Randle-Sevcik equation with a pseudocapacitance correction [208],

$$i_{p,eff} = i_p - C_{DL}v = 0.4463nFAC_{el} \left(\frac{nFD}{RT} \right)^{\frac{1}{2}} v^{\frac{1}{2}} \quad (\text{C.8})$$

with i_p the maximal current of the CV curve, C_{DL} the double layer capacitance of the electrode, n the amount of electrons transferred, F the Faraday constant, C_{el} the electrolyte concentration, R the universal gas constant, T the temperature, and D the diffusion coefficient. This approach is necessary due to the relatively high amount of carbon black introduced in the electrode and due to the different particle sizes. Knowing the effective area of both active carbon and the LFP particles (the latter from BET measurements), we can estimate the value of C_{DL} by assuming a plate capacitor. This leads to

$$C_{DL} = \frac{\epsilon_{el}\epsilon_0 A}{d_{DL}} \quad (\text{C.9})$$

with ϵ_{el} and ϵ_0 the dielectric constants of the electrolyte and vacuum, A the electrode surface, and d_{DL} the size of the electrochemical double layer. Based on literature values [68], we estimate ϵ_{el} as a 1:1 linear combination of the dielectric constants of dimethyl carbonate ($\epsilon = 3$) and ethylene carbonate ($\epsilon = 90$). For the electrochemical double layer size we assume a distance of 5 Å [202]. Furthermore, we assume the dielectric constants to be temperature independent.

Though some of these assumptions are not perfectly accurate, this calculations can provide the correct order of magnitude. In addition, the contribution of the double layer capacitance is smaller than 15% of the total current making errors in the double layer capacitance estimation less critical.

After correcting the peak current for the double layer capacitance, we perform a linear regression with a fixed intercept at zero current. From the regression curve slope and its error, the diffusion coefficient follows. Repeating this approach at different temperatures leads then to multiple diffusion values that are correlated with an Arrhenius-type fit (see main text).

C.6.3 Galvanostatic and electrochemical impedance spectroscopy measurements

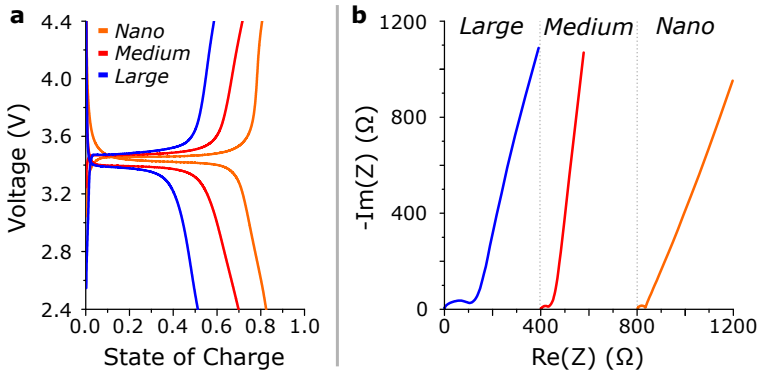


Figure C.12: a) Galvanostatic curves of the first cycle of half cells made from LiFePO_4 samples at a rate of 34 mA/g (corresponding to a $C/5$ rate). All samples exhibit the characteristic plateau at 3.4 V that opens up with increasing particle size due to overpotentials. The *Large* and the *Medium* sample have smaller capacities than the *Nano* sample, likely due to a reduced connectivity to the electrode network and due to Fe-Li antisite defects. b) Impedance curves of the samples with *Medium* and *Nano* shifted by 400Ω or 800Ω for clarity. The Warburg slope of the *Nano* sample is close to a 45° angle from the x axis suggesting a contribution to the ionic diffusion while the *Medium* sample is closer to a blocking state. The *Large* sample seems to have an additional semicircle appearing in the impedance range displayed here which could arise from the reduced adhesion to the current collector compared to the smaller samples.

Appendix D

Supporting Information to Part V

D.1 Experimental Methods

Density functional theory simulations We perform density functional theory (DFT) calculations with the Quickstep module in the CP2k program suite[201]. All calculations are carried out with a dual basis of localized Gaussians and plane waves [110] with a 280 Ry plane wave cut-off. We use Double-Zeta-Valence Polarization (DZVP) [200] and Goedecker-Teter-Hutter (GTH) [70] pseudopotentials for the core electron energy calculation and the Perdew-Burke-Enzerhof (PBE) exchange correlation functional [153]. To include the electronic correlation of the d orbitals in Fe, a GGA+U approach is chosen with an effective on-site Hubbard term U_{eff} of 4.3 eV [182, 208].

All simulations are performed on a rectangular LiFePO_4 slab of a size of 1, 3.5, and 2 unit cells along the [100], [010], and [001] lattice directions. Based on **Part 3 and 4**, the unit cell dimensions are set to $[a, b, c] = [10.4361 \text{ \AA}, 6.0950 \text{ \AA}, 4.7447 \text{ \AA}]$ leading to an effective simulation cell of $[a, 35 \text{ \AA}, 2c]$ with some free space at the b direction to allow for (010) surface relaxation. Finally, we enforce periodic boundary conditions along the a and c direction.

Before running more detailed calculations (see below), we relax the LFP slab via a geometric optimization implemented in the Quickstep

module. We utilize a Broyden-Fletcher-Goldfarb-Shanno (BFGS) optimizer with a 10^{-4} h/a₀ (15.4 meV/Å) maximum force for convergence criterion. Unless mentioned differently, a convergence to 10^{-8} in self-consistent field is enforced.

The coated LFP slabs are constructed using the geometrically relaxed pristine slab. On this slab, coating layers were constructed by manually placing the atoms to expected low energy steps. Specifically, in the case of the carbon coating, atoms were placed in energy potential minima at the LFP (010) surfaces. In the case of the ZnO coatings, we placed a relaxed (110) superstructure ($[a, b, c] = [10.4361 \text{ \AA}, 10 \text{ \AA}, 4.7447 \text{ \AA}]$) of wurtzite-type ZnO on the LiFePO₄ surface. Afterwards, the coatings are twice relaxed geometrically: i) only the surface is relaxed by fixing the atomic motion in the inner 1.5 unit cells of LFP and ii) all atoms are relaxed.

The partial electron density of states (PEDOS) of the slab is calculated with the Quickstep module of the CP2k program suite. To achieve both element and layer decomposition, the contribution of every single atom wave function to a given energy state is calculated first. In a second step, the atoms are sorted into groups of elements of a certain layer. This results in layer and element decomposed energy level diagrams (as displayed in **Figure 5.6a-d**). To obtain a PEDOS out of the energy states, an element and layer - weighted histogram of the energy states is created with a bin size of 0.1 meV. For reasons of clarity, the resulting PEDOS is smoothened using a moving average of two adjacent bins.

Ab initio molecular dynamics (AIMD) measurements are performed in the canonical ensemble at 1000 K using a canonical sampling through velocity rescaling (CSVR) thermostat [32] with a thermalization time constant of 15 fs. The AIMD simulations are typically run for 11-15 ps. To make sure the dynamics of the light Li atoms are properly reproduced, a time step of 1 fs was chosen. To stabilize the thermostat, the first 1 ps of the runs is discarded. All AIMD runs are performed twice per slab: once where the atomic motion of all atoms except for lithium is set to zero, and once with all atoms moving freely. To reduce the compu-

tation time of the latter AIMD run, the self-consistent field convergence for each time step is reduced to 10^{-7} and $0.5 \cdot 10^{-8}$ for the carbon atom termination and the ZnO coating, respectively.

The mean square displacements (MSD) are calculated using equation (D.1),

$$\text{MSD}(\tau) = \frac{1}{N_{At}} \sum_{i=1}^{N_{At}} (\mathbf{r}_i(\tau) - \mathbf{r}_i(0))^2 \quad (\text{D.1})$$

where N_{At} is the number of atoms of a certain element in a certain region and $r_i(\tau)$ is the position of the atom i at a timestep τ . Note that $r_i(\tau=0)$ is defined to be the first step after the thermostat is stabilized.

Preparation of coated LiFePO₄ nanoplatelets We prepare LFP samples in a modified solvothermal synthesis approach along the synthesis described in **Part 2** First, 20 ml of a 2.55 M aqueous solution of LiOH·H₂O (Sigma) is mixed with 20 ml of a 0.85 M solution of H₃PO₄ (diluted from 85 wt% H₃PO₄, Sigma). White Li₃PO₄ crystals form, which in a second step get separated from the solution by centrifugation. These crystals are then washed once in ethylene glycol (Sigma) before they get dispersed in 40ml anhydrous ethylene glycol (Sigma) and transferred into a stainless steel autoclave.

After stirring the Li₃PO₄ – ethylene glycol dispersion for about 15 min in the autoclave, preground FeSO₄·7H₂O (Sigma) is added in a 1:1 Fe:PO₄ stoichiometric ratio. The reactor is then flushed with N₂ for 10 min, closed and heated to 180°C. After stirring the solution for 6 h at 180°C, the reaction is stopped and the reactor opened. The resulting light grey particles are filtered and washed with the following sequence: i) distilled (DI) water ii) DI water, iii) 0.1M H₃PO₄, iv) DI water, v) Ethanol. The resulting grey LiFePO₄ nanoparticles are dried under inert atmosphere over night at a temperature of 80°C. Once the particles are dry they are coated in the manner described in **Section 2.4**.

Particle Characterization The LFP particle morphology is studied with a combination of microscopic methods. Scanning electron microscopy (SEM) images are collected with a Hitachi SU-8200. The dimensions of up to 1000 particles are measured using the ImageJ suite [167]. Scanning transmission electron microscopy energy dispersive x-ray scattering (STEM-EDS) images are taken with the FEI Talos F200X electron microscope.

X-ray diffraction (XRD) measurements on powder samples are performed on a Rigaku Smartlab diffractometer using $\text{CuK}\alpha 1$ radiation in Bragg-Brentano symmetry and a 2θ range between 10° and 90° . Rietveld refinements are carried out with the Maud software [120]. For the *operando* XRD measurement, coin cells with a Kapton window are measured in transmission mode using a parallel beam symmetry.

The X-ray photoemission spectroscopy (XPS) measurements are recorded on a PHI Quantes (ULVAC-PHI) spectrometer using monochromated $\text{Al-K}\alpha$ X-ray radiation at 1486.6 eV. All samples are mounted using conductive carbon tape and measured at 0° electron take-off angle. Charge neutralization is accomplished by a dual beam charge neutralization system, employing low energy electron and argon ion beams. Detailed acquisition parameters are given in **Table D.1**.

Data evaluation is performed using the CasaXPS software, applying a Shirley background and the GL(30) line shape for peak fitting. The binding energy scale for all samples is shifted to the main O1s peak at 533.6 eV [210, 211]. This procedure is chosen over the often used referencing to C1s due to the carbon coating present on one of the samples.

Table D.1: Acquisition parameters of the XPS measurements.

Spectrum	Energy range	Pass energy	Energy resolution	Acquisition time
XPS Survey	1100-0 eV	112 eV	0.1 eV	0.6 s/point
XPS Core levels	variable	55 eV	0.05 eV	0.9 s/point

Muon spin spectroscopy (μ^+ SR) measurements are performed on the EMU beamline at the ISIS Neutron and muon facility at the Rutherford Appleton Laboratories in Harwell, United Kingdom (Data DOI: 10.5286/ISIS.E.RB1720326). For the experiments, about 1.5 g of each LFP sample is pressed into a pellet and then transferred into a titanium sample holder with a 50 μm thick titanium window. The holder is then fixed on the thermostat of a closed cycle refrigerator (CCR) and cooled down to 50 K from where it is subsequently heated in 12.5-50 K steps. At each temperature step, four to five μ^+ SR spectra are collected: (i) a weak transverse field measurement $H_{\text{wTF}} = 20$ G, (ii) a zero field measurement $H_{\text{ext}} = 0$, and (iii-v) measurements at three different longitudinal fields. The subsequent data analysis is performed with the muSR Fit software [184]. For details about the μ^+ SR analysis, see **Section D.2**.

Ultraviolet absorption spectroscopy measurements are performed using the Agilent Cary 5000. For the measurements, approximately 20 mg of the LFP powder sample is dispersed in 3 ml water and sonicated for 30 min. After sonication, the sample is diluted until a translucent dispersion is obtained. This dispersion is then used for the optical characterization. To obtain the energy transitions from the spectra, a derivative analysis is performed [195].

Magnetic characterizations of the samples are performed with a magnetic property measurement system (MPMS XL, Quantum Design). The measurements are carried out on the MPMS devices of the Laboratory for Multiscale Materials Experiments, Paul Scherrer Institute, Villigen, Switzerland.

Electrochemical characterizations Electrochemical measurements are performed using half cells with metallic Li as counter electrode. For the LFP nanoparticle electrodes, we prepare aqueous slurries that contain 85 wt% (coated) LiFePO_4 , 10 wt% Super C65 carbon black (Timcal) and 5 wt% poly(acrylic acid) (Sigma, $M_v \sim 450'000$) at a solid content of approximately 20%. The slurry is blade casted on the Al current collector and dried slowly in air. The electrodes are typically compressed by 40%

using a calendaring system. After heating out at 80°C under vacuum for up to 12 h, the electrodes are assembled to a coin cell with a 1 mm thick glass fiber separator, a Li counter electrode and 500 μl of the electrolyte, a 1 M solution of LiPF_6 in a 1:1 mixture of ethylene carbonate and dimethyl carbonate (BASF). The electrochemical characterizations are performed using the Biologic MPG2 potentiostat.

For the *operando* cell, coin cells with an 80 μm thick Kapton window are assembled. For these cells, the amount of electrolyte is strongly reduced to a few droplets and a coated PE separator is used. The active material electrode remains unchanged. The *operando* electrochemical measurement is performed using a Biologic VSP-200 potentiostat.

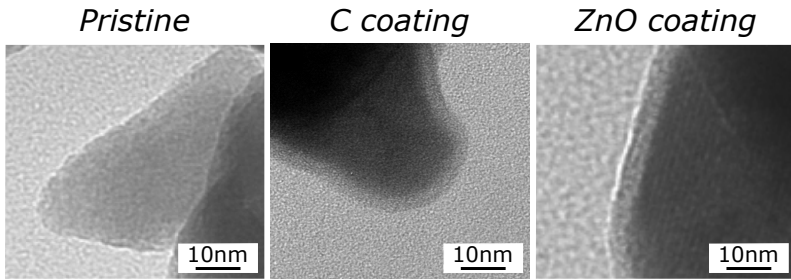


Figure D.1: Transmission electron microscopy (TEM) images of the different LiFePO₄ particle edges. For the carbon and ZnO coated samples, we observe a 3-5 nm thick coating layer.

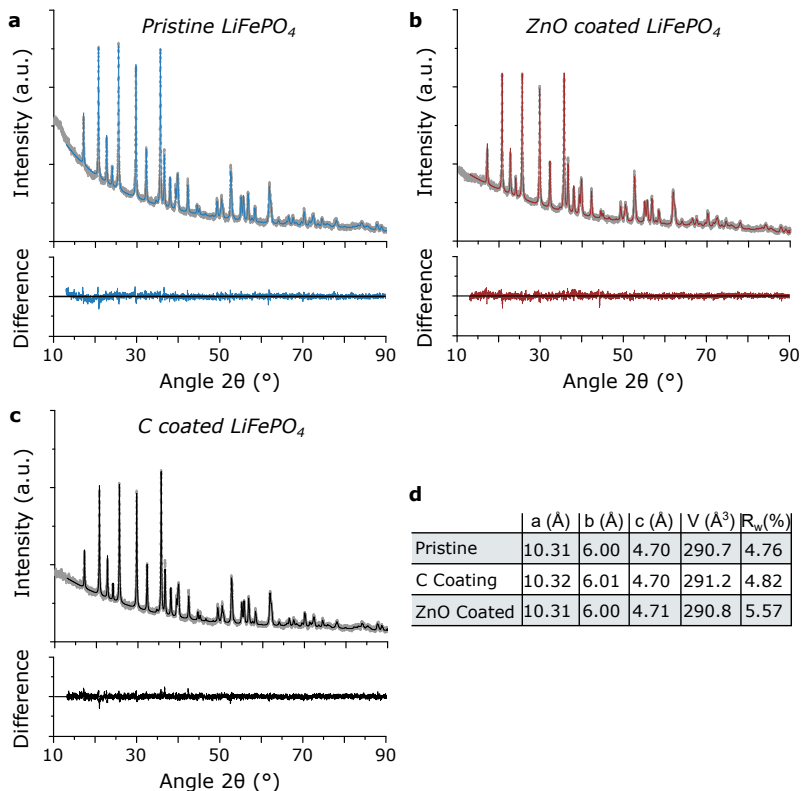


Figure D.2: X-ray diffraction patterns and Rietveld refinement of a) the Pristine LiFePO_4 (LFP) nanoparticles, b) the ZnO coated LFP nanoparticles, and c) the carbon coated LFP particles. d) Lattice constants and Pearson R value obtained from the Rietveld refinement. While the ZnO coated and pristine LFP samples have practically the same lattice constant, the carbon coating has a slightly enhanced lattice volume indicative for a small tensile stress due to Fe-C coordination. All LFP samples have been structurally refined in the Pnma space group with isotropic Debye-Waller factors. No texture refinement was necessary. The background change in the Pristine sample (a) is due to an additional air scattering contribution.

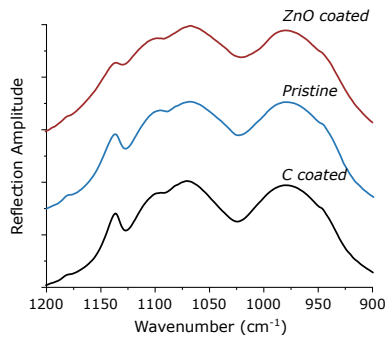


Figure D.3: Fourier transform infrared spectroscopy (FTIR) spectra of the P-O bonds. There is no visible difference in the spectra indicating a similar environment around the P-O bonds. Especially the broad peak at $\sim 980 \text{ cm}^{-1}$ does not change between the samples, suggesting no difference in the antisite defect concentration [158]

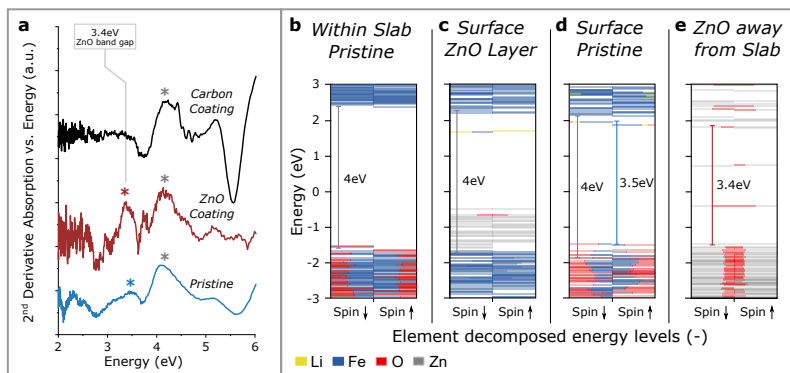


Figure D.4: Comparison of a) the derivative analysis of the ultraviolet (UV) spectra of the LiFePO₄ (LFP) nanoparticles samples with b-e) their calculated energy states. All UV spectra show a distinct peak at 4 eV (grey star) that overlaps very well with the literature value for LFP[235] and the DFT simulations (see **Figure D.8**) (grey transition in b-d)). In the carbon-coated sample, no peak is observed before hence suggesting no other transition above 2 eV. In the ZnO coated sample, a second equally strong peak is observed at 3.4 eV (red star) fitting very well to the reported values of the ZnO band gap[129] and with the electronic structure calculations (see **Figure D.10**) of the ZnO layer away from the slab (red transition in e)). The pristine sample has a broad additional peak at 3.5 eV (blue star) that might arise from surface states (blue transition in d)). Both ZnO and pristine show two transitions between 2 and 3 eV that likely arise either from defect states or impurities (note the grey color of the powder samples). Note, that the transitions marked in b-e) are not the exact band gap values reported in **Figures D.8-D.10** but the transitions found in the UV spectra.

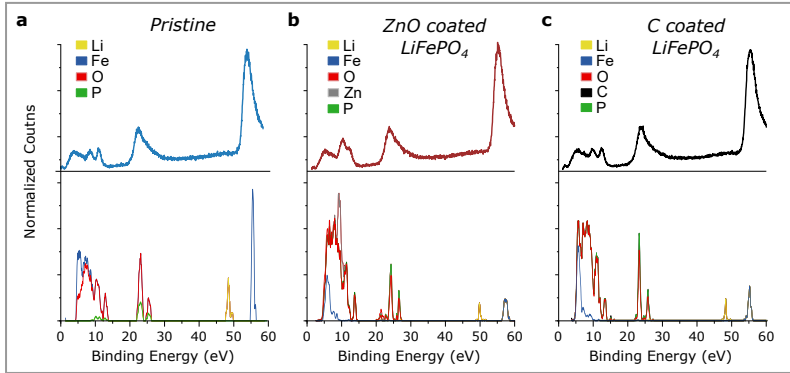


Figure D.5: Comparison of the valence band energies measured by x-ray photoemission spectroscopy (XPS) of the coated LiFePO_4 (LFP) samples with the calculated partial electronic density of states. In all samples, the contributions of the elements are stacked on top of each other to compare the overall shape of the XPS curve. A high overlap between measured and calculated energy density of states is found for all samples. Particularly in the binding energy range between 0 to 20 eV, the XPS peak fine structure is well characterized (see triple peak in a) and b), where the additional Zn states cause a peak at 10 eV to rise above the first peak at ~ 5 eV). Note that 0 eV is not well defined in XPS. As a result, all calculated energy levels have been shifted to fit the first XPS peaks at 2 eV. Furthermore, the peak intensity between DFT simulation and measurement can differ due to the x-ray scattering cross section and the normalization of the smoothed, calculated electron density of states.

D.2 Muon spin spectroscopy analysis: Fitting Approach

Due to the large gyromagnetic ratio of μ^+ it is possible to decouple ion motion of Li from paramagnetic fluctuations that origin from the transition metal nuclei (e.g., Fe) [179, 229]. In LiFePO_4 (LFP), the positively charged antimuon stops close to Oxygen atoms at two different sites close to the Fe and Li cations. Muons can only stop in the coating layers. In both the ZnO and C coating, however, we do not expect other contribution than added background since i) there are no mobile ions within the coating (see main text) and ii) both the Zn- μ^+ and C- μ^+ couplings are weak.

Antimuons can also interact with charges and cause local Jahn-Teller distortions [47, 48]. However, as $\text{Fe}^{3+}/\text{Fe}^{2+}$ atoms are in high-spin d^5/d^6 configuration [7, 235], the Jahn-Teller effect will be weak and we can expect any antimuon-induced changes in the lattice structure to be small.

To fit the antimuon spin polarization of the pristine and ZnO terminated LFP samples as a function of different applied longitudinal fields, we include contributions from the sample holder, a fast electronic component that accounts for the interactions between the antimuon and unpaired Fe electrons, and a dynamic nuclear spin contribution,

$$A_0 P(t) = A_{BG} + A_F e^{-\lambda_F t} + A_{KT1} G(H, \Delta_{KT1}, \nu_{KT1}, t) e^{-\lambda_{KT} t} \quad (\text{D.2})$$

where A_i are maximal asymmetries, λ_F is the field depolarization rate, G are Gaussian dynamic Kubo-Toyabe functions [94], H is the applied field, Δ the nuclear dipolar field distribution width, and ν the field fluctuation rate. The longitudinal field spectra are fitted together for one given temperature and sample. The fits obtained in this manner give sufficient accuracy (see **Figure D.6**). Especially at high temperature where an onset of lattice dynamics is expected, the fit of the zero field polarization is able to represent the entire time window while at lower temperatures the polarization is slightly overestimated after $8 \mu\text{s}$. The

D.2 Muon spin spectroscopy analysis: Fitting Approach

detailed fits of the carbon coated LiFePO_4 nanoparticle sample are part of the study shown in **Part 4**.

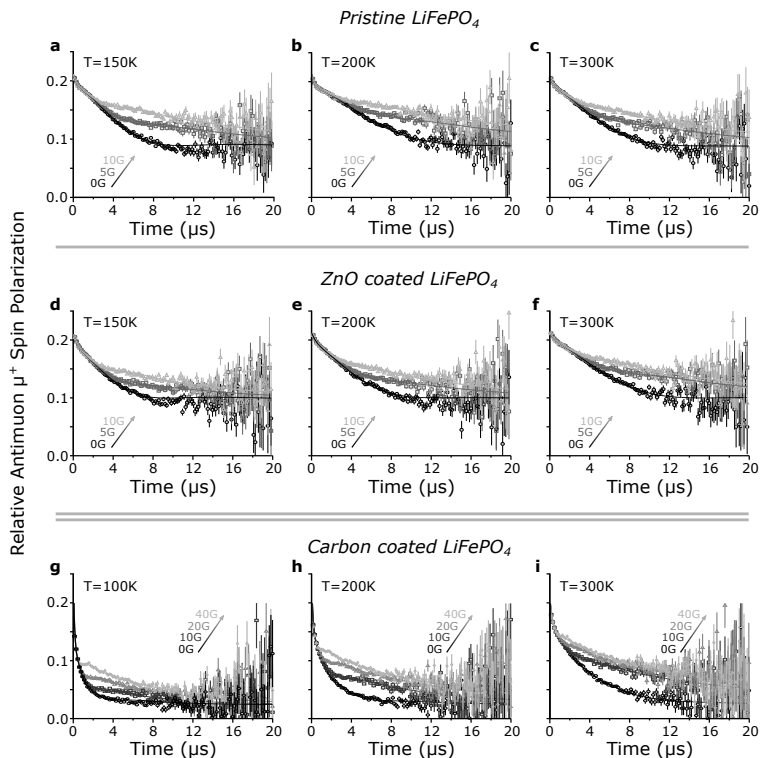


Figure D.6: Antimuon spin polarization of a-c) the pristine and d-f) the ZnO coated LiFePO_4 (LFP) nanoparticle samples at different longitudinal fields and different temperatures. Except at 150 K where the zero field (0 G) polarization is slightly overestimated after $8 \mu\text{s}$ (a,d), a very good agreement between experiment and fit is found. g-h) Antimuon spin polarization curves of the carbon coated LFP samples. Due to a magnetic impurity the shape of the polarization drops faster and an additional Kubo-Toyabe term is necessary. For a detailed discussion about the fitting approach of the data, see **Part 4**.

D.3 Muon spin spectroscopy: Validation of fitting parameters

Figure D.7 summarizes the parameters obtained using the fits described above. As described in the main text, the field fluctuation (**Figure D.7a**) i.e. the Li hopping rate remains relatively constant for both the pristine and the ZnO coated LiFePO₄ samples while the Li ion hopping increases exponentially for the carbon coating. This is in accordance to the changes of the field distribution width Δ as a function of temperature (**Figure D.7b**). In all samples we observe a characteristic decrease of Δ with increasing temperature that is distinctive for a motional narrowing process [179]. However, the motional narrowing is much stronger for the carbon coated LiFePO₄ sample, suggesting a faster atomic motion at elevated temperature. Note that this is also the case for the impurity phases that can cause an increase of the overall field distribution width at low temperature [21].

The normalized asymmetry $\frac{A_{KT/BG}}{A_{KT}+A_{BG}}$ provides an estimate of antimuons stopping positions and their experiences forces. Therefore, the temperature dependence of the normalized asymmetry can be descriptive for structural changes e.g. a magnetic transitions or a phase separation. (**Figure D.7c**) summarizes the normalized asymmetries obtained for the LiFePO₄ nanoparticle samples. For pristine LiFePO₄ we observe a temperature independent behaviour of the normalized asymmetry thereby agreeing to earlier studies where magnetic contributions of the LiFePO₄ are expected to be temperature independent between 100 K and 400 K [181]. In ZnO coated LiFePO₄, however, the paramagnetic fast contribution is not constant anymore, converging to the values found in the pristine sample with increasing temperatures. Such a behaviour can only be explained with a weak magnetic impurity that reduces its influence with increasing temperature, similar to the impurity found in the carbon coated sample [21]. Indeed, magnetic susceptibility measurements (**Figure D.8**) suggest a magnetic impurity in the ZnO coated LiFePO₄ sample that, contrasting from the carbon coated sample, contains a temperature dependent magnetic contribution that with higher temperature

becomes very small. This suggests that a magnetic impurity is formed (e.g. Fe doped ZnO [172]). This is further supported by the fact that no second dynamic spin relaxation term is needed to fit the antimuon spin polarization curves hence suggesting a rigid oxide lattice that does not contain lithium.

Overall, we observe that, apart from a magnetic oxide impurity, the dynamics and muon spin spectroscopy analysis of the pristine and the ZnO coated LiFePO₄ nanoparticles are analogous. In contrast, the carbon coated LiFePO₄ sample shows strongly enhanced dynamics not only in the Li ion hopping rate but also in the field distribution width.

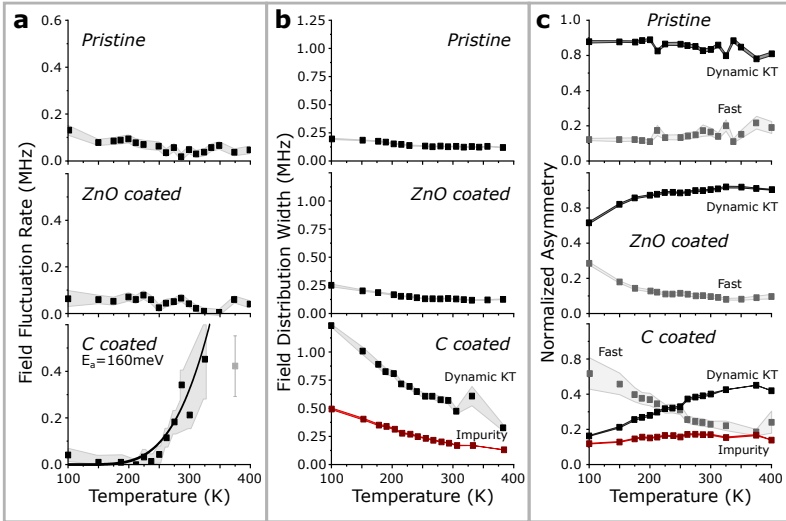


Figure D.7: Resulting parameters obtained from the muon spin spectroscopy fits with the temperature dependence of a) Field fluctuation rate (i.e. Li ion hopping rate [179]), b) the field distribution width, and c) the normalized asymmetry. The parameters obtained for the carbon coating are based on fits described in **Part 4**

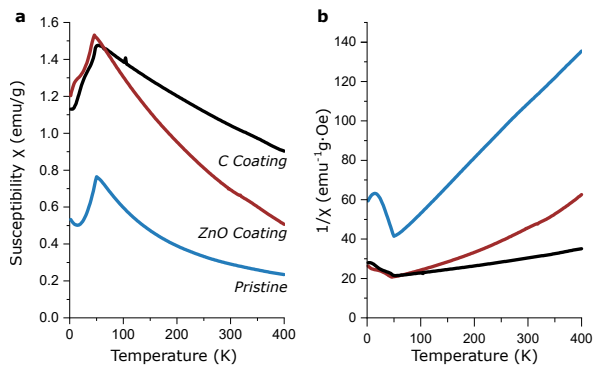


Figure D.8: a) Magnetic susceptibility of the LiFePO₄ nanoparticle samples. While the pristine LiFePO₄ particles behave as reported in other works [181, 235], the ZnO and carbon coated LiFePO₄ samples have a strongly enhanced magnetic susceptibility, suggesting a magnetic impurity. In the case of the carbon termination, this magnetic impurity is temperature-independent throughout the measuring range. In the case of the ZnO coating, the susceptibility drops significantly from a high level similar to the C coating towards the susceptibility of the pristine sample as it would be characteristic for a weakly magnetic impurity. b) The inverse susceptibility whose slope is a measure of the number of unpaired electrons in the material. Above the antiferromagnetic transition at 50 K, both the carbon coated and pristine LiFePO₄ samples have a constant slope that is characteristic for paramagnetic materials. The inverse susceptibility of the ZnO terminated sample, however, is curved which would suggest a magnetic. Note that the slope of the ZnO coating is converging towards the slope of the pristine sample further confirming this hypothesis.

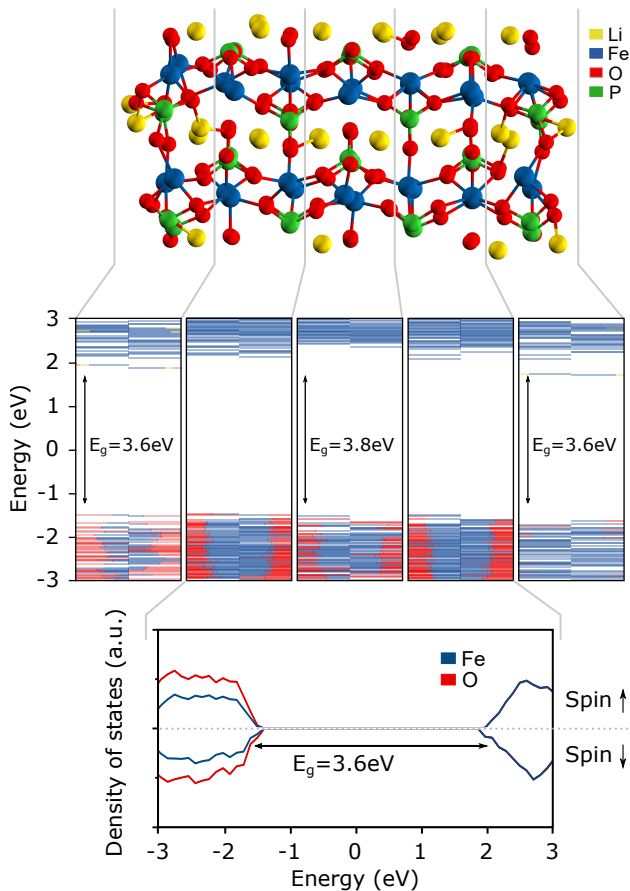


Figure D.9: Image of the pristine LiFePO₄ slab and the defined layers for the electronic characterization. We split the slab into five regions: two surface regions and three inner regions. For all of those regions we obtain an energy level diagram. By summing all of the energy states of the inner regions, we obtain a partial electronic density of states (PEDOS) of the bulk of the slab. Note that, for reasons of clarity, contributions to the energy levels are normalized to one. No such normalization is performed in the PEDOS calculation. Instead, the PEDOS is smoothed over 0.15 eV, leading to a decrease of the band gap compared to the energy levels.

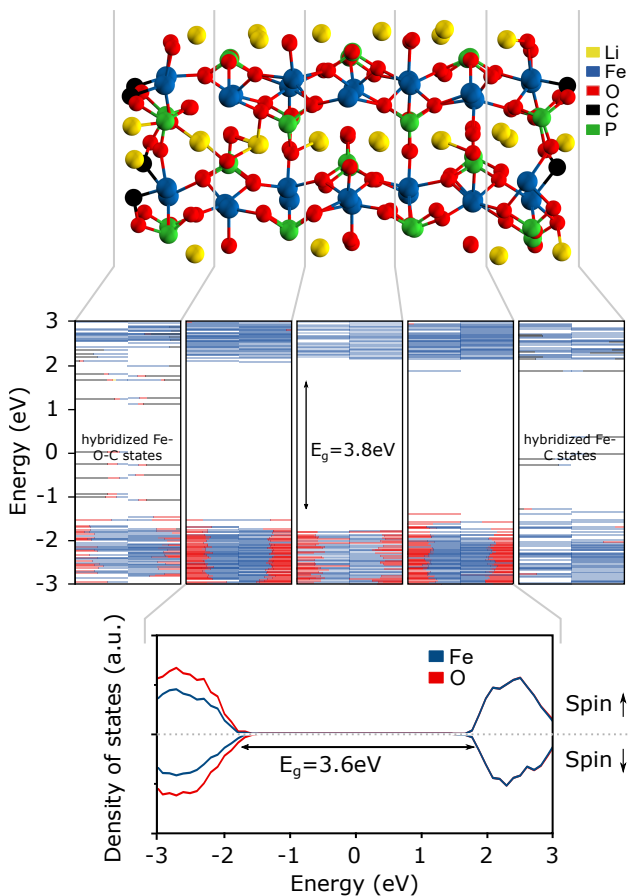


Figure D.10: Image of the C coated slab and the defined layers for the electronic characterization. We split the slab into five regions: two surface regions and three inner regions. For all of those regions we obtain an energy level diagram. By summing all of the energy states of the inner region, we obtain a partial electronic density of states (PEDOS) of the bulk of the slab. Note that, for reasons of clarity, contributions to the energy levels are normalized to one. No such normalization is performed in the PEDOS calculation.

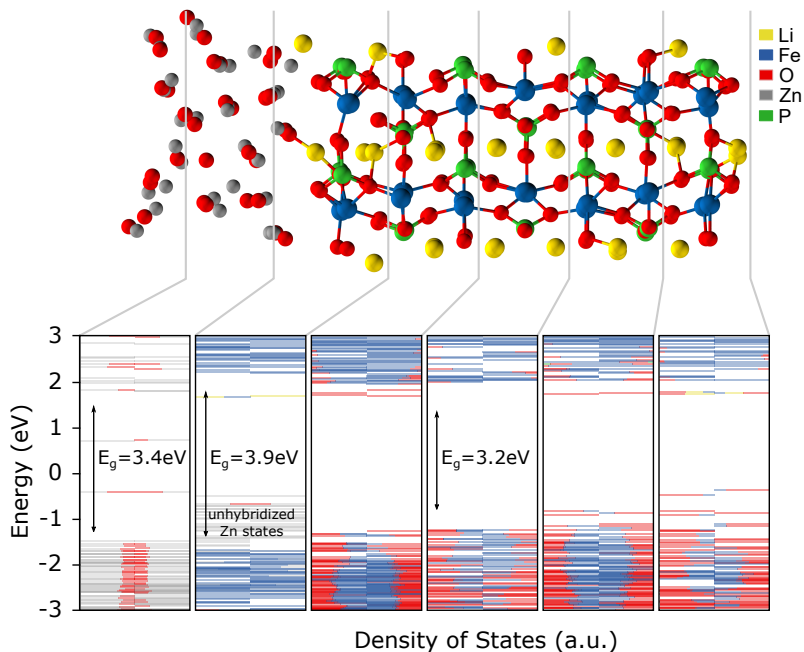


Figure D.11: Schematic drawing of the ZnO coated slab and the defined layers for the electronic characterization. We split the slab into six regions: one LiFePO₄ (LFP) surface region, three inner LFP regions, one region at the LFP-ZnO interface and one pure ZnO region. For all of those regions we obtain an energy level diagram. Note that for reasons of visibility, contributions to the energy levels are normalized to one. Furthermore, the band gap within the LFP slab is constantly reduced with increasing distance from the ZnO coating. We assume that this is due to the electronic dipole induced by the ZnO termination[24].

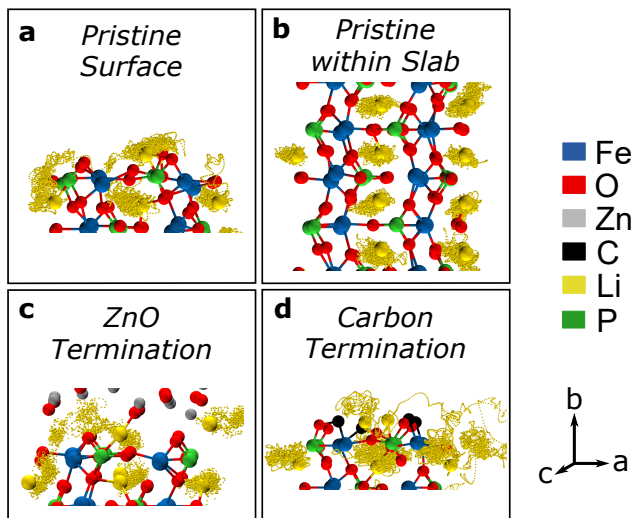


Figure D.12: Lithium trajectory during the *ab initio* molecular dynamics simulations at a cryostat temperature of 1000 K a) at the pristine slab surface, b) within the pristine slab c) at the ZnO terminated slab, and d) at carbon terminated slab. During the simulation all atoms were set free to move during the simulation. Following the initial Li position (depicted as large Li atom), Li positions (small yellow points) are updated after every 5 fs. For reasons of clarity, only the trajectory of the lithium atoms is shown.

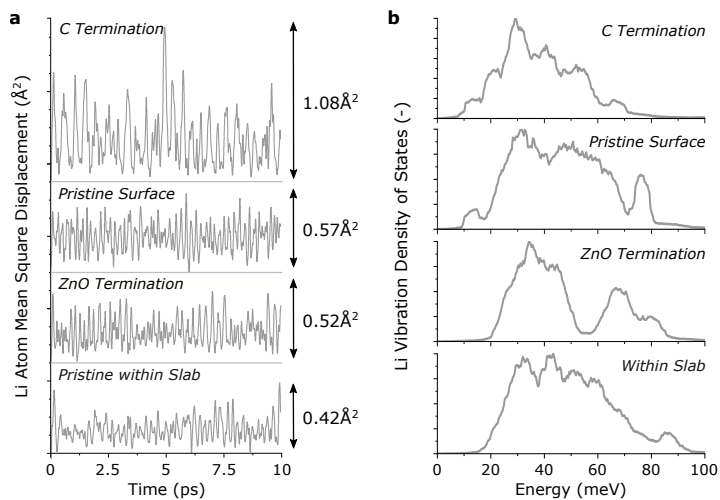


Figure D.13: a) Li atom Mean squared displacement in a Pinball model, where an ab initio molecular dynamics simulation is performed at 1000 K with all atoms except Li fixed to their 0 K equilibrium position. b) Density of Li vibrational states obtained in a Pinball model. As found in earlier studies[23, 182], all vibrations occur in an energy range of 10 to 90 meV.

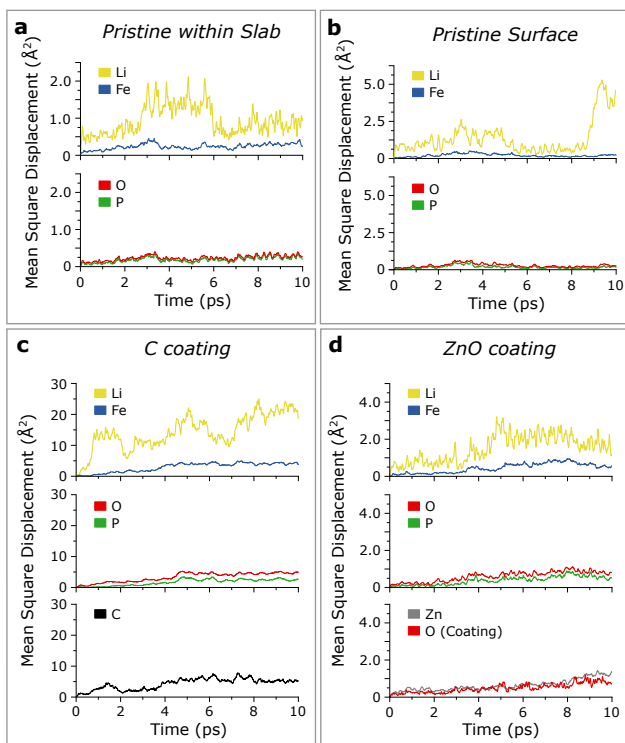


Figure D.14: Atom decomposed mean squared displacement (MSD) at a cryostat temperature of 1000 K of a) the pristine LiFePO_4 within the slab, b) the pristine slab at the surface, c) the carbon coated termination, and d) the ZnO termination. In all situations, the MSD of the host atoms Fe, P, and O are very similar suggesting a correlation between them. c) The same can be found for the MSD of the host atoms and carbon. d) While there is a clear correlation between Zn and the O with the ZnO layer, there is no visible correlation between the LiFePO_4 host atoms and ZnO.

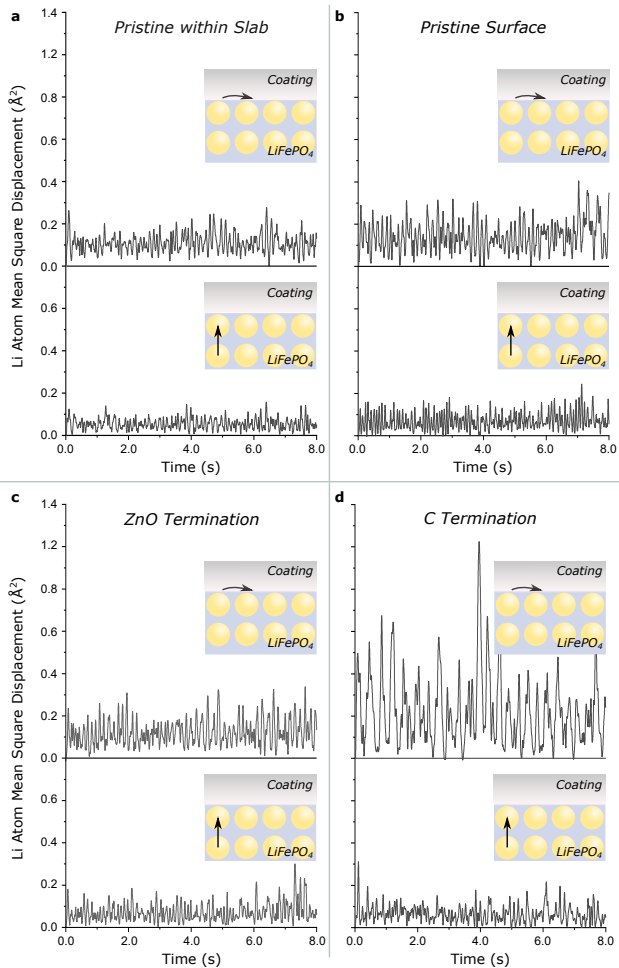


Figure D.15: Comparison of the surface diffusion (i.e., the crystallographic a-c plane) and interface diffusion (i.e., the b axis) contribution to the Li Mean squared displacement (MSD) with fixed host lattice (**Figure D.13**). While there is little change a) within the pristine slab, a small increase of the surface diffusivity is observed at both b) the pristine and c) the ZnO terminated surface. By far the strongest increase in surface diffusivity is found for the d) C coating. In all cases the interface diffusivity remains similar.

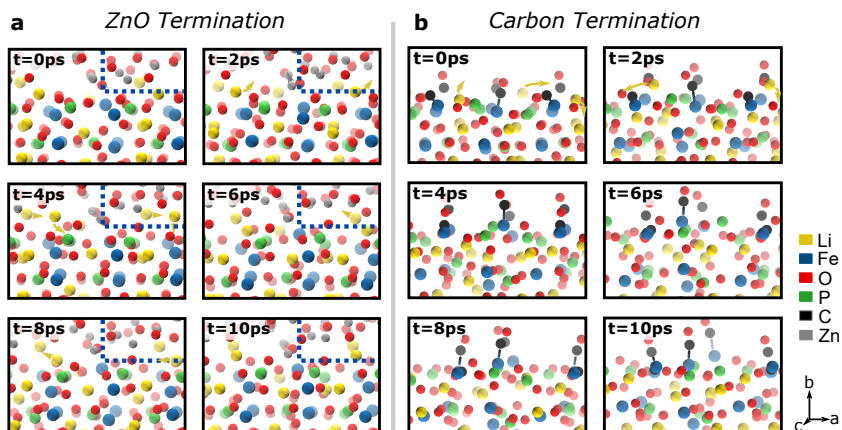


Figure D.16: Snapshots of the AIMD runs of a) the ZnO terminated LiFePO_4 (LFP) surface and b) the Carbon terminated LFP surface. a) Looking at the ZnO-LFP interface, only local motion of lithium atoms is observed. Zn atoms, on the other hand, are more dynamic at the interface. Nonetheless, there is no visible correlation between the movements of the Zn atoms and Fe/Li atoms. b) All carbon atoms coordinate with surface iron atoms (see Fe-C bonds). This bonds vibrate slowly forward and backward over the simulated time frame. In parallel, the Li ion atoms diffuse freely away from the surface towards the second layer of LFP.

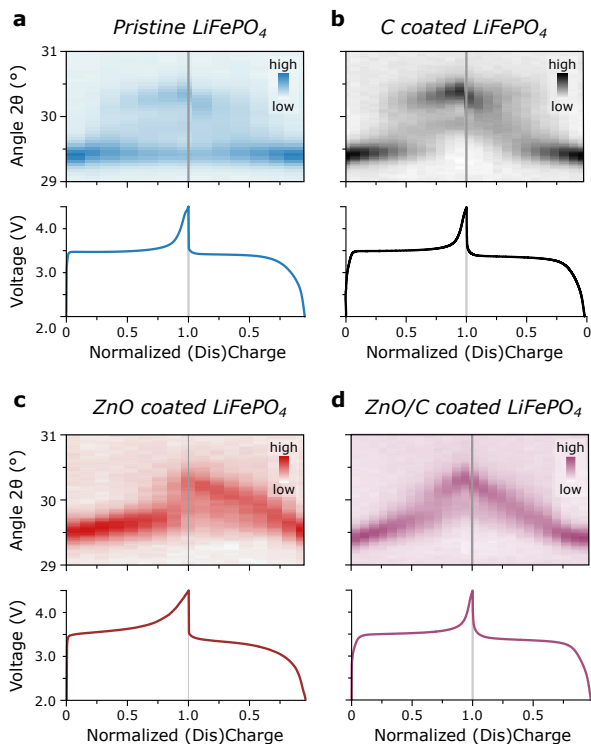


Figure D.17: *In Operando* x-ray diffraction measurement of the LiFePO_4 (LFP) nanoparticle samples at a cycling rate of 1C. To study the effect of phase separation, we focus on the (010)/(211) peak. Generally, the same trend as at a C/10 rate can be observed throughout all LFP samples. The pristine LFP sample (a) is an exception with a significant portion of the active material is not taking part in the reaction. We hypothesize that this is due to the increased cycling rate. Nonetheless, we still observe the phase separation of LFP during battery charge and a solid solution behaviour during discharge.

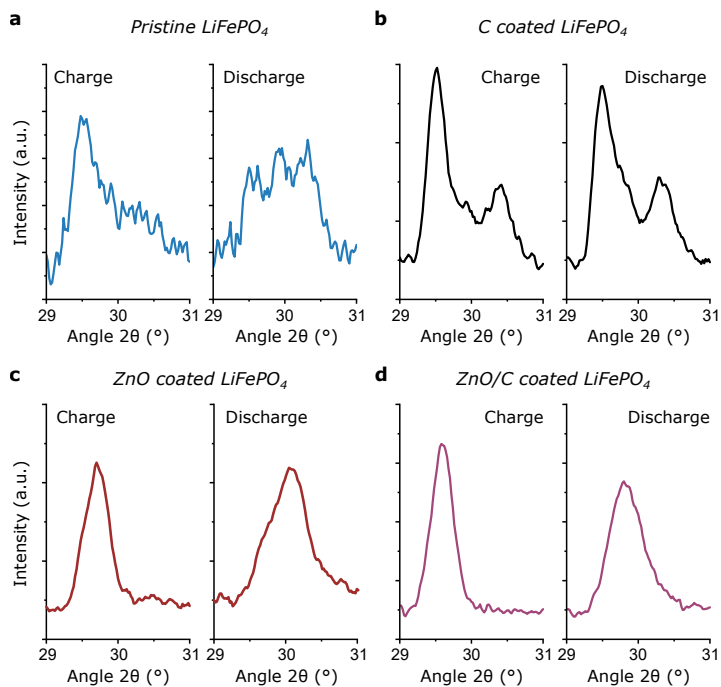


Figure D.18: Comparison of operando x-ray diffraction spectra for the different Li_xFePO_4 samples at a state of (dis)charge of 0.5. For the a) pristine and b) C coated LiFePO_4 sample, two peaks are visible during charging, suggesting a phase separation. During discharge, the pristine, the c) ZnO coated and d) ZnO/C coated LiFePO_4 samples show only one peak, indicative of a solid solution.

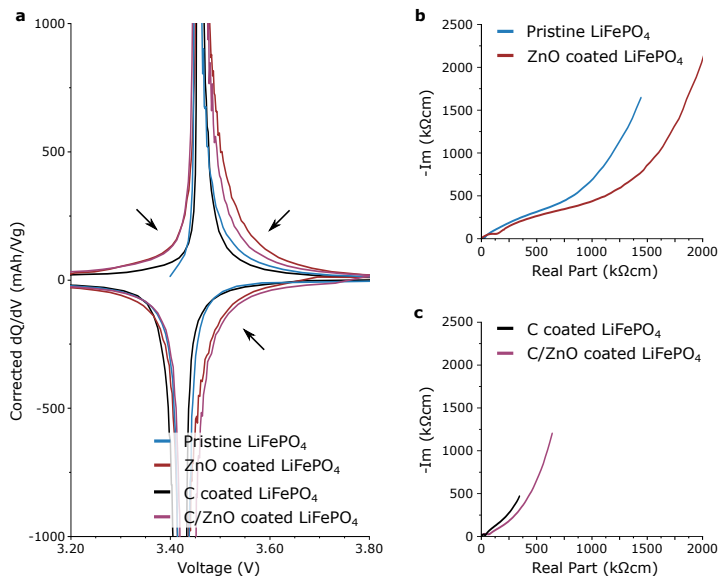


Figure D.19: a) dQ/dV vs voltage plot of the differently coated LiFePO₄ (LFP) samples. We find that the voltage peak that occurs at 3.45 V is significantly broadened in the ZnO/C and ZnO coated LFP samples. b- c) Electrochemical impedance spectra of electrodes containing b) the pristine and ZnO coated and c) carbon and carbon/ZnO coated LFP nanoparticles. The pristine termination and the ZnO coating clearly inhibit the conductivity of the electrodes. In contrast, the C and ZnO/C coated LFP exhibit much smaller resistances with the carbon coating having a slightly smaller impedance. All electrodes contain 10 wt% carbon black and 5 wt% poly(acrylic acid).

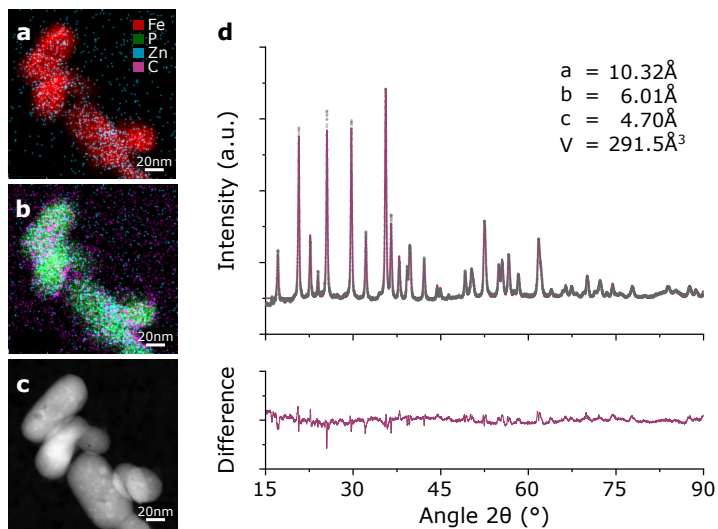


Figure D.20: a-c) EDS STEM images of the ZnO-C coated LiFePO₄ (LFP) nanoparticles. We find that Zn and carbon build a coating surrounding the LFP particles. A comparison of the Fe and Zn signal (a) suggests that the ZnO coating is forming irregular local defects. d) Rietveld refinement of the ZnO-C coated LFP nanoparticles. Using a single LFP phase provides an acceptable fit ($R_w = 4.8\%$).

List of Figures

1.1	a) Future LIB technologies targets for energy density, cycle lifetime and rate capabilities. To meet these targets the challenges between materials, (micro)structure, and interfaces have to be solved in the highly dynamic Li ion battery. b) Summary of all the techniques that can be provided at large-scale facilities with their matter of interaction within the studied samples.	3
1.2	a) Projection of a cross section of a $\text{LiNi}_{0.5}\text{Co}_{0.2}\text{Mn}_{0.3}\text{O}_2$ versus graphite electrode. The L_0 - L_4 regions depict the layers of x-ray diffraction (XRD) measurements. b) <i>Operando</i> XRD measurements of the regions L_0 - L_4 show that the average Li content in the graphite layer is not uniform but rather highest close to the separator while charging. Conversely, the Li concentrations requires the longest time to reduce in the L_4 region. The images are adapted from [228].	6
1.3	a) Resonant inelastic x-ray scattering (RIXS) pattern of the O K-edge in $\text{Li}_2\text{Ir}_{1.5}\text{Sn}_{0.5}\text{O}_3$. The white arrow marks a characteristic feature found in oxidized oxygen. b)-c) Proposed mechanism of the oxygen oxidation. The formation of antisite defects moves the Ir-O double bonds above the Fermi level and making them prone to oxidation. Images adapted from [222].	7
1.4	Raw and Segmented X-ray computed tomography (XCT) image of a silicon-graphite electrode with resolved carbon black binder domain (CBD). Figure taken from [140]. . .	9

- 1.5 Ptychographic x-ray computed tomography (PXCT) image of partially delithiated $\text{Li}_{0.5}\text{FePO}_4$ particles. Three arbitrary particles show the resolution capabilities with the ability to separate between LiFePO_4 rich (red), FePO_4 rich (blue) and the solid solution Fe_xPO_4 rich voxels (green). The scale bar for the single particles is 50 nm. Images adapted from [232]. 11
- 1.6 *Operando* small angle neutron scattering (SANS) measurements of mesoporous carbon vs. Li cells with 4M LiTFSI as electrolyte salt. The increase of the micropore scattering intensity arises from LiTFSI molecules aggregating and forming the SEI within the pores. In parallel, the pore-pore spacing increases due to co-intercalation into the carbon network. Image adapted from [83]. 13
- 1.7 a) Working principle of neutron depth profiling (NDP) where a neutron hits the ^6Li and induces a decay into ^3H and ^4He . b) NDP experimental design. c) *Operando* NDP measurements on Li deposition in a Carbon nanotube network. With increasing stripping and plating cycles the irreversible Li content close to the copper current collector increases resulting in a peak at the NDP spectra at a ^3H energy of 2400 keV. Images b-c adapted from [206]. 15
- 1.8 a) Inelastic neutron scattering (INS) spectra of LiFePO_4 particles as a function of particle size suggesting an energy increase of the Li-O phonon energy at the surface. b) A comparison of *ab initio* DFT simulations to determine the average within the slab and at its surface supports the findings. Images adapted from [23]. 16
- 1.9 a) Experimental design to study the solid-solid interface between LiCoO_2 and the LiPON solid electrolytes. b) Electron energy loss spectroscopy (EELS) patterns collected at different points at the ordered-disordered LiCoO_2 interface. When the cell is charged *in situ*, a phase between ordered and disordered LiCoO_2 arises. This interphase contains Li_2O_2 and Li_2O . Images adapted from [213]. 18

- 1.10 a) Bright field image of a LiFePO_4 nanoparticle with an enlarged area of the particle. The scale bar is 50 nm or 5 nm, respectively. b)-e) Heat map of lithium content x in Li_xFePO_4 at different time steps (blue to red for increasing x). The scale bars are 5 nm. f) Normalized Li concentration through different nanoparticle regions (see b) as a function of time. Locally, the Li concentration peaks and then reduces itself. On a larger scale, the Li concentration equilibrates to the typical LiFePO_4 polarization curve. Image adapted from [238]. 19
- 1.11 a) Cryogenic electron microscopy (cryo-EM) image of the solid electrolyte interphase (SEI) grown on a Li metal anode. The inset below shows the energy-dispersive x-ray scattering (EDS) spectrum which suggests an inorganic-rich SEI. b) Cross sections of Li metal anodes before and after 60 and 100 cycles, respectively. The LiFSI electrolyte solution with DME-TFEO additive creates a dense SEI thereby passivating the Li layer and reducing the dendrite growth. Images adapted from [35]. 20
- 1.12 a)-c) Working principle of a) Li-NMR exemplified exemplified on ^7Li -NMR, b) μ^+ SR and c) β -NMR. d) Flow chart of using polarized beams for lithium ion diffusion measurements. 22
- 1.13 a) Muon stopping depth in a $\text{Li}_4\text{Ti}_5\text{O}_{12}$ anode. b) Lithium ion hopping rate of $\text{Li}_4\text{Ti}_5\text{O}_{12}$ powder and thin films (film thickness: 190 nm) as a function of temperature. The hopping rate shows a good overlap between the two samples. Images taken from [134]. 23
- 1.14 Two-dimensional DNP-NMR spectrum of the outer SEI on reduced graphene oxide. The molecular fragments found in the SEI are shown right of the two-dimensional spectrum. Image adapted from [101]. 24

2.1	Specific energy consumption of the LFP synthesis step as a function of hydrothermal reaction temperature and total precursor concentration. The blue shaded region indicates the energy consumption of typical hydrothermal syntheses, the synthesis reported here is indicated green. The iso-energy line corresponding to 3 MJ/kg is shown in bold, corresponding to the specific energy consumption of a solid-state synthesis. The shaded triangular region below this line represents a temperature and precursor concentration window where a hydrothermal synthesis consumes less energy than a solid-state synthesis.	34
2.2	Preparation procedure of battery grade LiFePO ₄	35
2.3	Dependence of defect concentration and particle morphology as a function of molar concentration of precursors, C _{tot} , in water. Precursors are fixed in a ratio of [Li] : [Fe] : [PO ₄] : [EG] = 3 : 1 : 1 : 0.1. (a) FTIR spectra and (b) position of the symmetric P–O stretching band peak for samples synthesized at different precursor concentrations. (c) SEM images, (d) mean particle thickness, and (e) mean particle diameter are also shown for different precursor concentrations.	36
2.4	Two different batches (circles, triangles) of LFP platelets synthesized under the same conditions are sampled as a function of reaction time and their thickness (a) and the peak position of the symmetric P–O stretching mode (b) is plotted. Shading indicates the standard deviation of the measurements. (c) Polarization curves at C/10 rate of LFP samples prepared with different reaction times. (d) Specific discharge capacity at different C rates (1 C = 0.17 A g ⁻¹) of LFP synthesized at 115 °C at a precursor concentration of C _{tot} = 0.55 M and a reaction time of 48 h. Shading indicates the error bars on the measurements, which are determined by measuring five cells containing different electrodes prepared from two different batches of material.	38
2.5	Schematic drawing of the LiFePO ₄ platelet particle size series.	41

2.6	Scanning electron microscopy (SEM) images of the a) Large, b) Meso, c) Medium, and d) Nano LFP samples. Their size characterization is summarized in Table 2.2	42
2.7	a,b) Scanning and transmission electron microscopy (SEM and TEM) images of a) the pristine and b) the C coated <i>Large</i> LFP particles. c) Raman spectrum of the C coated LFP particles.	45
2.8	Energy dispersive x-ray scattering scanning transmission electron microscopy (EDS-STEM) images of a) C coated, b) Pristine, c) ZnO coated, and d) ZnO/C coated <i>LiFePO₄ Nano</i> particles.	46
3.1	a) Schematic drawing of the <i>LiFePO₄ (LFP)</i> platelet particles. b) Schematic view of the Li ion transport channels along the [010] direction and the carbon coating at the particle surface. c) Crystal structure of LFP.	50
3.2	Transmission electron microscopy (TEM) image of the <i>Large</i> LFP sample with the carbon coating. TEM images of the <i>Medium</i> and <i>Nano</i> sample are shown in Figure B.6	51
3.3	The experimentally measured phonon density of states for a) <i>LiFePO₄ (LFP)</i> and (b) delithiated LFP (i.e., <i>FePO₄</i>) samples of different sizes. The shading around the points indicates the error of the measurement. The dashed lines show the calculated phonon density of states.c) Calculated total and elemental partial phonon density of states of LFP (black) and <i>FePO₄</i> (gray) from bulk density functional theory simulations. Full spectra are shown in Figure B.10	53
3.4	Rendering of the particle slab on which the DFT calculations are performed, showing the atoms included as an inner slab and the surface contributions. Inset: depiction of metal–oxygen bond lengths in bulk <i>LiFePO₄</i> obtained from Rietveld refinement.	55

3.5	Three different LFP surfaces are simulated: b) a vacuum terminated surface, b) a carbon terminated surface, and c) a Li-deficient surface. The mean calculated bond lengths in the inner part of the slab (line) and for the different surfaces (points) and the experimental bond lengths obtained from Rietveld refinement (left) are shown for d) Li-O, e) P-O, and f) Fe-O. The width of the line and the error bars for the calculated values indicate deviations in the mean value for the given dataset.	57
4.1	a) Lithium and electron diffusion in a lithium-ion battery electrode while charging. b) Lithium-ion and electron diffusion at a single-particle level. Electrons move through the carbon black network, while lithium ions are transferred by the electrolyte (marked in brown hexagons). c) Mechanisms of ion diffusion in a system of one-dimensional ion transport channels. Four processes can be distinguished: bulk diffusion (<i>i.e.</i> , away from the particle interface), charge transfer, in-plane diffusion, and interface diffusion.	62
4.2	a) Lithium-ion trajectories found in the slab by performing NEB calculations. b) Resulting energy of the paths shown in a). The gray area in the background shows the range of reported values from earlier simulations.	64
4.3	a) Working principle of μ^+ SR measurements. A pulse of spin-polarized anti-muons impinges on the sample, and the anti-muons stop at a local energy minima. b-d) Example μ^+ SR spectra (asymmetry curves) of the <i>Large</i> , <i>Medium</i> , and <i>Nano</i> samples at different temperatures and magnetic field $B = 0$ Gauss. e-g) Temperature dependence of the field fluctuation rate, ν_{KT1} , for the samples <i>Large</i> , <i>Medium</i> , and <i>Nano</i> extracted from fitting of the asymmetry curves (see Appendix C.5). The inset in e) shows an Arrhenius-type fit with an activation energy of 450 ± 150 meV.	68

4.4	a) CV measurement at different sweep rates performed on LFP electrodes in a half-cell geometry. b) Linear fit of the maximal current vs the sweep rate at different temperatures for the <i>Nano</i> sample (after correcting for the contribution of the electrochemical double layer). The slope of this curve gives values for the diffusion coefficient, D . c) Linear regression of the natural logarithm of the diffusion coefficient ($\ln D$) vs the inverse temperature (T^{-1}) for each sample. The slope is the activation energy for the diffusion process. d) Resulting activation energies for the samples. Error bars come from the measurements performed on a number of samples.	70
5.1	Comparison of the local current density in the vicinity of the active particles in the case of a) solid solution behavior and b) phase separation and the resulting voltage polarization.	76
5.2	Strategies to mitigate phase separation. a) By reducing the particle size, surface strain can destabilize the spinodal decomposition. b) Charge dynamics at the particle interface can lead to two scenarios. When the surface charge diffusion is faster than the charge transfer, lithium ions can phase separate into Li rich and Li poor regions. Conversely, a reduction of the surface charge diffusion allows for solid solution behavior	78
5.3	a) Schematic image of the four different diffusion pathways have to be considered in coated LiFePO_4 particles. b) General bulk diffusion mechanism in LiFePO_4 . Li ions and electrons move collectively along the lattice via one interstitial Li ion site.	80
5.4	a) Energy dispersive x-ray scattering scanning transmission electron microscopy image of the pristine, ZnO, and C coated LiFePO_4 nanoparticles. b) Particle size dispersion of the three samples. c) X-ray photoemission spectra of the three samples, displayed at the Fe L edge.	81

5.5	Li ion hopping rate of the coated LiFePO_4 (LFP) nanoparticle powders obtained from muon spin spectroscopy. On the carbon coated LFP, Li ion dynamics show an activation energy of 160 meV.	83
5.6	a) Structure of the LFP slabs with a classification between atoms at the surface and within the slab. Furthermore, the partial electron density of states (PEDOS) is shown for the pristine LFP sample within the slab. b-d) Energy level diagram of the b) pristine, c) ZnO terminated, and d) C terminated LFP surface. For all samples, an image of the three highest occupied and three lowest unoccupied wave functions is shown.)	85
5.7	Amplitude of the Li atom mean squared displacement (MSD) when the host lattice is fixed. The Li atoms are significantly more flexible close to the carbon termination with the other interfaces being relatively similar to Li ion dynamics. Inset: Li ion trajectory of the pristine LFP sample when all atoms are allowed to move.	86
5.8	<i>Operando</i> x-ray diffraction spectra of the $\text{LiFePO}_4/\text{FePO}_4$ (020) peak as a function of state of charge for a) C coated, b) Pristine, and c) ZnO coated LiFePO_4 nanoparticles. All spectra were measured at a current of 17 mA/g, corresponding to a rate of C/10.	89
5.9	a) Comparison of the x-ray diffraction spectra of the ZnO coated LiFePO_4 sample at 50% (dis)charge. During particle charge, surface stress prevents phase separation. During discharge, the resistance due to the ZnO coating leads to a situation where charge transfer is faster than Li diffusion. b) Discharge Capacity of the coated LiFePO_4 samples at different (dis)charge rates.	90
5.10	Schematic explanation of the ZnO+C Coating. Due to the ZnO defect regions, the surface diffusion of Li is impeded and the coating mechanically stabilized while the carbon matrix still allows for high rate capability and capacity retention.	91

5.11	a) <i>Operando</i> x-ray diffraction spectra of the $\text{LiFePO}_4/\text{FePO}_4$ (020) peak as a function of state of charge for ZnO+C coated LiFePO_4 nanoparticles, measured at a current of 17mA/g, corresponding to a rate of C/10. b) Discharge Capacity of the coated LiFePO_4 samples at different (dis)charge rates.	92
A.1	Schematic of the reactor.	106
A.2	Rietveld refinement of the XRD spectra of LFP particles synthesized at different precursor concentrations, C_{tot} . For $C_{\text{tot}} = 0.1 \text{ M}$, no refinement was possible due to further Li_3PO_4 and $\text{Fe}_2(\text{PO}_4)_3 \cdot 8\text{H}_2\text{O}$ impurities. For the other LFP samples, the resulting crystal parameters, the unit cell volume and the antisite defect concentration (n) are given. The difference between refinement and the data is plotted below for each diffractogram.	108
A.3	a) Comparison of XRD patterns of LFP samples synthesized at different precursor concentrations, C_{tot} . b) Plot of the resulting antisite defect concentration of the LFP sample as a function of precursor concentration. The antisite defect concentration was obtained from the Rietveld refinements of the LFP data in Figure A.2	109
A.4	Schematic of the sampling reactor.	111
A.5	a) Galvanostatic curves showing (dis)charge of LFP samples (reaction time: 48 h) at different C-rates. b) Discharge capacity as a function of cycles measured at 1C discharge and C/2 charge.	112
A.6	Specific energy consumption of the LFP synthesis step as a function of hydrothermal reaction temperature (reactor pressure) and reaction time. The energy consumption of typical hydrothermal syntheses of LFP particles is indicated with the blue shading. The 3 MJ kg^{-1} energy consumption for a solid state approach is highlighted (blue region and blue line, respectively).	113

A.7	Comparison of FTIR spectra, SEM and TEM images, and XRD patterns for LFP particles a) before and b) after annealing. The small change in the asymmetric PO_4 stretching mode likely comes from loss of water and some high temperature recrystallization during the annealing step. The XRD patterns show similar degrees of crystallization before and after annealing, indicating that no additional phases arise during the annealing.	114
A.8	Example size distributions for the LFP particles. The mean distance and the standard deviation of the particle length and thickness for each sample is obtained from the size distributions obtained by measuring 100-200 particles in multiple SEM images.	115
A.9	Size distribution of the <i>Nano</i> , <i>Medium</i> , and <i>Large</i> LFP platelet samples. The particle diameter $d_{(010)}$ and channel length $L_{[010]}$ distributions are shown in a) and b), respectively.	115
A.10	Platelet diameter and channel length distribution of the <i>Meso</i> LFP samples.	116
A.11	Schematic image of the LFP disk used for the calculations and its transformation to an ellipse with a square lattice.	119
B.1	a) Schematic image of the stacking of the four-layer pouch cell before welding the tabs to a contact. b) Image of the stacked electrode with the welded contacts on the cathode and anode tabs.	123

B.2	Preparation steps of the FePO_4 samples after cycling. a) Image of a cycled pouch cell. The wood plates are used to apply pressure on the pouch cell and the scotch tape around the contacts to avoid accidental short circuits during transfer to the glovebox. b) Image of the lithiated copper current collector and the glass fiber separator showing evidence of lithium dendrites. c) Image of the other side of the glass fiber separator and the LFP electrode. We observe no dendrites growing through the separator. d) Once the stacked pouch cell is disassembled, the electrode material is scratched from the electrode with a spatula and transferred in a centrifuge tube. e) After extensive washing and centrifuging, the dark brown LFP powder is separated from the PVDF and carbon black mixture and isolated.	125
B.3	a) Schematic image of the stacking of the four-layer pouch cell before welding the tabs to a contact. b) Image of the stacked electrode with the welded contacts on the cathode and anode tabs.	125
B.4	Galvanostatic (dis)charge curves of the LFP samples used in this study for a rate of C/10 corresponding to a specific current of 17 mA g^{-1} . The galvanostatic curves here are from the second C/10 cycle.	126
B.5	Rate-dependent discharge capacity of the samples used in this study. The dots show the average capacity from at least three cells from different slurries with the standard deviation depicted by the shading. The given rate was used for both charge and discharge.	127
B.6	TEM image of the <i>Large</i> sample with b) the selected area diffraction pattern. c),d) TEM images of the <i>Medium</i> and <i>Nano</i> particles, respectively with the crystallographic [201] or [001] direction depicted, respectively.	128

B.7 Time-of-flight spectrum of the *Nano* sample. Due to beam time restrictions, a short time of flight pulse of 4 ms was chosen. On such a short pulse, neutrons from the previous pulse reach the sample at the start of the next pulse. This effect is called frame overlap and leads to an artifact in the PDOS (see inset) where the PDOS seemingly increases at high energy transfers. Comparing the PDOS measured on *Nano* LFP with (orange) and without (blue) the frame overlap, one can infer that frame overlap does not affect the shape of the PDOS in the important energy range in this study (50-100 meV). 129

B.8 Time-of-flight spectra of the LiFePO_4 samples measured in this study. As mentioned above, all samples have a short pulse, leading to significant frame overlap. 130

B.9 Phonon density of states spectra of a) *Nano* LiFePO_4 and b) *Nano* FePO_4 as a function of selected scattering vectors Q . The influence of paramagnetic scattering can be significantly reduced by analyzing a restricted Q range above 3 \AA^{-1} (orange). 130

B.10 The experimentally-measured phonon density of states for a) LiFePO_4 (LFP) and b) delithiated LFP (i.e., FePO_4) samples of different sizes. The shading around the points indicates the error of the measurement. The dashed lines show the calculated phonon density of states. c) Calculated total and elemental partial phonon density of states of LFP (black) and FePO_4 (gray) from bulk density functional theory simulations. 131

B.11 FTIR spectra in the P-O vibrational range of the *Nano*, *Medium*, and *Large* samples show that the right-most peak is positioned at around 980 cm^{-1} , suggesting the same antisite defect concentration in the three samples. Note, that the Li_3PO_4 impurity in the *Nano* sample leads to a shoulder at 1050 cm^{-1} 132

- B.12 X-ray diffraction spectra of *Large*, *Medium*, and *Nano* LFP. We find that the samples are single phase LiFePO_4 except for the Li_3PO_4 impurity in the *Nano* samples (marked with an asterisk). 133
- B.13 Comparison of phonon density of states of the *Nano* and *Large* samples with the measured phonon density of states of $^7\text{Li}_3\text{PO}_4$. Note the very broad, almost constant, Li_3PO_4 phonon mode in the range of interest of 50-100 meV. . . . 133
- B.14 Rietveld Refinements of the *Large*, *Medium*, and *Nano* LiFePO_4 samples used in this study. For all the three samples the unit cell volume does not change significantly, indicating a similar defect concentration and small strain effects. 134
- B.15 Schemes of the slabs used for the CP2k calculations after their geometrical optimization. a)-c) Full slabs of the pristine LFP slab, the slab with one carbon atom on each side, and the Li deficient slab, respectively. d)-f) Top view of the slab for each of the three cases. g)-i) Bottom view of the slab for each of the three cases. 135
- B.16 Histograms of the a) Fe-O, b) Li-O, and c) P-O bond lengths in the interior of the LFP slabs. Black bars mark the bond lengths obtained from the Rietveld refinement of the *Large* LFP sample. 136
- B.17 Comparison of the interior (dark grey) and the surface bond lengths (light blue) of the slabs for the a) vacuum, b) carbon, and c) lithium deficient surface termination. The distribution of bond lengths broaden and, in the case of Li-O and Fe-O bonds, shift towards smaller energies. . . 137

C.1 a) Contour map of the electrostatic potential in the LiFePO_4 slab parallel to the (001) plane at $c = 7 \text{ \AA}$, which corresponds to the plane where the nudged elastic band (NEB) simulations are carried out (depicted with the arrows here). The atomic core potentials are set constant such that the potential landscape next to the atoms becomes visible. Red areas describe points of lower energy for positively charged particles (such as the anti-muon or the lithium ion). We find a low energy area close at the surface towards which the NEB trajectory is shifted. In addition, we see that within the bulk, the local potentials are not completely symmetric throughout the ion trajectory for the NEB characterization. This could cause the discrepancy between initial and final energy position found in the NEB calculations (b). 143

C.2 a-c) Scanning electron microscopy images of representative particles for the *Large*, *Medium*, and *Nano* sample. d-f) Transmission electron microscopy images of *Large*, *Medium*, and *Nano* sample particles and their coatings. Inset d): Selected area electron diffraction pattern of the *Large* platelet confirming the (010) orientation of the particle. g,h) Platelet diameter and channel length distribution of the *Large*, *Medium* and *Nano* sample. Note that the channel length for the *Nano* sample could only be determined via atomic force microscopy and hence resulted in smaller statistics. 145

- C.3 a-c) Rietveld refinement of the x-ray spectra of each LiFePO_4 sample. We find an unassignable impurity in the *Large* and *Medium* sample that does not appear in the *Nano* sample. Yet, the main phase is crystalline LiFePO_4 . d) Lattice parameters obtained from the Rietveld refinement. The lattice volume of the *Large* and *Medium* are considerably smaller than for the *Nano* sample. This could arise from tensile stress due to the carbon coating or from lithium deficiencies in the *Large* and *Medium* sample. The error of the lattice parameter obtained from Rietveld refinement is less than 0.01 \AA 146
- C.4 a) Mössbauer spectrum of the *Nano* sample. The Fe^{2+} doublet is well visible while the Fe^{3+} doublet does not appear. This suggests a negligible amount of Fe^{3+} impurities. b) FTIR spectra of the P-O vibrations of each LiFePO_4 sample. The spectra overlap well with the theoretical spectra (see [7]). We find a characteristic shift of the antisymmetric P-O bonding mode from the *Large* to the *Nano* sample characteristic for the increase of ethylene glycol as co-solvent. 147
- C.5 Weak transverse field measurements at a-c) 100 K, d-f) 200 K and g-i) 300 K of the samples *Large*, *Medium*, and *Nano*, respectively. 149
- C.6 Longitudinal Field fit of the μ^+ SR spectra at different 100 K, 200 K, and 300 K for the samples a-c) *Large*, d-f) *Medium*, and g-i) *Nano*. 151
- C.7 Comparison of the longitudinal field measurements at 200 K using a-c) one single and d-f) two Gaussian dynamic Kubo-Toyabe function(s) (KT). While the single Gaussian KT fits relatively well for the *Medium* sample (except for high longitudinal fields), the double Gaussian KT provides a better fit for the *Nano* and *Large* samples. 152

C.8 Comparison of the fitted results of the *Large* sample when the field fluctuation rate of the 2nd Kubo-Toyabe function, ν_{KT2} , is a free parameter (a,c,e) or a constant (b,d,f) in the fit. No significant differences between field fluctuation rate (a,b), normalized asymmetries (c,d), and field distribution width (e,f) are visible. For the interpretation of the parameter changes, see **Appendix C.5.3**. 153

C.9 Temperature dependence of the longitudinal field μ^+SR fitting parameters and their standard deviations (marked as coloured area behind the points). a-c) Normalized asymmetries of the platelet samples. d) Field depolarization rate of the fast relaxation process. e-g) Field distribution width of the two Gaussian dynamic Kubo-Toyabe functions KT1 and KT2. h-j) Temperature-dependant field fluctuation rates KT1 and KT2. 157

C.10 a) Mass normalized susceptibility of different samples as a function of temperature. All samples exhibit a very similar behavior at high temperature, except for a shift of the background. This suggests a contribution of a magnetic impurity (such as Fe) which is largest for the *Large* and the *Nano* sample. b) Inverse molar magnetic susceptibility as a function of temperature. We obtain effective magnetic moments of each sample via equation (C.1). . . . 158

C.11 Scanning electron microscopy images of the *Medium* and *Large* sample with the sample studied by Sugiyama *et al.* [181]. As with the other two samples, the particles consist of platelets. The diameter of these particles is relatively polydisperse ranging from well below 100 nm to 1 μm . In average, however, they are larger than the *Medium* particles and substantially smaller than the *Large* platelets. Circled areas in the *Medium* sample that show fragments of diamond shaped secondary particles. 158

- C.12 a) Galvanostatic curves of the first cycle of half cells made from LiFePO_4 samples at a rate of 34 mA/g (corresponding to a $C/5$ rate). All samples exhibit the characteristic plateau at 3.4 V that opens up with increasing particle size due to overpotentials. The *Large* and the *Medium* sample have smaller capacities than the *Nano* sample, likely due to a reduced connectivity to the electrode network and due to Fe-Li antisite defects. b) Impedance curves of the samples with *Medium* and *Nano* shifted by 400Ω or 800Ω for clarity. The Warburg slope of the *Nano* sample is close to a 45° angle from the x axis suggesting a contribution to the ionic diffusion while the *Medium* sample is closer to a blocking state. The *Large* sample seems to have an additional semicircle appearing in the impedance range displayed here which could arise from the reduced adhesion to the current collector compared to the smaller samples. 161
- D.1 Transmission electron microscopy (TEM) images of the different LiFePO_4 particle edges. For the carbon and ZnO coated samples, we observe a 3-5 nm thick coating layer. . 169
- D.2 X-ray diffraction patterns and Rietveld refinement of a) the Pristine LiFePO_4 (LFP) nanoparticles, b) the ZnO coated LFP nanoparticles, and c) the carbon coated LFP particles. d) Lattice constants and Pearson R value obtained from the Rietveld refinement. While the ZnO coated and pristine LFP samples have practically the same lattice constant, the carbon coating has a slightly enhanced lattice volume indicative for a small tensile stress due to Fe-C coordination. All LFP samples have been structurally refined in the Pnma space group with isotropic Debye-Waller factors. No texture refinement was necessary. The background change in the Pristine sample (a) is due to an additional air scattering contribution. 170

D.3 Fourier transform infrared spectroscopy (FTIR) spectra of the P-O bonds. There is no visible difference in the spectra indicating a similar environment around the P-O bonds. Especially the broad peak at $\sim 980\text{ cm}^{-1}$ does not change between the samples, suggesting no difference in the antisite defect concentration [158] 171

D.4 Comparison of a) the derivative analysis of the ultraviolet (UV) spectra of the LiFePO_4 (LFP) nanoparticles samples with b-e) their calculated energy states. All UV spectra show a distinct peak at 4 eV (grey star) that overlaps very well with the literature value for LFP[235] and the DFT simulations (see **Figure D.8**) (grey transition in b-d)). In the carbon-coated sample, no peak is observed before hence suggesting no other transition above 2 eV. In the ZnO coated sample, a second equally strong peak is observed at 3.4 eV (red star) fitting very well to the reported values of the ZnO band gap[129] and with the electronic structure calculations (see **Figure D.10**) of the ZnO layer away from the slab (red transition in e)). The pristine sample has a broad additional peak at 3.5 eV (blue star) that might arise from surface states (blue transition in d)). Both ZnO and pristine show two transitions between 2 and 3 eV that likely arise either from defect states or impurities (note the grey color of the powder samples). Note, that the transitions marked in b-e) are not the exact band gap values reported in **Figures D.8-D.10** but the transitions found in the UV spectra. 172

D.5 Comparison of the valence band energies measured by x-ray photoemission spectroscopy (XPS) of the coated LiFePO_4 (LFP) samples with the calculated partial electronic density of states. In all samples, the contributions of the elements are stacked on top of each other to compare the overall shape of the XPS curve. A high overlap between measured and calculated energy density of states is found for all samples. Particularly in the binding energy range between 0 to 20 eV, the XPS peak fine structure is well characterized (see triple peak in a) and b), where the additional Zn states cause a peak at 10 eV to rise above the first peak at ~ 5 eV). Note that 0 eV is not well defined in XPS. As a result, all calculated energy levels have been shifted to fit the first XPS peaks at 2 eV. Furthermore, the peak intensity between DFT simulation and measurement can differ due to the x-ray scattering cross section and the normalization of the smoothed, calculated electron density of states. 173

D.6 Antimuon spin polarization of a-c) the pristine and d-f) the ZnO coated LiFePO_4 (LFP) nanoparticle samples at different longitudinal fields and different temperatures. Except at 150 K where the zero field (0 G) polarization is slightly overestimated after $8 \mu\text{s}$ (a,d), a very good agreement between experiment and fit is found. g-h) Antimuon spin polarization curves of the carbon coated LFP samples. Due to a magnetic impurity the shape of the polarization drops faster and an additional Kubo-Toyabe term is necessary. For a detailed discussion about the fitting approach of the data, see **Part 4**. 176

D.7 Resulting parameters obtained from the muon spin spectroscopy fits with the temperature dependence of a) Field fluctuation rate (i.e. Li ion hopping rate [179]), b) the field distribution width, and c) the normalized asymmetry. The parameters obtained for the carbon coating are based on fits described in **Part 4** 178

D.8 a) Magnetic susceptibility of the LiFePO_4 nanoparticle samples. While the pristine LiFePO_4 particles behave as reported in other works [181, 235], the ZnO and carbon coated LiFePO_4 samples have a strongly enhanced magnetic susceptibility, suggesting a magnetic impurity. In the case of the carbon termination, this magnetic impurity is temperature-independent throughout the measuring range. In the case of the ZnO coating, the susceptibility drops significantly from a high level similar to the C coating towards the susceptibility of the pristine sample as it would be characteristic for a weakly magnetic impurity. b) The inverse susceptibility whose slope is a measure of the number of unpaired electrons in the material. Above the antiferromagnetic transition at 50 K, both the carbon coated and pristine LiFePO_4 samples have a constant slope that is characteristic for paramagnetic materials. The inverse susceptibility of the ZnO terminated sample, however, is curved which would suggest a magnetic. Note that the slope of the ZnO coating is converging towards the slope of the pristine sample further confirming this hypothesis. 179

D.9 Image of the pristine LiFePO_4 slab and the defined layers for the electronic characterization. We split the slab into five regions: two surface regions and three inner regions. For all of those regions we obtain an energy level diagram. By summing all of the energy states of the inner regions, we obtain a partial electronic density of states (PEDOS) of the bulk of the slab. Note that, for reasons of clarity, contributions to the energy levels are normalized to one. No such normalization is performed in the PEDOS calculation. Instead, the PEDOS is smoothened over 0.15 eV, leading to a decrease of the band gap compared to the energy levels. 180

- D.10 Image of the C coated slab and the defined layers for the electronic characterization. We split the slab into five regions: two surface regions and three inner regions. For all of those regions we obtain an energy level diagram. By summing all of the energy states of the inner region, we obtain a partial electronic density of states (PEDOS) of the bulk of the slab. Note that, for reasons of clarity, contributions to the energy levels are normalized to one. No such normalization is performed in the PEDOS calculation. 181
- D.11 Schematic drawing of the ZnO coated slab and the defined layers for the electronic characterization. We split the slab into six regions: one LiFePO₄ (LFP) surface region, three inner LFP regions, one region at the LFP-ZnO interface and one pure ZnO region. For all of those regions we obtain an energy level diagram. Note that for reasons of visibility, contributions to the energy levels are normalized to one. Furthermore, the band gap within the LFP slab is constantly reduced with increasing distance from the ZnO coating. We assume that this is due to the electronic dipole induced by the ZnO termination[24]. 182
- D.12 Lithium trajectory during the *ab initio* molecular dynamics simulations at a cryostat temperature of 1000 K a) at the pristine slab surface, b) within the pristine slab c) at the ZnO terminated slab, and d) at carbon terminated slab. During the simulation all atoms were set free to move during the simulation. Following the initial Li position (depicted as large Li atom), Li positions (small yellow points) are updated after every 5 fs. For reasons of clarity, only the trajectory of the lithium atoms is shown. 183
- D.13 a) Li atom Mean squared displacement in a Pinball model, where an *ab initio* molecular dynamics simulation is performed at 1000 K with all atoms except Li fixed to their 0K equilibrium position. b) Density of Li vibrational states obtained in a Pinball model. As found in earlier studies[23, 182], all vibrations occur in an energy range of 10 to 90 meV. 184

- D.14 Atom decomposed mean squared displacement (MSD) at a cryostat temperature of 1000 K of a) the pristine LiFePO_4 within the slab, b) the pristine slab at the surface, c) the carbon coated termination, and d) the ZnO termination. In all situations, the MSD of the host atoms Fe, P, and O are very similar suggesting a correlation between them. c) The same can be found for the MSD of the host atoms and carbon. d) While there is a clear correlation between Zn and the O with the ZnO layer, there is no visible correlation between the LiFePO_4 host atoms and ZnO. . . . 185
- D.15 Comparison of the surface diffusion (i.e., the crystallographic a-c plane) and interface diffusion (i.e., the b axis) contribution to the Li Mean squared displacement (MSD) with fixed host lattice (**Figure D.13**). While there is little change a) within the pristine slab, a small increase of the surface diffusivity is observed at both b) the pristine and c) the ZnO terminated surface. By far the strongest increase in surface diffusivity is found for the d) C coating. In all cases the interface diffusivity remains similar. 186
- D.16 Snapshots of the AIMD runs of a) the ZnO terminated LiFePO_4 (LFP) surface and b) the Carbon terminated LFP surface. a) Looking at the ZnO-LFP interface, only local motion of lithium atoms is observed. Zn atoms, on the other hand, are more dynamic at the interface. Nonetheless, there is no visible correlation between the movements of the Zn atoms and Fe/Li atoms. b) All carbon atoms coordinate with surface iron atoms (see Fe-C bonds). This bonds vibrate slowly forward and backward over the simulated time frame. In parallel, the Li ion atoms diffuse freely away from the surface towards the second layer of LFP. 187

- D.17 *In Operando* x-ray diffraction measurement of the LiFePO_4 (LFP) nanoparticle samples at a cycling rate of 1C. To study the effect of phase separation, we focus on the (010)/(211) peak. Generally, the same trend as at a C/10 rate can be observed throughout all LFP samples. The pristine LFP sample (a) is an exception with a significant portion of the active material is not taking part in the reaction. We hypothesize that this is due to the increased cycling rate. Nonetheless, we still observe the phase separation of LFP during battery charge and a solid solution behaviour during discharge. 188
- D.18 Comparison of operando x-ray diffraction spectra for the different Li_xFePO_4 samples at a state of (dis)charge of 0.5. For the a) pristine and b) C coated LiFePO_4 sample, two peaks are visible during charging, suggesting a phase separation. During discharge, the pristine, the c) ZnO coated and d) ZnO/C coated LiFePO_4 samples show only one peak, indicative of a solid solution. 189
- D.19 a) dQ/dV vs voltage plot of the of the differently coated LiFePO_4 (LFP) samples. We find that the voltage peak that occurs at 3.45 V is significantly broadened in the ZnO/C and ZnO coated LFP samples. b-c) Electrochemical impedance spectra of electrodes containing b) the pristine and ZnO coated and c) carbon and carbon/ZnO coated LFP nanoparticles. The pristine termination and the ZnO coating clearly inhibit the conductivity of the electrodes. In contrast, the C and ZnO/C coated LFP exhibit much smaller resistances with the carbon coating having a slightly smaller impedance. All electrodes contain 10 wt% carbon black and 5 wt% poly(acrylic acid). . . 190

D.20 a-c) EDS STEM images of the ZnO-C coated LiFePO_4 (LFP) nanoparticles. We find that Zn and carbon build a coating surrounding the LFP particles. A comparison of the Fe and Zn signal (a) suggests that the ZnO coating is forming irregular local defects. d) Rietveld refinement of the ZnO-C coated LFP nanoparticles. Using a single LFP phase provides an acceptable fit ($R_w = 4.8\%$). 191

List of Tables

1.1	Summary of the upcoming upgrades of the strongest neutron sources worldwide.	28
1.2	Summary of the upcoming upgrades of the strongest μ^+ SR sources worldwide.	29
2.1	Overview of the specific energy consumption of LFP prepared by different synthetic approaches.	40
2.2	Measured dimensions of the LiFePO_4 (010) platelet particles.	42
2.3	Morphology characteristics obtained from the platelet dimensions of the LiFePO_4 (010) platelet particles.	43
4.1	Summary of obtained activation barriers for the bulk and interface diffusion.	72
A.1	Summary of the hydrothermal conditions.	102
A.2	Mass of precursors needed for LFP synthesis, energy needed for precursor synthesis, and energy needed for LFP synthesis in a hydrothermal and solid state approach.	106
A.3	Values and expressions used in the energy consumption analysis.	107
B.1	Overview of the LFP unit cell parameters and average bond lengths.	136
C.1	Coordinates for the initial and final position of the moving Li ion during the NEB calculations.	142

List of Tables

C.2	Particle Specific Size parameters. The channel length and platelet diameter are measured scanning electron microscopy (SEM) or atomic force microscopy (AFM). The surface atom ratios are calculated based on the procedure reported in section A.9 . The specific surface area is measured with a Brunauer-Emmett-Teller (BET) setup. . . .	144
D.1	Acquisition parameters of the XPS measurements. . . .	166

Bibliography

- [1] 2020 ISIS Annual Review. Technical report.
- [2] Battery Interface Genome - Material Acceleration Platform (BIG-MAP).
- [3] ESS Instruments.
- [4] ILL Annual Report 2019. Technical report.
- [5] J-PARC MLF Annual Report 2019. Technical report.
- [6] Proton Power Upgrade SNS.
- [7] A. Ait Salah, P. Jozwiak, K. Zaghib, J. Garbarczyk, F. Gendron, A. Mauger, and C. M. Julien. FTIR features of lithium-iron phosphates as electrode materials for rechargeable lithium batteries. *Spectrochim Acta A Mol Biomol Spectrosc*, 65(5):1007–1013, 2006.
- [8] J. Alvarado, M. A. Schroeder, M. Zhang, O. Borodin, E. Gobrogge, M. Olguin, M. S. Ding, M. Gobet, S. Greenbaum, Y. S. Meng, and K. Xu. A carbonate-free, sulfone-based electrolyte for high-voltage Li-ion batteries. *Materials Today*, 21(4):341–353, 2018.
- [9] R. Amin, J. Maier, P. Balaya, D. P. Chen, and C. T. Lin. Ionic and electronic transport in single crystalline LiFePO₄ grown by optical floating zone technique. *Solid State Ionics*, 179(27):1683–1687, 2008.
- [10] M. Armand and J. M. Tarascon. Building better batteries. *Nature*, 451:6, 2008.
- [11] T. E. Ashton, J. V. Laveda, D. A. MacLaren, P. J. Baker, A. Porch, M. O. Jones, and S. A. Corr. Muon studies of Li⁺ diffusion in

- LiFePO₄ nanoparticles of different polymorphs. *Journal of Materials Chemistry A*, 2(17):6238–6245, 2014.
- [12] P. Axmann, C. Stinner, M. Wohlfahrt-Mehrens, A. Mauger, F. Gendron, and C. M. Julien. Nonstoichiometric LiFePO₄: Defects and Related Properties. *Chemistry of Materials*, 21(8):1636–1644, 2009.
- [13] R. T. Azuah, L. R. Kneller, Y. Qiu, P. L. W. Tregenna-Piggott, C. M. Brown, J. R. D. Copley, and R. M. Dimeo. DAVE: A Comprehensive Software Suite for the Reduction, Visualization, and Analysis of Low Energy Neutron Spectroscopic Data. *Journal of Research of the National Institute of Standards and Technology*, 114(6):341–358, 2009.
- [14] P. Bai, D. A. Cogswell, and M. Z. Bazant. Suppression of Phase Separation in LiFePO₄ Nanoparticles During Battery Discharge. *Nano Letters*, 11(11):4890–4896, nov 2011.
- [15] S.-M. Bak, Z. Shadik, R. Lin, X. Yu, and X.-Q. Yang. In situ/operando synchrotron-based X-ray techniques for lithium-ion battery research. *NPG Asia Materials*, 10(7):563–580, 2018.
- [16] P. J. Baker, I. Franke, F. L. Pratt, T. Lancaster, D. Prabhakaran, W. Hayes, and S. J. Blundell. Probing magnetic order in LiMPO₄ (M= Ni, Co, Fe) and lithium diffusion in Li_xFePO₄. *Physical Review B*, 84(17):174403, nov 2011.
- [17] A. Banerjee, X. Wang, C. Fang, E. A. Wu, and Y. S. Meng. Interfaces and Interphases in All-Solid-State Batteries with Inorganic Solid Electrolytes. *Chemical Reviews*, jun 2020.
- [18] S. Baroni, S. de Gironcoli, A. Dal Corso, and P. Giannozzi. Phonons and related crystal properties from density-functional perturbation theory. *Reviews of Modern Physics*, 73(2):515–562, 2001.
- [19] M. Z. Bazant. Theory of Chemical Kinetics and Charge Transfer based on Nonequilibrium Thermodynamics. *Accounts of chemical research*, 46(5):17, 2013.

- [20] M. Z. Bazant. Thermodynamic stability of driven open systems and control of phase separation by electro-autocatalysis. *Faraday Discussions*, 199(0):423–463, 2017.
- [21] P. Benedek, O. K. Forslund, E. Nocerino, N. Yazdani, N. Matsubara, Y. Sassa, F. Jurányi, M. Medarde, M. Telling, M. Månsson, and V. Wood. Quantifying Diffusion through Interfaces of Lithium-Ion Battery Active Materials. *ACS Applied Materials & Interfaces*, 12(14):16243–16249, apr 2020.
- [22] P. Benedek, N. Wenzler, M. Yarema, and V. C. Wood. Low temperature hydrothermal synthesis of battery grade lithium iron phosphate. *RSC Advances*, 7(29):17763–17767, 2017.
- [23] P. Benedek, N. Yazdani, H. Chen, N. Wenzler, F. Juranyi, M. Månsson, M. S. Islam, and V. C. Wood. Surface phonons of lithium ion battery active materials. *Sustainable Energy & Fuels*, 3(2):508–513, 2019.
- [24] L. Bengtsson. Dipole correction for surface supercell calculations. *Physical Review B*, 59(19):12301–12304, may 1999.
- [25] P. Bleith, M. Valla, P. Novák, and C. Villevieille. Elucidation of the reaction mechanism upon lithiation and delithiation of $\text{Cu}_{0.5}\text{TiOPO}_4$. *Journal of Materials Chemistry A*, 2(31):12513–12518, 2014.
- [26] P. E. Blöchl, O. Jepsen, and O. K. Andersen. Improved tetrahedron method for Brillouin-zone integrations. *Physical Review B*, 49(23):16223–16233, 1994.
- [27] M. G. Boebinger, D. Yeh, M. Xu, B. C. Miles, B. Wang, M. Papyriakou, J. A. Lewis, N. P. Kondekar, F. J. Q. Cortes, S. Hwang, X. Sang, D. Su, R. R. Unocic, S. Xia, T. Zhu, and M. T. McDowell. Avoiding Fracture in a Conversion Battery Material through Reaction with Larger Ions. *Joule*, 2(9):1783–1799, 2018.

- [28] O. J. Borkiewicz, K. M. Wiaderek, P. J. Chupas, and K. W. Chapman. Best Practices for Operando Battery Experiments: Influences of X-ray Experiment Design on Observed Electrochemical Reactivity. *The Journal of Physical Chemistry Letters*, 6(11):2081–2085, jun 2015.
- [29] L. Boulet-Roblin, P. Borel, D. Sheptyakov, C. Tessier, P. Novák, and C. Villeveille. Operando Neutron Powder Diffraction Using Cylindrical Cell Design: The Case of $\text{LiNi}_{0.5}\text{Mn}_{1.5}\text{O}_4$ vs Graphite. *The Journal of Physical Chemistry C*, 120(31):17268–17273, aug 2016.
- [30] T. L. Burnett, R. Kelley, B. Winiarski, L. Contreras, M. Daly, A. Gholinia, M. G. Burke, and P. J. Withers. Large volume serial section tomography by Xe Plasma FIB dual beam microscopy. *Ultramicroscopy*, 161:119–129, 2016.
- [31] T. L. Burnett and P. J. Withers. Completing the picture through correlative characterization. *Nature Materials*, 2019.
- [32] G. Bussi, D. Donadio, and M. Parrinello. Canonical sampling through velocity rescaling. *The Journal of Chemical Physics*, 126(1):14101, 2007.
- [33] Z. Cabán-Huertas, O. Ayyad, D. P. Dubal, and P. Gómez-Romero. Aqueous synthesis of LiFePO_4 with Fractal Granularity. *Scientific Reports*, 6:27024, 2016.
- [34] J. Cabana, J. Shirakawa, G. Chen, T. J. Richardson, and C. P. Grey. MAS NMR Study of the Metastable Solid Solutions Found in the $\text{LiFePO}_4/\text{FePO}_4$ System. *Chemistry of Materials*, 22(3):1249–1262, feb 2010.
- [35] X. Cao, X. Ren, L. Zou, M. H. Engelhard, W. Huang, H. Wang, B. E. Matthews, H. Lee, C. Niu, B. W. Arey, Y. Cui, C. Wang, J. Xiao, J. Liu, W. Xu, and J.-G. Zhang. Monolithic solid–electrolyte interphases formed in fluorinated orthoformate-based electrolytes minimize Li depletion and pulverization. *Nature Energy*, 4(9):796–805, 2019.

- [36] H. Chen, P. Benedek, K.-J. Fisher, V. Wood, and Y. Cui. Self-assembled materials for electrochemical energy storage. *MRS Bulletin*, 45(10):815–822, 2020.
- [37] J. Chen, M. J. Vacchio, S. Wang, N. Chernova, P. Y. Zavalij, and M. S. Whittingham. The hydrothermal synthesis and characterization of olivines and related compounds for electrochemical applications. *Solid State Ionics*, 178(31-32):1676–1693, 2008.
- [38] L. Chen, X. Fan, E. Hu, X. Ji, J. Chen, S. Hou, T. Deng, J. Li, D. Su, X. Yang, and C. Wang. Achieving High Energy Density through Increasing the Output Voltage: A Highly Reversible 5.3 V Battery. *Chem*, 5(4):896–912, 2019.
- [39] J. Cheng, E. Sivonxay, and K. A. Persson. Evaluation of Amorphous Oxide Coatings for High-Voltage Li-Ion Battery Applications Using a First-Principles Framework. *ACS Applied Materials & Interfaces*, 12(31):35748–35756, aug 2020.
- [40] S.-Y. Chung, S.-Y. Choi, T. Yamamoto, and Y. Ikuhara. Atomic-Scale Visualization of Antisite Defects in LiFePO₄. *Physical Review Letters*, 100(12):125502, mar 2008.
- [41] S.-Y. Chung, Y.-M. Kim, and S.-Y. Choi. Direct Physical Imaging and Chemical Probing of LiFePO₄ for Lithium-Ion Batteries. *Advanced Functional Materials*, 20(24):4219–4232, 2010.
- [42] M. A. Citrin, H. Yang, S. K. Nieh, J. Berry, W. Gao, X. Pan, D. J. Srolovitz, and J. R. Greer. From ion to atom to dendrite: Formation and nanomechanical behavior of electrodeposited lithium. *MRS Bulletin*, pages 1–14, 2020.
- [43] D. A. Cogswell and M. Z. Bazant. Coherency Strain and the Kinetics of Phase Separation in LiFePO₄ Nanoparticles. *ACS Nano*, 6(3):2215–2225, 2012.
- [44] F. J. Q. Cortes, M. G. Boebinger, M. Xu, A. Ulvestad, and M. T. McDowell. Operando Synchrotron Measurement of Strain Evolution in Individual Alloying Anode Particles within Lithium Batteries. *ACS Energy Letters*, 3(2):349–355, feb 2018.

- [45] G. K. P. Dathar, D. Sheppard, K. J. Stevenson, and G. Henkelman. Calculations of Li-Ion Diffusion in Olivine Phosphates. *Chemistry of Materials*, 23(17):4032–4037, 2011.
- [46] R. Dedryvère, M. Maccario, L. Croguennec, F. Le Cras, C. Delmas, and D. Gonbeau. X-Ray Photoelectron Spectroscopy Investigations of Carbon-Coated Li_xFePO_4 Materials. *Chemistry of Materials*, 20(22):7164–7170, nov 2008.
- [47] M. H. Dehn, J. K. Shenton, D. J. Arseneau, W. A. MacFarlane, G. D. Morris, A. Maigné, N. A. Spaldin, and R. F. Kiefl. Local Electronic Structure and Dynamics of Muon-Polaron Complexes in Fe_2O_3 . *Physical Review Letters*, 126(3):37202, jan 2021.
- [48] M. H. Dehn, J. K. Shenton, S. Holenstein, Q. N. Meier, D. J. Arseneau, D. L. Cortie, B. Hitti, A. C. Y. Fang, W. A. MacFarlane, R. M. L. McFadden, G. D. Morris, Z. Salman, H. Luetkens, N. A. Spaldin, M. Fechner, and R. F. Kiefl. Observation of a Charge-Neutral Muon-Polaron Complex in Antiferromagnetic Cr_2O_3 . *Physical Review X*, 10(1):11036, feb 2020.
- [49] M. M. Doeff, Y. Hu, F. McLarnon, and R. Kostecki. Effect of Surface Carbon Structure on the Electrochemical Performance of LiFePO_4 . *Electrochemical and Solid-State Letters*, 6(10):A207, 2003.
- [50] K. Dokko, S. Koizumi, H. Nakano, and K. Kanamura. Particle morphology, crystal orientation, and electrochemical reactivity of LiFePO_4 synthesized by the hydrothermal method at 443 K. *Journal of Materials Chemistry*, 17(45):4803, 2007.
- [51] J. B. Dunn, L. Gaines, J. C. Kelly, C. James, and K. G. Gallagher. The significance of Li-ion batteries in electric vehicle life-cycle energy and emissions and recycling’s role in its reduction. *Energy & Environmental Science*, 8(1):158–168, 2015.
- [52] A. Dunst, V. Epp, I. Hanzu, S. A. Freunberger, and M. Wilkening. Short-range Li diffusion vs. long-range ionic conduction in nanocrystalline lithium peroxide Li_2O_2 —the discharge product in

- lithium-air batteries. *Energy & Environmental Science*, 7(8):2739–2752, 2014.
- [53] M. Ebner, D.-W. Chung, R. E. García, and V. Wood. Tortuosity Anisotropy in Lithium-Ion Battery Electrodes. *Advanced Energy Materials*, 4(5):1301278, apr 2014.
- [54] M. Ebner, F. Marone, M. Stampanoni, and V. Wood. Visualization and quantification of electrochemical and mechanical degradation in Li ion batteries. *Science*, 342(6159):716–720, 2013.
- [55] B. Ellis, W. H. Kan, W. R. M. Makahnouk, and L. F. Nazar. Synthesis of nanocrystals and morphology control of hydrothermally prepared LiFePO₄. *Journal of Materials Chemistry*, 17(30):3248, 2007.
- [56] B. Ellis, L. K. Perry, D. H. Ryan, and L. F. Nazar. Small Polaron Hopping in Li_xFePO₄ Solid Solutions: Coupled Lithium-Ion and Electron Mobility. *Journal of the American Chemical Society*, 128(35):11416–11422, 2006.
- [57] A. K. C. Estandarte, J. Diao, A. V. Llewellyn, A. Jnawali, T. M. M. Heenan, S. R. Daemi, J. J. Bailey, S. Cipiccia, D. Batey, X. Shi, C. Rau, D. J. L. Brett, R. Jervis, I. K. Robinson, and P. R. Shearing. Operando Bragg Coherent Diffraction Imaging of LiNi_{0.8}Mn_{0.1}Co_{0.1}O₂ Primary Particles within Commercially Printed NMC811 Electrode Sheets. *ACS Nano*, 15(1):1321–1330, jan 2021.
- [58] V. Etacheri, R. Marom, R. Elazari, G. Salitra, and D. Aurbach. Challenges in the development of advanced Li-ion batteries: a review. *Energy & Environmental Science*, 4(9):3243, 2011.
- [59] J. W. Fergus. Recent developments in cathode materials for lithium ion batteries. *Journal of Power Sources*, 195(4):939–954, 2010.
- [60] D. P. Finegan, E. Darcy, M. Keyser, B. Tjaden, T. M. M. Heenan, R. Jervis, J. J. Bailey, N. T. Vo, O. V. Magdysyuk, M. Drakopoulos, M. Di Michiel, A. Rack, G. Hinds, D. J. L. Brett, and P. R.

- Shearing. Identifying the Cause of Rupture of Li-Ion Batteries during Thermal Runaway. *Advanced Science*, 5(1):1700369, jan 2018.
- [61] C. A. J. Fisher and M. S. Islam. Surface structures and crystal morphologies of LiFePO₄: relevance to electrochemical behaviour. *Journal of Materials Chemistry*, 18(11):1209, 2008.
- [62] D. Fraggedakis, M. McEldrew, R. B. Smith, Y. Krishnan, Y. Zhang, P. Bai, W. C. Chueh, Y. Shao-Horn, and M. Z. Bazant. Theory of coupled ion-electron transfer kinetics. *Electrochimica Acta*, 367:137432, 2021.
- [63] M. Gaberscek, J. Moskon, B. Erjavec, R. Dominko, and J. Jamnik. The Importance of Interphase Contacts in Li Ion Electrodes: The Meaning of the High-Frequency Impedance Arc. *Electrochemical and Solid-State Letters*, 11(10):A170–A174, 2008.
- [64] P. Goel, M. K. Gupta, R. Mittal, S. Rols, S. J. Patwe, S. N. Achary, A. K. Tyagi, and S. L. Chaplot. Phonons, lithium diffusion and thermodynamics of LiMPO₄ (M = Mn, Fe). *Journal of Materials Chemistry A*, 2(35):14729–14738, 2014.
- [65] W. Goldammer, W. Ludwig, W. Zierau, and C. Falter. Surface phonons and reconstruction of a silicon surface. *Surface Science*, 141(1):139–157, 1984.
- [66] E. Gorham-Bergeron and D. Emin. Phonon-assisted hopping due to interaction with both acoustical and optical phonons. *Physical Review B*, 15(8):3667–3680, 1977.
- [67] C. P. Grey and J. M. Tarascon. Sustainability and in situ monitoring in battery development. *Nature Materials*, 16(1):45–56, jan 2017.
- [68] D. S. Hall, J. Self, and J. R. Dahn. Dielectric Constants for Quantum Chemistry and Li-Ion Batteries: Solvent Blends of Ethylene Carbonate and Ethyl Methyl Carbonate. *The Journal of Physical Chemistry C*, 119(39):22322–22330, oct 2015.

- [69] J. E. Harlow, X. Ma, J. Li, E. Logan, Y. Liu, N. Zhang, L. Ma, S. L. Glazier, M. M. E. Cormier, M. Genovese, S. Buteau, A. Cameron, J. E. Stark, and J. R. Dahn. A Wide Range of Testing Results on an Excellent Lithium-Ion Cell Chemistry to be used as Benchmarks for New Battery Technologies. *Journal of The Electrochemical Society*, 166(13):A3031–A3044, jan 2019.
- [70] C. Hartwigsen, S. Goedecker, and J. Hutter. Relativistic separable dual-space Gaussian pseudopotentials from H to Rn. *Physical Review B*, 58(7):3641–3662, 1998.
- [71] T. M. M. Heenan, C. Tan, J. Hack, D. J. L. Brett, and P. R. Shearing. Developments in X-ray tomography characterization for electrochemical devices. *Materials Today*, 2019.
- [72] G. Henkelman and H. Jónsson. Improved tangent estimate in the nudged elastic band method for finding minimum energy paths and saddle points. *The Journal of Chemical Physics*, 113(22):9978–9985, 2000.
- [73] C. R. Hernandez, A. Etienne, T. Douillard, D. Mazouzi, Z. Karkar, E. Maire, D. Guyomard, B. Lestriez, and L. Roué. A Facile and Very Effective Method to Enhance the Mechanical Strength and the Cyclability of Si-Based Electrodes for Li-Ion Batteries. *Advanced Energy Materials*, 8(6):1701787, feb 2018.
- [74] M. Hess, T. Sasaki, C. Villevieille, and P. Novák. Combined operando X-ray diffraction–electrochemical impedance spectroscopy detecting solid solution reactions of LiFePO₄ in batteries. 6:8169, 2015.
- [75] B. Horstmann, B. Gallant, R. Mitchell, W. G. Bessler, Y. Shao-Horn, and M. Z. Bazant. Rate-Dependent Morphology of Li₂O₂ Growth in Li–O₂ Batteries. *The Journal of Physical Chemistry Letters*, 4(24):4217–4222, dec 2013.
- [76] X. Hua, A. S. Eggeman, E. Castillo-Martínez, R. Robert, H. S. Geddes, Z. Lu, C. J. Pickard, W. Meng, K. M. Wiaderek, N. Pereira, G. G. Amatucci, P. A. Midgley, K. W. Chapman,

- U. Steiner, A. L. Goodwin, and C. P. Grey. Revisiting metal fluorides as lithium-ion battery cathodes. *Nature Materials*, 2021.
- [77] H. Huang, S.-C. Yin, and L. F. Nazar. Approaching Theoretical Capacity of LiFePO₄ at Room Temperature at High Rates. *Electrochemical and Solid-State Letters*, 4(10):A170, 2001.
- [78] W. Huang, P. M. Attia, H. Wang, S. E. Renfrew, N. Jin, S. Das, Z. Zhang, D. T. Boyle, Y. Li, M. Z. Bazant, B. D. McCloskey, W. C. Chueh, and Y. Cui. Evolution of the Solid–Electrolyte Interphase on Carbonaceous Anodes Visualized by Atomic-Resolution Cryogenic Electron Microscopy. *Nano Letters*, 19(8):5140–5148, aug 2019.
- [79] J. Hutter, M. Iannuzzi, F. Schiffmann, and J. VandeVondele. cp2k: atomistic simulations of condensed matter systems. *Wiley Interdisciplinary Reviews: Computational Molecular Science*, 4(1):15–25, 2013.
- [80] M. S. Islam, D. J. Driscoll, C. A. J. Fisher, and P. R. Slater. Atomic-Scale Investigation of Defects, Dopants, and Lithium Transport in the LiFePO₄ Olivine-Type Battery Material. *Chemistry of Materials*, 17(20):5085–5092, 2005.
- [81] M. S. Islam and C. A. J. Fisher. Lithium and sodium battery cathode materials: computational insights into voltage, diffusion and nanostructural properties. *Chem. Soc. Rev.*, 43(1):185–204, 2014.
- [82] C. J. Jafta, X.-G. Sun, H. Lyu, H. Chen, B. P. Thapaliya, W. T. Heller, M. J. Cuneo, R. T. Mayes, M. P. Paranthaman, S. Dai, and C. A. Bridges. Insight into the Solid Electrolyte Interphase Formation in Bis(fluorosulfonyl)Imide Based Ionic Liquid Electrolytes. *Advanced Functional Materials*, n/a(n/a):2008708, feb 2021.
- [83] C. J. Jafta, X.-G. Sun, G. M. Veith, G. V. Jensen, S. M. Mahurin, M. P. Paranthaman, S. Dai, and C. A. Bridges. Probing microstructure and electrolyte concentration dependent cell chem-

- istry via operando small angle neutron scattering. *Energy & Environmental Science*, 12(6):1866–1877, 2019.
- [84] Y. Jin, N.-J. H. Kneusels, L. E. Marbella, E. Castillo-Martínez, P. C. M. M. Magusin, R. S. Weatherup, E. Jónsson, T. Liu, S. Paul, and C. P. Grey. Understanding Fluoroethylene Carbonate and Vinylene Carbonate Based Electrolytes for Si Anodes in Lithium Ion Batteries with NMR Spectroscopy. *Journal of the American Chemical Society*, 140(31):9854–9867, aug 2018.
- [85] I. D. Johnson, T. E. Ashton, E. Blagovidova, G. J. Smales, M. Lübke, P. J. Baker, S. A. Corr, and J. A. Darr. Mechanistic insights of Li⁺ diffusion within doped LiFePO₄ from Muon Spectroscopy. *Scientific Reports*, 8(1):4114, 2018.
- [86] M. C. Johnson, I. Palou-Rivera, and E. D. Frank. Energy consumption during the manufacture of nutrients for algae cultivation. *Algal Research*, 2(4):426–436, oct 2013.
- [87] C. M. Julien, A. Mauger, and K. Zaghib. Surface effects on electrochemical properties of nano-sized LiFePO₄. *Journal of Materials Chemistry*, 21(27):9955–9968, 2011.
- [88] L. Kahle, A. Marcolongo, and N. Marzari. Modeling lithium-ion solid-state electrolytes with a pinball model. *Physical Review Materials*, 2(6):65405, jun 2018.
- [89] S. V. Kalinin, O. Dyck, N. Balke, S. Neumayer, W.-Y. Tsai, R. Vasudevan, D. Lingerfelt, M. Ahmadi, M. Ziatdinov, M. T. McDowell, and E. Strelcov. Toward Electrochemical Studies on the Nanometer and Atomic Scales: Progress, Challenges, and Opportunities. *ACS Nano*, aug 2019.
- [90] K. Kamazawa, H. Nozaki, M. Harada, K. Mukai, Y. Ikedo, K. Iida, T. J. Sato, Y. Qiu, M. Tyagi, and J. Sugiyama. Interrelationship between Li⁺ diffusion, charge, and magnetism in 7-LiMn₂O₄ and 7-Li_{1.1}Mn_{1.9}O₄ spinels: Elastic, inelastic, and quasielastic neutron scattering. *Physical Review B*, 83(9):94401, 2011.

- [91] B. Kang and G. Ceder. Battery materials for ultrafast charging and discharging. *Nature*, 458(7235):190–193, 2009.
- [92] G. Kresse and J. Furthmüller. Efficient iterative schemes for ab initio total-energy calculations using a plane-wave basis set. *Physical Review B*, 54(16):11169–11186, 1996.
- [93] P. T. Kristiansen, M. Dahbi, T. Gustafsson, K. Edström, D. Newby, K. E. Smith, and L.-C. Duda. X-ray absorption spectroscopy and resonant inelastic scattering study of the first lithiation cycle of the Li-ion battery cathode $\text{Li}_{2-x}\text{MnSiO}_4$. *Physical Chemistry Chemical Physics*, 16(8):3846–3852, 2014.
- [94] R. Kubo. A stochastic theory of spin relaxation. *Hyperfine Interactions*, 8(4):731–738, 1981.
- [95] S. G. Kwon and T. Hyeon. Formation mechanisms of uniform nanocrystals via hot-injection and heat-up methods. *Small*, 7(19):2685–2702, 2011.
- [96] M. F. Lagadec, R. Zahn, S. Müller, and V. Wood. Topological and network analysis of lithium ion battery components: the importance of pore space connectivity for cell operation. *Energy & Environmental Science*, 11(11):3194–3200, 2018.
- [97] M. F. Lagadec, R. Zahn, and V. Wood. Characterization and performance evaluation of lithium-ion battery separators. *Nature Energy*, 4(1):16–25, 2019.
- [98] T. Lancaster, F. Xiao, B. M. Huddart, R. C. Williams, F. L. Pratt, S. J. Blundell, S. J. Clark, R. Scheuermann, T. Goko, S. Ward, J. L. Manson, C. Rüegg, and K. W. Krämer. Quantum magnetism in molecular spin ladders probed with muon-spin spectroscopy. *New Journal of Physics*, 20(10):103002, 2018.
- [99] J. Landesfeind, M. Ebner, A. Eldiven, V. Wood, and H. A. Gasteiger. Tortuosity of Battery Electrodes: Validation of Impedance-Derived Values and Critical Comparison with 3D Tomography. *Journal of The Electrochemical Society*, 165(3):A469–A476, jan 2018.

- [100] B. León, C. P. Vicente, J. L. Tirado, P. Biensan, and C. Tessier. Optimized Chemical Stability and Electrochemical Performance of LiFePO₄ Composite Materials Obtained by ZnO Coating. *Journal of The Electrochemical Society*, 155(3):A211, 2008.
- [101] M. Leskes, G. Kim, T. Liu, A. L. Michan, F. Aussenac, P. Dorffer, S. Paul, and C. P. Grey. Surface-Sensitive NMR Detection of the Solid Electrolyte Interphase Layer on Reduced Graphene Oxide. *The Journal of Physical Chemistry Letters*, 8(5):1078–1085, mar 2017.
- [102] J. A. Lewis, F. J. Q. Cortes, M. G. Boebinger, J. Tippens, T. S. Marchese, N. Kondekar, X. Liu, M. Chi, and M. T. McDowell. Interphase Morphology between a Solid-State Electrolyte and Lithium Controls Cell Failure. *ACS Energy Letters*, 4(2):591–599, feb 2019.
- [103] X. Li and N. A. Benedek. Enhancement of Ionic Transport in Complex Oxides through Soft Lattice Modes and Epitaxial Strain. *Chemistry of Materials*, 27(7):2647–2652, apr 2015.
- [104] Y. Li. A review of recent research on nonequilibrium solid solution behavior in LiXFePO₄. *Solid State Ionics*, 323:142–150, 2018.
- [105] Y. Li, H. Chen, K. Lim, H. D. Deng, J. Lim, D. Fraggadakis, P. M. Attia, S. C. Lee, N. Jin, J. Moškon, Z. Guan, W. E. Gent, J. Hong, Y.-S. Yu, M. Gaberšček, M. S. Islam, M. Z. Bazant, and W. C. Chueh. Fluid-enhanced surface diffusion controls intraparticle phase transformations. *Nature Materials*, 17(10):915–922, 2018.
- [106] Y. Li, F. El Gabaly, T. R. Ferguson, R. B. Smith, N. C. Bartelt, J. D. Sugar, K. R. Fenton, D. A. Cogswell, A. L. D. Kilcoyne, T. Tyliczszak, M. Z. Bazant, and W. C. Chueh. Current-induced transition from particle-by-particle to concurrent intercalation in phase-separating battery electrodes. *Nature Materials*, 13(12):1149–1156, dec 2014.

- [107] Y. Li, J. N. Weker, W. E. Gent, D. N. Mueller, J. Lim, D. A. Cogswell, T. Tylizszczak, and W. C. Chueh. Dichotomy in the Lithiation Pathway of Ellipsoidal and Platelet LiFePO₄ Particles Revealed through Nanoscale Operando State-of-Charge Imaging. *Advanced Functional Materials*, 25(24):3677–3687, jun 2015.
- [108] G. Liang, C. Didier, Z. Guo, W. K. Pang, and V. K. Peterson. Understanding Rechargeable Battery Function Using In Operando Neutron Powder Diffraction. *Advanced Materials*, 32(18):1904528, may 2020.
- [109] J. Lim, Y. Li, D. H. Alsem, H. So, S. C. Lee, P. Bai, D. A. Cogswell, X. Liu, N. Jin, Y.-s. Yu, N. J. Salmon, D. A. Shapiro, M. Z. Bazant, T. Tylizszczak, and W. C. Chueh. Origin and hysteresis of lithium compositional spatiodynamics within battery primary particles. *Science*, 353(6299):566–571, aug 2016.
- [110] G. Lippert, J. Hutter, and M. Parinello. A hybrid Gaussian and plane wave density functional scheme. *Molecular Physics*, 92(3):477–488, 1997.
- [111] C.-T. Liu and W. T. Lindsay. Vapor pressure of deuterated water from 106 to 300.deg. *Journal of Chemical & Engineering Data*, 15(4):510–513, oct 1970.
- [112] D. X. Liu, L. R. Cao, and A. C. Co. Demonstrating the Feasibility of Al as Anode Current Collector in Li-Ion Batteries via In Situ Neutron Depth Profiling. *Chemistry of Materials*, 28(2):556–563, jan 2016.
- [113] H. Liu, M.-J. Choe, R. A. Enrique, B. Orvañanos, L. Zhou, T. Liu, K. Thornton, and C. P. Grey. Effects of Antisite Defects on Li Diffusion in LiFePO₄ Revealed by Li Isotope Exchange. *The Journal of Physical Chemistry C*, 121(22):12025–12036, jun 2017.
- [114] H. Liu, F. C. Strobridge, O. J. Borkiewicz, K. M. Wiaderek, K. W. Chapman, P. J. Chupas, and C. P. Grey. Capturing metastable structures during high-rate cycling of LiFePO₄ nanoparticle electrodes. *Science*, 344(6191):1252817, 2014.

- [115] J. Liu, Z. Bao, Y. Cui, E. J. Dufek, J. B. Goodenough, P. Khalifah, Q. Li, B. Y. Liaw, P. Liu, A. Manthiram, Y. S. Meng, V. R. Subramanian, M. F. Toney, V. V. Viswanathan, M. S. Whittingham, J. Xiao, W. Xu, J. Yang, X.-Q. Yang, and J.-G. Zhang. Pathways for practical high-energy long-cycling lithium metal batteries. *Nature Energy*, 4(3):180–186, 2019.
- [116] X. H. Liu, H. Zheng, L. Zhong, S. Huang, K. Karki, L. Q. Zhang, Y. Liu, A. Kushima, W. T. Liang, J. W. Wang, J.-H. Cho, E. Epstein, S. A. Dayeh, S. T. Picraux, T. Zhu, J. Li, J. P. Sullivan, J. Cumings, C. Wang, S. X. Mao, Z. Z. Ye, S. Zhang, and J. Y. Huang. Anisotropic Swelling and Fracture of Silicon Nanowires during Lithiation. *Nano Lett*, 11(8):3312–3318, 2011.
- [117] Y. Liu, Y. Zhu, and Y. Cui. Challenges and opportunities towards fast-charging battery materials. *Nature Energy*, 4(7):540–550, jul 2019.
- [118] J. Lu, T. Wu, and K. Amine. State-of-the-art characterization techniques for advanced lithium-ion batteries. *Nature Energy*, 2:17011, mar 2017.
- [119] Z. Lu, H. Chen, R. Robert, B. Y. X. Zhu, J. Deng, L. Wu, C. Y. Chung, and C. P. Grey. Citric Acid- and Ammonium-Mediated Morphological Transformations of Olivine LiFePO₄ Particles. *Chemistry of Materials*, 23(11):2848–2859, 2011.
- [120] L. Lutterotti, D. Chateigner, S. Ferrari, and J. Ricote. Texture, residual stress and structural analysis of thin films using a combined X-ray analysis. *Thin Solid Films*, 450(1):34–41, 2004.
- [121] H. Ma, X. Xiong, P. Gao, X. Li, Y. Yan, A. A. Volinsky, and Y. Su. Eigenstress model for electrochemistry of solid surfaces. *Scientific Reports*, 6:26897, 2016.
- [122] W. A. MacFarlane. Implanted-ion β NMR: A new probe for nanoscience. *Solid State Nuclear Magnetic Resonance*, 68-69:1–12, 2015.

- [123] G. Majeau-Bettez, T. R. Hawkins, and A. H. Strømman. Life Cycle Environmental Assessment of Lithium-Ion and Nickel Metal Hydride Batteries for Plug-In Hybrid and Battery Electric Vehicles. *Environmental Science & Technology*, 45(10):4548–4554, 2011.
- [124] R. Malik, A. Abdellahi, and G. Ceder. A Critical Review of the Li Insertion Mechanisms in LiFePO₄ Electrodes. *Journal of The Electrochemical Society*, 160(5):A3179–A3197, 2013.
- [125] R. Malik, D. Burch, M. Bazant, and G. Ceder. Particle Size Dependence of the Ionic Diffusivity. *Nano Letters*, 10(10):4123–4127, oct 2010.
- [126] R. Malik, F. Zhou, and G. Ceder. Kinetics of non-equilibrium lithium incorporation in LiFePO₄. *Nature Materials*, 10(8):587–590, aug 2011.
- [127] M. Månsson and J. Sugiyama. Muon-spin relaxation study on Li- and Na-diffusion in solids. *Physica Scripta*, 88(6):68509, 2013.
- [128] N. M. Marković, B. N. Grgur, and P. N. Ross. Temperature-Dependent Hydrogen Electrochemistry on Platinum Low-Index Single-Crystal Surfaces in Acid Solutions. *The Journal of Physical Chemistry B*, 101(27):5405–5413, 1997.
- [129] R. E. Marotti, P. Giorgi, G. Machado, and E. A. Dalchiele. Crystallite size dependence of band gap energy for electrodeposited ZnO grown at different temperatures. *Solar Energy Materials and Solar Cells*, 90(15):2356–2361, 2006.
- [130] C. Masquelier and L. Croguennec. Polyanionic (Phosphates, Silicates, Sulfates) Frameworks as Electrode Materials for Rechargeable Li (or Na) Batteries. *Chemical Reviews*, 113(8):6552–6591, aug 2013.
- [131] T. Maxisch, F. Zhou, and G. Ceder. Ab initio study of the migration of small polarons in olivine Li_xFePO₄ and their association with lithium ions and vacancies. *Physical Review B*, 73(10):104301, 2006.

- [132] I. McClelland, S. G. Booth, H. El-Shinawi, B. I. J. Johnston, J. Clough, W. Guo, E. J. Cussen, P. J. Baker, and S. A. Corr. In Situ Diffusion Measurements of a NASICON-Structured All-Solid-State Battery Using Muon Spin Relaxation. *ACS Applied Energy Materials*, jan 2021.
- [133] I. McKenzie, D. L. Cortie, M. Harada, R. F. Kiefl, C. D. P. Levy, W. A. MacFarlane, R. M. L. McFadden, G. D. Morris, S.-I. Ogata, M. R. Pearson, and J. Sugiyama. β -NMR measurements of molecular-scale lithium-ion dynamics in poly(ethylene oxide)-lithium-salt thin films. *The Journal of Chemical Physics*, 146(24):244903, jun 2017.
- [134] I. McKenzie, M. Harada, R. F. Kiefl, C. D. P. Levy, W. A. MacFarlane, G. D. Morris, S.-I. Ogata, M. R. Pearson, and J. Sugiyama. β -NMR Measurements of Lithium Ion Transport in Thin Films of Pure and Lithium-Salt-Doped Poly(ethylene oxide). *Journal of the American Chemical Society*, 136(22):7833–7836, jun 2014.
- [135] N. Meethong, H.-Y. S. Huang, W. C. Carter, and Y.-M. Chiang. Size-Dependent Lithium Miscibility Gap in Nanoscale Li_xFePO_4 . *Electrochemical and Solid-State Letters*, 10(5):A134, 2007.
- [136] J. Miao, T. Ishikawa, I. K. Robinson, and M. M. Murnane. Beyond crystallography: Diffractive imaging using coherent x-ray light sources. *Science*, 348(6234):530–535, may 2015.
- [137] S. L. Morelly, J. Gelb, F. Iacoviello, P. R. Shearing, S. J. Harris, N. J. Alvarez, and M. H. Tang. Three-Dimensional Visualization of Conductive Domains in Battery Electrodes with Contrast-Enhancing Nanoparticles. *ACS Applied Energy Materials*, 1(9):4479–4484, sep 2018.
- [138] D. Morgan, A. Van der Ven, and G. Ceder. Li Conductivity in Li_xMPO_4 ($M = \text{Mn, Fe, Co, Ni}$) Olivine Materials. *Electrochemical and Solid-State Letters*, 7(2):A30, 2004.

- [139] S. Müller, M. Lippuner, M. Verezhak, V. De Andrade, F. De Carlo, and V. Wood. Multimodal Nanoscale Tomographic Imaging for Battery Electrodes. *Advanced Energy Materials*, n/a(n/a):1904119, may 2020.
- [140] S. Müller, P. Pietsch, B.-E. Brandt, P. Baade, V. De Andrade, F. De Carlo, and V. Wood. Quantification and modeling of mechanical degradation in lithium-ion batteries based on nanoscale imaging. *Nature Communications*, 9(1):2340, 2018.
- [141] S. Muy, J. C. Bachman, L. Giordano, H.-H. Chang, D. L. Abernathy, D. Bansal, O. Delaire, S. Hori, R. Kanno, F. Maglia, S. Lupart, P. Lamp, and Y. Shao-Horn. Tuning mobility and stability of lithium ion conductors based on lattice dynamics. *Energy & Environmental Science*, 11(4):850–859, 2018.
- [142] N. Nadkarni, E. Rejovitsky, D. Fraggedakis, C. V. Di Leo, R. B. Smith, P. Bai, and M. Z. Bazant. Interplay of phase boundary anisotropy and electro-auto-catalytic surface reactions on the lithium intercalation dynamics in LiXFePO₄ plateletlike nanoparticles. *Physical Review Materials*, 2(8):85406, aug 2018.
- [143] J. Nelson Weker and M. F. Toney. Emerging In Situ and Operando Nanoscale X-Ray Imaging Techniques for Energy Storage Materials. *Advanced Functional Materials*, 25(11):1622–1637, mar 2015.
- [144] S.-i. Nishimura, G. Kobayashi, K. Ohoyama, R. Kanno, M. Yashima, and A. Yamada. Experimental visualization of lithium diffusion in Li_xFePO₄. *Nature Materials*, 7(9):707–711, sep 2008.
- [145] N. Nitta, F. Wu, J. T. Lee, and G. Yushin. Li-ion battery materials: present and future. *Materials Today*, 18(5):252–264, 2015.
- [146] L. Nowack, D. Grolimund, V. Samson, F. Marone, and V. Wood. Rapid Mapping of Lithiation Dynamics in Transition Metal Oxide Particles with Operando X-ray Absorption Spectroscopy. *Scientific Reports*, 6:21479, feb 2016.

- [147] D. Şopu, J. Kotakoski, and K. Albe. Finite-size effects in the phonon density of states of nanostructured germanium: A comparative study of nanoparticles, nanocrystals, nanoglasses, and bulk phases. *Physical Review B*, 83(24):245416, 2011.
- [148] W. Ostwald. Über die vermeintliche Isomerie des roten und gelben Quecksilberoxyds und die Oberflächenspannung fester Körper. *Zeitschrift für Physikalische Chemie*, 34U(1):495–503, 1900.
- [149] C. Ouyang, S. Shi, Z. Wang, X. Huang, and L. Chen. First-principles study of Li ion diffusion in LiFePO₄. *Physical Review B*, 69(10):104303, 2004.
- [150] J. Park, H. Zhao, S. D. Kang, K. Lim, C.-C. Chen, Y.-S. Yu, R. D. Braatz, D. A. Shapiro, J. Hong, M. F. Toney, M. Z. Bazant, and W. C. Chueh. Fictitious phase separation in Li layered oxides driven by electro-autocatalysis. *Nature Materials*, 2021.
- [151] K.-S. Park, P. Xiao, S.-Y. Kim, A. Dylla, Y.-M. Choi, G. Henkelman, K. J. Stevenson, and J. B. Goodenough. Enhanced Charge-Transfer Kinetics by Anion Surface Modification of LiFePO₄. *Chemistry of Materials*, 24(16):3212–3218, 2012.
- [152] K.-Y. Park, I. Park, H. Kim, G. Yoon, H. Gwon, Y. Cho, Y. S. Yun, J.-J. Kim, S. Lee, D. Ahn, Y. Kim, H. Kim, I. Hwang, W.-S. Yoon, and K. Kang. Lithium-excess olivine electrode for lithium rechargeable batteries. *Energy & Environmental Science*, 9(9):2902–2915, 2016.
- [153] J. P. Perdew, K. Burke, and M. Ernzerhof. Generalized Gradient Approximation Made Simple. *Physical Review Letters*, 77(18):3865–3868, oct 1996.
- [154] J. P. Perdew, A. Ruzsinszky, G. I. Csonka, O. A. Vydrov, G. E. Scuseria, L. A. Constantin, X. Zhou, and K. Burke. Restoring the Density-Gradient Expansion for Exchange in Solids and Surfaces. *Physical Review Letters*, 100(13):136406, 2008.
- [155] P. Pietsch, D. Westhoff, J. Feinauer, J. Eller, F. Marone, M. Stampioni, V. Schmidt, and V. Wood. Quantifying microstructural

- dynamics and electrochemical activity of graphite and silicon-graphite lithium ion battery anodes. *Nature Communications*, 7:12909, sep 2016.
- [156] P. Pietsch and V. Wood. X-Ray Tomography for Lithium Ion Battery Research: A Practical Guide. *Annual Review of Materials Research*, 47(1):451–479, jul 2017.
- [157] C. Prehal, C. Koczwara, N. Jäckel, A. Schreiber, M. Burian, H. Amenitsch, M. A. Hartmann, V. Presser, and O. Paris. Quantification of ion confinement and desolvation in nanoporous carbon supercapacitors with modelling and in situ X-ray scattering. *Nature Energy*, 2:16215, jan 2017.
- [158] X. Qin, J. Wang, J. Xie, F. Li, L. Wen, and X. Wang. Hydrothermally synthesized LiFePO₄ crystals with enhanced electrochemical properties: simultaneous suppression of crystal growth along [010] and antisite defect formation. *Phys Chem Chem Phys*, 14(8):2669–2677, 2012.
- [159] P. M. Richards. Theory of one-dimensional hopping conductivity and diffusion. *Physical Review B*, 16(4):1393–1409, 1977.
- [160] J. B. Robinson, J. A. Darr, D. S. Eastwood, G. Hinds, P. D. Lee, P. R. Shearing, O. O. Taiwo, and D. J. L. Brett. Non-uniform temperature distribution in Li-ion batteries during discharge – A combined thermal imaging, X-ray micro-tomography and electrochemical impedance approach. *Journal of Power Sources*, 252:51–57, 2014.
- [161] M.-T. F. Rodrigues, G. Babu, H. Gullapalli, K. Kalaga, F. N. Sayed, K. Kato, J. Joyner, and P. M. Ajayan. A materials perspective on Li-ion batteries at extreme temperatures. *Nature Energy*, 2:17108, jul 2017.
- [162] L. Romano Brandt, J.-J. Marie, T. Moxham, D. P. Förstermann, E. Salvati, C. Besnard, C. Papadaki, Z. Wang, P. G. Bruce,

- and A. M. Korsunsky. Synchrotron X-ray quantitative evaluation of transient deformation and damage phenomena in a single nickel-rich cathode particle. *Energy & Environmental Science*, 13(10):3556–3566, 2020.
- [163] F. D. Rossini. Heat capacities in some aqueous solutions. In *Bureau of Standards Journal of Research*, pages 313–327. National Bureau of Standards, 1930.
- [164] J. Rumble. *CRC Handbook of Chemistry and Physics*. CRC Press, Boca Raton, Florida, 97 edition, 2017.
- [165] L. Salvati Manni, S. Assenza, M. Duss, J. J. Vallooran, F. Juranyi, S. Jurt, O. Zerbe, E. M. Landau, and R. Mezzenga. Soft biomimetic nanoconfinement promotes amorphous water over ice. *Nature Nanotechnology*, 14(6):609–615, 2019.
- [166] S. Schmidt, D. Sheptyakov, J.-C. Jumas, M. Medarde, P. Benedek, P. Novák, S. Sallard, and C. Villevieille. Lithium Iron Methylenediphosphonate: A Model Material for New Organic–Inorganic Hybrid Positive Electrode Materials for Li Ion Batteries. *Chemistry of Materials*, 27(23):7889–7895, dec 2015.
- [167] C. A. Schneider, W. S. Rasband, and K. W. Eliceiri. NIH Image to ImageJ: 25 years of image analysis. *Nature Methods*, 9:671, jun 2012.
- [168] V. F. Sears. Neutron scattering lengths and cross sections. *Neutron News*, 3(3):26–37, 1992.
- [169] S. Seidlmayer, J. Hattendorff, I. Buchberger, L. Karge, H. A. Gasteiger, and R. Gilles. In Operando Small-Angle Neutron Scattering (SANS) on Li-Ion Batteries. *Journal of The Electrochemical Society*, 162(2):A3116–A3125, jan 2015.
- [170] Z. Shadike, H. Lee, O. Borodin, X. Cao, X. Fan, X. Wang, R. Lin, S.-M. Bak, S. Ghose, K. Xu, C. Wang, J. Liu, J. Xiao, X.-Q. Yang, and E. Hu. Identification of LiH and nanocrystalline LiF in the solid–electrolyte interphase of lithium metal anodes. *Nature Nanotechnology*, 2021.

- [171] D. A. Shapiro, Y.-S. Yu, T. Tyliczszak, J. Cabana, R. Celestre, W. Chao, K. Kaznatcheev, A. L. D. Kilcoyne, F. Maia, S. Marchesini, Y. S. Meng, T. Warwick, L. L. Yang, and H. A. Padmore. Chemical composition mapping with nanometre resolution by soft X-ray microscopy. *Nature Photonics*, 8:765, sep 2014.
- [172] P. K. Sharma, R. K. Dutta, A. C. Pandey, S. Layek, and H. C. Verma. Effect of iron doping concentration on magnetic properties of ZnO nanoparticles. *Journal of Magnetism and Magnetic Materials*, 321(17):2587–2591, 2009.
- [173] W. A. Sławiński, H. Y. Playford, S. Hull, S. T. Norberg, S. G. Eriksson, T. Gustafsson, K. Edström, and W. R. Brant. Neutron Pair Distribution Function Study of FePO₄ and LiFePO₄. *Chemistry of Materials*, 31(14):5024–5034, jul 2019.
- [174] A. Sood, A. D. Poletayev, D. A. Cogswell, P. M. Csernica, J. T. Mefford, D. Fraggedakis, M. F. Toney, A. M. Lindenberg, M. Z. Bazant, and W. C. Chueh. Electrochemical Ion Insertion: From Atoms to Devices, 2020.
- [175] D. A. Stevens and J. R. Dahn. The Mechanisms of Lithium and Sodium Insertion in Carbon Materials. *Journal of The Electrochemical Society*, 148(8):A803–A811, aug 2001.
- [176] J. M. Stratford, M. Mayo, P. K. Allan, O. Pecher, O. J. Borkiewicz, K. M. Wiaderek, K. W. Chapman, C. J. Pickard, A. J. Morris, and C. P. Grey. Investigating Sodium Storage Mechanisms in Tin Anodes: A Combined Pair Distribution Function Analysis, Density Functional Theory, and Solid-State NMR Approach. *Journal of the American Chemical Society*, 139(21):7273–7286, may 2017.
- [177] D. R. Stull. Vapor Pressure of Pure Substances. Organic and Inorganic Compounds. *Industrial & Engineering Chemistry*, 39(4):517–540, apr 1947.
- [178] J. Sugiyama. Spin polarized beam for battery materials research: $\mu\pm$ SR and β -NMR. *Hyperfine Interactions*, 240(1):17, 2019.

- [179] J. Sugiyama, K. Mukai, Y. Ikedo, H. Nozaki, M. Månsson, and I. Watanabe. Li Diffusion in LiCoO₂ Probed by Muon-Spin Spectroscopy. *Physical Review Letters*, 103(14):147601, sep 2009.
- [180] J. Sugiyama, H. Nozaki, M. Harada, K. Kamazawa, Y. Ikedo, Y. Miyake, O. Ofer, M. Månsson, E. J. Ansaldo, K. H. Chow, G. Kobayashi, and R. Kanno. Diffusive behavior in LiMPO₄ with M=Fe, Co, Ni probed by muon-spin relaxation. *Physical Review B*, 85(5):54111, 2012.
- [181] J. Sugiyama, H. Nozaki, M. Harada, K. Kamazawa, O. Ofer, M. Månsson, J. H. Brewer, E. J. Ansaldo, K. H. Chow, Y. Ikedo, Y. Miyake, K. Ohishi, I. Watanabe, G. Kobayashi, and R. Kanno. Magnetic and diffusive nature of LiFePO₄ investigated by muon spin rotation and relaxation. *Physical Review B*, 84(5):054430, aug 2011.
- [182] M. Sumita, Y. Tanaka, M. Ikeda, and T. Ohno. Theoretically Designed Li₃PO₄ (100)/LiFePO₄ (010) Coherent Electrolyte/Cathode Interface for All Solid-State Li Ion Secondary Batteries. *The Journal of Physical Chemistry C*, 119(1):14–22, 2015.
- [183] C. Sun, S. Rajasekhara, J. B. Goodenough, and F. Zhou. Monodisperse Porous LiFePO₄ Microspheres for a High Power Li-Ion Battery Cathode. *Journal of the American Chemical Society*, 133(7):2132–2135, feb 2011.
- [184] A. Suter and B. M. Wojek. Musrfit: A Free Platform-Independent Framework for μ SR Data Analysis. *Physics Procedia*, 30:69–73, 2012.
- [185] D. Suter and R. R. Ernst. Spin diffusion in resolved solid-state NMR spectra. *Physical Review B*, 32(9):5608–5627, nov 1985.
- [186] B. S. Swartzentruber. Direct Measurement of Surface Diffusion Using Atom-Tracking Scanning Tunneling Microscopy. *Physical Review Letters*, 76(3):459–462, jan 1996.
- [187] K. R. Tallman, G. P. Wheeler, C. J. Kern, E. Stavitski, X. Tong, K. J. Takeuchi, A. C. Marschilok, D. C. Bock, and E. S. Takeuchi.

- Nickel-rich Nickel Manganese Cobalt (NMC622) Cathode Lithiation Mechanism and Extended Cycling Effects Using Operando X-ray Absorption Spectroscopy. *The Journal of Physical Chemistry C*, 125(1):58–73, jan 2021.
- [188] K. Tang, X. Yu, J. Sun, H. Li, and X. Huang. Kinetic analysis on LiFePO₄ thin films by CV, GITT, and EIS. *Electrochimica Acta*, 56(13):4869–4875, 2011.
- [189] M. Tang, A. Dalzini, X. Li, X. Feng, P.-H. Chien, L. Song, and Y.-Y. Hu. Operando EPR for Simultaneous Monitoring of Anionic and Cationic Redox Processes in Li-Rich Metal Oxide Cathodes. *The Journal of Physical Chemistry Letters*, 8(17):4009–4016, sep 2017.
- [190] Y. Tian, Y. Sun, D. C. Hannah, Y. Xiao, H. Liu, K. W. Chapman, S.-H. Bo, and G. Ceder. Reactivity-Guided Interface Design in Na Metal Solid-State Batteries. *Joule*, 3(4):1037–1050, 2019.
- [191] R. Toft-Petersen, M. Reehuis, T. B. S. Jensen, N. H. Andersen, J. Li, M. D. Le, M. Laver, C. Niedermayer, B. Klemke, K. Lefmann, and D. Vaknin. Anomalous magnetic structure and spin dynamics in magnetoelectric LiFePO₄. *Physical Review B*, 92(2):24404, jul 2015.
- [192] A. Togo and I. Tanaka. First principles phonon calculations in materials science. *Scripta Materialia*, 108:1–5, 2015.
- [193] K. Toyoura, Y. Koyama, A. Kuwabara, F. Oba, and I. Tanaka. First-principles approach to chemical diffusion of lithium atoms in a graphite intercalation compound. *Physical Review B*, 78(21):214303, 2008.
- [194] E. H. R. Tsai, J. Billaud, D. F. Sanchez, J. Ihli, M. Odstrčil, M. Holler, D. Grolimund, C. Villevieille, and M. Guizar-Sicairos. Correlated X-Ray 3D Ptychography and Diffraction Microscopy Visualize Links between Morphology and Crystal Structure of Lithium-Rich Cathode Materials. *iScience*, 11:356–365, 2019.

- [195] F. Tsai and W. Philpot. Derivative Analysis of Hyperspectral Data. *Remote Sensing of Environment*, 66(1):41–51, 1998.
- [196] P.-C. Tsai, B. Wen, M. Wolfman, M.-J. Choe, M. S. Pan, L. Su, K. Thornton, J. Cabana, and Y.-M. Chiang. Single-particle measurements of electrochemical kinetics in NMC and NCA cathodes for Li-ion batteries. *Energy & Environmental Science*, 11(4):860–871, 2018.
- [197] M. Tyagi and S. M. Chathoth. Quasielastic Neutron Scattering: An Advanced Technique for Studying the Relaxation Processes in Condensed Matter BT - X-ray and Neutron Techniques for Nanomaterials Characterization. pages 761–813. Springer Berlin Heidelberg, Berlin, Heidelberg, 2016.
- [198] I. Umegaki, S. Kawauchi, H. Sawada, H. Nozaki, Y. Higuchi, K. Miwa, Y. Kondo, M. Månsson, M. Telling, F. C. Coomer, S. P. Cottrell, T. Sasaki, T. Kobayashi, and J. Sugiyama. Li-ion diffusion in Li intercalated graphite C6Li and C12Li probed by μ +SR. *Physical Chemistry Chemical Physics*, 19(29):19058–19066, 2017.
- [199] A. Van der Ven, J. Bhattacharya, and A. A. Belak. Understanding Li Diffusion in Li-Intercalation Compounds. *Accounts of chemical research*, 46(5):1216–1225, 2013.
- [200] J. VandeVondele and J. Hutter. Gaussian basis sets for accurate calculations on molecular systems in gas and condensed phases. *The Journal of Chemical Physics*, 127(11):114105, 2007.
- [201] J. VandeVondele, M. Krack, F. Mohamed, M. Parrinello, T. Chassaing, and J. Hutter. Quickstep: Fast and accurate density functional calculations using a mixed Gaussian and plane waves approach. *Computer Physics Communications*, 167(2):103–128, 2005.
- [202] J. Vatamanu, O. Borodin, and G. D. Smith. Molecular Dynamics Simulation Studies of the Structure of a Mixed Carbonate/LiPF6

- Electrolyte near Graphite Surface as a Function of Electrode Potential. *The Journal of Physical Chemistry C*, 116(1):1114–1121, jan 2012.
- [203] T. W. Verhallen, S. Lv, and M. Wagemaker. Operando Neutron Depth Profiling to Determine the Spatial Distribution of Li in Li-ion Batteries, 2018.
- [204] P. Verma, P. Maire, and P. Novák. A review of the features and analyses of the solid electrolyte interphase in Li-ion batteries. *Electrochimica Acta*, 55(22):6332–6341, 2010.
- [205] M. Wagemaker, F. M. Mulder, and A. Van der Ven. The Role of Surface and Interface Energy on Phase Stability of Nanosized Insertion Compounds. *Advanced Materials*, 21(25-26):2703–2709, 2009.
- [206] C. Wang, Y. Gong, J. Dai, L. Zhang, H. Xie, G. Pastel, B. Liu, E. Wachsman, H. Wang, and L. Hu. In Situ Neutron Depth Profiling of Lithium Metal–Garnet Interfaces for Solid State Batteries. *Journal of the American Chemical Society*, 139(40):14257–14264, oct 2017.
- [207] J. Wang and X. Sun. Understanding and recent development of carbon coating on LiFePO₄ cathode materials for lithium-ion batteries. *Energy & Environmental Science*, 5(1):5163–5185, 2012.
- [208] L. Wang, F. Zhou, Y. Meng, and G. Ceder. First-principles study of surface properties of LiFePO₄: Surface energy, structure, Wulff shape, and surface redox potential. *Physical Review B*, 76(16), 2007.
- [209] X. Wang, Y. Li, and Y. S. Meng. Cryogenic Electron Microscopy for Characterizing and Diagnosing Batteries. *Joule*, 2(11):2225–2234, 2018.
- [210] Y. Wang, D. J. Asunsakis, and P. M. A. Sherwood. Iron (II) Phosphate (Fe₃(PO₄)₂) by XPS. *Surface Science Spectra*, 9(1):91–98, dec 2002.

- [211] Y. Wang and P. M. A. Sherwood. Iron (III) Phosphate (FePO₄) by XPS. *Surface Science Spectra*, 9(1):99–105, dec 2002.
- [212] Y. Wang, D. Zhang, C. Chang, L. Deng, and K. Huang. Controllable growth of LiFePO₄ microplates of (010) and (001) lattice planes for Li ion batteries: A case of the growth manner on the Li ion diffusion coefficient and electrochemical performance. *Materials Chemistry and Physics*, 148(3):933–939, 2014.
- [213] Z. Wang, D. Santhanagopalan, W. Zhang, F. Wang, H. L. Xin, K. He, J. Li, N. Dudney, and Y. S. Meng. In Situ STEM-EELS Observation of Nanoscale Interfacial Phenomena in All-Solid-State Batteries. *Nano Letters*, 16(6):3760–3767, jun 2016.
- [214] M. Wilkening, V. Epp, A. Feldhoff, and P. Heitjans. Tuning the Li Diffusivity of Poor Ionic Conductors by Mechanical Treatment: High Li Conductivity of Strongly Defective LiTaO₃ Nanoparticles. *The Journal of Physical Chemistry C*, 112(25):9291–9300, jun 2008.
- [215] J. M. Wilkinson and S. J. Blundell. Information and decoherence in a muon-fluorine coupled system. *Phys. Rev. Lett.*, 125:087201, Aug 2020.
- [216] B. Winiarski. Plasma FIB Spin Milling Accelerates Battery Research. *Microscopy and Microanalysis*, 26(S2):2226–2227, 2020.
- [217] M. Winter. The Solid Electrolyte Interphase – The Most Important and the Least Understood Solid Electrolyte in Rechargeable Li Batteries. *Zeitschrift für Physikalische Chemie*, 223(10-11):1395–1406, dec 2009.
- [218] M. Winter, B. Barnett, and K. Xu. Before Li Ion Batteries. *Chemical Reviews*, 118(23):11433–11456, dec 2018.
- [219] J. Woerle, T. Prokscha, and U. Grossner. Low-Energy Muons as a Tool for a Depth-Resolved Analysis of the SiO₂/4H-SiC Interface. *Materials Science Forum*, 1004:581–586, 2020.

- [220] V. Wood. X-ray tomography for battery research and development. *Nature Reviews Materials*, 3(9):293–295, 2018.
- [221] F. Wu and N. Yao. Advances in sealed liquid cells for in-situ TEM electrochemical investigation of lithium-ion battery. *Nano Energy*, 11:196–210, 2015.
- [222] J. Wu, Q. Li, S. Sallis, Z. Zhuo, W. E. Gent, W. C. Chueh, S. Yan, Y.-d. Chuang, and W. Yang. Fingerprint Oxygen Redox Reactions in Batteries through High-Efficiency Mapping of Resonant Inelastic X-ray Scattering. *Condensed Matter*, 4(1):5, 2019.
- [223] O. Xiuqin, P. Lin, G. Haichen, W. Yichen, and L. Jianwei. Temperature-dependent crystallinity and morphology of LiFePO₄ prepared by hydrothermal synthesis. *Journal of Materials Chemistry*, 22(18):9064, 2012.
- [224] P. Yan, J. Zheng, J. Zheng, Z. Wang, G. Teng, S. Kuppan, J. Xiao, G. Chen, F. Pan, J.-G. Zhang, and C.-M. Wang. Ni and Co Segregations on Selective Surface Facets and Rational Design of Layered Lithium Transition-Metal Oxide Cathodes. *Advanced Energy Materials*, 6(9):1502455, may 2016.
- [225] H. Yang, C. N. Savory, B. J. Morgan, D. O. Scanlon, J. M. Skelton, and A. Walsh. Chemical Trends in the Lattice Thermal Conductivity of Li(Ni, Mn, Co)O₂ (NMC) Battery Cathodes. *Chemistry of Materials*, 32(17):7542–7550, sep 2020.
- [226] J. Yang and J. S. Tse. Li Ion Diffusion Mechanisms in LiFePO₄: An ab Initio Molecular Dynamics Study. *The Journal of Physical Chemistry A*, 115(45):13045–13049, 2011.
- [227] S. Yang, X. Zhou, J. Zhang, and Z. Liu. Morphology-controlled solvothermal synthesis of LiFePO₄ as a cathode material for lithium-ion batteries. *Journal of Materials Chemistry*, 20(37):8086, 2010.
- [228] K. P. C. Yao, J. S. Okasinski, K. Kalaga, I. A. Shkrob, and D. P. Abraham. Quantifying lithium concentration gradients in the

- graphite electrode of Li-ion cells using operando energy dispersive X-ray diffraction. *Energy & Environmental Science*, 12(2):656–665, 2019.
- [229] A. Yaouanc and P. Dalmas de Réotier. *Muon Spin Rotation, Relaxation, and Resonance: Applications to Condensed Matter*. International Series of Monogr. OUP Oxford, 2011.
- [230] Y. Yiu, M. D. Le, R. Toft-Petersen, G. Ehlers, R. J. McQueeney, and D. Vaknin. Hybrid excitations due to crystal field, spin-orbit coupling, and spin waves in LiFePO₄. *Physical Review B*, 95(10):104409, 2017.
- [231] M. Yoshimura and K. Byrappa. Hydrothermal processing of materials: past, present and future. *Journal of Materials Science*, 43(7):2085–2103, 2008.
- [232] Y.-S. Yu, M. Farmand, C. Kim, Y. Liu, C. P. Grey, F. C. Strobridge, T. Tyliszczak, R. Celestre, P. Denes, J. Joseph, H. Krishnan, F. R. N. C. Maia, A. L. D. Kilcoyne, S. Marchesini, T. P. C. Leite, T. Warwick, H. Padmore, J. Cabana, and D. A. Shapiro. Three-dimensional localization of nanoscale battery reactions using soft X-ray tomography. *Nature Communications*, 9(1):921, 2018.
- [233] M. J. Zachman, Z. Tu, S. Choudhury, L. A. Archer, and L. F. Kourkoutis. Cryo-STEM mapping of solid–liquid interfaces and dendrites in lithium-metal batteries. *Nature*, 560(7718):345–349, 2018.
- [234] K. Zaghbi, A. Mauger, F. Gendron, and C. M. Julien. Surface Effects on the Physical and Electrochemical Properties of Thin LiFePO₄ Particles. *Chemistry of Materials*, 20(2):462–469, 2008.
- [235] K. Zaghbi, A. Mauger, J. B. Goodenough, F. Gendron, and C. M. Julien. Electronic, Optical, and Magnetic Properties of LiFePO₄: Small Magnetic Polaron Effects. *Chemistry of Materials*, 19(15):3740–3747, 2007.

- [236] R. Zahn, M. F. Lagadec, M. Hess, and V. Wood. Improving Ionic Conductivity and Lithium-Ion Transference Number in Lithium-Ion Battery Separators. *ACS Applied Materials & Interfaces*, 8(48):32637–32642, dec 2016.
- [237] H. Zeng, Y. Gu, G. Teng, Y. Liu, J. Zheng, and F. Pan. Ab initio identification of the Li-rich phase in LiFePO₄. *Physical Chemistry Chemical Physics*, 20(25):17497–17503, 2018.
- [238] W. Zhang, H.-C. Yu, L. Wu, H. Liu, A. Abdellahi, B. Qiu, J. Bai, B. Orvananos, F. C. Strobridge, X. Zhou, Z. Liu, G. Ceder, Y. Zhu, K. Thornton, C. P. Grey, and F. Wang. Localized concentration reversal of lithium during intercalation into nanoparticles. *Science Advances*, 4(1):eaao2608, jan 2018.
- [239] X. Zhang, I. Belharouak, L. Li, Y. Lei, J. W. Elam, A. Nie, X. Chen, R. S. Yassar, and R. L. Axelbaum. Structural and Electrochemical Study of Al₂O₃ and TiO₂ Coated Li_{1.2}Ni_{0.13}Mn_{0.54}Co_{0.13}O₂ Cathode Material Using ALD. *Advanced Energy Materials*, 3(10):1299–1307, oct 2013.
- [240] X. Zhang, M. van Hulzen, D. P. Singh, A. Brownrigg, J. P. Wright, N. H. van Dijk, and M. Wagemaker. Rate-Induced Solubility and Suppression of the First-Order Phase Transition in Olivine LiFePO₄. *Nano Letters*, 14(5):2279–2285, may 2014.
- [241] E. Zhao, Z.-G. Zhang, X. Li, L. He, X. Yu, H. Li, and F. Wang. Neutron-based characterization techniques for lithium-ion battery research. *Chinese Physics B*, 29(1):18201, 2020.

Curriculum Vitae

Personal Data

Name	Peter Benedek
Date of birth	December 26, 1990
Citizen of	Aarwangen, BE, Switzerland
Nationality	Swiss

Education

2015 – 2021	Doctoral student, ETH Zürich, Materials and Device Engineering group, Institute for Electronics, Department of Information Technology and Electrical Engineering
2013 – 2015	M. Sc. Interdisciplinary Sciences, major in Physics and Chemistry, ETH Zürich. M. Sc. with distinction, Apr. 2015. GPA: 5.86/6.00
2009 – 2013	B. Sc. Interdisciplinary Sciences, major in Physics and Chemistry, ETH Zürich B. Sc., Jan. 2013. GPA: 5.06/6.00
2005 – 2009	Kantonsschule Oberaargau, Langenthal, Switzerland. Matura in June, 2009

Journal Papers

- (8) Chen H.*; **Benedek, P.***; Fisher, J.*; Wood, V. C.; Cui, Y.; Self-assembled materials for electrochemical energy storage. *MRS Bulletin* **45** (10), 815-822 **2020**.
- (7) **Benedek, P.**; Forslund, O. K.; Nocerino, E.; Yazdani, N.; Matsubara, N.; Sassa, Y.; Juranyi, F.; Medarde, M.; Telling, M.; Månsson, M.; Wood, V.C.; Quantifying Diffusion through Interfaces of Lithium Ion Batteries Active Materials. *ACS Appl. Mater. Interfaces* **12** (14), 16243-16249 **2020**.
- (6) **Benedek, P.**; Yazdani, N.; Chen, H.; Wenzler, N.; Juranyi, F.; Månsson, M.; Islam, M. S.; Wood, V. C.; Surface phonons of lithium ion battery active materials. *Sustain. Energy Fuels* **3** (2), 508-513, **2019**.
- (5) **Benedek, P.**; Wenzler, N.; Yarema, M.; Wood, V. C.; Low temperature hydrothermal synthesis of battery grade lithium iron phosphate. *RSC Advances* **7** (29) 17763-17767, **2017**.
- (4) Schmidt, S.; Sheptyakov, D.M; Juams, J.; Medarde, M.; **Benedek, P.**; Novák, P.; Sallard, S.; Villeveille, C.; Lithium Iron Methylenediphosphate: A Model Material for New Organic-Inorganic Hybrid Positive Electrode Materials for Li Ion Batteries. *Chem. Mater.* **27** (23) 7889-7895, **2015**.
- (3) Shunmugasundaram, R.; Arumugan, R.; Baade, P; **Benedek P.**; Yarema, M.; Wood, V.C.; Water based preparation of High Ni content layered oxide cathode materials, *in Preparation*.
- (2) **Benedek, P.**; Wood, V. C.; How large scale facilities enable the Development of Li ion Batteries, *in Preparation*.
- (1) **P. Benedek**, X. Zhao, E. Billeter, A. Moser, O. Forslund, N. Matsubara, E. Nocerino, S. Cottrell, M. Medarde, Y. Sassa, R. Shunmugasundaram, A. Borgschulte, F. Jurányi, M. Mansson, V. Wood; Controlling lithium ion battery (de)intercalation dynamics through interface design, *in Preparation*.

Organization of Conferences

- 2019 – 2023 Co-chair Gordon Research Seminar
Nanomaterials in Applications for Energy Technology
- 2019 – 2020 Member of the organization committee
Material and Processes Virtual Graduate Symposium

Invited Contributions

- (4) **Material and Processes Graduate Symposium, 2021.** *Discussion leader* Thematic Energy Group
- (3) **Stanford University, Jaramillo group** *Invited Talk:* Controlling lithium ion battery (de)intercalation dynamics through interface design.
- (2) **Swedish Neutron Week 2019:** Surface Phonons of Lithium Ion Battery Active Materials.
- (1) **Stanford University/SLAC, Seminar Chueh, Lindenberg group** *Invited Talk:* Surface Dynamics in Lithium ion Battery active Materials.

Contributed Oral Presentations

- (8) **Materials and Processes Graduate Symposium (2021):** Controlling lithium ion battery (de)intercalation dynamics through interface design.
- (7) **Material Research Society Spring Meeting (2021):** Controlling lithium ion battery (de)intercalation dynamics through interface design.
- (6) **Swiss Chemical Society Meeting (2020):** Quantifying diffusion through lithium ion battery interfaces.
- (5) **Swiss Battery Days and Surrounding (2019):** Surface Phonons of Lithium Ion Battery Active Materials.
- (4) **Materials and Processes Graduate Symposium (2019):** Surface Phonons of Lithium Ion Battery Active Materials (*Science Pitch*).
- (3) **Gordon Research Seminar: Nanomaterials for Applications in Energy Technology (2019):** Surface Phonons of Lithium Ion Battery Active Materials.

- (2) **Material Research Society Fall Meeting (2018)**: Surface Phonons of Lithium Ion Battery Active Materials.
- (1) **Hermes Summer School (2018)**: Surface Phonons of Lithium Ion Battery Active Materials (*Science Pitch*).

